THE MAGNETIC STRUCTURES AND THEIR ROLE IN THE EVOLUTION OF CORONAL MASS EJECTIONS

EDITED BY: Qiang Hu, Hongqiang Song and HengQiang Feng
PUBLISHED IN: Frontiers in Physics

frontiers Research Topics

ISSN 1664-8714
ISBN 978-2-88974-303-2
DOI 10.3389/978-2-88974-303-2

About Frontiers

Frontiers is more than just an open-access publisher of scholarly articles: it is a pioneering approach to the world of academia, radically improving the way scholarly research is managed. The grand vision of Frontiers is a world where all people have an equal opportunity to seek, share and generate knowledge. Frontiers provides immediate and permanent online open access to all its publications, but this alone is not enough to realize our grand goals.

Frontiers Journal Series

The Frontiers Journal Series is a multi-tier and interdisciplinary set of open-access, online journals, promising a paradigm shift from the current review, selection and dissemination processes in academic publishing. All Frontiers journals are driven by researchers for researchers; therefore, they constitute a service to the scholarly community. At the same time, the Frontiers Journal Series operates on a revolutionary invention, the tiered publishing system, initially addressing specific communities of scholars, and gradually climbing up to broader public understanding, thus serving the interests of the lay society, too.

Dedication to Quality

Each Frontiers article is a landmark of the highest quality, thanks to genuinely collaborative interactions between authors and review editors, who include some of the world's best academicians. Research must be certified by peers before entering a stream of knowledge that may eventually reach the public - and shape society; therefore, Frontiers only applies the most rigorous and unbiased reviews.
Frontiers revolutionizes research publishing by freely delivering the most outstanding research, evaluated with no bias from both the academic and social point of view. By applying the most advanced information technologies, Frontiers is catapulting scholarly publishing into a new generation.

What are Frontiers Research Topics?

Frontiers Research Topics are very popular trademarks of the Frontiers Journals Series: they are collections of at least ten articles, all centered on a particular subject. With their unique mix of varied contributions from Original Research to Review Articles, Frontiers Research Topics unify the most influential researchers, the latest key findings and historical advances in a hot research area! Find out more on how to host your own Frontiers Research Topic or contribute to one as an author by contacting the Frontiers Editorial Office: frontiersin.org/about/contact

THE MAGNETIC STRUCTURES AND THEIR ROLE IN THE EVOLUTION OF CORONAL MASS EJECTIONS

Topic Editors:
Qiang Hu, University of Alabama in Huntsville, United States
Hongqiang Song, Shandong University, China
HengQiang Feng, Luoyang Normal University, China

Citation: Hu, Q., Song, H., Feng, H., eds. (2022). The Magnetic Structures and Their Role in the Evolution of Coronal Mass Ejections. Lausanne: Frontiers Media SA. doi: 10.3389/978-2-88974-303-2

Table of Contents

frontiers in Physics

EDITORIAL
published: 21 December 2021
doi: 10.3389/fphy.2021.820476

Editorial: The Magnetic Structures and Their Role in The Evolution of Coronal Mass Ejections

Hengqiang Feng[1], *Qiang Hu*[2]* *and Hongqiang Song*[3]

[1]Institute of Space Physics, Luoyang Normal University, Luoyang, China, [2]Department of Space Science and CSPAR, The University of Alabama in Huntsville, Huntsville, AL, United States, [3]Shandong Provincial Key Laboratory of Optical Astronomy and Solar-Terrestrial Environment, and Institute of Space Sciences, Shandong University, Weihai, China

Keywords: heliophysics, space weather, coronal mass ejection, solar corona and wind, space physics, plasma physics

Editorial on the Research Topic

The Magnetic Structures and Their Role in The Evolution of Coronal Mass Ejections

Coronal mass ejections (CMEs) are the most energetic eruptions from the Sun and an important driver for space weather [1], which has significant impact on the technological systems of modern society. The aim of this research topic is to present multi-faceted research, from distinctive perspectives involving the forefront of Heliophysics—the science about the Sun, the Earth, and what's in-between, on the magnetic structures and other key ingredients of CMEs at different evolution stages. Multiple analysis tools, including theoretical, numerical, and observational ones, are employed, making use of a variety of ground-based and space-borne remote-sensing and *in-situ* measurements [2–5].

The magnetic structures of the solar source regions (usually the so-called active regions, i.e., ARs) are key to understanding the origination of CMEs [6–9]. Jiang et al. report a detailed analysis of the formation of a magnetic flux rope, the typical magnetic field configuration embodied by a CME, during the eruption process associated with solar flares/CMEs. They perform the state-of-the-art magnetohydrodynamic (MHD) numerical simulation for a general source region magnetic field topology. Their results reveal the corresponding topological change of the magnetic flux rope configuration. They find that the flux rope is formed via magnetic reconnection through a well-known process, and additionally in the later phase, the reconnection proceeds between the field lines of the flux rope. The corresponding "increase-to-decrease" change in the amount of toroidal magnetic flux agrees with the latest observational results. In a related numerical study, combined with observations, but focusing more on particular event studies, Vemareddy presents the topological analysis of two ARs that produced multiple CMEs, and shows the co-location between the remote-sensing signatures of flare ribbons, the brightening features as observed during flares, and the extrapolated magnetic field above the AR (indicative of magnetic flux rope structure at one particular point in time) based on a non-linear force-free field (NLFFF) model. This study confirms the role of magnetic flux rope in forming the core magnetic structures of CMEs. In another study, Xue et al. discuss the relatively rare spectroscopic observation of a prominence eruption leading to CME. A prominence is generally considered to be a proxy of magnetic flux rope. They are able to derive the change in plasma properties and kinematics associated with this prominence eruption.

As CMEs erupt and propagate into the interplanetary space, they may be detected *in-situ* when passing one or more spacecraft (thus identified and named as interplanetary CMEs, i.e., ICMEs), in addition to continuous remote-sensing observations such as coronagraphic imaging and radio waves. Such *in-situ* observations often yield a more complete and quantitative set of magnetic field and bulk

OPEN ACCESS

Edited and reviewed by:
Scott William McIntosh, National Center for Atmospheric Research (UCAR), United States

***Correspondence:**
Qiang Hu
qiang.hu@uah.edu

Specialty section:
This article was submitted to Stellar and Solar Physics, a section of the journal Frontiers in Physics

Received: *23 November 2021*
Accepted: *30 November 2021*
Published: *21 December 2021*

Citation:
Feng H, Hu Q and Song H (2021) Editorial: The Magnetic Structures and Their Role in The Evolution of Coronal Mass Ejections. Front. Phys. 9:820476. doi: 10.3389/fphy.2021.820476

plasma parameters, albeit only along one or more discrete points/lines across the structures. This has enabled many studies of ICMEs (including the so-called magnetic clouds, or large-scale magnetic flux ropes) for decades. Wu et al. present a large study by using a simple model for magnetic flux ropes based on the Wind spacecraft *in-situ* measurements. They show modifications and improvement to the original model by applying to many Wind spacecraft events. Hu et al. present a detailed study of a magnetic flux rope event detected *in-situ* by two spacecraft that were approximately aligned radially but separated by about 0.2 astronomical units in radial distance. By applying both a two-dimensional (2D) and a three-dimensional (3D) magnetic flux rope model, they reveal the reconstructed magnetic flux rope configurations characterized by spiral magnetic field lines. It is worth noting that the evolution of ICMEs in interplanetary space is also affected by the background solar wind medium. Therefore an improved characterization of the ambient solar wind conditions, e.g., via numerical means, is also being actively pursued, as demonstrated by Liu et al. They report a numerical study for improving the performance of a 3D MHD model of the interplanetary medium in which CMEs propagate. Shen et al. investigate the role of ICMEs in causing geomagnetic disturbances, especially by imposing strong and long-duration southward magnetic field onto near-Earth environment. They find that the interactions between large-scale structures including multiple ICMEs and interplanetary shock waves lead to intensified southward field component. A unique study by Zhang et al. examines the solar radio burst signatures often associated with the CMEs upon their eruptions and propagation. They employ the advanced deep learning algorithms to automatically identify and classify different types of radio bursts.

In addition to the direct employment of magnetic and plasma fluid property measurements of ICMEs, the discrete particle populations including streaming electrons and heavy ions are also important in probing the magnetic structures and other relevant conditions in the heliospheric environment. In addition, a series of studies looks into the relatively small-scale structures or those with more intermittent occurrence in the solar wind. Wang and Zhao find magnetic reconnection signatures that deviate from a quasi-steady state. Liu et al. perform a statistical study of small-scale magnetic flux ropes near the heliospheric current sheet (HCS) and find that they may mostly originate from the HCS. The role of magnetic reconnection in the interplanetary space on the change of topology/connectivity of magnetic flux ropes is further examined by Feng et al., using primarily the high-resolution magnetic field and plasma measurements, together with the suprathermal electrons (in the energy range of a few hundred eV) that always stream away from the Sun along magnetic field lines. Different topologies can be inferred from these observations and the results indicate that magnetic reconnection is an active process for magnetic flux ropes in the interplanetary space. Ruan et al. study the solar wind dynamic pressure pulses (DPPs) often embedded within the ICME streams. DPPs are found to be related to intermittency, an intrinsic feature of solar wind turbulence. This type of studies helps improve our understanding of dynamic processes across multiple scales. Finally, Song et al. carry out a unique study by using the elemental composition measurements of heavy ions, including Helium, Carbon, Oxygen, and Iron ions with different charge states. By examining their variations along two spacecraft paths, widely separated but crossing the same ICME structure, it is concluded that significant inhomogeneity of composition exists along the axial dimension. Such analysis has significant implications for the origination of CMEs because the composition signatures are generally believed to preserve the conditions in solar corona where the formation of CMEs involving coronal plasmas takes place.

It is especially fitting and timely for this new collection to come to light, when we enter the era of Parker Solar Probe (PSP) [10], Solar Orbiter (SO) [11], and additional forthcoming spacecraft missions like Solar Ring (see Shen et al.), among others. We may conclude by quoting from Hu et al., "*It is worth noting that as multi-spacecraft measurements become increasingly more available, . . . , new and exciting multi-messenger science will be enabled by using multiple analysis tools. It is highly anticipated that the constellations of current and future missions will usher in new frontiers in heliophysics research*".

AUTHOR CONTRIBUTIONS

QH drafted the manuscript and all authors contributed to the final editing and proofreading of the manuscript.

ACKNOWLEDGMENTS

We thank all the authors, reviewers, the Chief Editor, and the Frontiers editorial staff, for making this collection a reality.

REFERENCES

1. Temmer M. Space Weather: the Solar Perspective. *Living Rev Solar Phys* (2021) 18:4. doi:10.1007/s41116-021-00030-3
2. Feng HQ, Zhao GQ, Wang JM. Counterstreaming Electrons in Small Interplanetary Magnetic Flux Ropes. *J Geophys Res Space Phys* (2015) 120(10):175–10. doi:10.1002/2015JA021643
3. Jiang C, Wu ST, Feng X, Hu Q. Data-driven Magnetohydrodynamic Modelling of a Flux-Emerging Active Region Leading to Solar Eruption. *Nat Commun* (2016) 7:11522. doi:10.1038/ncomms11522
4. Hu Q. The Grad-Shafranov Reconstruction in Twenty Years: 1996 - 2016. *Sci China Earth Sci* (2017) 60:1466–94. doi:10.1007/s11430-017-9067-2
5. Song H, Yao S. Characteristics and Applications of Interplanetary Coronal Mass Ejection Composition. *Sci China Technol Sci* (2020) 1–17.
6. Chen PF. Coronal Mass Ejections: Models and Their Observational Basis. *Living Rev Solar Phys* (2011) 8:1. doi:10.12942/lrsp-2011-1
7. Wyper PF, Antiochos SK, DeVore CR. A Universal Model for Solar Eruptions. *Nature* (2017) 544:452–5.
8. Amari T, Canou A, Aly JJ, Delyon F, Alauzet F. *Magnetic Cage and Rope as the Key for Solar Eruptions*, 554 (2018). p. 211–5. doi:10.1038/nature24671

9. Jiang C, Feng X, Liu R, Yan X, Hu Q, Moore RL, et al. A Fundamental Mechanism of Solar Eruption Initiation. *Nat Astron* (2021). doi:10.1038/s41550-021-01414-z
10. Fox N, Velli M, Bale S, Decker R, Driesman A, Howard R, et al. The Solar Probe Plus mission: Humanity's First Visit to Our star. *Space Sci Rev* (2016) 204:7–48.
11. Müller D, Cyr OC, Zouganelis I, Gilbert HR, Marsden R, et al. The Solar Orbiter mission - Science Overview. *A&A* (2020) 642:A1. doi:10.1051/0004-6361/202038467

Conflict of Interest: The authors declare that the research was conducted in the absence of any commercial or financial relationships that could be construed as a potential conflict of interest.

Publisher's Note: All claims expressed in this article are solely those of the authors and do not necessarily represent those of their affiliated organizations, or those of the publisher, the editors and the reviewers. Any product that may be evaluated in this article, or claim that may be made by its manufacturer, is not guaranteed or endorsed by the publisher.

frontiers in Physics

ORIGINAL RESEARCH
published: 12 May 2021
doi: 10.3389/fphy.2021.679780

Observations of Magnetic Flux Ropes Opened or Disconnected From the Sun by Magnetic Reconnection in Interplanetary Space

Hengqiang Feng[1,2]*, *Yan Zhao*[1,2], *Jiemin Wang*[1,2], *Qiang Liu*[1,2] and *Guoqing Zhao*[1,2]

[1] Institute of Space Physics, Luoyang Normal University, Luoyang, China, [2] Henan Key Laboratory of Electromagnetic Transformation and Detection, Luoyang, China

OPEN ACCESS

Edited by:
Xueshang Feng,
National Space Science Center (CAS), China

Reviewed by:
Chenglong Shen,
University of Science and Technology of China, China
Xiaojun Xu,
Macau University of Science and Technology, China

***Correspondence:**
Hengqiang Feng
fenghq9921@163.com

Specialty section:
This article was submitted to Stellar and Solar Physics, a section of the journal Frontiers in Physics

Received: 12 March 2021
Accepted: 14 April 2021
Published: 12 May 2021

Citation:
Feng H, Zhao Y, Wang J, Liu Q and Zhao G (2021) Observations of Magnetic Flux Ropes Opened or Disconnected From the Sun by Magnetic Reconnection in Interplanetary Space. Front. Phys. 9:679780. doi: 10.3389/fphy.2021.679780

During solar eruptions, many closed magnetic flux ropes are ejected into interplanetary space, which contribute to the heliospheric magnetic field and have important space weather effect because of their coherent magnetic field. Therefore, understanding the evolution of these closed flux ropes in the interplanetary space is important. In this paper, we examined all the magnetic and plasma data measured in 1997 by the Wind spacecraft and identified 621 reconnection exhausts. Of the 621 reconnection events, 31 were observed at the boundaries of magnetic flux ropes and were thought to cause the opening or disconnection magnetic field lines of the adjacent ropes. Of the 31 magnetic reconnection events, 29 were interchange reconnections and the closed field lines of these related flux ropes were opened by them. Only 2 of the 31 magnetic reconnection events disconnected the opened field lines of the original flux ropes. These observations indicate that interchange reconnection and disconnection may be two important mechanisms changing the magnetic topology of the magnetic flux ropes during their propagation during the interplanetary space.

Keywords: magnetic flux rope, interchange reconnection, magnetic disconnection, magnetic reconnection, interplanetary space

KEY POINTS

- Of the 621 reconnection events, 31 magnetic reconnection events are interchange reconnections, and the closed field lines of these related flux ropes were opening by them.
- Only 2 of the 31 magnetic reconnection events were disconnecting the opened field lines of flux ropes.
- These observations indicate that the interplanetary magnetic reconnections near the boundaries of flux ropes make important contributions to their evolution in the interplanetary space.

INTRODUCTION

During solar eruptions, many magnetic flux ropes are ejected from the corona in the form of coronal mass ejections (CMEs). The magnetic field lines of flux ropes are attached to the Sun at both ends and are referred to as closed flux ropes [1]. The durations of these closed ropes vary from tens of minutes (e.g., the small scale interplanetary flux ropes) to a few days (e.g., magnetic clouds) [2, 3]. The ejected flux ropes have significant effect on the space weather because of their coherent magnetic structures [4–6]. Besides, the magnitude of the magnetic field in the heliosphere will increase as the closed flux ropes ceaselessly ejected into the interplanetary space, which is not consistent with observations. Therefore, understanding the evolution of the closed flux ropes as they propagate in the interplanetary space is important.

As Crooker et al. [7] pointed out, without change in magnetic topology, the magnetic field magnitude in the heliosphere would increase indefinitely because of the ceaseless ejection of closed flux ropes, leading to a "magnetic field magnitude catastrophe" [8, 9]. Magnetic reconnection is an important mechanism changing the topology of the magnetic field. Crooker and Owens [10] summarized two possibilities to avoid the "magnetic field magnitude catastrophe": (1) that closed magnetic field lines of a rope are gradually opened through interchange reconnection between one of its legs and the surrounding open magnetic field

TABLE 1 | The magnetic reconnection exhausts and their related flux ropes.

No.	Front boundary[a]	Rear boundary[b]	Start[c]	End[d]	Type[e]
001	1997/02/01 19:05:04	1997/02/01 19:06:49	1997/02/01 17:56:31	1997/02/01 19:05:04	O
002	1997/02/03 13:11:41	1997/02/03 13:12:21	1997/02/03 13:12:21	1997/02/03 14:32:44	O
003	1997/03/19 12:53:39	1997/03/19 12:54:54	1997/03/19 12:54:54	1997/03/19 14:50:05	O
004	1997/04/16 19:07:46	1997/04/16 19:09:23	1997/04/16 18:28.42	1997/04/16 19:07:46	O
005	1997/05/13 19:30:59	1997/05/13 19:30:59	1997/05/13 18:18:15	1997/05/13 19:30:59	D
006	1997/05/18 01:28:14	1997/05/18 01:34:56	1997/05/18 01:34:56	1997/05/18 03:40:22	O
007	1997/05/19 18:33:36	1997/05/19 18:34:07	1997/05/19 18:34:07	1997/05/19 19:58:33	O
008	1997/05/24 07:39:47	1997/05/24 07:40:13	1997/05/24 07:40:13	1997/05/24 09:58:15	O
009	1997/05/26 15:49:00	1997/05/26 15:50:24	1997/05/26 15:50:24	1997/05/27 06:31:14	O
010	1997/06/20 15:24:55	1997/06/20 15:26:29	1997/06/20 15:26:29	1997/06/20 22:45:36	O
011	1997/07/13 18:59:29	1997/07/13 19:00:27	1997/07/13 17:57:31	1997/07/13 18:59:29	O
012	1997/08/14 11:22:02	1997/08/14 11:27:13	1997/08/14 10:12:46	1997/08/14 11:27:13	O
013	1997/08/16 22:30:26	1997/08/16 22:33:34	1997/08/16 20:13:34	1997/08/16 22:30:26	O
014	1997/08/17 01:45:15	1997/08/17 01:49:24	1997/08/17 01:49:24	1997/08/17 04:57:48	O
015	1997/09/01 07:35:22	1997/09/01 07:36:33	1997/09/01 06:42:35	1997/09/01 07:35:22	O
016	1997/09/02 15:46:37	1997/09/02 15:50:14	1997/09/02 15:50:14	1997/09/02 16:20:04	O
017	1997/09/03 15:54:59	1997/09/03 15:55:35	1997/09/03 15:55:35	1997/09/03 20:38:21	O
018	1997/09/10 22:06:10	1997/09/10 22:06:46	1997/09/10 22:06:46	1997/09/10 22:59:18	O
019	1997/09/17 13:53:29	1997/09/17 13:54:20	1997/09/17 13:23:18	1997/09/17 13:53:29	O
020	1997/10/09 06:04:35	1997/10/09 06:06:21	1997/10/09 06:06:21	1997/10/09 07:23:01	O
021	1997/10/14 14:36:16	1997/10/14 14:38:04	1997/10/14 14:38:04	1997/10/14 15:48:54	O
022	1997/10/20 01:53:18	1997/10/20 01:53:59	1997/10/20 01:53:59	1997/10/20 02:32:46	O
023	1997/11/01 16:07:08	1997/11/01 16:08:06	1997/11/01 14:24:43	1997/11/01 16:07:08	O
024	1997/11/09 11:16:30	1997/11/09 11:19:00	1997/11/09 11:18:58	1997/11/09 13:49:36	D
025	1997/11/16 14:44:28	1997/11/16 14:46:24	1997/11/16 14:46:28	1997/11/16 16:42:01	O
026	1997/11/16 16:42:30	1997/11/16 16:46:37	1997/11/16 14:46:28	1997/11/16 16:42:01	O
027	1997/11/28 17:08:01	1997/11/28 17:08:49	1997/11/28 17:08:49	1997/11/28 18:30:04	O
028	1997/12/01 15:02:59	1997/12/01 15:05:43	1997/12/01 14:37:01	1997/12/01 15:02:59	O
029	1997/12/20 13:08:20	1997/12/20 13:08:21	1997/12/20 13:08:21	1997/12/20 14:17:42	O
030	1997/12/23 08:35:12	1997/12/23 08:35:27	1997/12/23 07:08:33	1997/12/23 08:35:12	O
031	1997/12/28 17:08:32	1997/12/28 17:13:07	1997/12/28 17:13:07	1997/12/28 18:00:02	O

[a] *The front boundary of the reconnection exhaust (UT).*
[b] *The rear boundary of the reconnection exhaust (UT).*
[C] *The start time of the magnetic flux rope (UT).*
[d] *The end time of the magnetic flux rope (UT).*
[e] *T The type of flux ropes was opening or were being disconnected by the related magnetic reconnections, "O" indicates opening and "D" indicates being disconnected. These ropes were assumed originally closed.*

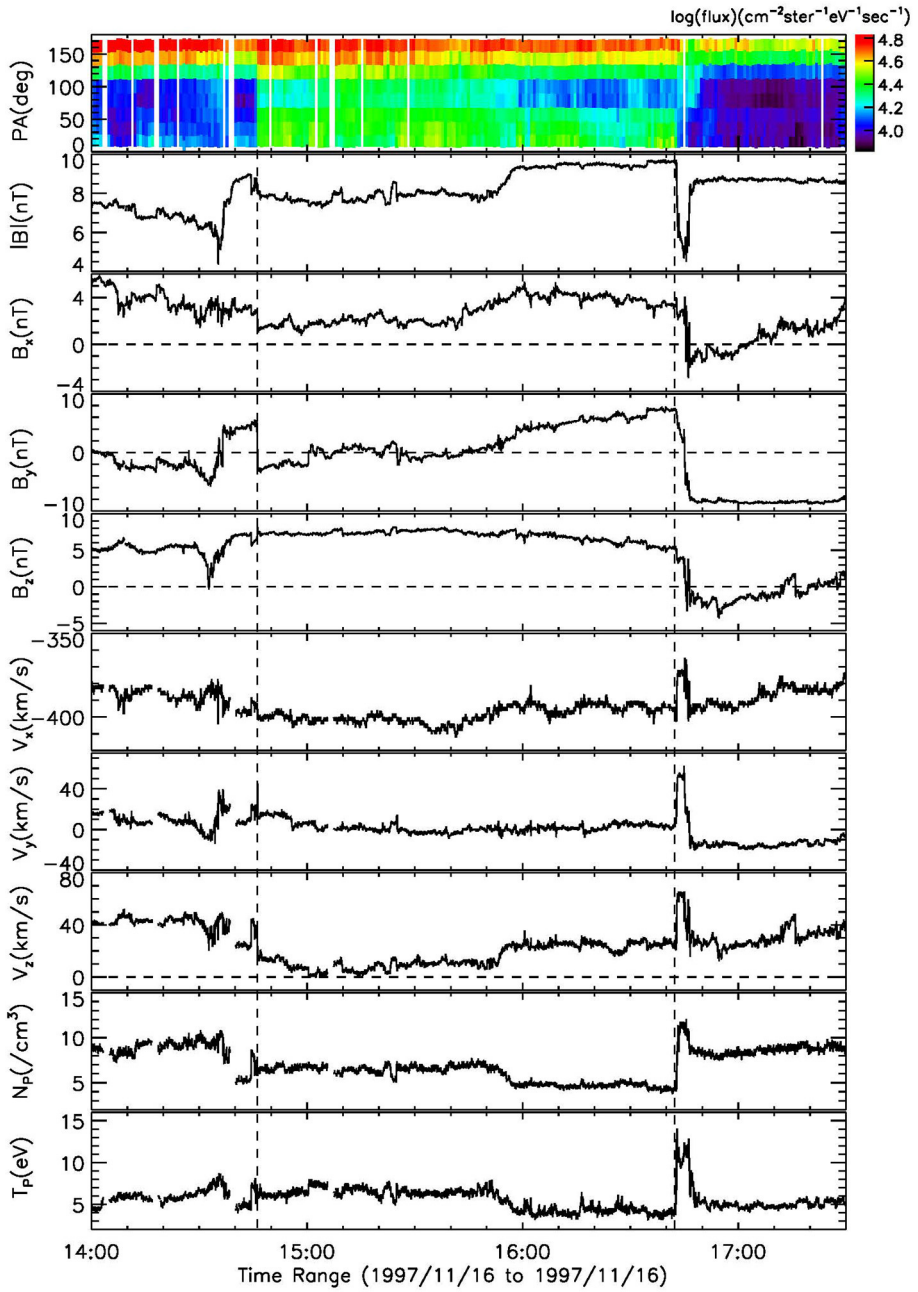

FIGURE 1 | Suprathermal electron pitch angle distributions of 228.17 eV, magnetic field, and plasma data measured by Wind during the November 16th, 1997 flux rope passage. The two vertical dashed lines denote the boundaries of the flux rope.

lines near the Sun [7, 11]; (2) that open magnetic field lines of ropes are reconnected with opposite polarity open magnetic field lines, thus disconnecting them from the Sun [7, 12]. Previous studies provide some supports for these possibilities [e.g., [13–15]].

A large number of interplanetary magnetic reconnections associated with magnetic flux ropes have been observed [16, 17]. Although the interplanetary magnetic reconnection is not assumed to play any role in the heliospheric magnetic magnitude budget [18], it is thought important in changing the magnetic topology of the interplanetary flux ropes. For example, Ruffenach et al. [19] thought that magnetic reconnection near the boundary of magnetic clouds can erode them causing an imbalance in the azimuthal flux. Wang et al. [17] reported a small flux rope associated with a magnetic reconnection exhaust, which had closed field lines that were opened by

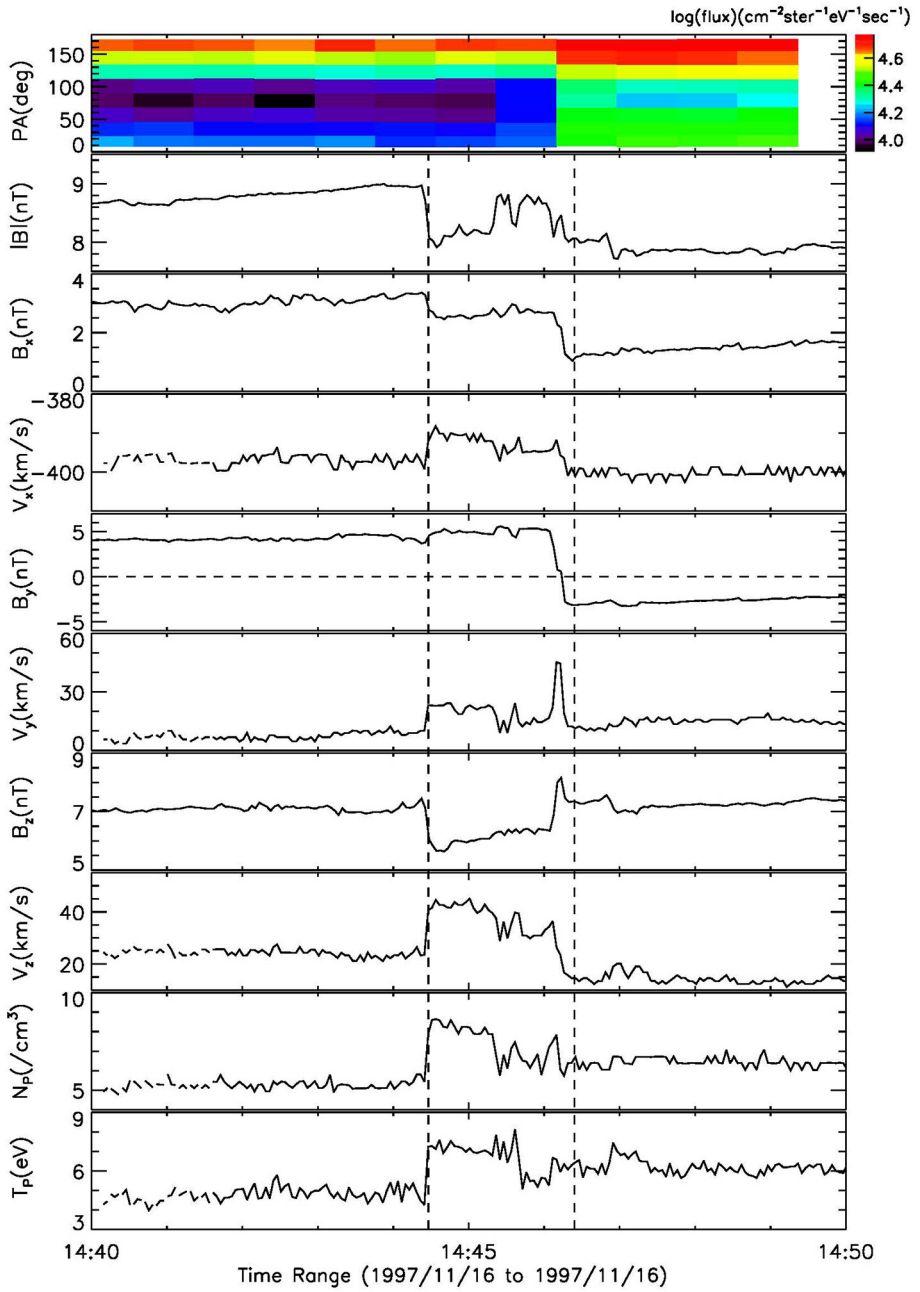

FIGURE 2 | Magnified images of the suprathermal electron distributions, magnetic field, and plasma data of the reconnection exhaust around 14:45 UT November 16th measured by Wind. The two vertical dashed lines denote the reconnection exhaust interval.

an interplanetary magnetic reconnection. The reconnection exhaust and the following small magnetic flux rope were observed on February 2nd, 2002 by Wind and ACE. Their observations provided direct evidence that closed field lines can be opened by interplanetary interchange magnetic reconnection. In 2018, Feng et al. [20] reported a flux rope associated with a reconnection exhaust. In that study, some field lines before the rear boundary of the flux rope were opened, and the opened magnetic field lines were merging with the open field lines after the rope to produce disconnected field lines. The observations of Feng et al. [20] clearly indicate that the open and disconnection of flux ropes can happen in no particular order, supporting the suggestion by Wang et al. [17]. Since the reported interplanetary reconnection exhausts associated with opened (or disconnected) field lines have been very rare, it is uncertain whether interplanetary reconnection is important in

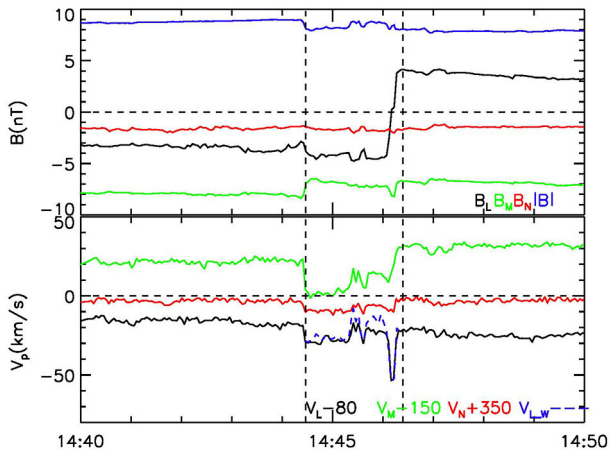

FIGURE 3 | Magnetic field and velocity curves measured in LMN coordinate system of the reconnection exhaust around 14:45 UT November 16th, and the blue dashed curve presents the V_L velocity derived from the Walén relation. The two vertical dashed lines denote the reconnection exhaust interval.

the openness and/or disconnection of the magnetic field of the interplanetary flux ropes.

In this study, we aimed to search for interplanetary flux ropes that were opened or disconnected from the Sun by interplanetary magnetic reconnections. We examined all the magnetic and plasma data measured in 1997 by the Wind spacecraft and identified hundreds of interplanetary reconnection exhausts. Further analysis showed that 30 flux ropes were opened or disconnected by 31 reconnection exhausts. Our observations confirmed that interplanetary magnetic reconnections do play important role in the openness and/or disconnection of the magnetic field of the interplanetary flux ropes.

DATA AND METHODS

The data used in this study were obtained from two instruments on board the Wind spacecraft. The magnetic field and plasma data with time resolutions of 3 s are, respectively, from the Fluxgate Magnetometer experiment [21] and the Three-Dimension Plasma (3DP) instrument [22]. The suprathermal electron data were also obtained from the 3DP analyzer. The electrons were measured by the 3DP at 8 pitch angles as spectrograms in terms of energy. The suprathermal electrons used in our analysis were about 220 eV, and their angular and time resolutions were 22.5° and 48 s, respectively. If not specified, the GSE coordinate system (the Geocentric Solar Ecliptic coordinate system in which the x-axis directs from the Earth to the Sun, the z-axis points north, perpendicular to the ecliptic plane, the y-axis completes the right-handed coordinate system) is used in this study.

Suprathermal electron strahls in the solar wind come from the Sun, and they are focused along magnetic field lines [23–28]. Therefore, the suprathermal electron signatures of flux ropes are used to judge the state of their magnetic fields. The presence of counter-streaming suprathermal electron strahls indicates that the magnetic field lines are still attached to the Sun at both ends, unidirectional strahls indicate that the field lines are open, and the disappearance of strahls indicates that the field lines are completely disconnected from the Sun. Magnetic flux ropes are field topologies characterized by bundles of helical magnetic field lines collectively spiraling around a common axis, and their essential observational properties are enhanced magnetic field strength and smooth rotations [29, 30]. Hence, flux ropes were identified to have enhanced magnetic field strength and smooth rotating magnetic field components. This study used the criterion of Gosling et al. [18] to identify interplanetary reconnection exhausts. This criterion requires them to satisfy the following conditions: (1) a roughly Alfvénic jet, (2) an enhancement of proton density and temperature (not all interplanetary reconnection exhausts), and (3) a depression of the magnetic-field strength.

OBSERVATIONS

Using the magnetic reconnection exhaust criteria of Gosling et al. [18], the high-resolution (3 s) plasma and magnetic field data from Wind were examined, and 621 magnetic reconnection exhausts were identified. We then investigated magnetic field characteristics and suprathermal electron signatures near these magnetic reconnection exhausts and found 31 reconnection exhausts may open the closed flux ropes or disconnect field lines of flux ropes from the Sun. **Table 1** lists the 31 magnetic reconnection exhausts and their related flux ropes. The second and third columns show the front and rear boundaries of the reconnection exhausts, and the fourth and fifth columns list the start and end times of the flux ropes. The sixth column shows the flux ropes that were opened or disconnected from the Sun by the related magnetic reconnections ("O" indicates opened and "D" indicates disconnected. The use of "opened" and "disconnection" meant that these ropes were assumed originally closed). In this section, we will discuss two flux ropes, and their related reconnection exhausts, as examples to exhibit the process of open or disconnection. The first is the flux rope observed on November 16, 1997, whose closed field lines were thought to reconnect to the adjacent open solar wind magnetic field lines at the front and rear boundaries. The other is a flux rope that was observed on November 9, 1997, but whose open field lines were disconnected by reconnecting to the disconnected solar wind magnetic field lines before the flux rope.

Figure 1 shows the suprathermal electron pitch angle distributions, the magnetic field, and the plasma data measured by the Wind spacecraft during the November 16, 1997 flux rope passage. The top panel shows the distributions for the

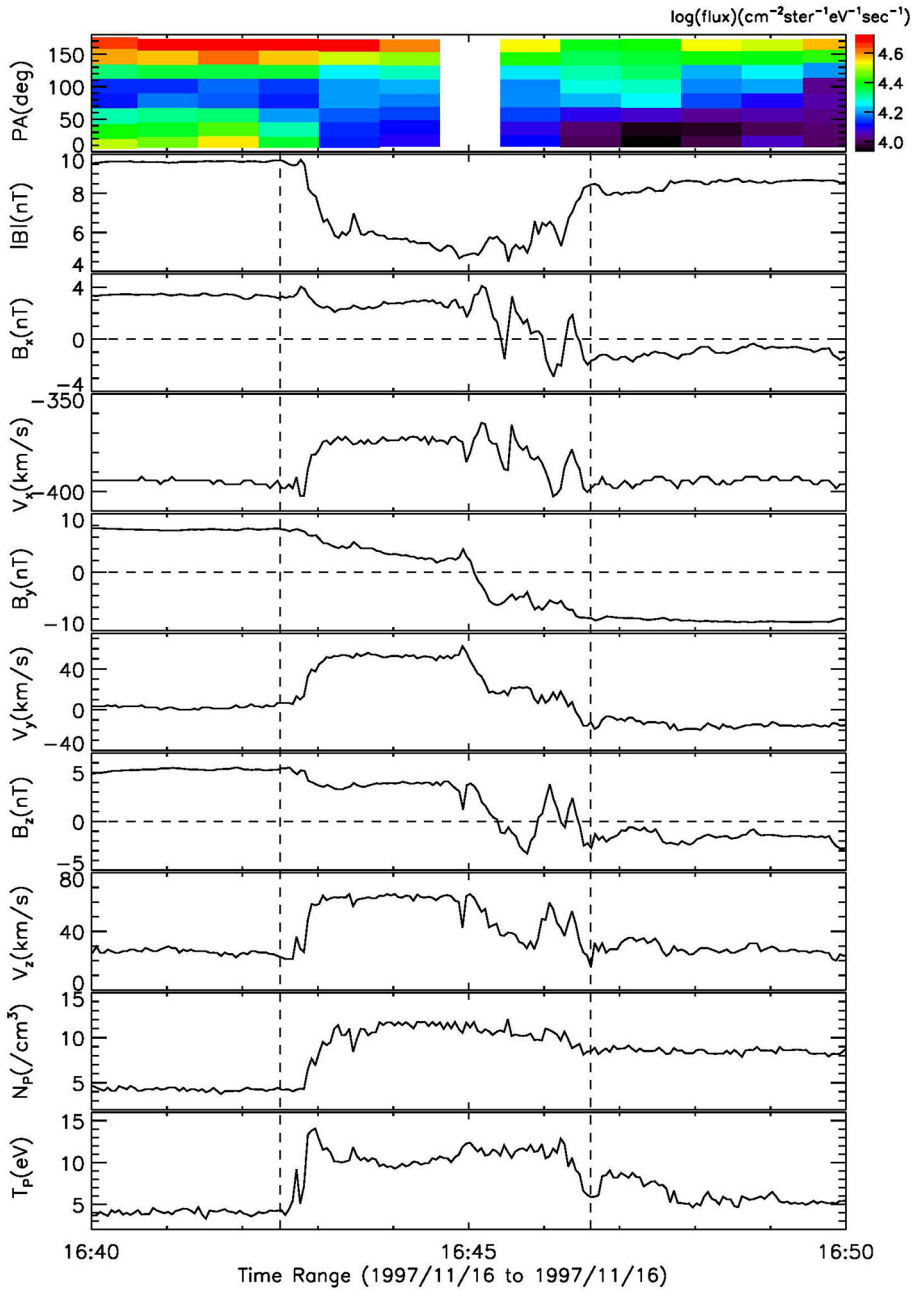

FIGURE 4 | The reconnection exhaust around 16:45 UT November 16th measured by Wind. The format of the figure is same as **Figure 2**.

suprathermal electron pitch angle of 228.17 eV. The subsequent panels display the magnitude of the total magnetic field (|B|); the x, y, z components of the magnetic field (B_x, B_y, B_z); and the x, y, z components of the proton speed (V_x, V_y, V_z), proton density (N_P), and the proton temperature (T_p). In **Figure 1**, there is a small duration (labeled by two vertical dashed lines) that possessed the flux-rope signature of the enhanced magnetic field strength and smoothly rotating magnetic fields. More specifically, the bipolar field appeared in the B_y component, and the core field appeared in the B_z components. The suprathermal electron pitch angle distribution shows that (1) counter-streaming suprathermal electron strahls were present almost throughout the duration of the small flux rope, but (2) all parallel (0°) suprathermal electron strahls were absent before and after the rope. As mentioned above, the presence of suprathermal electron strahls indicates magnetic

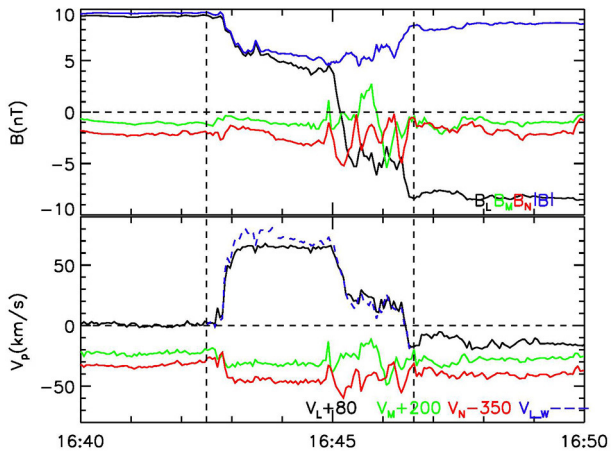

FIGURE 5 | The reconnection exhaust around 16:45 UT November 16th measured by Wind. The format of the figure is same as **Figure 3**.

connection to the Sun, whereas the absence of suprathermal electron strahls indicates magnetic disconnection from the Sun [31]. Therefore, these observations indicated that almost all magnetic field lines of the small rope were closed and still were connected to the Sun on both ends. However, the surrounding magnetic field lines of the rope were connected to the Sun only on one end. In **Figure 1**, we see that near the boundaries of the rope, the magnetic strength exhibited depression, some magnetic field component directions were reversed, the proton density and temperature were enhanced, and the accelerated plasma flow was observed. All these features satisfied the criteria of reconnection exhausts [18], and we further confirmed that these are two reconnection exhausts. We will discuss the observations of the two reconnection exhausts in detail below.

Figure 2 shows the expanded views of the reconnection exhaust near the front boundary of the flux rope. We can see in this figure that outstanding accelerated plasma flow was observed in the y direction, and the y direction magnetic field component was reversed across the accelerated flow, in which the proton density and temperature were also enhanced. All these features are characteristic of interplanetary reconnection exhausts. The Walén relation is often used to identify whether or not the accelerated plasma flows are Alfvénic waves bounding the exhausts [e.g., [32–35]]. We performed a minimum variance analysis (MVA) of the magnetic field data near the reconnection exhaust, and established the LMN coordinate system, where L, M and N represented the directions of maximum, intermediate, and minimum variance of the field component. L was assumed to be along the reconnection outflow direction and N along the normal direction of the reconnection current sheet. **Figure 3** shows the magnetic field and velocity curves measured in LMN coordinate system. As shown in the figure, the enhancement of the plasma velocity was mainly in the L direction. **Figure 3** also shows the predicted V_L velocity from the Walén relation as a blue dashed curve, and the expected V_L velocity curve was consistent with the observed velocity curve. Therefore, the observed accelerated flow was an exhaust of a magnetic reconnection. **Figure 2** also shows that the antiparallel suprathermal electron strahls occurred throughout the region and that the parallel suprathermal electron strahls were absent before the front boundary of the exhaust, though the weak strahls appeared after the rear boundary of the exhaust. These observations indicated that the field lines prior to the exhaust were opened, but those after the exhaust were still closed. Namely, an interchange reconnection occurred between open magnetic fields before the flux rope and closed magnetic field lines of the flux ropes, and the closed flux ropes were gradually opened by the interchange reconnection at its front boundary. Although here we adopted the term "interchange reconnection" from Crooker and Owens [10], one should keep remember that the reconnection exhausts discussed in this paper were detected in the interplanetary space. The term "disconnection" should also be interpreted in this way.

Figure 4 shows the expanded views of the reconnection exhaust near the rear boundary of the flux rope. In this figure, accelerated plasma flow was observed in all the three directions from 16:42:30 UT to 16:46:37 UT, during which time all the magnetic field components were reversed and both proton density and temperature were enhanced. **Figure 5** provides the magnetic field and velocity curves of the magnetic reconnection exhaust in the LMN coordinate system, and the exhibited expected V_L velocity curve was approximately consistent with the observed velocity curve. The suprathermal electron distributions in **Figure 5** show that the field lines prior to the exhaust were closed, while those after the exhaust were open; the magnetic reconnection event was also an interchange reconnection. In the same way, this closed flux rope was gradually opened by the reconnection event at its rear boundary.

Figure 6 shows the suprathermal electron pitch angle distributions, magnetic field, and plasma data of the November 9, 1997 flux rope passage, as well as the preceding magnetic reconnection exhaust. The top panel indicated that (1) the parallel suprathermal electron strahls occurred almost throughout the duration of the rope except for a few brief intervals, but (2) the antiparallel suprathermal electrons strahls were absent except for a brief interval. These observations indicated that most magnetic field lines of the small flux rope were open, and some magnetic field lines were disconnected from the Sun. Before the small rope, all suprathermal electron strahls disappeared, which meant that all the magnetic field lines before the rope were open. **Figure 7** provides expanded views of the magnetic reconnection event, which shows that the accelerated flow from 11:17:13 UT to 11:18:58 UT had all the typical observable characteristics of an interplanetary reconnection exhaust. We also tested if the accelerated flow was a reconnection exhaust using the Walén relation

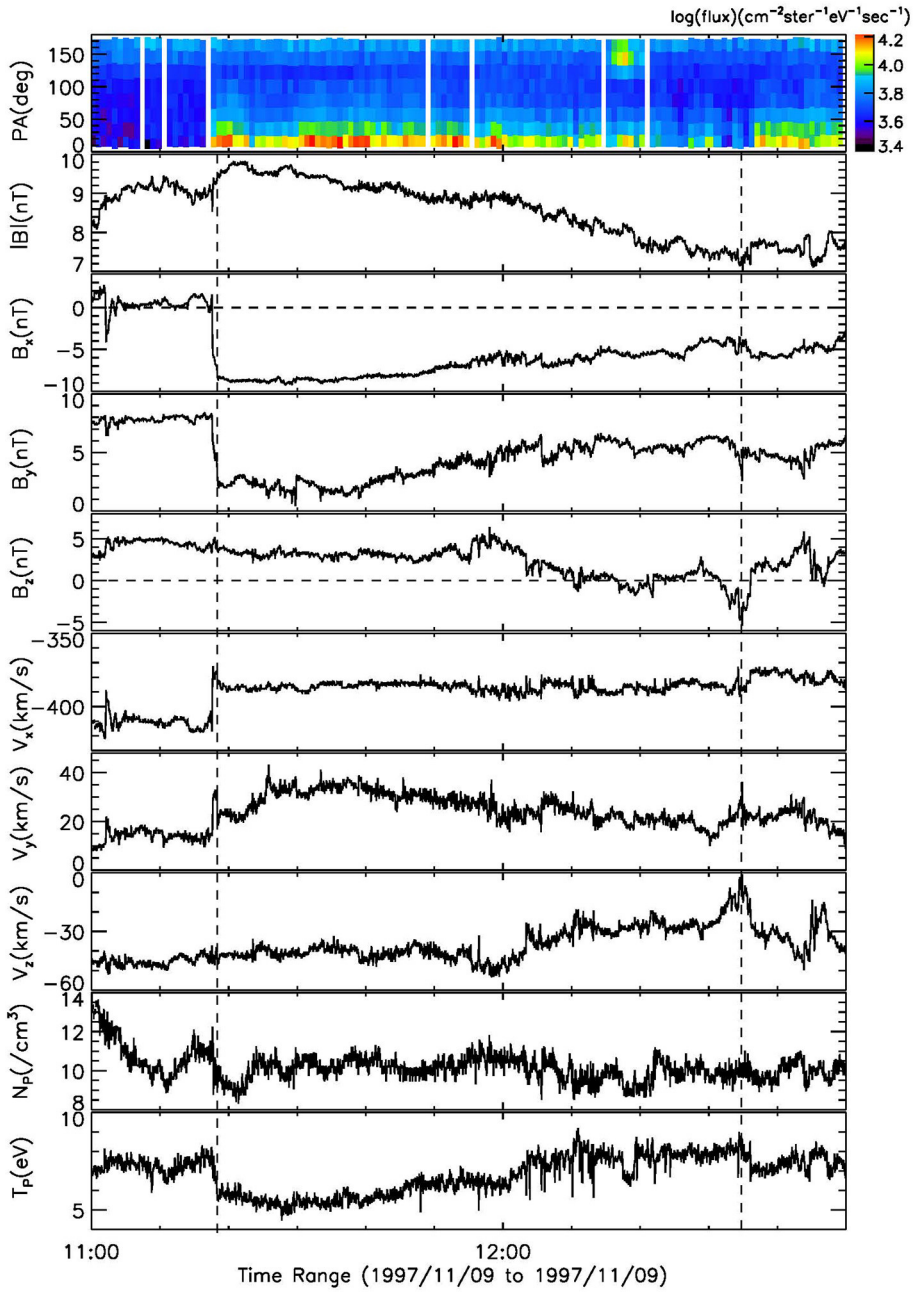

FIGURE 6 | Observations of the November 9th, 1997 flux rope passage. The format of the figure is same as **Figure 1**.

(**Figure 8**). These observations revealed that the open field lines of the flux rope were reconnected with disconnected field lines to produce new U-shaped field lines with no connection to the Sun. This type of disconnection for flux ropes has never been reported before. The previously reported disconnections associated with reconnection exhausts are very rare and only show disconnection that describes two open field lines reconnecting.

RESULTS AND SUMMARY

In this study, the magnetic reconnection exhaust criteria of Gosling et al. [18] was used to examine the plasma and magnetic field data measured by Wind in 1997. Using these data, 621 reconnection exhausts were identified, and 31 of the 621 reconnection events were observed at the boundaries of magnetic flux ropes that were thought to lead to the open

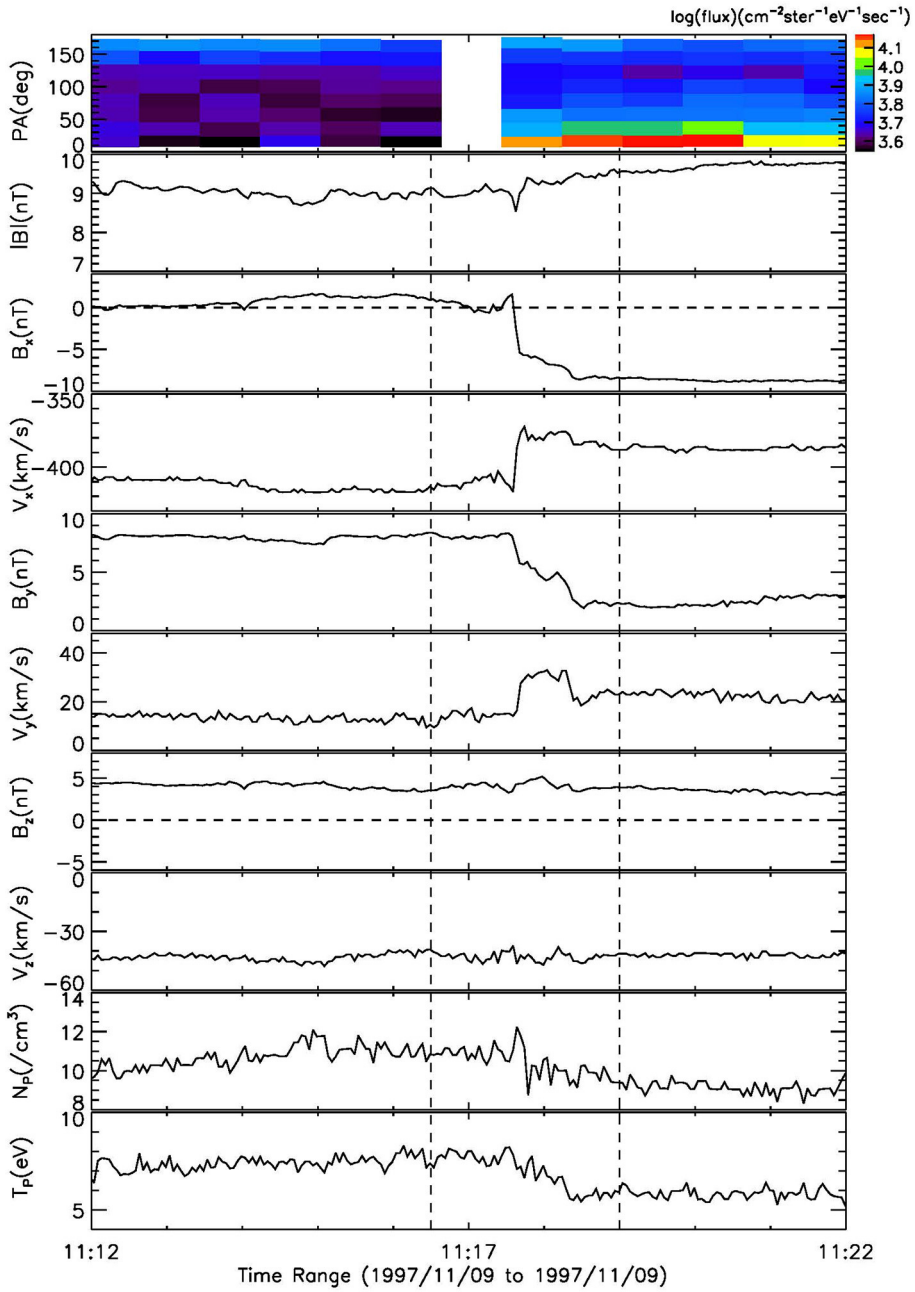

FIGURE 7 | The reconnection exhaust around 11:18 UT November 16th measured by Wind. The format of the figure is same as **Figure 2**.

and/or disconnection of the magnetic field lines of the adjacent ropes. The 31 magnetic reconnection exhausts and their related flux ropes are listed in **Table 1**. The results of **Table 1** can be summarized as follows: (1) 29 of the 31 magnetic reconnection events were interchange reconnections (a type of magnetic reconnection between open magnetic fields and closed magnetic field lines where the closed field lines of these related flux ropes were opened by them); (2) only 2 of the 31 magnetic reconnection events disconnected the opened field lines of flux ropes (one reconnection type was reconnecting with the adjacent open field lines and the other was reconnecting with the adjacent disconnected field lines); and (3) the scales of most magnetic flux ropes are small, and the average time scale is only 127 min. Interchange reconnection and disconnection are two mechanisms proposed to balance the heliospheric magnetic flux increased by the ceaselessly ejection of closed flux

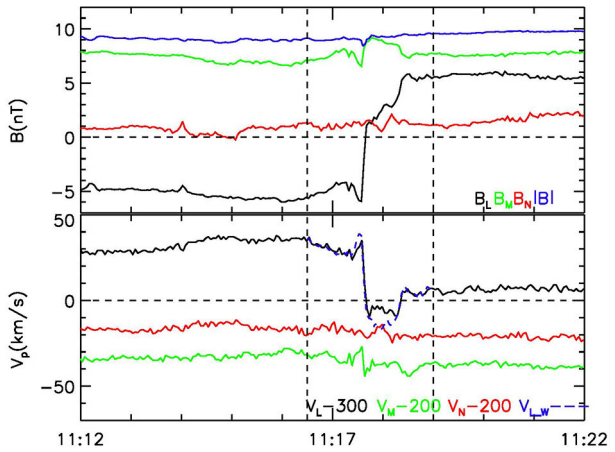

FIGURE 8 | The reconnection exhaust around 11:18 UT November 16th measured by Wind. The format of the figure is same as **Figure 3**.

ropes from the Sun. Although we used the terms "interchange reconnection" and "disconnection" here, we were not sure if the reconnection reported here make contribution to the balance of the heliospheric magnetic flux. Since although reconnection was ongoing when the exhaust was detected, the closed magnetic flux produced by the reconnection could not go back to the Sun.

In summary, the results presented here revealed that: (1) flux ropes with magnetic reconnections at their boundaries are more likely to remain attached to the sun, which is consistent with previously observations that most of the flux ropes at 1 AU have closed magnetic field [e.g., [1, 25, 27]]; (2) few magnetic flux ropes are open near 1 AU and seldom do the open magnetic field lines of these flux ropes disconnect by interplanetary magnetic reconnection; (3) field lines of small magnetic flux ropes are easy to open or disconnect when magnetic flux ropes move from the Sun to the interplanetary space; and (4) the closed magnetic flux ropes can be gradually opened and/or disconnected through interplanetary magnetic reconnections, and the percentage of closed field lines should continually decrease when magnetic flux ropes move away.

DATA AVAILABILITY STATEMENT

Publicly available datasets were analyzed in this study. This data can be found at: http://cdaweb.gsfc.nasa.gov/cdaweb/istp_public/.

AUTHOR CONTRIBUTIONS

HF drafted the manuscript and led the observational analysis. YZ, QL, GZ, and JW conducted analysis of the current layer and flux rope. All authors contributed to the interpretation of the results and helped draft the manuscript.

ACKNOWLEDGMENTS

We acknowledge supports from NSFC under Grant Nos. 41974197 and 41804162. We thank NASA/GSFC for the use of data from the Wind. These data can obtain freely from the Coordinated Data Analysis Web (http://cdaweb.gsfc.nasa.gov/cdaweb/istp_public/).

REFERENCES

1. Wang J, Zhao Y, Feng H, Tian Z, Li H, Zhao A, et al. Comparison of counterstreaming suprathermal electron signatures of ICMEs with and without magnetic cloud: are all ICMEs flux ropes?. *Astron Astrophys.* (2019) 632:A129. doi: 10.1051/0004-6361/201936733
2. Moldwin MB, Ford S, Lepping R, Slavin JA, Szabo A. Small-scale magnetic flux ropes in the solar wind. *Geophys Res Lett*. (2000) 27:57–60.
3. Feng H, Zhao G, Wang JM. Small interplanetary magnetic flux rope. *Sci China Tech Sci*. (2019) 62:183–94. doi: 10.1007/s11431-018-9481-1
4. Gonzalez WD, Tsurutani BT, Clúa de Gonzalez AL. Interplanetary origin of magnetic storms. *Space Sci Rev.* (1999) 88:529–62. doi: 10.1023/A:1005160129098
5. Feng H, Chao JK, Lyu LH, Lee LC. The relationship between small interplanetary magnetic flux rope and the substorm expansion phase. *J Geophys Res.* (2010) 115:A09108. doi: 10.1029/2009JA015191
6. Zhang XY, Moldwin MB, Cartwright M. The geo-effectiveness of interplanetary small-scale magnetic flux ropes. *J Atmos Solar-Terr Phys.* (2013) 95–96:1–14. doi: 10.1016/j.jastp.2012.12.006
7. Crooker NU, Gosling JT, Kahler SW. Reducing heliospheric magnetic flux from coronal mass ejections without disconnection. *J Geophys Res.* (2002) 107:1028. doi: 10.1029/2001JA000236
8. Gosling JT. Large scale inhomogeneities in the solar wind of solar origin, *Rev Geophys.* (1975) 13:1053–8. doi: 10.1029/RG013i003p01053
9. McComas DJ. Tongues, bottles, and disconnected loops: the opening and closing of the interplanetary magnetic field. US. Natl. Rep. Int. Union Geod. Geophys. (1995) 1991–1994, *Rev Geophys.* (1995) 33:603–8. doi: 10.1029/95RG00124
10. Crooker NU, Owens MJ. Interchange reconnection: remote sensing of solar signature and role in heliospheric magnetic flux budget. *Space Sci Rev*. (2012) 172:201–8. doi: 10.1007/s11214-011-9748-1
11. Gosling JT, Birn J, Hesse M. Three-dimensional magnetic reconnection and the magnetic topology of coronal mass ejection events. *Geophys Res Lett*. (1995) 22:869–72. doi: 10.1029/95GL00270
12. Crooker NU, Owens MJ. SOHO-23: understanding a peculiar solar minimum. In: Cranmer SR, Hoeksma T, Kohl JL, editors. *ASP Conf. Ser. 428*. San Francisco, CA: ASP (2010). p. 279.
13. Baker D, Rouillard AP, van Driel-Gesztelyi1 L, Démoulin P, Harra1 LK, Lavraud B, et al. Signatures of interchange reconnection: STEREO, ACE and Hinode observations combined. *AnGeo*. (2009) 27:3883. doi: 10.5194/angeo-27-3883-2009
14. Lavraud B, Owens MJ, Rouillard AP. In situ signatures of interchange reconnection between magnetic clouds and open magnetic fields: a mechanism for the erosion of polar coronal holes? *Solar Phys*. (2011) 270:285. doi: 10.1007/s11207-011-9717-6
15. DeForest CE, Howard TA, McComas DJ. Disconnecting open solar magnetic flux. *Astrophys J*. (2012) 745:36. doi: 10.1088/0004-637X/745/1/36
16. Tian H, Yao S, Zong Q, Jiansen He J, Qi Y, et al. Signatures of magnetic reconnection at boundaries of interplanetary small-scale magnetic flux ropes. *Astrophys J*. (2010) 720:454.
17. Wang JM, Feng H, Zhao G. Observations of a small interplanetary magnetic flux rope opening by interchange reconnection. *Astrophys J*. (2018) 853:94. doi: 10.3847/1538-4357/aaa131

18. Gosling JT, Skoug RM, Smith CW. Direct evidence for magnetic reconnection in the solar wind near 1 AU. *J Geophys Res.* (2005) 110:A01107. doi: 10.1029/2004JA010809
19. Ruffenach A, Lavraud B, Owens MJ, Sauvaud J-A, Savani NP, Rouillard AP, et al. Multispacecraft observation of magnetic cloud erosion by magnetic reconnection during propagation. *J Geophys Res.* (2012) 117:A09101. doi: 10.1029/2012JA017624
20. Feng H, Wang JM, Zhao G, Zhao Y. Observations on the magnetic disconnections of a magnetic cloud from the sun through magnetic reconnection. *Astrophys J.* (2018) 864:101. doi: 10.3847/1538-4357/aad95e
21. Lepping RP, AcunaMH, Burlaga LF, FarrellWM, Slavin JA, Schatten KH, et al. The wind magnetic field investigation, edited by Russell, C. T. *Space Sci Rev*. (1995) 71:207–29. doi: 10.1007/BF00751330
22. Lin RP, Anderson KA, Ashford S, Carlson C, Curtis D, Ergun R, et al. A three-dimensional plasma and energetic particle investigation for the wind spacecraft. *Space Sci Rev*. (1995) 71:125–53. doi: 10.1007/BF00751328
23. Feldman WC, Anderson RC, Asbridge JR, Bame SJ, Gosling JT, Zwickl RD, et al. Plasma electron signature of magnetic connection to the Earth's bow shock: ISEE 3. *J Geophys Res*. (1982) 87:632–42. doi: 10.1029/JA087iA02p00632
24. Larson DE, Lin RP, McTiernan JM, McFadden JP, Ergun RE, McCarthy M, et al. Tracing the topology of the October 18–20, 1995 magnetic cloud with ∼0.1–102 keV electrons. *Geophys Res Lett*. (1997) 24:1911–4. doi: 10.1029/97GL01878
25. Shodhan S, Crooker NU, Kahler SW, Fitzenreiter RJ, Larson DE, Lepping RP, et al. Counterstreaming electrons in magnetic clouds. *J. Geophys. Res.* (2000) 105:27261–8. doi: 10.1029/2000JA000060
26. Crooker NU, Forsyth R, Rees A, Gosling JT, Kahler SW. Counterstreaming electrons in magnetic clouds near 5 AU. *J Geophys Res*. (2004) 109:A06110. doi: 10.1029/2004JA010426
27. Feng H, Zhao G, Wang JM. Counterstreaming electrons in small interplanetary magnetic flux ropes. *J Geophys Res*: *Space Phys.* (2015) 120:10175–84. doi: 10.1002/2015JA021643
28. Xu M, Shen C, Hu Q, Wang Y, Chi Y. Whether small flux ropes and magnetic clouds have the same origin: a statistical study of small flux ropes in different types of solar wind. *Astrophys J*. (2020) 904:122. doi: 10.3847/1538-4357/abbe21
29. Feng H, Wu D, Lin C, Chao JK, Lee CL, and Lyu LH. Interplanetary small- and intermediate-sized magnetic flux ropes during 1995–2005. *J Geophys Res*. (2008) 113:A12105. doi: 10.1029/2008JA013103
30. Feng H, Wu D, Chao JK. Comment on "Comparison of small-scale flux rope magnetic properties to large-scale magnetic clouds: evidence for reconnection across the HCS"? by M. L. Cartwright and M. B. Moldwin. *J Geophys Res*. (2010) 115:A10109. doi: 10.1029/2010JA015588
31. McComas DJ, Gosling JT, Phillips JL, Bame SJ, Luhmann JG, Smith EJ. Electron heat flux dropouts in the solar wind: evidence for interplanetary magnetic field reconnection?. *J Geophys Res.* (1989) 94:6907–16. doi: 10.1029/JA094iA06p06907
32. Paschmann G, Papamastorakis I, Baumjohann W, Sckopke N, Carlson CW, Sonnerup BUÖ, et al. The magnetopause for large magnetic shear: AMPTE/IRM observations. *J Geophys Res.* (1986) 91:11099–115. doi: 10.1029/JA091iA10p11099
33. Phan TD, Gosling JT, Davis MS, Skoug RM, Øieroset M, Lin RP, et al. A magnetic reconnection X-line extending more than 390 Earth radii in the solar wind. *Nature*. (2006) 439:175–8. doi: 10.1038/nature04393
34. Xu X, Wei F, Feng X. Observations of reconnection exhausts associated with large-scale current sheets within a complex ICME at 1 AU. *J Geophys Res*. (2011) 116:A05105. doi: 10.1029/2010JA01615
35. Feng H, Zhao Y, Zhao G, Liu Q, Wu D. Observations on a series of merging magnetic flux ropes within an interplanetary coronal mass ejection. *Geophys Res Lett*. (2019) 146:5–10. doi: 10.1029/2018GL080063

Conflict of Interest: The authors declare that the research was conducted in the absence of any commercial or financial relationships that could be construed as a potential conflict of interest.

frontiers in Physics

ORIGINAL RESEARCH
published: 15 July 2021
doi: 10.3389/fphy.2021.684345

The Inhomogeneity of Composition Along the Magnetic Cloud Axis

Hongqiang Song[1,2], Qiang Hu[3], Xin Cheng[4], Jie Zhang[5], Leping Li[2], Ake Zhao[6], Bing Wang[1], Ruisheng Zheng[1] and Yao Chen[1]*

[1]Shandong Provincial Key Laboratory of Optical Astronomy and Solar-Terrestrial Environment, and Institute of Space Sciences, Shandong University, Weihai, China, [2]CAS Key Laboratory of Solar Activity, National Astronomical Observatories, Chinese Academy of Sciences, Beijing, China, [3]Department of Space Science and CSPAR, University of Alabama in Huntsville, Huntsville, AL, United States, [4]School of Astronomy and Space Science, Nanjing University, Nanjing, China, [5]Department of Physics and Astronomy, George Mason University, Fairfax, VA, United States, [6]College of Physics and Electric Information, Luoyang Normal University, Luoyang, China

Coronal mass ejections (CMEs) are one of the most energetic explosions in the solar system. It is generally accepted that CMEs result from eruptions of magnetic flux ropes, which are dubbed as magnetic clouds (MCs) in interplanetary space. The composition (including the ionic charge states and elemental abundances) is determined prior to and/or during CME eruptions in the solar atmosphere and does not alter during MC propagation to 1 AU and beyond. It has been known that the composition is not uniform within a cross section perpendicular to the MC axis, and the distribution of ionic charge states within a cross section provides us an important clue to investigate the formation and eruption processes of flux ropes due to the freeze-in effect. The flux rope is a three-dimensional magnetic structure intrinsically, and it remains unclear whether the composition is uniform along the flux rope axis as most MCs are only detected by one spacecraft. In this study, we report an MC that was observed by Advanced Composition Explorer at ~1 AU during March 4–6, 1998, and Ulysses at ~5.4 AU during March 24–28, 1998, sequentially. At these times, both spacecraft were located around the ecliptic plane, and the latitudinal and longitudinal separations between them were ~2.2° and ~5.5°, respectively. It provides us an excellent opportunity to explore the axial inhomogeneity of flux rope composition, as both spacecraft almost intersected the cloud center at different sites along its axis. Our study shows that the average values of ionic charge states exhibit significant difference along the axis for carbon, and the differences are relatively slight but still obvious for charge states of oxygen and iron as well as the elemental abundances of iron and helium. Besides the means, the composition profiles within the cloud measured by both spacecraft also exhibit some discrepancies. We conclude that the inhomogeneity of composition exists along the cloud axis.

Keywords: coronal mass ejection, magnetic flux rope, interplanetary coronal mass ejection, magnetic cloud, ionic charge state, elemental abundance

OPEN ACCESS

Edited by:
Markus Roth,
Albert Ludwigs Universität Freiburg, Germany

Reviewed by:
Wageesh Mishra,
Indian Institute of Astrophysics, India
Bhuwan Joshi,
Physical Research Laboratory, India

****Correspondence:***
Hongqiang Song
hqsong@sdu.edu.cn

Specialty section:
This article was submitted to Stellar and Solar Physics, a section of the journal Frontiers in Physics

Received: *23 March 2021*
Accepted: *17 June 2021*
Published: *15 July 2021*

Citation:
Song H, Hu Q, Cheng X, Zhang J, Li L, Zhao A, Wang B, Zheng R and Chen Y (2021) The Inhomogeneity of Composition Along the Magnetic Cloud Axis. Front. Phys. 9:684345. doi: 10.3389/fphy.2021.684345

1 INTRODUCTION

Coronal mass ejections (CMEs) are an energetic explosive phenomenon in the solar atmosphere [1–4], and they are called interplanetary coronal mass ejections (ICMEs) after leaving the corona. When ICMEs interact with the Earth's magnetosphere, they can cause geomagnetic storms [5–7] and influence the normal work of high-tech equipments, such as satellites, power grids, and GPS navigation systems [8, 9]. Therefore, it is of great significance to grasp the trigger mechanisms and eruption processes of CMEs.

The researchers of the solar physics community have reached a consensus that CMEs result from eruptions of magnetic flux ropes (MFRs), which refer to a volumetric current channel with the helical magnetic field lines wrapped around the central axial field [10, 11]. In white light coronagraph images, CMEs often exhibit a three-part structure, that is, a bright front, a dark cavity, and a bright core [12]. The cavity and core have been considered as the MFR cross section and erupted filament, respectively, for several decades. However, recent studies clearly demonstrated that both the filaments and hot channel MFRs can appear as the bright core [13–16]. The hot channels are first revealed through extreme ultraviolet passbands sensitive to high temperatures (e.g., 131 and 94 Å) [17], and they can also be observed in hard X-ray [18] and microwave [19] images. Researchers also suggest that the dark cavity corresponds to a low-density region with a sheared magnetic field in the early eruption stage [16].

Both theoretical and observational studies reveal that MFRs can form prior to [17, 20–23] and during [24–28] solar eruptions, while they might exist before eruptions in more events [29]. The numerical simulations demonstrate that the repetitive magnetic reconnections could play an important role during the MFR evolution [30]. The remote-sensing observations have been widely used to investigate the MFR formation process [26, 31, 32]. The charge states within ICMEs are frozen-in near the Sun [33], and the relative abundances of elements with different first ionization potentials (FIPs) are different obviously in the corona and photosphere [34, 35]. As the composition does not alter during CME propagation to 1 AU and beyond [36], the *in situ* data are also employed to analyze the MFR formation [28, 37, 38] and plasma origin [39, 40] of CMEs. So far, the most complete composition data of ICMEs are provided by the solar wind ion composition spectrometer (SWICS) aboard Advanced Composition Explorer (ACE) and Ulysses, which can provide the charge states and elemental abundances of ~10 elements [41].

When an ICME has its nose pass through a spacecraft, the MFR will be detected as a magnetic cloud (MC) [42–44]. This is schematically shown in **Figure 1A** (also see [45, 46] for a similar cartoon), where the purple arrow depicts a spacecraft trajectory crossing one ICME through its nose portion as marked with the blue rectangle. **Figure 1B** displays the MFR within the rectangle, and the green dots represent the center of each cross section. The black, blue, and red arrows depict three different trajectories.

Several statistical studies have been conducted on ICME composition. Huang et al. [47] analyzed the composition inside 124 MCs and reported that fast MCs have higher charge states and relative elemental abundances (except the C/O) than slow ones. Owens [48] analyzed the charge states of carbon, oxygen, and iron within 215 ICMEs, including 97 MCs and 118 non-cloud events, and found that MCs exhibit higher ionic charge states than non-cloud events. Zurbuchen et al. [49] performed a comprehensive analysis of the elemental abundances of 310 ICMEs from 1998 March to 2011 August. They reported that the abundances of low-FIP elements within ICMEs exhibit a systematic increase compared to the solar wind, and the ICMEs with elevated iron charge states possess higher FIP fractionation than the other ICMEs. Very recently, Song et al. [50] reported that all the ICME compositions possess the solar cycle dependence.

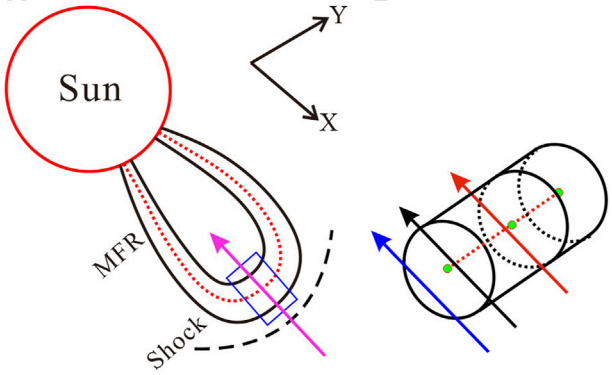

FIGURE 1 | Schematic drawing of the spacecraft trajectory crossing an ICME. The black dashed and solid lines represent the shock and MFR, respectively. The red dotted lines delineate the MFR axis. The ICME nose portion is marked with the blue rectangle in Panel **(A)**, which is enlarged for details in Panel **(B)**. The blue, black, and red arrows describe the different trajectories of spacecraft, and the green dots denote the center of each cross section.

In the meantime, some attentions are paid on the composition distribution inside each MC. Song et al. [37] found that the average values of iron charge states ($<Q_{Fe}>$) can present four regular profiles along the spacecraft trajectories throughout MCs, that is, (i) a bimodal profile with both peaks higher than 12+, (ii) a unimodal profile with peaks higher than 12+, and (iii) and (iv) the $<Q_{Fe}>$ profile remains beyond and below 12+ throughout the spacecraft trajectory inside an MC, respectively. Their studies demonstrated that the charge states can be non-uniform within the cross section of a specified MC and suggested that the above profiles are tightly correlated with both the impact factor of spacecraft trajectories and the formation process of MFRs. For example, the bimodal profile implies that the MFR exists prior to eruption; see Figure 8 in [37] for more details. In addition, the elemental abundances are not uniform within one cross section either [39]. Therefore, a spacecraft can detect different composition profiles when it crosses one MC along the blue and black arrows as shown in **Figure 1B**, which are located in the same cross section perpendicular to the axis but with different impact factors. However, whether the inhomogeneity of composition exists along the MC axis remains unclear because most MCs are detected only by either ACE or Ulysses. Given the MC is a three-dimensional (3D) structure intrinsically, the axial distribution of composition can reveal whether different portions

along the MFR axis experience different eruption processes in the corona.

In this study, we report an intriguing event, in which an MC was observed by ACE at ~1 AU during March 4–6, 1998, and Ulysses at ~5.4 AU during March 24–28, 1998. At these times, both spacecraft were located around the ecliptic plane, and the latitudinal and longitudinal separations between them were ~2.2° and ~5.5°, respectively. The Grad–Shafranov (GS) reconstruction [51, 52] demonstrated that the MC axis oriented in an approximate east–west direction with the axis direction at Ulysses being tilted slightly away from that at ACE, and both spacecraft almost intersected the MC center [53]. This implies that the two spacecraft cross the MC along two trajectories resembling the black and red arrows in **Figure 1B**, respectively, and provide us an excellent opportunity to explore whether the composition is uniform along the axis. We introduce the data in **Section 2** and give the observations in **Section 3**. **Section 4** presents the conclusion and discussion.

2 DATA

The data used in this study are provided by several payloads on board the ACE and Ulysses spacecraft. ACE is in a halo orbit around the first Lagrangian point between the Earth and the Sun since it was launched in 1997. Ulysses was launched in 1990 and entered an elliptical and heliocentric orbit with an aphelion at ~5.4 AU from the Sun and a perihelion distance of ~1.34 AU. Magnetic field data are provided by ACE/MAG [54] and Ulysses/magnetic field [55] instruments. The bulk solar wind properties and the helium abundances are from the Solar Wind Electron, Proton, and Alpha Monitor (SWEPAM) [56] on board ACE and the Solar Wind Observations Over the Poles of the Sun (SWOOPS) [57] on board Ulysses. The SWICS instruments on board both spacecraft [58, 59] offer the composition of heavy ions.

3 OBSERVATIONS

The criteria used to identify MCs near 1 AU mainly include the enhanced magnetic field strength, smoothly changing of magnetic field direction, declining profile of solar wind velocity, low proton temperature (or low plasma β), and elevated He^{2+}/H^{+} ratio [42, 60, 61]. ACE detected an MC during March 4–6, 1998, as shown in **Figure 2**. The vertical dashed line denotes the shock driven by the ICME, and the two dash-dotted lines demarcate the MC boundaries.

Figure 2A shows the total magnetic field strength and its three components in RTN coordinate, where the x-axis (R) points from Sun center to spacecraft, the y-axis (T) is the cross product of solar rotational axis and X axis, lying in the solar equatorial plane towards the west limb, and the z-axis (N) is the cross product of x and y axes. The total magnetic field strength (black) increased obviously compared to the background solar wind, and the Bn component (blue) changed its direction gradually within the MC, which are the typical features of MCs. **Figures 2B–D** present the

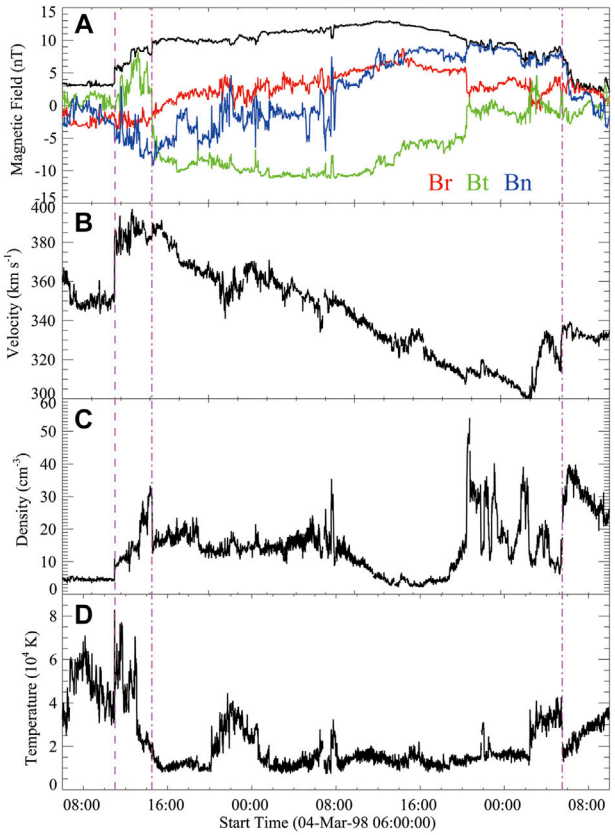

FIGURE 2 | Magnetic field and solar wind parameters measured by ACE near 1 AU. **(A)** Total magnetic field strength (black) and its three components in RTN coordinate and **(B–D)** velocity, density, and temperature of solar wind. The vertical dashed line denote the shock, and the dash-dotted lines demarcate the MC boundaries.

velocity, density, and temperature of the ICME sequentially. The declining profile of velocity indicates that the MFR is expanding.

Ulysses detected an MC during March 24–28 [62] as shown in **Figure 3**, where the magnetic field, velocity, density, and temperature are presented from top to bottom panels sequentially. The velocity profile in **Figure 3B** shows that the MC keeps expansion during the propagation to 5.4 AU. Due to the continuous expansion, the total magnetic field intensity within this MC decreased obviously near 5.4 AU compared to ~1 AU, see **Figures 2A**, **3A**. A shock exists within the MC as depicted with the red arrows in **Figures 3A,B**, and the MC rear boundary can be identified through the He^{2+}/H^{+} ratio and the plasma β value [53]. Note that the shock does not influence our analyses about the ionic charge states and elemental abundances.

Previous studies [53, 63] have confirmed that the MC displayed in **Figure 3** corresponds to that in **Figure 2**. Skoug et al. [63] fitted both MCs using a force-free model of the magnetic field [64] and found that their central speed and cloud axis direction were very similar. The increase in MC diameter between 1 and 5.4 AU was also consistent with an expanding MC. Besides, both MCs had left-handed field structure and contained the similar magnetic fluxes, which

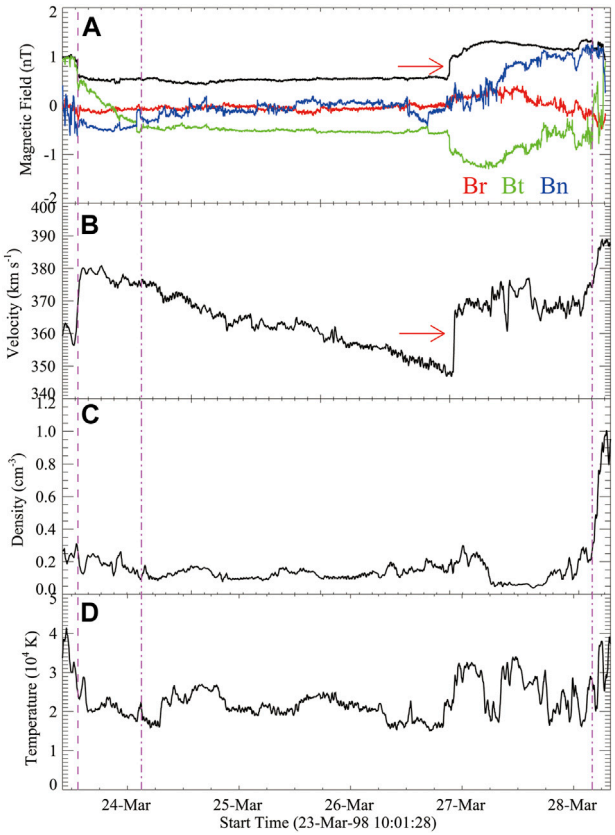

FIGURE 3 | Magnetic field and solar wind parameters measured by Ulysses near 5.4 AU. **(A)** Total magnetic field strength (black) and its three components in RTN coordinate and **(B–D)** velocity, density, and temperature of solar wind. The vertical dashed line denotes the shock, and the dash-dotted lines demarcate the MC boundaries. The red arrows in **(A)** and **(B)** depict the shock inside the MC.

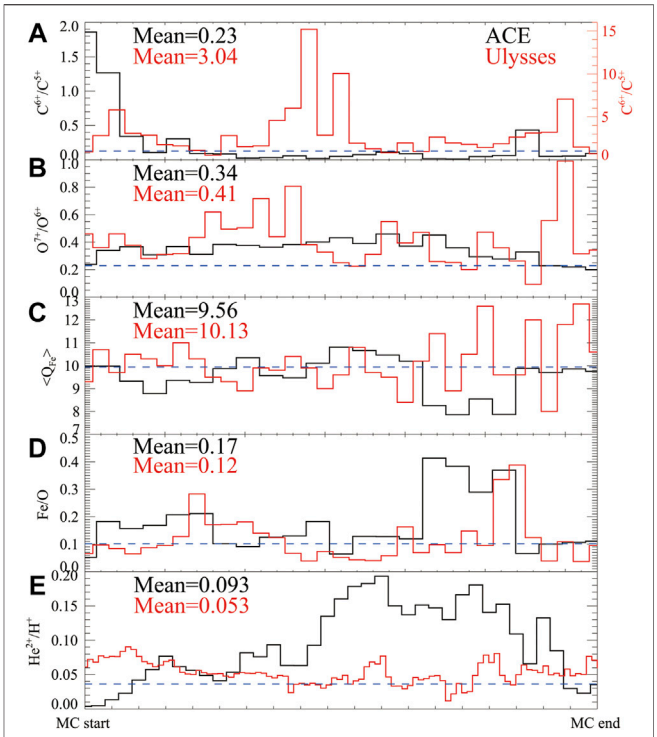

FIGURE 4 | Composition within the MC provided by SWICS aboard ACE (black) and Ulysses (red). Panels **(A–E)** show the C^{6+}/C^{5+}, O^{7+}/O^{6+},<Q_{Fe}>, Fe/O, and He^{2+}/H^{+} sequentially, and their average values are also presented in each panel. Note that the Ulysses values in Panel **(A)** correspond to the right ordinate. The blue horizontal dashed lines depict the corresponding means of slow wind during solar maximum [65]. The MC started from 14:30 UT on March 4 (3:00 UT on March 24) and ended at 5:30 UT on March 6 (4:00 UT on March 28) for ACE (Ulysses).

were further confirmed by Du et al. [53] with the GS reconstruction technique. In addition, Du et al. [53] input the plasma and magnetic field data observed by ACE to their magnetohydrodynamic model to simulate the MC propagation and evolution to the Ulysses location. They compared the model predictions and the Ulysses observations, and identified further that Ulysses and ACE observed the same MC. As mentioned, the ACE (at ~1 AU) and Ulysses (at ~5.4 AU) were located near the ecliptic plane with a latitudinal separation of ~2.2° and a longitudinal separation of ~5.5° when they detected the MC. The GS reconstruction showed that the MC axis oriented in an approximate east-west direction, and both spacecraft almost intersected the MC center [53], which support that ACE and Ulysses crossed the MC at different sites along its axis and provide us an excellent opportunity to explore whether the axial composition is uniform.

We compare the composition measured by both spacecraft in **Figure 4**, where the black and red lines represent the results of ACE and Ulysses, respectively. Please note that we only plot the composition within the MC, that is, the left/right boundary of each panel corresponds to the MC start/end time. The ionic charge states (C^{6+}/C^{5+}, O^{7+}/O^{6+}, and <Q_{Fe}> and elemental abundances (Fe/O and He^{2+}/H^{+}) are presented in **Figure 4A–E**. The average values within the MC are also shown in each panel. The blue horizontal dashed lines represent the corresponding means in the slow solar wind during solar maximum [65] for reference and comparison.

Our study shows that the average values of composition within an MC can possess significant differences along the axis. For example, the C^{6+}/C^{5+} ratio measured by Ulysses (3.04) is 12 times higher than that by ACE (0.23). In the meantime, the differences could be relatively slight for some compositions. For example, the O^{7+}/O^{6+}, ratio measured by Ulysses (0.41) is higher than that of ACE (0.34) by ~21%. The means of <Q_{Fe}> detected by both spacecraft are nearly identical (~10). As to the elemental abundance, the Fe/O ratio by ACE (0.17) is ~42% higher than that by Ulysses (0.12), and the He^{2+}/H^{+} ratio of ACE (0.093) is higher than that of Ulysses (0.053) by ~75%.

Besides the average values, the composition profiles measured by both spacecraft also exhibit discrepancy. **Figure 4A** shows that the C^{6+}/C^{5+} of Ulysses elevated at the MC center, while the ACE profile did not exhibit the central peak. The O^{7+}/O^{6+} of Ulysses presented a multi-peak profile, while ACE did not detect obvious peaks as shown in **Figure 4B**. The He^{2+}/H^{+} of ACE elevated in the

second half as displayed in **Figure 4E**, different from the profile of Ulysses that did not have large variation along the whole path. These can rule out the possibility that the inhomogeneity of composition is induced by the erosion [66] completely during propagation from 1 to 5.4 AU. Moreover, the erosion effect should be small for this event as both MCs have the similar magnetic fluxes as mentioned. The profiles of $<Q_{Fe}>$ and Fe/O measured by both spacecraft also exhibit some different fluctuation characteristics as displayed in **Figures 4C,D**. The above results prove that the composition is inhomogeneous along the MC axis.

4 CONCLUSION AND DISCUSSION

An MC was detected by ACE at ~1 AU and Ulysses at ~5.4 AU sequentially during March 1998, when both spacecraft were located around the ecliptic plane. The latitudinal and longitudinal separations between them were ~2.2° and ~5.5°, respectively. The GS reconstruction [53] showed that the axis oriented in an approximate east–west direction, and both spacecraft almost intersected the MC center, which provided an excellent opportunity to explore whether the composition is uniform along the axis. We compared the ionic charge states of carbon, oxygen, and iron (C^{6+}/C^{5+}, O^{7+}/O^{6+}, and $<Q_{Fe}>$), as well as the elemental abundances of iron and helium (Fe/O and He^{2+}/H^{+}) along the two trajectories. The results showed that the average values of C^{6+}/C^{5+} exhibit significant difference along the axis, while the differences are relatively slight but still obvious for O^{7+}/O^{6+}, $<Q_{Fe}>$, Fe/O, and He^{2+}/H^{+}. Besides the means, the composition profiles within the MC measured by both spacecraft also exhibit obvious discrepancies. We conclude that the inhomogeneity of composition exists along the MC axis.

The magnetic field within the MC measured by Ulysses did not exhibit the obvious changing of direction compared with the measurements of ACE, see **Figures 2A**, **3A**. This might indicate that Ulysses passed through the ICME along a path a little far from the MC center than ACE. **Figure 4A** showed that Ulysses detected high C^{6+}/C^{5+} at its central portion, which should also be observed by ACE if the composition is uniform along the MC axis. However, the C^{6+}/C^{5+} profile of ACE did not present the elevated center. Therefore, if assuming there were some uncertainties about the spacecraft path in the GS reconstruction, it will not change our conclusion about the axial inhomogeneity of MC composition.

The charge states of carbon, oxygen, and iron are frozen-in sequentially in the corona, that is, the frozen-in altitudes of carbon and iron are the lowest and highest, respectively, in these three elements. For example, carbon is frozen-in below 1.5 solar radii [67, 68], while the iron around three to four solar radii [69, 70]. Therefore, the obvious differences of C^{6+}/C^{5+} along the MC axis imply that the different portions of MFR along the axis experience eruption processes with different physical parameters (e.g., temperature, density, and velocity) in the low corona. The similar values of $<Q_{Fe}>$ indicate that the physical parameters along the axis approached in the high corona. These should be taken into account in 3D simulations of CMEs. The axial inhomogeneity of elemental abundances implies that the abundances are not uniform throughout the MC source region on the Sun.

Our study demonstrated that the axial composition is non-uniform inside an MC, while we cannot conclude that this large inhomogeneity exists within each MC. More events are necessary to investigate the inhomogeneity of composition along the MC axis, which needs a CME being detected by several spacecraft sequentially or simultaneously at different locations. This becomes more realizable as Solar Orbiter was launched in 2020 [71]. Besides, Chinese solar physicists are proposing several space missions [72] to explore the Sun and solar eruption further. The Lay a Finger on the Sun [73] will launch a spacecraft to explore the solar eruption near the Sun; thus, it will provide more MC cases that are measured sequentially near the Sun and around 1 AU combined with other spacecraft. The Solar Ring [74] plans to deploy six spacecraft, grouped in three pairs, on a sub-AU orbit around the Sun. The two spacecraft in each group are separated by ~30° and every two groups by ~120°, which can provide more cases that are measured simultaneously by two or more spacecraft around the ecliptic plane. All of these missions will facilitate the studies of solar eruptions and other related issues.

AUTHOR CONTRIBUTIONS

HS led the analysis and drafted the manuscript. QH contributed to further understand the GS reconstruction results in [53]. XC, JZ, LL, and AZ provided suggestions to improve the research. BW helped to plot **Figure 1**. RZ and YC contributed to improve the manuscript.

DATA AVAILABILITY STATEMENT

The plasma and magnetic field data of both ACE and Ulysses are publicly available at the ACE science center (http://www.srl.caltech.edu/ACE/ASC/level2/index.html) and the Ulysses Final Archive (http://ufa.esac.esa.int/ufa/), respectively.

FUNDING

This work was supported by CAS grants XDA-17040507 and NSFC grants U2031109, 11790303 (No. 11790300), and No. 12073042. HS was also supported by the open research program of the CAS Key Laboratory of Solar Activity, KLSA202107.

ACKNOWLEDGMENTS

The authors thank the referees for their constructive comments and suggestions which helped improve the original manuscript considerably. The authors acknowledge the use of data provided by ACE and Ulysses missions. HS thanks Dr Ying D. Liu for the helpful discussions.

REFERENCES

1. Chen PF. Coronal Mass Ejections: Models and Their Observational Basis. *Living Rev Solar Phys* (2011) 8:1. doi:10.12942/lrsp-2011-1
2. Webb DF, and Howard TA. Coronal Mass Ejections: Observations. *Living Rev Solar Phys* (2012) 9:3. doi:10.12942/lrsp-2012-3
3. Cheng X, Guo Y, and Ding M. Origin and Structures of Solar Eruptions I: Magnetic Flux Rope. *Sci China Earth Sci* (2017) 60:1383–407. doi:10.1007/s11430-017-9074-6
4. Guo Y, Cheng X, and Ding M. Origin and Structures of Solar Eruptions II: Magnetic Modeling. *Sci China Earth Sci* (2017) 60:1408–39. doi:10.1007/s11430-017-9081-x
5. Gosling JT, McComas DJ, Phillips JL, and Bame SJ. Geomagnetic Activity Associated with Earth Passage of Interplanetary Shock Disturbances and Coronal Mass Ejections. *J Geophys Res* (1991) 96:7831–9. doi:10.1029/91JA00316
6. Zhang J, Richardson IG, Webb DF, Gopalswamy N, Huttunen E, and Kasper JC. Solar and Interplanetary Sources of Major Geomagnetic Storms (Dst <= -100 nT) during 1996-2005. *J Geophys Res (Space Physics)* (2007) 112:A10102. doi:10.1029/2007JA012321
7. Xu M, Shen C, Wang Y, Luo B, and Chi Y. Importance of Shock Compression in Enhancing ICME's Geoeffectiveness. *ApJ* (2019) 884:L30. doi:10.3847/2041-8213/ab4717
8. Cannon PS. Extreme Space Weather-A Report Published by the UK Royal Academy of Engineering. *Space Weather* (2013) 11:138–9. doi:10.1002/swe.20032
9. Riley P, Baker D, Liu YD, Verronen P, Singer H, and Güdel M. Extreme Space Weather Events: From Cradle to Grave. *Space Sci Rev* (2018) 214:21. doi:10.1007/s11214-017-0456-3
10. Gibson SE, and Fan Y. Coronal Prominence Structure and Dynamics: A Magnetic Flux Rope Interpretation. *J Geophys Res* (2006) 111:A12103. doi:10.1029/2006JA011871
11. Canou A, and Amari T. A Twisted Flux Rope as the Magnetic Structure of a Filament in Active Region 10953 Observed Byhinode. *ApJ* (2010) 715:1566–74. doi:10.1088/0004-637X/715/2/1566
12. Illing RME, and Hundhausen AJ. Observation of a Coronal Transient from 1.2 to 6 Solar Radii. *J Geophys Res* (1985) 90:275–82. doi:10.1029/JA090iA01p00275
13. Howard TA, DeForest CE, Schneck UG, and Alden CR. Challenging Some Contemporary Views of Coronal Mass Ejections. II. The Case for Absent Filaments. *ApJ* (2017) 834:86. doi:10.3847/1538-4357/834/1/86
14. Song HQ, Cheng X, Chen Y, Zhang J, Wang B, Li LP, et al. The Three-Part Structure of a Filament-Unrelated Solar Coronal Mass Ejection. *ApJ* (2017) 848:21. doi:10.3847/1538-4357/aa8d1a
15. Song HQ, Zhang J, Cheng X, Li LP, Tang YZ, Wang B, et al. On the Nature of the Bright Core of Solar Coronal Mass Ejections. *ApJ* (2019) 883:43. doi:10.3847/1538-4357/ab304c
16. Song HQ, Zhang J, Li LP, Liu YD, Zhu B, Wang B, et al. The Structure of Solar Coronal Mass Ejections in the Extreme-Ultraviolet Passbands. *ApJ* (2019) 887:124. doi:10.3847/1538-4357/ab50b6
17. Zhang J, Cheng X, and Ding M-d. Observation of an Evolving Magnetic Flux Rope before and during a Solar Eruption. *Nat Commun* (2012) 3:747. doi:10.1038/ncomms1753
18. Sahu S, Joshi B, Mitra PK, Veronig AM, and Yurchyshyn V. Hard X-Ray Emission from an Activated Flux Rope and Subsequent Evolution of an Eruptive Long-Duration Solar Flare. *ApJ* (2020) 897:157. doi:10.3847/1538-4357/ab962b
19. Wu Z, Chen Y, Huang G, Nakajima H, Song H, Melnikov V, et al. Microwave Imaging of a Hot Flux Rope Structure during the Pre-impulsive Stage of an Eruptive M7.7 Solar Flare. *ApJ* (2016) 820:L29. doi:10.3847/2041-8205/820/2/L29
20. Chen J. Theory of Prominence Eruption and Propagation: Interplanetary Consequences. *J Geophys Res* (1996) 101:27499–519. doi:10.1029/96JA02644
21. Lin J, and Forbes TG. Effects of Reconnection on the Coronal Mass Ejection Process. *J Geophys Res* (2000) 105:2375–92. doi:10.1029/1999JA900477
22. Patsourakos S, Vourlidas A, and Stenborg G. Direct Evidence for a Fast Coronal Mass Ejection Driven by the Prior Formation and Subsequent Destabilization of a Magnetic Flux Rope. *ApJ* (2013) 764:125. doi:10.1088/0004-637X/764/2/125
23. Cheng X, Zhang J, Ding MD, Liu Y, and Poomvises W. The Driver of Coronal Mass Ejections in the Low Corona: A Flux Rope. *ApJ* (2013) 763:43. doi:10.1088/0004-637X/763/1/43
24. Mikic Z, and Linker JA. Disruption of Coronal Magnetic Field Arcades. *ApJ* (1994) 430:898. doi:10.1086/174460
25. Antiochos SK, DeVore CR, and Klimchuk JA. A Model for Solar Coronal Mass Ejections. *ApJ* (1999) 510:485–93. doi:10.1086/306563
26. Song HQ, Zhang J, Chen Y, and Cheng X. Direct Observations of Magnetic Flux Rope Formation during a Solar Coronal Mass Ejection. *ApJ* (2014) 792:L40. doi:10.1088/2041-8205/792/2/L40
27. Ouyang Y, Yang K, and Chen PF. Is Flux Rope a Necessary Condition for the Progenitor of Coronal Mass Ejections?. *Astrophys J* (2015) 815:72. doi:10.1088/0004-637X/815/1/72
28. Wang W, Liu R, Wang Y, Hu Q, Shen C, Jiang C, et al. Buildup of a Highly Twisted Magnetic Flux Rope during a Solar Eruption. *Nat Commun* (2017) 8:1330. doi:10.1038/s41467-017-01207-x
29. Ouyang Y, Zhou YH, Chen PF, and Fang C. Chirality and Magnetic Configurations of Solar Filaments. *Astrophys J* (2017) 835:94. doi:10.3847/1538-4357/835/1/94
30. Kumar S, Bhattacharyya R, Joshi B, and Smolarkiewicz PK. On the Role of Repetitive Magnetic Reconnections in Evolution of Magnetic Flux Ropes in Solar Corona. *ApJ* (2016) 830:80. doi:10.3847/0004-637X/830/2/80
31. Cheng X, Ding MD, and Fang C. Imaging and Spectroscopic Diagnostics on the Formation of Two Magnetic Flux Ropes Revealed Bysdo/aia Andiris. *ApJ* (2015) 804:82. doi:10.1088/0004-637X/804/2/82
32. Zheng R, Chen Y, Wang B, Song H, and Cao W. Formation of a Tiny Flux Rope in the center of an Active Region Driven by Magnetic Flux Emergence, Convergence, and Cancellation. *A&A* (2020) 642:A199. doi:10.1051/0004-6361/202037475
33. Owocki SP, Holzer TE, and Hundhausen AJ. The Solar Wind Ionization State as a Coronal Temperature Diagnostic. *ApJ* (1983) 275:354–66. doi:10.1086/161538
34. Laming JM. The FIP and Inverse FIP Effects in Solar and Stellar Coronae. *Living Rev Sol Phys* (2015) 12:2. doi:10.1007/lrsp-2015-2
35. Vadawale SV, Mondal B, Mithun NPS, Sarkar A, Janardhan P, Joshi B, et al. Observations of the Quiet Sun during the Deepest Solar Minimum of the Past Century with Chandrayaan-2 XSM: Elemental Abundances in the Quiescent Corona. *ApJL* (2021) 912:L12. doi:10.3847/2041-8213/abf35d
36. Song H, and Yao S. Characteristics and Applications of Interplanetary Coronal Mass Ejection Composition. *Sci China Technol Sci* (2020) 63:2171. doi:10.1007/s11431-020-1680-y
37. Song HQ, Zhong Z, Chen Y, Zhang J, Cheng X, Zhao L, et al. A Statistical Study of the Average Iron Charge State Distributions inside Magnetic Clouds for Solar Cycle 23. *ApJS* (2016) 224:27. doi:10.3847/0067-0049/224/2/27
38. Huang J, Liu YC-M, Peng J, Qi Z, Li H, Klecker B, et al. The Distributions of Iron Average Charge States in Small Flux Ropes in Interplanetary Space: Clues to Their Twisted Structures. *J Geophys Res Space Phys* (2018) 123:7167–80. doi:10.1029/2018JA025660
39. Song HQ, Chen Y, Li B, Li LP, Zhao L, He JS, et al. The Origin of Solar Filament Plasma Inferred from *In Situ* Observations of Elemental Abundances. *ApJ* (2017) 836:L11. doi:10.3847/2041-8213/aa5d54
40. Fu H, Harrison RA, Davies JA, Xia L, Zhu X, Li B, et al. The High Helium Abundance and Charge States of the Interplanetary CME and its Material Source on the Sun. *ApJ* (2020) 900:L18. doi:10.3847/2041-8213/abb083
41. Lepri ST, Zurbuchen TH, Fisk LA, Richardson IG, Cane HV, and Gloeckler G. Iron Charge Distribution as an Identifier of Interplanetary Coronal Mass Ejections. *J Geophys Res* (2001) 106:29231–8. doi:10.1029/2001JA000014
42. Burlaga L, Sittler E, Mariani F, and Schwenn R. Magnetic Loop behind an Interplanetary Shock: Voyager, Helios, and IMP 8 Observations. *J Geophys Res* (1981) 86:6673–84. doi:10.1029/JA086iA08p06673
43. Syed Ibrahim M, Joshi B, Cho K-S, Kim R-S, and Moon Y-J. Interplanetary Coronal Mass Ejections during Solar Cycles 23 and 24: Sun-Earth Propagation Characteristics and Consequences at the Near-Earth Region. *Sol Phys* (2019) 294:54. doi:10.1007/s11207-019-1443-5
44. Song HQ, Zhang J, Cheng X, Li G, Hu Q, Li LP, et al. Do All Interplanetary Coronal Mass Ejections Have a Magnetic Flux Rope Structure Near 1 au?. *ApJ* (2020) 901:L21. doi:10.3847/2041-8213/abb6ec

45. Gopalswamy N. Properties of Interplanetary Coronal Mass Ejections. *Space Sci Rev* (2007) 124:145–68. doi:10.1007/s11214-006-9102-1
46. Kim R-S, Gopalswamy N, Cho K-S, Moon Y-J, and Yashiro S. Propagation Characteristics of CMEs Associated with Magnetic Clouds and Ejecta. *Sol Phys* (2013) 284:77–88. doi:10.1007/s11207-013-0230-y
47. Huang J, Liu Y, Feng H, Zhao A, Abidin ZZ, Shen Y, et al. A Statistical Study of the Plasma and Composition Distribution inside Magnetic Clouds: 1998-2011. *ApJ* (2020) 893:136. doi:10.3847/1538-4357/ab7a28
48. Owens MJ. Solar Wind and Heavy Ion Properties of Interplanetary Coronal Mass Ejections. *Sol Phys* (2018) 293:122. doi:10.1007/s11207-018-1343-0
49. Zurbuchen TH, Weberg M, von Steiger R, Mewaldt RA, Lepri ST, and Antiochos SK. Composition of Coronal Mass Ejections. *ApJ* (2016) 826:10. doi:10.3847/0004-637X/826/1/10
50. Song H, Li L, Sun Y, Lv Q, Zheng R, and Chen Y. *Solar Cycle Dependence of ICME Composition*. arXiv:2106.03003 (2021).
51. Hu Q, and Sonnerup BUÖ. Reconstruction of Magnetic Clouds in the Solar Wind: Orientations and Configurations. *J Geophys Res* (2002) 107:1142. doi:10.1029/2001JA000293
52. Hu Q. The Grad-Shafranov Reconstruction in Twenty Years: 1996-2016. *Sci China Earth Sci* (2017) 60:1466–94. doi:10.1007/s11430-016-9052-110.1007/s11430-017-9067-2
53. Du D, Wang C, and Hu Q. Propagation and Evolution of a Magnetic Cloud from ACE to Ulysses. *J Geophys Res* (2007) 112:a. doi:10.1029/2007JA012482
54. Smith CW, L'Heureux J, Ness NF, Acuña MH, Burlaga LF, and Scheifele J. The ACE Magnetic Fields Experiment. *Space Sci Rev* (1998) 86:613–32. doi:10.1023/A:100509221666810.1007/978-94-011-4762-0_21
55. Balogh A, Beek TJ, Forsyth RJ, Hedgecock PC, Marquedant RJ, Smith EJ, et al. The Magnetic Field Investigation on the ULYSSES mission - Instrumentation and Preliminary Scientific Results. *Astron Astrophys Suppl* (1992) 92:221–36.
56. McComas DJ, Bame SJ, Barker P, Feldman WC, Phillips JL, Riley P, et al. Solar Wind Electron Proton Alpha Monitor (SWEPAM) for the Advanced Composition Explorer. *Space Sci Rev* (1998) 86:563–612. doi:10.1023/A:100504023259710.1007/978-94-011-4762-0_20
57. Bame SJ, McComas DJ, Barraclough BL, Phillips JL, Sofaly KJ, Chavez JC, et al. The ULYSSES Solar Wind Plasma experiment. *Astron Astrophys Suppl* (1992) 92:237–65.
58. Gloeckler G, Cain J, Ipavich FM, Tums EO, Bedini P, Fisk LA, et al. Investigation of the Composition of Solar and Interstellar Matter Using Solar Wind and Pickup Ion Measurements with SWICS and SWIMS on the ACE Spacecraft. *Space Sci Rev* (1998) 86:497–539. doi:10.1023/A:100503613168910.1007/978-94-011-4762-0_18
59. Geiss J, Gloeckler G, Balsiger H, Fisk LA, Galvin AB, Gliem F, et al. Plasma Composition in Jupiter's Magnetosphere: Initial Results from the Solar Wind Ion Composition Spectrometer. *Science* (1992) 257:1535–9. doi:10.1126/science.257.5076.1535
60. Cane HV, and Richardson IG. Interplanetary Coronal Mass Ejections in the Near-Earth Solar Wind during 1996-2002. *J Geophys Res* (2003) 108:1156. doi:10.1029/2002JA009817
61. Chi Y, Shen C, Wang Y, Xu M, Ye P, and Wang S. Statistical Study of the Interplanetary Coronal Mass Ejections from 1995 to 2015. *Sol Phys* (2016) 291:2419–39. doi:10.1007/s11207-016-0971-5
62. Du D, Zuo PB, and Zhang XX. Interplanetary Coronal Mass Ejections Observed by Ulysses through its Three Solar Orbits. *Sol Phys* (2010) 262:171–90. doi:10.1007/s11207-009-9505-8
63. Skoug RM, Feldman WC, Gosling JT, McComas DJ, Reisenfeld DB, Smith CW, et al. Radial Variation of Solar Wind Electrons inside a Magnetic Cloud Observed at 1 and 5 AU. *J Geophys Res* (2000) 105:27269–75. doi:10.1029/2000JA000095
64. Lepping RP, Jones JA, and Burlaga LF. Magnetic Field Structure of Interplanetary Magnetic Clouds at 1 AU. *J Geophys Res* (1990) 95:11957–65. doi:10.1029/JA095iA08p11957
65. Lepri ST, Landi E, and Zurbuchen TH. Solar Wind Heavy Ions over Solar Cycle 23:Ace/swics Measurements. *ApJ* (2013) 768:94. doi:10.1088/0004-637X/768/1/94
66. Ruffenach A, Lavraud B, Owens MJ, Sauvaud J-A, Savani NP, Rouillard AP, et al. Multispacecraft Observation of Magnetic Cloud Erosion by Magnetic Reconnection during Propagation. *J Geophys Res* (2012) 117:a. doi:10.1029/2012JA017624
67. Chen Y, Esser R, and Hu Y. Formation of Minor-Ion Charge States in the Fast Solar Wind: Roles of Differential Flow Speeds of Ions of the Same Element. *ApJ* (2003) 582:467–74. doi:10.1086/344642
68. Landi E, Gruesbeck JR, Lepri ST, Zurbuchen TH, and Fisk LA. Charge State Evolution in the Solar Wind. II. Plasma Charge State Composition in the Inner Corona and Accelerating Fast Solar Wind. *ApJ* (2012) 761:48. doi:10.1088/0004-637X/761/1/48
69. Buergi A, and Geiss J. Helium and Minor Ions in the Corona and Solar Wind - Dynamics and Charge States. *Solar Phys* (1986) 103:347–83. doi:10.1007/BF00147835
70. Boe B, Habbal S, Druckmüller M, Landi E, Kourkchi E, Ding A, et al. The First Empirical Determination of the Fe10+ and Fe13+ Freeze-In Distances in the Solar Corona. *ApJ* (2018) 859:155. doi:10.3847/1538-4357/aabfb7
71. Müller D, Marsden RG, Marsden RG, St. Cyr OC, and Gilbert HR. Solar Orbiter. *Sol Phys* (2013) 285:25–70. doi:10.1007/s11207-012-0085-7
72. Gan W, Yan Y, and Huang Y. Prospect for Space Solar Physics in 2016-2030. *Scientia Sinica Physica, Mechanica & Astronomica* (2019) 49:059602. doi:10.1360/SSPMA2018-00301
73. Lin J, Wang M, Tian H, Song H, Fu H, and Huang M. In Situmeasurements of the Solar Eruption. *Scientia Sinica Physica, Mechanica & Astronomica* (2019) 49:059607. doi:10.1360/SSPMA2018-00308
74. Wang Y, Ji H, Wang Y, Xia L, Shen C, Guo J, et al. Concept of the Solar Ring mission: An Overview. *Sci China Technol Sci* (2020) 63:1699–713. doi:10.1007/s11431-020-1603-2

Conflict of Interest: The authors declare that the research was conducted in the absence of any commercial or financial relationships that could be construed as a potential conflict of interest.

frontiers in Physics

ORIGINAL RESEARCH
published: 22 July 2021
doi: 10.3389/fphy.2021.706056

Configuration of a Magnetic Cloud From Solar Orbiter and Wind Spacecraft *In-situ* Measurements

Qiang Hu[1]*, *Wen He*[1], *Lingling Zhao*[1] and *Edward Lu*[2]

[1]Center for Space Plasma and Aeronomic Research, Department of Space Science, The University of Alabama in Huntsville, Huntsville, AL, United States, [2]Department of Electrical Engineering and Computer Science, Massachusetts Institute of Technology, Cambridge, MA, United States

Coronal mass ejections (CMEs) represent one type of the major eruption from the Sun. Their interplanetary counterparts, the interplanetary CMEs (ICMEs), are the direct manifestations of these structures when they propagate into the heliosphere and encounter one or more observing spacecraft. The ICMEs generally exhibit a set of distinctive signatures from the *in-situ* spacecraft measurements. A particular subset of ICMEs, the so-called Magnetic Clouds (MCs), is more uniquely defined and has been studied for decades, based on *in-situ* magnetic field and plasma measurements. By utilizing the latest multiple spacecraft measurements and analysis tools, we report a detailed study of the internal magnetic field configuration of an MC event observed by both the Solar Orbiter (SO) and Wind spacecraft in the solar wind near the Sun-Earth line. Both two-dimensional (2D) and three-dimensional (3D) models are applied to reveal the flux rope configurations of the MC. Various geometrical as well as physical parameters are derived and found to be similar within error estimates for the two methods. These results quantitatively characterize the coherent MC flux rope structure crossed by the two spacecraft along different paths. The implication for the radial evolution of this MC event is also discussed.

Keywords: magnetic clouds, magnetic flux ropes, coronal mass ejections, grad-shafranov equation, force-free field, solar orbiter, wind

OPEN ACCESS

Edited by:
Daniel Verscharen,
University College London,
United Kingdom

Reviewed by:
Nandita Srivastava,
Physical Research Laboratory, India
Yeimy Rivera,
Harvard University, United States

***Correspondence:**
Qiang Hu
qh0001@uah.edu

Specialty section:
This article was submitted to Stellar and Solar Physics, a section of the journal Frontiers in Physics

Received: *06 May 2021*
Accepted: *07 July 2021*
Published: *22 July 2021*

Citation:
Hu Q, He W, Zhao L and Lu E (2021) Configuration of a Magnetic Cloud From Solar Orbiter and Wind Spacecraft In-situ *Measurements. Front. Phys. 9:706056. doi: 10.3389/fphy.2021.706056*

1 INTRODUCTION

Magnetic clouds (MCs) represent an important type of space plasma structures observed by *in-situ* spacecraft missions in the solar wind. They have been first identified in the *in-situ* spacecraft measurements of magnetic field and plasma parameters, and have been studied for decades, based on heliospheric mission datasets [1–4]. These include the earlier missions such as the Interplanetary Monitoring Platform (IMP), Helios, and Voyager missions. In later times, a number of NASA/ESA flagship missions, including Advanced Composition Explorer (ACE) [5], Wind [6], Ulysses [7], and Solar and TErrestrial RElations Observatory (STEREO) [8], have contributed greatly to the study of Solar-Terrestrial physics in general, and to the characterization of MC structures in particular. Generally speaking, the opportunities for one MC structure to be encountered by two or more spacecraft are rare, but when they do occur, it offers a unique opportunity for correlative and combined analysis between multiple spacecraft datasets (see references below).

A few such examples include an early study by [9] by using five spacecraft and the series of MC events in May 2007. During 19–23 May 2007, the newly launched twin STEREO spacecraft, Ahead

and Behind, i.e., STEREO-A and B, respectively, were separated from Earth by ~6° and ~3°, longitudinally, near 1 au. Therefore, the ACE, Wind, and STEREO spacecraft constellations observed a series of MC events, which enabled a number of correlative studies by using multi-spacecraft measurements [10–13]. Additionally, a number of studies took advantage of the rare occurrence of radial alignment of mostly two spacecraft separated in heliocentric distances, r_h, from the Sun. For example, Du et al. [14] studied an MC event and its evolution between the ACE and Ulysses spacecraft when they were separated radially by a distance of ~ 4 au. They found that although the time-series data have evolved significantly between the two spacecraft, a flux rope configuration was still obtained at each spacecraft location and their magnetic field properties were compared. In this research topic collection, Song et al. [15] re-examined this event from the perspective of implications for elemental charge states in MCs. Lately, Davies et al. [16] analyzed an MC event detected *in-situ* by the Solar Orbiter (SO), Wind, and Bepi Colombo spacecraft in April 2020, and related to its solar source CME eruption by using the coronagraphic imaging observations from STEREO. We will re-examine this MC event by using the *in-situ* measurements from both SO and Wind spacecraft. We focus on the reconstruction of the magnetic field configurations and characterizations of the MC flux rope derived from the Wind spacecraft *in-situ* data. Quantitative comparison will be made with the magnetic field measurements along the projected SO spacecraft path across the same flux rope structure.

One commonly applied quantitative analysis method for MCs based on single-spacecraft *in-situ* data usually adopts the approach of an optimal fitting to an analytic solution, such as the well-known linear force-free field (LFFF) Lundquist solution [17], against the time series of magnetic field components within a selected interval. These solutions have limited one-dimensional (1D) spatial dependence, i.e., exhibit spatial variation in the radial dimension away from a central axis only. Recently we have improved the optimal fitting approach by extending the Lundquist solution to a quasi-three dimensional (3D) geometry [18, 19], based on the so-called Freidberg solution [20]. It represents a more general 3D configuration that can account for, to a greater degree, the significant variability in the *in-situ* measurements of MCs, such as the asymmetric magnetic field profile and sometimes the relatively large radial field component. An alternative two-dimensional (2D) method has also been applied to *in-situ* modeling of MCs, by employing the Grad-Shafranov (GS) equation, describing a two and a half dimensional (2–1/2D) configuration in quasi-static equilibrium [21–24]. This so-called GS reconstruction method is able to derive a 2D cross section of the structure traversed by a single spacecraft, yielding a complete quantitative characterization of the magnetic field configuration composed of nested cylindrical flux surfaces for a flux rope. Such a solution generally conforms to a cylindrical flux rope configuration with an arbitrary 2D cross section. The GS reconstruction method has been applied in a number of multi-spacecraft studies of MCs [see, e.g. [14, 25]], including the aforementioned MC events in May 2007 during the earlier stage of the STEREO mission. In addition, it has been widely applied to a variety of space plasma regimes with extended capability and additional improvement [26].

A new era has begun for solar and heliospheric physics with the launch of the Parker Solar Probe (PSP) [27] and the Solar Orbiter (SO) [28] missions. They will not only yield unprecedented new discoveries of never-before explored territories, but also provide two additional sets of *in-situ* measurements at different locations in the heliosphere. PSP will plunge closer to the Sun and reach a heliocentric distance below 0.1 au, and SO will provide highly anticipated measurements over a range of heliocentric distances and beyond the ecliptic plane. In this study, we examine one MC event detected during the month of April 2020 by both SO and Wind spacecraft when they were approximately aligned radially from the Sun, but separated by a radial distance of ~ 0.2 au. We present an overview of the event in **Section 2**. The analysis results by using both the GS reconstruction and the optimal fitting methods are described in **Section 3**. In **Section 4**, we discuss the implications for the radial evolution of MCs under the condition of a nearly constant solar wind speed, based on the current event study results. We then summarize the results from this event study in the last section.

2 EVENT OVERVIEW

The SO mission observed its first ICME event on April 19, 2020 (day of year, DOY 110) at a heliocentric distance ~ 0.81 au near the Sun-Earth line [16, 29]. As summarized in [16], the ICME complex arrived at SO at 05:06 UT, as marked by an interplanetary shock, and followed by a "magnetic obstacle" 3.88 h later, which may embody a flux rope structure, and lasted for about 24 h. The Wind spacecraft subsequently observed the same structures about 1 day later. **Figures 1A,C** show the *in situ* measurements from the spacecraft Wind and SO (magnetic field only [30]), respectively. **Figure 1B** shows the relative locations of a number of objects of interest including SO and Earth (Wind) on the X-Y plane of the Earth Ecliptic (HEE) coordinate system. Relative to Wind, SO was offset from the Sun-Earth (Wind) line by about 4.02° to the East, while it was North of the ecliptic plane with a latitude of about 1.22° [16].

In **Figure 1A**, two intervals are marked for the subsequent analysis of the ICME/MC flux rope structure *via* the GS reconstruction method (between 11:36 and 22:28 UT) and the optimal 3D Freidberg solution fitting approach (between 12:41 and 23:15 UT) on April 20, 2020. The *in-situ* measurements enclosed by the vertical lines indicate clear signatures for an MC: 1) elevated magnetic field magnitude, 2) relatively smooth rotation in field components (i.e., mainly the GSE-Z component varying from negative to positive values), and 3) depressed proton temperature and β value. The corresponding measurements of magnetic field components at SO show similar features with slightly enhanced magnetic field magnitude. The plasma measurements were not available during these earlier time periods of the mission [16]. In particular, the rotation in the N component of the magnetic field at SO corresponds well to the rotation in the GSE-Z component at Wind, while the East-West components (along T and the GSE-Y directions) are approximately reversed. For a typical cylindrical flux rope

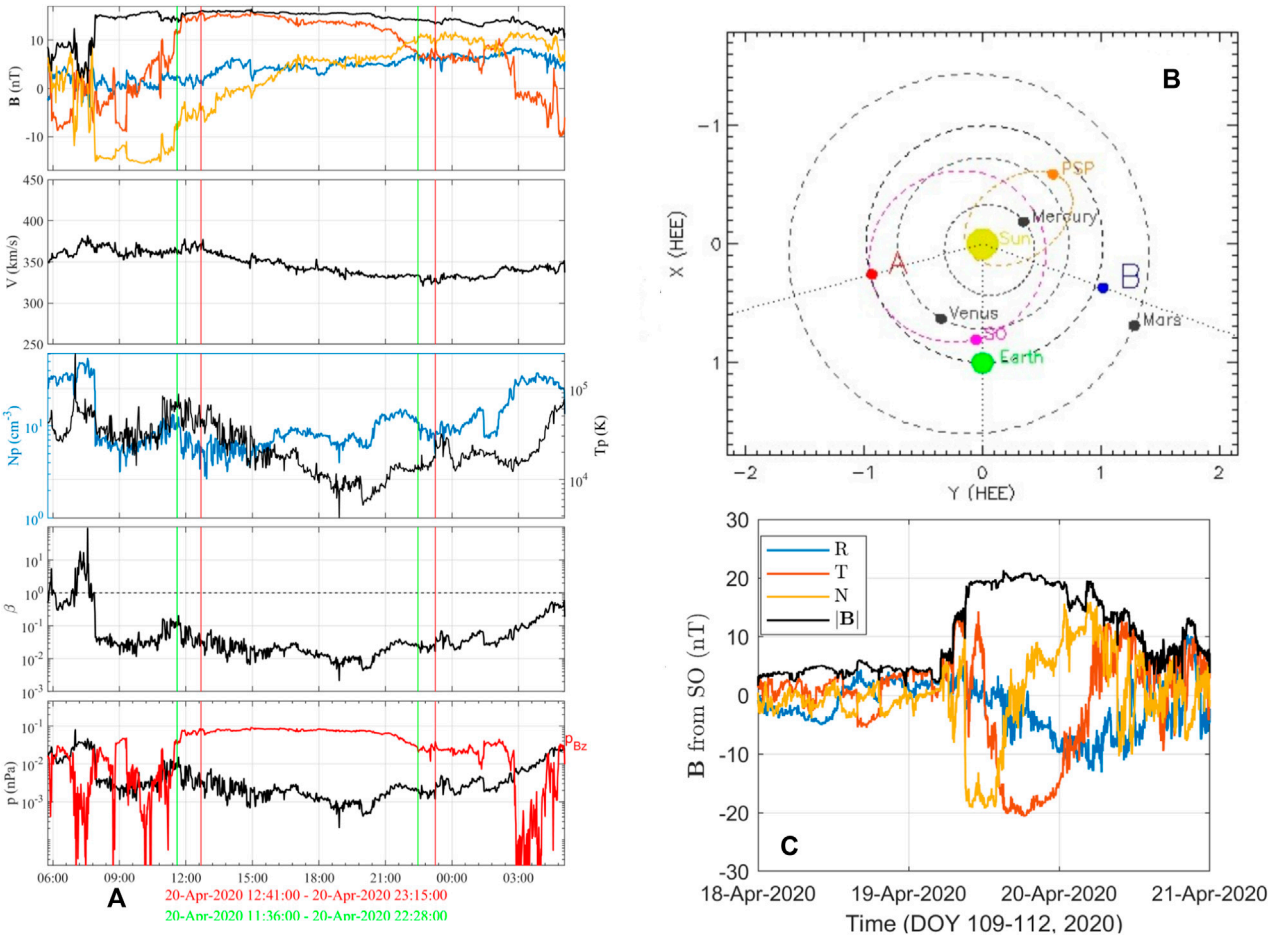

FIGURE 1 | (A) Time series data from Wind spacecraft (from **top to bottom panels**) the magnetic field components in GSE-X (blue), Y (red), and Z (gold) coordinates and the magnitude (black), the solar wind speed, the proton number density (blue; left axis) and temperature (black; right axis), the proton β, and the proton plasma pressure and the axial magnetic pressure (red). Two sets of vertical lines mark the intervals for the GS reconstruction (green) and the optimal fitting to the Freidberg solution (red), respectively, and are denoted beneath the last panel. **(B)** The multiple spacecraft and planets locations around April 20, 2020 in the ecliptic plane (courtesy of the STEREO Science Center). **(C)** The corresponding SO magnetic field measurements in the RTN coordinates (see legend).

configuration crossed by a single spacecraft, the magnetic field component with a uni-polar pattern usually corresponds to the field component along the axis of the flux rope, while the change in the north-south or east-west component usually indicates the rotation of the transverse field about the axis. Therefore these signatures, for this particular MC event, hint at a flux rope configuration lying near the ecliptic with the axial direction pointing eastward (positive GSE-Y component, aligned with the thumb of the left hand) with respect to the Sun and with a left-handed chirality (the handedness; GSE-Z component rotating from southward to northward direction, aligned with the other four fingers). Given the difference in the magnetic field magnitude and a 1-day time delay consistent with the radial separation distance between SO and Wind [16], it is plausible to consider an evolution between the two spacecraft as well as the spatial variation, assuming that the two spacecraft crossed the same structure along different paths mainly due to their longitudinal separation. In what follows, we present our analysis results and discuss the interpretations.

3 METHODS AND RESULTS

We have developed and applied both 2D and 3D flux rope models to *in-situ* spacecraft measurements of MCs. The 2D model is based on the Grad-Shafranov (GS) equation and is able to derive a 2D cylindrical configuration with nested flux surfaces of arbitrary cross section shape [see, e.g. [26]]. The 3D model is based on a more general LFFF formulation, the so-called Freidberg solution [20], and accounts for a greater deal of variability in the *in-situ* data through a rigorous χ^2 optimal fitting approach. This approach was recently developed and described in [18, 19]. Both methods can yield a set of parameters characterizing the geometrical and physical properties of the structure, including the axial orientation in space, the handedness (i.e., chirality, sign of magnetic helicity), and the axial magnetic flux content (sum of axial flux over a cross-section area), for a flux rope configuration. We apply both methods to the Wind spacecraft data of the MC intervals marked in **Figure 1A**,

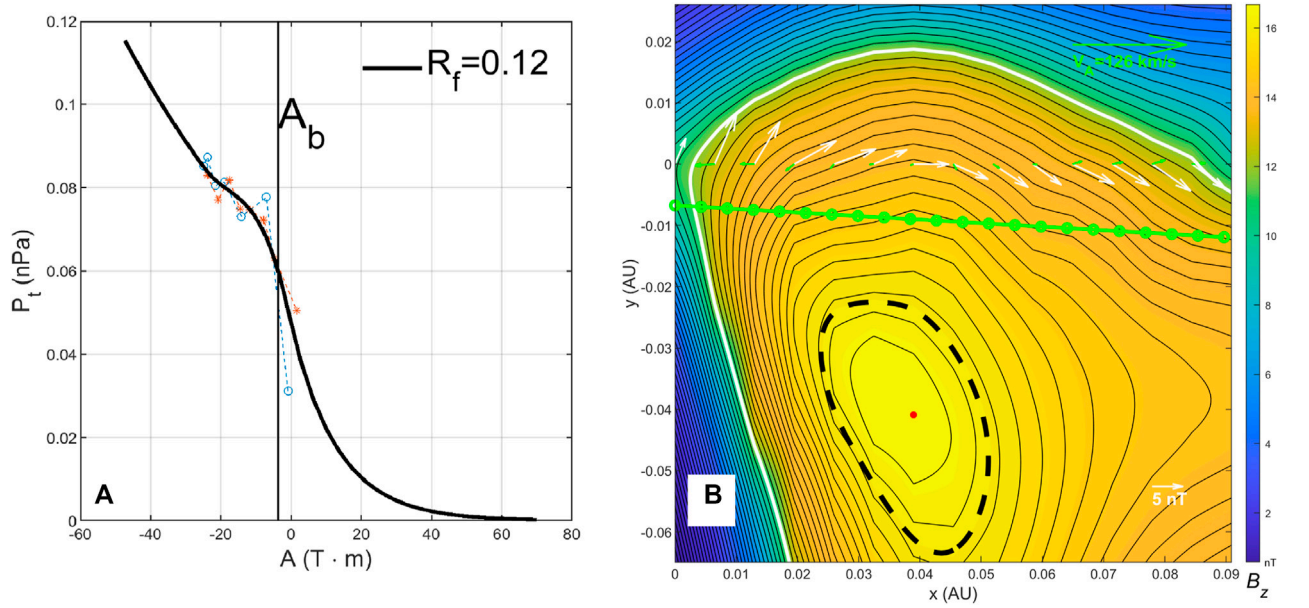

FIGURE 2 | (A) The P_t versus A data (symbols) along the Wind spacecraft path, and the fitted $P_t(A)$ curve (thick black curve) with the corresponding fitting residue R_f denoted. The vertical line marks the boundary defined by $A = A_b$, **(B)** The cross section map from the GS reconstruction for the MC interval marked in **Figure 1**. The black contours are the iso-surfaces of $A(x, y)$, and the filled color contours indicate the axial field $B_z(A)$ with scales given by the colorbar. The Wind spacecraft path is projected along $y = 0$ with white (green) arrows representing the measured transverse magnetic field (remaining flow) vectors. A reference vector proportional in magnitude for each set is provided, respectively, with the white reference vector in the lower right of magnitude 5 nT and the green reference vector of the magnitude of the average Alfvén speed in the top right. The SO spacecraft path is projected onto the same map as the green line with green circles. The thick dashed contour line highlights the outermost closed loop surrounding the center marked by the red dot where B_z reaches the maximum B_{z0}.

and cross-check with the corresponding magnetic field measurements along the separate SO spacecraft path across the same structure.

3.1 Grad-Shafranov Reconstruction Results

The GS reconstruction utilizes the spacecraft measurements of magnetic field $\boldsymbol{B}$ and solar wind velocity $\boldsymbol{V}$, and additional plasma parameters as initial conditions to solve the scalar GS equation, which governs the 2–1/2D magnetic field configuration across the cross section plane perpendicular to the z axis with $B_z \neq 0$ and $\partial/\partial z \approx 0$. The solution to the GS equation is obtained in the form of a 2D magnetic flux function $A(x, y)$, which fully characterizes the three components of the magnetic field especially including the axial field $B_z(A)$, among other quantities being single-variable functions of A. **Figure 2A** shows the data points along the Wind spacecraft path across the MC interval, and the functional form for $P_t(A) = p + B_z^2/2\mu_0$, the sum of the plasma pressure and the axial magnetic pressure. Each quantity is a single-variable function of A as required by the GS equation. An optimal z axis orientation is found for which the requirement of $P_t(A)$ being single-valued is best satisfied [for details, see, 23]. For this case, the z axis orientation is found to be $(\delta, \phi) = (79, 96) \pm (4, 9)$[1] degrees, with uncertainties estimated by error propagation [24]. Then these functions, especially the fitted function $P_t(A)$, are used to solve the GS equation and obtain a cross section map of the 2D magnetic field structure given in **Figure 2B** for this event. It shows a flux rope configuration with distinct nested flux surfaces (iso-surfaces or contours of A), on which the field lines are winding along the z dimension and the axial field B_z remains the same on each surface. The left-handedness (negative chirality) is readily seen from this cross section map, by pointing the thumb of the left hand upward in the positive B_z direction, while wrapping the other four fingers around the direction marked by the white arrows along $y = 0$. The center of the flux rope defined by the location of the maximum B_z value appears to be away from the spacecraft path at $y = 0$ in this case.

This is a typical rendering of the GS reconstruction result as viewed down the z axis such that the flux surfaces (contours of A) are projected onto the cross-section plane as closed loops surrounding the center for a flux rope configuration. The axial magnetic field usually reaches the maximum at the center and decreases monotonically toward the outer boundary. Along the spacecraft path at $y = 0$, the observed transverse magnetic field vectors are tangential to the contours. It is also indicated that the remaining flow (green vectors along $y = 0$; see also below) as viewed in the frame moving with the flux rope structure is negligible compared with the average Alfvén speed (denoted in the top right-hand corner of magnitude 126 km/s). The effect associated with the inertial force in the magnetohydrodynamics (MHD) framework is assessed *via* the de Hoffmann-Teller (HT) analysis [see, e.g. [18]]. **Figure 3** shows the HT analysis result for

[1]The polar angle δ is from the ecliptic north, and the azimuthal angle ϕ is measured from GSE-X towards GSE-Y axes, all in degrees.

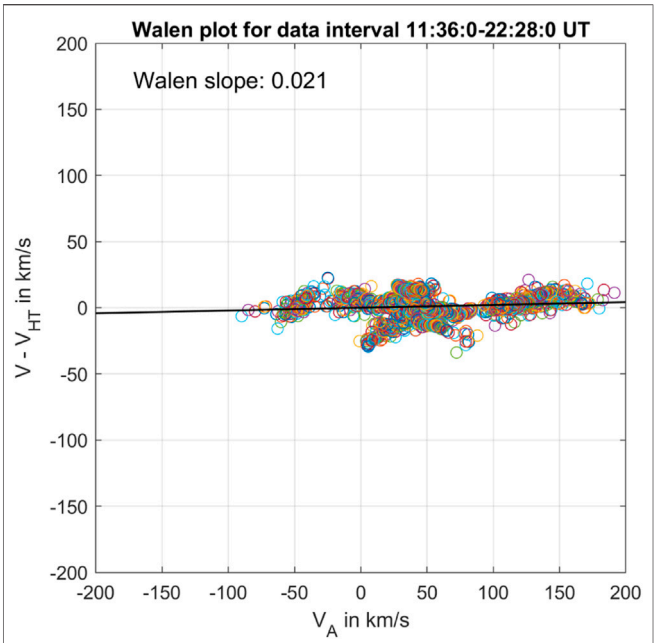

FIGURE 3 | The Walén plot for the MC interval at Wind for which the GS reconstruction is applied. The HT analysis yields an HT frame velocity [−346.52, −10.81, 21.10] km/s, in the GSE coordinates. The slope of the regression line shown is denoted the Walén slope.

this MC interval, in terms of the Walén plot, yielding a slope 0.021 of the regression line. This indicates a negligible ratio between the remaining flow $\boldsymbol{V} - \boldsymbol{V}_{HT}$ and the local Alfvén velocity. Thus a quasi-static equilibrium as dictated by the GS equation in the HT frame moving with frame velocity $\boldsymbol{V}_{HT}$ is approximately satisfied. For this event, since the SO spacecraft crossed the same structure at a close separation distance but at an earlier time, it is useful to project the SO path onto the cross section map generated by the Wind *in-situ* measurements, as indicated by the green line with circles in **Figure 2B**. We will further discuss the implications for the radial evolution between SO and Wind in **Section 4**.

It is also informative to illustrate the magnetic field configuration in the perspective view toward the Sun with both Wind and SO spacecraft locations marked in **Figure 4**. This provides a direct 3D view toward the Sun (located at the same position as Wind in this view but at a distance 1 au away) along the Sun-Earth line. It is seen that the reconstructed flux rope structure based on the Wind *in-situ* data along its path shows selected spiral field lines with arbitrary colors winding around a central axis represented by the red straight field line, along the z axis direction, pointing approximately horizontally to the East with both Wind and SO spacecraft passing beneath the center of the flux rope, and separated mostly in the East-West direction. With the 2D reconstruction result from the Wind spacecraft, it enables a direct comparison between the derived magnetic field components along the SO spacecraft path, as shown in **Figure 2B**, and the actual measured ones returned by the spacecraft. **Figure 5** shows such comparison of the three magnetic field components in the SO centered RTN coordinates. **Figure 5A** shows the component-wise time series within the MC interval at SO, while **Figure 5B** shows the corresponding one-to-one correlation plot, yielding a correlation coefficient $cc = 0.95$, for all three components combined. When the correlation coefficients are computed separately for each component, they yield $cc_R = 0.65$, $cc_T = 0.12$, and $cc_N = 0.95$, respectively, as denoted in **Figure 5B**.

One main discrepancy is the underestimated magnitude of the B_T component. If one assumes the conservation of axial magnetic flux, it can be established $B_z \propto 1/r_h$ (i.e., inversely proportional to the heliocentric distance, r_h) with the additional supporting evidence of negligible inertial force provided by, e.g., the HT analysis. When this is the case, the dependence of the cross-section area becomes $\propto r_h$, considering largely the angular expansion but little expansion in the radial dimension, for a flux rope configuration with a z axis orientation nearly perpendicular to the radial direction. The so-called Walén slope as shown in **Figure 3** signifies the relative importance of the inertial force, including the effect of radial expansion, to the Lorentz force in an MHD equilibrium. A small Walén slope magnitude is thus generally a prerequisite condition for the GS reconstruction and the subsequent optimal fitting approach [18], when they are all based on an approximate magnetohydrostatic equilibrium, sometimes with even stricter additional condition of being force-free. An adjustment based on the argument of the $1/r_h$ dependence of the axial field can be made to the model output at SO location, as shown in **Figure 5A** by the dashed curves. This yields a correlation coefficient (between the dashed curves and circles) $cc' = 0.94$, and correspondingly, $cc'_R = 0.65$, $cc'_T = 0.23$, and $cc'_N = 0.95$, although visually they appear to have improved agreement, especially in the B_T component and the magnitude. We defer additional discussions regarding the radial evolution of MC to **Section 4**.

3.2 A Quasi-3D Configuration Based on the Freidberg Solution

We also apply an optimal fitting approach based on the quasi-3D Freidberg solution to the MC interval denoted in **Figure 1A**. For this interval, an HT frame velocity is obtained $\boldsymbol{V}_{HT} =$

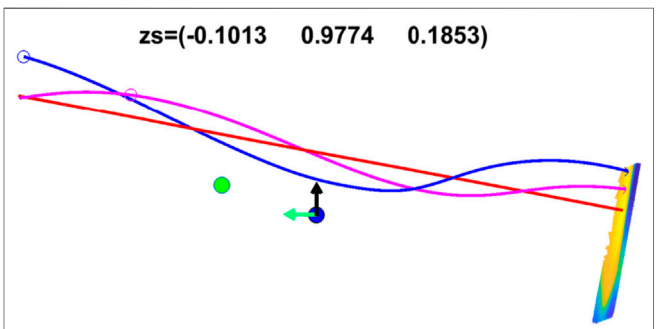

FIGURE 4 | The 3D view toward the Sun (along the +GSE-X direction) of the selected field lines (with arbitrary colors) from the GS reconstruction result corresponding to **Figure 2**. The unit vectors of the GSE-Y and Z coordinates are denoted in green and black arrows, respectively. The cross section as seen in **Figure 2B** is shown to the right where the field lines originate and spiral along the z axis. The red straight field line originates from the center of the flux rope as marked in **Figure 2B**. The spacecraft locations of Wind and SO are marked by the blue and green dots, respectively. The z axis direction is denoted on top in the GSE coordinates.

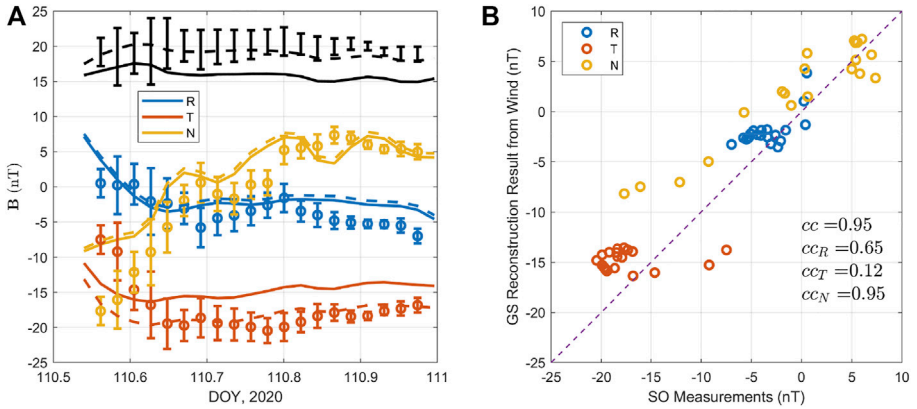

FIGURE 5 | (A) The comparison between the derived magnetic field components (solid curves) based on the GS reconstruction result from Wind in **Figure 2**, and the actual measurements (circles and error bars), along the SO spacecraft path. The field magnitude is in black. **(B)** The corresponding component-wise one-to-one scatter plot with the correlation coefficients between the two sets for all three components, *cc*, and each individual component are denoted. The dashed line marks the one-to-one diagonal line. The dashed curves in **(A)** represent an alternative estimate/adjustment based on an argument of the $1/r_h$ dependence of the axial field.

$[-340.95, -4.16, 22.24]$ km/s, in the GSE coordinates, with the corresponding Walén slope −0.0262. The average proton β is 0.023. The three magnetic field components of the Freidberg solution in a local cylindrical coordinates (r, θ, z) are given in or by [20], each with dependence on all three dimensions,

$$\frac{B_z(\boldsymbol{r})}{B_{z0}} = J_0(\mu r) + CJ_1(\alpha r)\cos(\theta + kz) \quad (1)$$

$$\frac{B_\theta(\boldsymbol{r})}{B_{z0}} = J_1(\mu r) - \frac{C}{\alpha}\left[\mu J'_1(\alpha r) + \frac{k}{\alpha r}J_1(\alpha r)\right]\cos(\theta + kz) \quad (2)$$

$$\frac{B_r(\boldsymbol{r})}{B_{z0}} = -\frac{C}{\alpha}\left[kJ'_1(\alpha r) + \frac{\mu}{\alpha r}J_1(\alpha r)\right]\sin(\theta + kz) \quad (3)$$

Here the solution involves the Bessel's functions of the first kind, J_0 and J_1. A set of free parameters includes mainly C, μ (the force-free constant, sign of μ representing chirality), and k, and additional geometrical parameters accounting for the arbitrary orientation and location of the solution domain relative to the spacecraft path. The parameter B_{z0} is pre-determined as the maximum absolute value among all measured magnetic field components over the analysis interval and $\alpha = \sqrt{\mu^2 - k^2}$. It is clearly seen that for $C \equiv 0$, the solution reduces to the 1D Lundquist solution with only r dependence.

An optimal fitting approach based on χ^2 minimization with uncertainty estimates derived from *in-situ* spacecraft measurements was devised and applied to a few MC intervals [18, 19]. The results of minimum reduced $\chi^2 \lesssim 1$ were obtained in terms of the evaluation of the deviation between the model output from the Freidberg solution and the corresponding spacecraft measurements of the magnetic field components along a single-spacecraft path across the structure. Detailed descriptions of the fitting procedures and comparison of results with the GS reconstruction output and multiple spacecraft measurements are presented in [18]. We apply this newly developed approach to the Wind spacecraft data and obtain an optima fitting result as shown in **Figure 6**. The minimum reduced

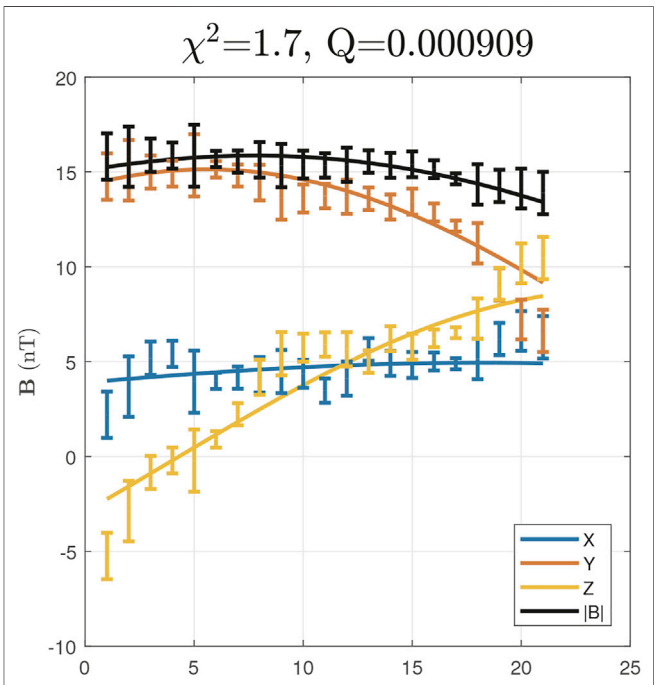

FIGURE 6 | The optimal fitting result to the Freidberg solution for the MC interval marked in **Figure 1A**. The Wind spacecraft measurements of the magnetic field with uncertainty estimates are shown as error bars, while the corresponding analytic solution is given by solid curves (see legend). The horizontal axis is the integral index of the data points.

$\chi^2 \approx 1.7$ is obtained with associated accumulative probability $Q \approx 0.001$, an indication of the quality of the goodness-of-fit, marginally considered acceptable (for $Q \gtrsim 0.001$) [31]. In addition, the error estimates on the fitted parameters can be obtained *via* the standard evaluation of confidence limits applicable to such χ^2 minimization as described in [31]. For example, the z axis orientation is found to be

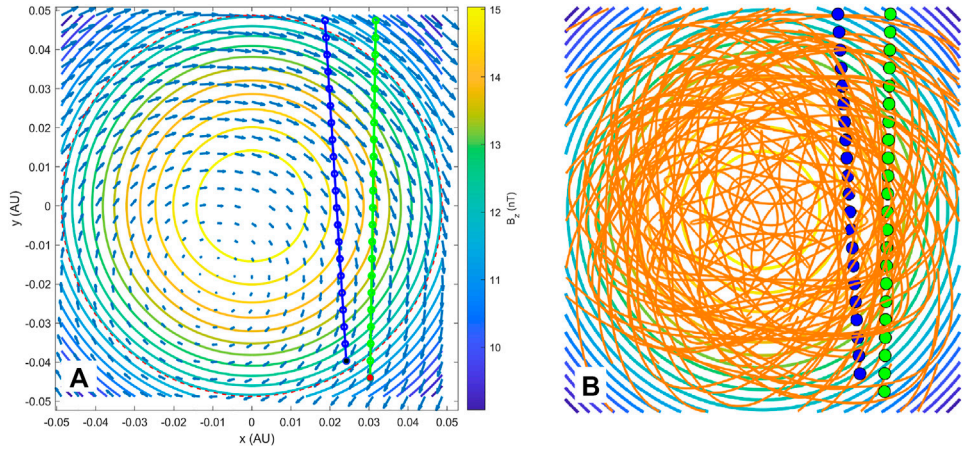

FIGURE 7 | (A) One cross section of the optimal Freidberg solution where the colored contours represent B_z distribution and arrows represent the transverse field components. The Wind and SO spacecraft paths are shown by the blue and green lines with dots, respectively. **(B)** The same view and contour lines for B_z as **(A)**. The orange lines are the field lines originating from the cross section plane, and viewed down the z axis.

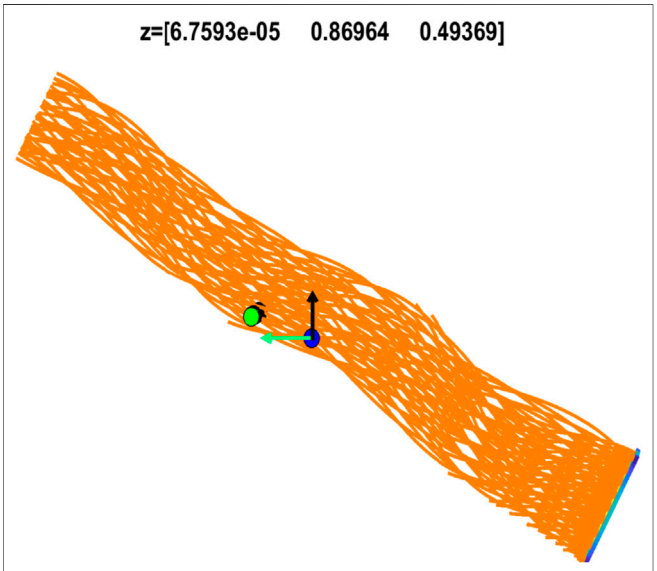

FIGURE 8 | The 3D view of the field lines or the flux bundle of the Freidberg solution given in **Figure 7B**, from the same viewpoint and in the same format as **Figure 4**. The z axis orientation and the locations of Wind (blue dot) and SO (green dot) spacecraft are also marked.

(δ, ϕ)=(60,90) ± (7, 9) degrees with 90% confidence limits. We present the other parameters in **Section 5**.

When compared with the GS reconstruction result, the significant distinction of this configuration represented by the Freidberg solution is the 3D nature, not present in any 2D configurations. There no longer exists distinctive 2D flux surfaces, and the field lines exhibit more general 3D features, not lying on discernable individual flux surfaces. **Figure 7A** demonstrates one cross section perpendicular to the z axis. The transverse field vectors are not tangential to the contours of B_z. There is no translation symmetry in the z dimension. To further illustrate this feature, **Figure 7B** shows the same view, but with a bundle of field lines drawn in orange color and originating from the bottom plane. No distinctive nested loops (flux surfaces) are seen. As a result, there does not exist a single central field line that is straight along z. **Figure 8** is the same bundle of field lines viewed from the perspective of the Wind spacecraft toward the Sun. The flux bundle possesses an overall winding along the z dimension, likely related to the topological feature of writhe, giving rise to the 3D feature seen. It also contributes to the individual field line twist, which can be evaluated by the means used for the topological analysis of solar active region magnetic field [e.g. [32]]. The SO spacecraft appears to cross the flux rope bundle mostly to the East of the Wind spacecraft path, apart from a nominal time delay due to the radial separation. **Figure 9** shows the comparison in a format similar to **Figure 5**, but for the optimal fitting result of the Freidberg solution to the Wind spacecraft data. The correlation coefficient between the field components from the optimal Freidberg solution and those from the actual measurements along the SO spacecraft path is $cc = 0.96$ (additionally $cc_R = 0.62$, $cc_T = 0.57$, and $cc_N = 0.92$). The combined correlation coefficient cc remains the same if adjustments are made as represented by the dashed curves in **Figure 9A**, while correspondingly, the correlation between each individual component becomes $cc'_R = 0.66$, $cc'_T = 0.63$, and $cc'_N = 0.92$, based on the argument of solely angular expansion to be discussed in the next section.

4 DISCUSSION

We lay out, briefly, a consideration for the radial evolution of the MC, given the difference in the average magnetic field magnitude between SO and Wind during the MC interval, which can be partially accounted for by the spatial variations [see, also [16]]. Because the solar wind flow speed at Wind shows little variation, the expansion in the radial direction may be negligible for this

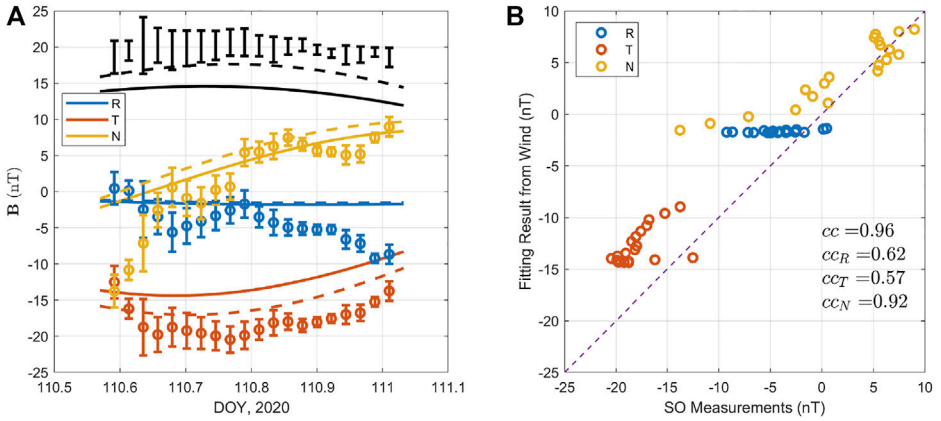

FIGURE 9 | The comparison between the derived magnetic field components based on the optimal Freidberg solution fit to Wind spacecraft data, and the actual measurements, along the SO spacecraft path across the solution domain. Format is the same as **Figure 5**.

TABLE 1 | Summary of geometrical and physical parameters for the MC based on Wind spacecraft measurements.

Parameters	B_{z0} (nT)	C	μ	k	$(\delta, \phi)^a$	Φ_z (Mx)	Chirality
GS result	16–17	...	...	0	(79, 96)	1.5–2.1	–
	—	—	—	—	± (4, 9)	$\times 10^{20}$	(Left-handed)
Freidberg sol.	15	−0.0047	−0.9848	-0.9845	(60, 90)	2.7–2.8	–
	—	± 0.0027	± 0.0098	± 0.0098	± (7, 9)	$\times 10^{20}$	(Left-handed)

[a]*The polar angle δ from the ecliptic north, and the azimuthal angle ϕ measured from GSE-X towards GSE-Y axes, all in degrees.*

event (also justified by the small Walén slope as shown in **Figure 3**). Therefore by assuming conservation of axial magnetic flux content and a constant angular extent of the MC flux rope cross section, ΔΘ, the following relation is assumed to be approximately satisfied,

$$\langle B_z \rangle \Delta r_h \cdot r_h \Delta\Theta \sim \Phi_z \approx Const. \quad (4)$$

Here the average axial field $\langle B_z \rangle$ is obtained over the cross-section area of the flux rope, which is approximated by the product $\Delta r_h \cdot r_h \Delta\Theta$. The cross-section length scale Δr_h is approximately constant if there is little change in the solar wind speed such that any inertial effect including expansion can be omitted (again as judged by the Walén slope). Then, it follows that the average axial field $\langle B_z \rangle$ or approximately B_{z0} changes proportionally with r_h^{-1}. This seems to be true for this particular MC event (**Table 1**), and also consistent with [16]. Specifically, they found that the radial change of the mean MC field strength follows the dependence $\propto r_h^{-1.12 \pm 0.14}$. They also concluded that this MC flux rope was not likely undergoing "self-similar or cylindrically symmetric expansion." For this event, from **Eq. 4** and **Table 1**, it is derived $\langle B_z \rangle \approx 15$ nT at 1 au. It should increase to about 18 nT at SO. From time-series data, the mean (maximum) total magnetic field strength at SO and Wind are 19 (21) nT and 15 (16) nT, respectively. It also has to be cautioned that all the reconstructions are based on single-point measurements. In order to further establish this type of relationship, more event studies are needed.

This study represents one step forward in the direction of quantifying how realistic MC model outputs are, based on one event study with available two-spacecraft *in-situ* observations. Future work would involve additional measurements and analysis based on remote-sensing observations, which will provide characterizations of solar source region (magnetic) properties of certain MC events to help further assess the fidelity of each model. The present implementations represent the best effort we have made in accounting for the variability in the *in-situ* measurements of MCs and proper error/uncertainty estimates of output parameters. Two models employed are deemed complementary and both are worth applying for individual event studies, as judged by the metrics, mainly, the combined correlation coefficients obtained from this two-spacecraft study with $cc > 0.9$. In addition, the correlation coefficients for individual components are better for the Freidberg solution as compared to the GS result. When the radial evolution is considered as assumed by **Eq. 4**, the corresponding correlation coefficients for both methods slightly improve. There also seems to be a tendency that the Freidberg fitting method is more versatile which yields an acceptable solution when the GS reconstruction method fails [e.g., [19]]. Whether this holds for more number of events has yet to be explored.

5 SUMMARY

In summary, we have examined one MC event in the solar wind by using the *in-situ* spacecraft measurements from both the Wind and SO missions located at heliocentric distances ~1 and

~ 0.8 au, respectively. Two spacecraft were largely aligned along the Sun-Earth line and nearly on the ecliptic plane, but SO was to the East of Wind with a longitudinal separation angle of ~ 4°. The magnetic field measurements from both spacecraft show strong signatures of a magnetic flux rope configuration. In particular, the Wind plasma (not available from SO) and magnetic field measurements confirm the identification of an MC interval, which correlates with the corresponding magnetic field measurements at SO subject to a nominal time delay [see, also, [16]]. We apply both the 2D GS reconstruction method and the optimal quasi-3D Freidberg solution fitting method to the Wind spacecraft measurements and obtain the characterizations of the magnetic field topology at 1 au. A set of parameters from the analysis is summarized in **Table 1**. The error estimates of the parameters for the Freidberg solution are obtained at the 90% confidence limits, except for B_{z0} and Φ_z. The former is predetermined and fixed, while the latter is not a free fitting parameter. For the GS result, an uncertainty range for B_{z0} is also obtained, while the parameters C, μ, and k are not applicable ($k = 0$ for being 2D). Both methods yield a flux rope configuration with left-handed chirality ("−") and their axial directions are oriented mainly along the West-East direction, with inclination angles relative to the ecliptic plane, about 11 and 30°, respectively. The axial magnetic flux content is 1.5–2.1×10^{20} Mx, and 2.7–2.8×10^{20} Mx, respectively, as indirectly derived from the model outputs, taking into account the uncertainties. Although the lack of plasma data from SO prohibits the same types of rigorous analysis at SO, we use the available magnetic field measurements at SO to correlate with the corresponding model outputs from the aforementioned quantitative analysis based on the Wind spacecraft data. This becomes feasible for this event study when the two spacecraft were positioned with an appropriate separation distance. We conclude that both spacecraft crossed the same structure exhibiting a flux rope configuration, as characterized by the set of parameters summarized above. Such an interpretation is supported by the analysis result that the combined correlation coefficients for the GS reconstruction result and the Freidberg solution fitting result are 0.95 and 0.96, respectively.

It is worth noting that as multi-spacecraft measurements become increasingly more available, as partially illustrated in **Figure 1B**, new and exciting multi-messenger science will be enabled by using multiple analysis tools. It is highly anticipated that the constellations of current and future missions will usher in new frontiers in heliophysics research.

DATA AVAILABILITY STATEMENT

Publicly available datasets were analyzed in this study. This data can be found here: NASA CDAWeb: https://cdaweb.gsfc.nasa.gov/index.html/.

AUTHOR CONTRIBUTIONS

QH carried out the analysis and wrote the draft of the manuscript. WH helped with the visualization of the analysis results. LZ obtained the time-series data from SO and participated in the interpretation of the results. EL helped with the analytic verification of the Freidberg solution.

FUNDING

Funding is provided, in part, by NASA Grant Nos. 80NSSC21K0003, 80NSSC19K0276, 80NSSC18K0622, 80NSSC17K0016, and NSF Grant Nos. AGS-1650854 and AGS-1954503, to The University of Alabama in Huntsville.

ACKNOWLEDGMENTS

WH and QH acknowledge NSO/NSF DKIST Ambassador program for support. The authors wish to thank Ms. Constance Hu for proofreading the manuscript. We thank the reviewers for useful comments that have helped improve the presentation of this manuscript.

REFERENCES

1. Burlaga LF. Magnetic Clouds and Force-free fields with Constant Alpha. *J Geophys Res* (1988) 93:7217–24. doi:10.1029/JA093iA07p07217
2. Lepping RP, Jones JA, and Burlaga LF. Magnetic Field Structure of Interplanetary Magnetic Clouds at 1 AU. *J Geophys Res* (1990) 95: 11957–65. doi:10.1029/JA095iA08p11957
3. Burlaga LF. Interplanetary Magnetohydrodynamics. In *International Series in Astronomy and Astrophysics*, 3. New York, NY: Oxford University Press (1995).
4. Lepping RP, Burlaga LF, Szabo A, Ogilvie KW, Mish WH, Vassiliadis D, et al. The Wind Magnetic Cloud and Events of October 18-20, 1995: Interplanetary Properties and as Triggers for Geomagnetic Activity. *J Geophys Res* (1997) 102: 14049–64. doi:10.1029/97JA00272
5. Stone EC, Frandsen AM, Mewaldt RA, Christian ER, Margolies D, Ormes JF, et al. The Advanced Composition Explorer. *Space Sci Rev* (1998) 86:1–22. doi:10.1023/A:100508252623710.1007/978-94-011-4762-0_1
6. Acuña MH, Ogilvie KW, Baker DN, Curtis SA, Fairfield DH, and Mish WH. The Global Geospace Science Program and its Investigations. *Space Sci Rev* (1995) 71:5–21. doi:10.1007/BF00751323
7. Longdon N. *The Ulysses Data Book. A Summary of the Technical Elements of the Ulysses Spacecraft and its Scientific Payload* (1990). European Space Agency, Paris, France: European Space Agency.
8. Kaiser ML, Kucera TA, Davila JM, St Cyr OC, Guhathakurta M, and Christian E. The STEREO Mission: An Introduction. *Space Sci Rev* (2008) 136:5–16. doi:10.1007/s11214-007-9277-0
9. Burlaga L, Sittler E, Mariani F, and Schwenn R. Magnetic Loop behind an Interplanetary Shock: Voyager, Helios, and Imp 8 Observations. *J Geophys Res Space Phys* (1981) 86:6673–84. doi:10.1029/JA086iA08p06673
10. Kilpua EKJ, Liewer PC, Farrugia C, Luhmann JG, Möstl C, Li Y, et al. Multispacecraft Observations of Magnetic Clouds and Their Solar Origins between 19 and 23 May 2007. *Solar Phys* (2009) 254:325–44. doi:10.1007/s11207-008-9300-y
11. Möstl C, Farrugia CJ, Miklenic C, Temmer M, Galvin AB, Luhmann JG, et al. Multispacecraft Recovery of a Magnetic Cloud and its Origin from Magnetic

Reconnection on the Sun. *J Geophys Res (Space Physics)* (2009) 114:A04102. doi:10.1029/2008JA013657
12. Möstl C, Farrugia CJ, Biernat HK, Leitner M, Kilpua EKJ, Galvin AB, et al. Optimized Grad - Shafranov Reconstruction of a Magnetic Cloud Using STEREO- Wind Observations. *Solar Phys* (2009) 256:427–41. doi:10.1007/s11207-009-9360-7
13. Chollet EE, Mewaldt RA, Cummings AC, Gosling JT, Haggerty DK, Hu Q, et al. Multipoint Connectivity Analysis of the May 2007 Solar Energetic Particle Events. *J Geophys Res Space Phys* (2010) 115, A12106. doi:10.1029/2010JA015552
14. Du D, Wang C, and Hu Q. Propagation and Evolution of a Magnetic Cloud from ACE to Ulysses. *J Geophys Res (Space Physics)* (2007) 112:A09101. doi:10.1029/2007JA012482
15. Song H, Hu Q, Cheng X, Zhang J, Li L, Zhao A, et al. The Inhomogeneity of Composition along the Magnetic Cloud Axis. *Frontiers* (2021) 9, 375. in press. doi:10.3389/fphy.2021.684345
16. Davies EE, Möstl C, Owens MJ, Weiss A, Amerstorfer T, Hinterreiter J, et al. *In Situ* multi-spacecraft and Remote Imaging Observations of the First Cme Detected by Solar Orbiter and Bepicolombo. *Astron Astrophysics* (2021). doi:10.1051/0004-6361/202040113
17. Lundquist S. On Force-free Solution. *Ark Fys* (1950) 2:361.
18. Hu Q. Optimal Fitting of the Freidberg Solution to *In Situ* Spacecraft Measurements of Magnetic Clouds. *Sol Phys* (2021) 296, 101. Available at: https://arxiv.org/abs/2104.09352. doi:10.1007/s11207-021-01843-z
19. Hu Q, He W, Qiu J, Vourlidas A, and Zhu C. On the Quasi-Three Dimensional Configuration of Magnetic Clouds. *Geophys Res Lett* (2021) 48: e2020GL090630. doi:10.1029/2020GL090630
20. Freidberg JP. *Ideal MHD*. Cambridge, UK: Cambridge University Press (2014). p. 546–7.
21. Hau LN, and Sonnerup BUÖ. Two-dimensional Coherent Structures in the Magnetopause: Recovery of Static Equilibria from Single-Spacecraft Data. *J Geophys Res* (1999) 104:6899–918. doi:10.1029/1999JA900002
22. Hu Q, and Sonnerup BUÖ. Reconstruction of Magnetic Flux Ropes in the Solar Wind. *Geophys Res Lett* (2001) 28:467–70. doi:10.1029/2000GL012232
23. Hu Q, and Sonnerup BUÖ. Reconstruction of Magnetic Clouds in the Solar Wind: Orientations and Configurations. *J Geophys Res (Space Physics)* (2002) 107:1142. doi:10.1029/2001JA000293
24. Hu Q, Smith CW, Ness NF, and Skoug RM. Multiple Flux Rope Magnetic Ejecta in the Solar Wind. *J Geophys Res (Space Physics)* (2004) 109:A03102. doi:10.1029/2003JA010101
25. Hu Q, Smith CW, Ness NF, and Skoug RM. On the Magnetic Topology of October/November 2003 Events. *J Geophys Res (Space Physics)* (2005) 110: A09S03. doi:10.1029/2004JA010886
26. Hu Q. The Grad-Shafranov Reconstruction in Twenty Years: 1996 - 2016. *Sci China Earth Sci* (2017) 60:1466–94. doi:10.1007/s11430-017-9067-2
27. Fox N, Velli M, Bale S, Decker R, Driesman A, Howard R, et al. The Solar Probe Plus mission: Humanity's First Visit to Our star. *Space Sci Rev* (2016) 204:7–48. doi:10.1007/s11214-015-0211-6
28. Müller D, St Cyr OC, Zouganelis I, Gilbert HR, Marsden R, Nieves-Chinchilla T, et al. The Solar Orbiter mission - Science Overview. *A&A* (2020) 642:A1. doi:10.1051/0004-6361/202038467
29. Zhao LL, Zank GP, He JS, Telloni D, Hu Q, Li G, et al. *Turbulence/wave Transmission at an ICME-Driven Shock Observed by Solar Orbiter and Wind*. e-prints. arXiv (2021). arXiv:2102.03301.
30. Horbury TS, O'Brien H, Carrasco Blazquez I, Bendyk M, Brown P, Hudson R, et al. The Solar Orbiter Magnetometer. *Astron Astrophys* (2020) 642, A9. doi:10.1051/0004-6361/201937257
31. Press WH, Teukolsky SA, Vetterling WT, and Flannery BP. *Numerical Recipes in C++ : The Art of Scientific Computing*. New York: Cambridge Univ. Press (2007). 778. Available at: http://numerical.recipes/.
32. Liu R, Kliem B, Titov VS, Chen J, Wang Y, Wang H, et al. Structure, Stability, and Evolution of Magnetic Flux Ropes from the Perspective of Magnetic Twist. *Astrophysical J* (2016) 818:148. doi:10.3847/0004-637x/818/2/148

Conflict of Interest: The authors declare that the research was conducted in the absence of any commercial or financial relationships that could be construed as a potential conflict of interest.

frontiers in Physics

ORIGINAL RESEARCH
published: 30 July 2021
doi: 10.3389/fphy.2021.705744

Numerical Study of Divergence Cleaning and Coronal Heating/ Acceleration Methods in the 3D COIN-TVD MHD Model

Chang Liu[1,2], *Fang Shen*[1,2]*, *Yousheng Liu*[1,2], *Man Zhang*[1,2] *and Xiaojing Liu*[1,2]

[1]SIGMA Weather Group, State Key Laboratory for Space Weather, National Space Science Center, Chinese Academy of Sciences, Beijing, China, [2]College of Earth and Planetary Sciences, University of Chinese Academy of Sciences, Beijing, China

In the solar coronal numerical simulation, the coronal heating/acceleration and the magnetic divergence cleaning techniques are very important. The coronal–interplanetary total variation diminishing (COIN-TVD) magnetohydrodynamic (MHD) model is developed in recent years that can effectively realize the coronal–interplanetary three-dimensional (3D) solar wind simulation. In this study, we focus on the 3D coronal solar wind simulation by using the COIN-TVD MHD model. In order to simulate the heating and acceleration of solar wind in the coronal region, the volume heating term in the model is improved efficiently. Then, the influence of the different methods to reduce the $\nabla \cdot \boldsymbol{B}$ constraint error on the coronal solar wind structure is discussed. Here, we choose Carrington Rotation (CR) 2199 as a study case and try to make a comparison of the simulation results among the different magnetic divergence cleaning methods, including the diffusive method, the Powell method, and the composite diffusive/Powell method, by using the 3D COIN-TVD MHD model. Our simulation results show that with the different magnetic divergence cleaning methods, the $\nabla \cdot \boldsymbol{B}$ error can be reduced in different levels during the solar wind simulation. Among the three divergence cleaning methods we used, the composite diffusive/Powell method can maintain the divergence cleaning constraint better to a certain extent, and the relative magnetic field divergence error can be controlled in the order of 10^{-9}. Although these numerical simulations are performed for the background solar corona, these methods are also suitable for the simulation of CME initiation and propagation.

Keywords: MHD simulation, corona heating and acceleration, magnetic divergence cleaning, solar wind, volumn heating

OPEN ACCESS

Edited by:
Qiang Hu,
University of Alabama in Huntsville, United States

Reviewed by:
Keiji Hayashi,
Stanford University, United States
Mehmet Yalim,
University of Alabama in Huntsville, United States

***Correspondence:**
Fang Shen
fshen@spaceweather.ac.cn

Specialty section:
This article was submitted to Stellar and Solar Physics, a section of the journal Frontiers in Physics

Received: *06 May 2021*
Accepted: *13 July 2021*
Published: *30 July 2021*

Citation:
Liu C, Shen F, Liu Y, Zhang M and Liu X (2021) Numerical Study of Divergence Cleaning and Coronal Heating/ Acceleration Methods in the 3D COIN-TVD MHD Model. Front. Phys. 9:705744. doi: 10.3389/fphy.2021.705744

INTRODUCTION

The 3D COIN-TVD MHD model which was proposed in [1–3] and was improved in [4–8] in recent years can effectively realize the coronal–interplanetary 3D solar wind simulation. This model uses the TVD Lax–Friedrichs (TVD-LF) scheme uniformly in the corona region and the interplanetary space region, and a combination of Open Multi-Processing (OpenMP) based on shared memory and Message Passing Interface (MPI) based on distributed memory has been successfully used to study the solar wind background from the corona to the interplanetary space.

The solar energy is stored in the solar nucleus, and the generated radiant energy spreads from the inside to the outside. The solar temperature should theoretically decrease with the increase of the heliocentric distance. However, the temperature of the upper atmosphere corona is much higher than that of the lower atmosphere (photosphere). The reason for the abnormal warming of the atmosphere has not yet been investigated. Therefore, coronal heating/acceleration is a central issue in the solar coronal simulation and has been discussed by many researchers (e.g., [9–16]). Parker proposed a basic theory for the problem of heating an expanding solar corona [17–19]. Later, various methods for solar wind acceleration and coronal heating have been developed. For example, the Alfvén wave heating method (AHM) can accelerate solar wind through the exchange of momentum and energy between large-scale Alfvén wave turbulence and solar wind plasma [10]. The turbulent heating method (THM) assumes that the turbulent free energy is transformed into the energy accelerated by the solar wind when the turbulent free energy changes with the heliocentric distance [10]; By adding momentum and energy source terms to the MHD equations [16], the volume heating method (VHM) has been widely used in solar wind simulation (e.g., [15, 20, 21].

In the MHD simulation, the divergence of the magnetic field should be strictly controlled to zero. The nonzero divergence of the magnetic field can lead to the $\nabla \cdot \boldsymbol{B}$ error during the calculation. When this occurs, numerical instability may develop and the simulation can break down. Therefore, scientists have proposed many methods to control the divergence of the magnetic field, such as the generalized Lagrange multiplier (GLM) method [22–24], the CT method [21, 25–27], the projection method [28], the vector potential method [29, 30], the Powell method [31, 32], the diffusion method [7] and the globally solenoidality-preserving (GSP) method [33].

In this study, we adopt the COIN-TVD model to simulate the coronal solar wind. Similar to [20, 21], we use the volume heating sources to model the solar wind heating/acceleration process in the simulation.

In *Governing Equations of Coronal Interplanetary-Total Variation Diminishing Model*, we introduce the equations of the COIN-TVD MHD model. *Mesh Grid System and Numerical Scheme* describes mesh grid system and boundary conditions. *Volume Heating Method and Magnetic Field Divergence Cleaning Methods* presents the VHM method and three magnetic field divergence processing methods. *Numerical Results* shows the results of numerical simulation and comparisons of three methods for processing magnetic field divergence. In *Conclusions and Discussions*, we make the conclusion and discussion.

GOVERNING EQUATIONS OF CORONAL–INTERPLANETARY TOTAL VARIATION DIMINISHING MODEL

The ideal MHD equations are used to simulate the coronal solar wind. Under the Corotating coordinate system, equations can be written as:

$$\frac{\partial \rho}{\partial t} + \nabla \cdot (\rho \boldsymbol{v}) = 0 \tag{1}$$

$$\left(\frac{\partial \rho \boldsymbol{v}}{\partial t}\right) + \nabla \cdot \left[\left(\boldsymbol{P} + \frac{\boldsymbol{B}^2}{2\mu_0}\right)\boldsymbol{I} + \rho \boldsymbol{v}\boldsymbol{v} - \frac{\boldsymbol{B}\boldsymbol{B}}{\mu_0}\right] = -\frac{\rho G M_s}{r^2}\frac{\boldsymbol{r}}{r} + \rho \boldsymbol{f} \tag{2}$$

$$\frac{\partial \boldsymbol{B}}{\partial t} + \nabla \cdot (\boldsymbol{v}\boldsymbol{B} - \boldsymbol{B}\boldsymbol{v}) = 0 \tag{3}$$

$$\frac{\partial \boldsymbol{P}}{\partial t} + \nabla \cdot (\boldsymbol{\rho}\boldsymbol{v}) = -(\gamma - 1)\boldsymbol{P}\nabla \cdot \boldsymbol{v} \tag{4}$$

where ρ is the mass density, $\boldsymbol{v}$ is the plasma velocity, $\boldsymbol{B}$ is the magnetic field, $\boldsymbol{P}$ is pressure, μ_0 is the magnetic permeability of free space, $\boldsymbol{I}$ is the unit tensor, G is the gravitational constant, M_s is the solar mass, $\boldsymbol{f} = -\boldsymbol{\omega} \times (\boldsymbol{\omega} \times \boldsymbol{r} + 2\boldsymbol{\omega} \times \boldsymbol{v})$ is the additional fictitious force densities, in which $\boldsymbol{\omega}$ is the angular velocity of the rotation, and γ is the polytrophic index, which is set to be 1.05 in this study.

MESH GRID SYSTEM AND NUMERICAL SCHEME

Mesh Grid System

In the spherical coordinate, the range of the calculation area is expressed as $1\mathrm{Rs} \le r \le 22.5\mathrm{Rs}$, $-\frac{\pi}{2} \le \theta \le \frac{\pi}{2}$, and $0 \le \varnothing \le 2\pi$, where r is the radial distance from the solar center to the solar surface, θ is latitude, and $\varnothing$ is longitude. To avoid the singularity, the computation domain is divided into six identical component meshes to envelop a spherical surface with partial overlap on their boundaries [34]. The following grid partitions are employed; the grid mesh is built in the form of $224\,(r) \times 180\,(\theta) \times 360\,(\varnothing)$. The radial direction uses a proportional grid, the radial step length increases from $0.0161\mathrm{R_S}$ at the inner boundary of $1\mathrm{R_S}$ to $0.3636\mathrm{R_S}$ at the outer boundary near $22.5\mathrm{R_S}$, and the total number of grids at r-direction is 224. In the latitudinal and longitudinal directions, the grid resolution is $\Delta\theta = \Delta\varnothing = 1^\circ$.

Numerical Scheme

In the COIN-TVD model, all of the physical quantities are computed from the TVD-LF numerical scheme in a face-centered grid structure (e.g., [7, 8]). And this scheme is performed in the six-component mesh grid system.

The inner boundary is located on the surface of the Sun, where the inner boundary setting depends on local fluid conditions (e.g., [2]; 2007, [16, 21, 33]). When $v_r > 0$, $\rho = \rho_0$, and $T = T_0$, $\boldsymbol{B} = \boldsymbol{B}_0$, and $\nabla \cdot (\rho \boldsymbol{v}) = 0$; when $v_r < 0$, $\partial\rho/\partial r = 0$, $\partial T/\partial r = 0$, $\boldsymbol{B} = \boldsymbol{B}_0$, $\boldsymbol{v} = 0$.

The Carrington Rotation (CR) 2199 is chosen for background establishment. The initial magnetic field $\boldsymbol{B_0}$ is given by using the potential field source surface (PFSS) model [35, 36], the spherical harmonics coefficients were used to obtain the initial PFSS solution is 6. And other initial parameters, such as plasma density ρ_0, temperature $\mathrm{T_0}$, and velocity $\mathbf{v}$, are calculated by Parker's solar wind flow solution [17]. The temperature and the number density on the solar surface are set to be $1.5 \times 10^6\,\mathrm{K}$ and $1.67 \times 10^8\,\mathrm{cm^{-3}}$, respectively. The boundary condition of the magnetic field at the inner surface also remains fixed all through the simulation.

The parameters at the outer boundary are set according to the projected characteristic boundary conditions e.g., [32, 37, 38].

VOLUME HEATING METHOD AND MAGNETIC FIELD DIVERGENCE CLEANING METHODS

In this section, we introduce the numerical schemes of the volume heating method and three methods to constrain $\nabla \cdot \boldsymbol{B}$ in MHD simulation.

Volume Heating Method

Due to the limitations of observation and theory, there is no mature theoretical model to describe the mechanism of coronal heating and solar wind acceleration. Here, we use the volume heating method to solve the issue of coronal heating and solar wind acceleration. We add the source terms of momentum S_M and energy Q_E to the MHD **Eq. 1**, **Eq. 2**, **Eq. 3**, and **Eq. 4** as follows:

$$\frac{\partial \rho}{\partial t} + \nabla \cdot (\rho \boldsymbol{v}) = 0 \tag{5}$$

$$\left(\frac{\partial \rho \boldsymbol{v}}{\partial t}\right) + \nabla \cdot \left[\left(\boldsymbol{P} + \frac{\boldsymbol{B}^2}{2\mu_0}\right)\boldsymbol{I} + \rho \boldsymbol{v}\boldsymbol{v} - \frac{\boldsymbol{B}\boldsymbol{B}}{\mu_0}\right] = -\frac{\rho G M_s}{r^2}\frac{\boldsymbol{r}}{r} + \rho \boldsymbol{f} + S_M \tag{6}$$

$$\frac{\partial \boldsymbol{B}}{\partial t} + \nabla \cdot (\boldsymbol{v}\boldsymbol{B} - \boldsymbol{B}\boldsymbol{v}) = 0 \tag{7}$$

$$\frac{\partial \boldsymbol{P}}{\partial t} + \nabla \cdot (\rho \boldsymbol{v}) = -(\gamma - 1)\boldsymbol{P}\nabla \cdot \boldsymbol{v} + (\gamma - 1)Q_E \tag{8}$$

According to the work in [7, 39–41], we set energy and momentum source terms as follows:

$$\begin{aligned} Q_E &= Q_1 (r-1) e^{(-r/L_{Q_1})} \\ S_M &= S_1 (r-1) e^{(-r/L_M)} \end{aligned} \tag{9}$$

Here, $\gamma = 1.05$, which is the polytrophic index. In the calculation region, the polytropic index γ need not be set very large. $\gamma = 1.05$ can heat the corona and accelerate solar wind.

Here, r is the heliocentric distance, Q_1 and L_{Q_1} are the intensity and attenuation length of heating, and S_1 and L_M are the intensity and decay length of the momentum addition. The parameters L_{Q_1} and L_M are set to be 1, $Q_1 = Q_0 C_a$, and $S_1 = S_0 C_a$. To test the influence of the parameter of energy and momentum source terms, we set two groups of different parameters for comparison. In model A, we set: $Q_0 = 6 \times 10^{-10} J \cdot m^{-3} \cdot s^{-1}$, $S_0 = 7.6 \times 10^{-14} N \cdot m^{-3}$ and $C_a = \frac{(1-0.8e^{(-(\theta_b/1)^2)^2})}{(1+f_s)^{9/2}}$ and find that the coronal heating and solar wind acceleration were not obvious. In model B, we adjust the parameters based on [33], which are $Q_0 = 6 \times 10^{-8} J \cdot m^{-3} \cdot s^{-1}$, $S_0 = 7.9 \times 10^{-14} N \cdot m^{-3}$ and $C_a = \frac{C_{a'}}{max C_{a'}}$, where $C_a^{'} = \frac{(1-0.8e^{(-(\theta_b/1)^1)^1})}{(1+f_s)^{9/2}}$. Here, $f_s = \left(\frac{R_s}{R_{ss}}\right)^2 \frac{\boldsymbol{B}_{R_s}}{\boldsymbol{B}_{Rss}}$ is the expansion factor, where Rs is the solar radius, $R_{SS} = 2.5 R_S$, and $\boldsymbol{B}_{R_S}$ and $\boldsymbol{B}_{R_{SS}}$ are magnetic field strength at the solar surface and at R_{SS}, respectively. Inspired by the Wang–Sheeley–Arge (WSA) model [42, 43], the solar wind speed is related to the magnetic field expansion factor f_s and the minimum angular distance θ_b. As f_s increases, the speed decreases, the high-speed stream originating from the center of the open field region always has large θ_b, and the low-speed stream from the coronal hole boundary has a relatively small θ_b.

Following [20, 44, 45], the source term Q_E also contains a heat conduction term, the expression of the heat conduction term is $\nabla\left(\xi T^{\frac{5}{2}} \frac{\nabla T \cdot \boldsymbol{B}}{\boldsymbol{B}^2}\right) \cdot \boldsymbol{B}$, ξ is the collisional thermal conductivity parallel to the magnetic field as given in [46] and the proton and electron temperatures are equal to T. If we add the heat conduction term in the Q_E, the partial differential in the formula decreases the calculation accuracy. And after the research in [45], many works (e.g., Feng, 2012, [21]; 2017 [33]) verify that without adding heat conduction item, the coronal solar wind can also be accelerated and heated.

Powell Method

The Powell method to maintain the magnetic divergence cleaning constraint is given as follows.

Two divergence source terms, $-(\nabla \cdot \boldsymbol{B})\boldsymbol{B}$ and $-(\nabla \cdot \boldsymbol{B})\boldsymbol{v}$, are added separately on the right side of **Eq. (6)** and **Eq. (7)** to get the following MHD equations:

$$\begin{cases} \dfrac{\partial \rho}{\partial t} + \nabla \cdot (\rho \boldsymbol{v}) = 0 \\ \left(\dfrac{\partial \rho \boldsymbol{v}}{\partial t}\right) + \nabla \cdot \left[\left(\boldsymbol{P} + \dfrac{\boldsymbol{B}^2}{2\mu_0}\right)\boldsymbol{I} + \rho \boldsymbol{v}\boldsymbol{v} - \dfrac{\boldsymbol{B}\boldsymbol{B}}{\mu_0}\right] = -\dfrac{\rho G M_s}{r^2}\dfrac{\boldsymbol{r}}{r} + \rho \boldsymbol{f} + S_M - (\nabla \cdot \boldsymbol{B})\boldsymbol{B} \\ \dfrac{\partial \boldsymbol{B}}{\partial t} + \nabla \cdot (\boldsymbol{v}\boldsymbol{B} - \boldsymbol{B}\boldsymbol{v}) = -(\nabla \cdot \boldsymbol{B})\boldsymbol{v} \\ \dfrac{\partial \boldsymbol{P}}{\partial t} + \nabla \cdot (\rho \boldsymbol{v}) = -(\gamma - 1)\boldsymbol{P}\nabla \cdot \boldsymbol{v} + (\gamma - 1)Q_E \end{cases} \tag{10}$$

In this way, the divergence of the magnetic field can be propagated to the boundary to reduce the numerical error of $\nabla \cdot \boldsymbol{B}$ in the computational region [31]. From **Eq. 10** with the source term, the quantity $\nabla \cdot \boldsymbol{B}/\rho$ satisfies the advection equation, which is,

$$\frac{\partial}{\partial t}\left(\frac{\nabla \cdot \boldsymbol{B}}{\rho}\right) + \nabla \cdot \left(\boldsymbol{v} \cdot \frac{\nabla \cdot \boldsymbol{B}}{\rho}\right) = 0 \tag{11}$$

This means that the $\nabla \cdot \boldsymbol{B}$ must be transported by the plasma motions when Powell correction is applied, since the initial and boundary conditions satisfy $\nabla \cdot \boldsymbol{B} = 0$, and the $\nabla \cdot \boldsymbol{B}$ will be near zero for all later times throughout the simulation.

Diffusive Method

The diffusive method is proposed to reduce the error of the magnetic divergence, in which an artificial diffusivity is added at each time step as $\frac{\partial \boldsymbol{B}}{\partial t} = \eta \nabla (\nabla \cdot \boldsymbol{B})$. Under the condition of $\Delta t \leq \mu \frac{(\Delta x)^2}{\eta}$, where $\mu \in (0, 2)$, the error of the magnetic divergence is diffused away at the maximal rate allowed by iterating:

$$\boldsymbol{B}^{k+1} = \boldsymbol{B}^k + \mu (\Delta x)^2 \nabla \nabla \cdot \boldsymbol{B}^k, k = 0, 1, 2 \ldots\ldots K \tag{12}$$

Here, $(\Delta x)^2 = \frac{1}{\frac{1}{(\Delta r)^2} + \frac{1}{(r\Delta\theta)^2} + \frac{1}{(r \sin\theta \Delta\varnothing)^2}}$.

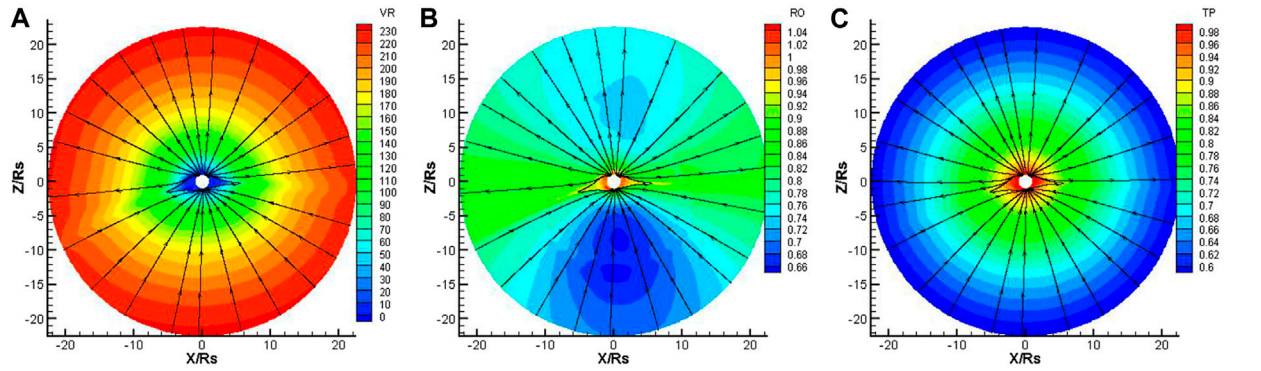

FIGURE 1 | The distribution of the radial speed *VR* (km/s) **(A)**, density *RO* × 10^8 (/cm^3) **(B)** and temperature *TP* × 10^6 (K) **(C)** on the meridional plane of $\Phi = 180^\circ$–0° from 1 to 22.5R_s, deduced from model A. The streamline represents the magnetic field lines.

For satisfying the condition $\max\left(\frac{\iint B_n ds}{\iint |B_n| ds}\right) \leq 10^{-2}$, less than ten iterations are needed at each time step. This method does not violate shock capturing property, at least to the second-order accuracy in smooth regions [8, 47].

Composite Diffusive/Powell Method

We combined the Powell method and the diffusive method together in the MHD calculation in the composite diffusive/Powell method for the first time, and this method can further control the error of the magnetic field divergence.

The composite diffusive/Powell method adds two divergence source terms, $-(\nabla \cdot \boldsymbol{B})\boldsymbol{B}$ and $-(\nabla \cdot \boldsymbol{B})\boldsymbol{v}$, to **Eq. 6** and **Eq. 7** to get **Eq. 10**. The divergence of the magnetic field can be propagated to the boundary, and the quantity $\nabla \cdot \boldsymbol{B}/\rho$ satisfies the advection equation (**Eq. 11**). When solving the equation, the error of magnetic divergence is diffused away at the maximal rate allowed by iterating **Eq. 12**.

NUMERICAL RESULTS

In this section, we show the numerical results of the solar coronal simulation from 1R_S to 22.5R_S for CR2199, which are obtained by executing the methods introduced in *Volume Heating Method and Magnetic Field Divergence Cleaning Methods*.

It takes about 100 h in physical time to obtain the steady state in our simulation. **Figures 1**,**2** present the distribution of the magnetic field lines, the radial velocity, the number density and the temperature on the meridional plane at $\Phi = 180^\circ$–0° from model A and model B, respectively. From these figures, it can be seen that the high latitude areas always have fast speed, high temperature, and low density. On the contrary, the radial speed is slower, the temperature is lower, and the number density is higher at lower latitudes around the heliospheric current sheet (HCS), and this is the characteristic feature of the solar wind in the corona [47]. Model B is successful in simulating the acceleration and heating of the solar wind in the corona, as shown in **Figure 2**. Compared with **Figure 1**, we can find that both the radial speed and temperature in **Figure 2** are higher than those in **Figure 1** obviously. This result indicates that the VHM can accelerate and heat the coronal solar wind, and the parameters S_0, Q_0, and C_a in VHM can affect the coronal heating and solar wind acceleration process significantly.

Then, we present the simulation results of the coronal solar wind with three magnetic divergence cleaning methods. **Figures 3**–**5**, respectively, show the variation in the radial speed, the number density, and the temperature along heliocentric distance from 1 to 22.5 Rs with different latitudes of $\theta = -80^\circ$ and $\theta = -10^\circ$ at the same longitude of $\Phi = 0^\circ$, where $\theta = -80^\circ$ locates at the open field region and $\theta = -10^\circ$ locates at the HCS region. Comparing the three figures, we can find that the radial speed in the open field region is larger than that in the HCS region, the temperature is higher in the open field, and the number density is smaller in the high latitude region.

The composite diffusive/Powell method which combines the diffusive method and the Powell method is our new try to handle the $\nabla \cdot B$ constraint. From **Figures 3**–**5**, we can also see that the curve from the composite diffusive/Powell method is always in the middle, so it can generate a stable solar wind structure like the other two methods.

To quantitatively see how $\nabla \cdot \boldsymbol{B}$ evolves, we define the relative divergence error [48] as follows:

$$Error(\boldsymbol{B}) = \frac{|\nabla \cdot \boldsymbol{B}|\Delta h}{|\boldsymbol{B}|} \tag{13}$$

Here, $\Delta h = \sqrt{\frac{3}{\frac{1}{(\Delta r)^2}+\frac{1}{(r\Delta\theta)^2}+\frac{1}{(r\sin\theta\Delta\varnothing)^2}}}$ is the characteristic length of the mesh element.

To investigate how the three magnetic divergence cleaning methods control the $\nabla \cdot \boldsymbol{B}$ error quantitaitvely, we make a numerical comparison for the *Error*($\boldsymbol{B}$) among the three methods.

Figures 6,**7** show the distributions of the *Error*($\boldsymbol{B}$) on the different meridional planes of $\Phi = 180^\circ$–0° and $\Phi = 270^\circ$–90°, respectively, for the steady-state solar wind. The three panels in **Figures 6**, **7** present the results from the composite diffusive/Powell method, the diffusive method and the Powell method, from left to right, respectively. It is obvious that the *Error*($\boldsymbol{B}$) deduced from the composite diffusive/Powell method is lower than that from the other two methods, on both meridional planes.

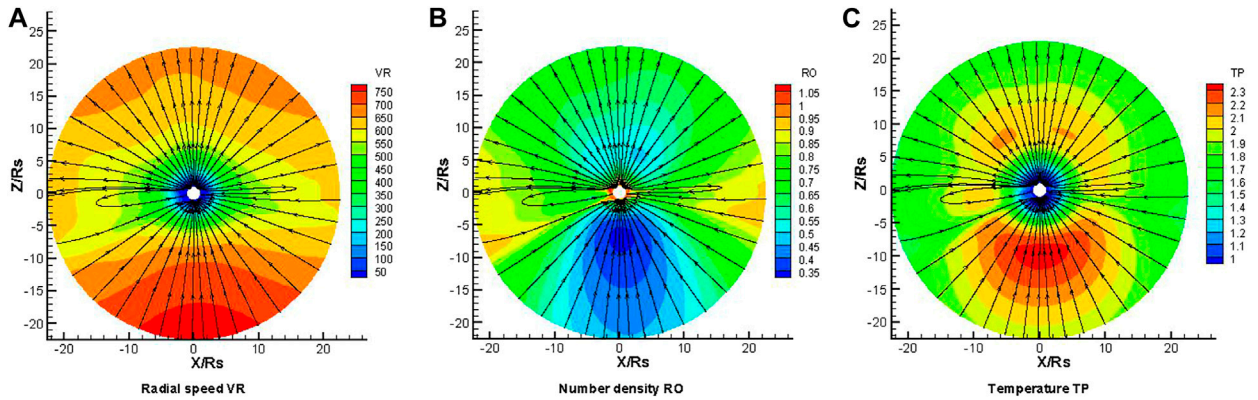

FIGURE 2 | The distribution of the radial speed *VR* (km/s) **(A)**, density *RO* × 10^8 (/cm^3) **(B)** and temperature *TP* × 10^6 (K) **(C)** on the meridional plane of $\Phi = 180^\circ$–0° from 1 to 22.5R_s, deduced from model B. The streamline represents the magnetic field lines.

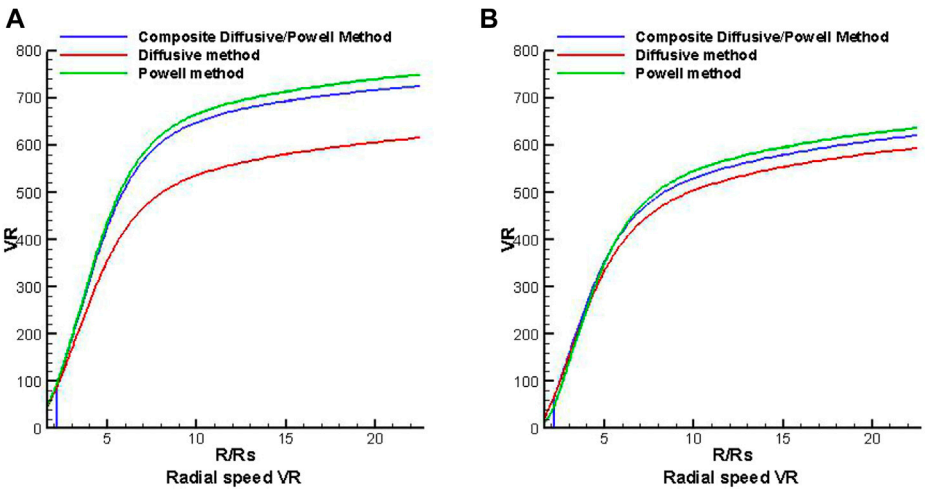

FIGURE 3 | The distribution of radial speed *VR* (km/s) along heliocentric distance with different latitudes of $\theta = -80^\circ$ **(A)** and $\theta = -10^\circ$ **(B)** at the same longitude $\Phi = 0^\circ$ from three divergence methods.

This indicates that the composite diffusive/Powell method is the most effective method among the three methods in dealing with the magnetic field divergence.

Here, we use the following metric for measuring divergence, which was also adopted by other research studies (e.g., [33, 47]):

$$Error\,(\boldsymbol{B})^{ave} = \sum_{k=1}^{M} \frac{|\nabla \cdot \boldsymbol{B}|\Delta h}{|\boldsymbol{B}|} \Big/ M \tag{14}$$

where M is the total number of grid points in the computational domain. We know that there are other metrics that can be used to measure the divergence. As pointed in [49], the metric defined by **Eq. 14** may rely on the spatial resolution. However, in this simulation, we make the comparison among the three cases with the same mesh system and the same metric definition; therefore, the influence of the spatial resolution on the comparison of the metric by **Eq. 14** can be ignored.

Figure 8 shows the evolution of the $Error(\boldsymbol{B})^{ave}$ with time deduced from the three methods. It can be recognized that the value of the $Error(\boldsymbol{B})^{ave}$ from the composite diffusive/Powell method is around $10^{-8.7}$–$10^{-8.5}$, from the diffusive method is around $10^{-8.6}$–$10^{-8.2}$, and from the Powell method is around $10^{-8.6}$–$10^{-7.1}$. The composite diffusive/Powell method has the smallest $Error(\boldsymbol{B})^{ave}$, and this method is a new try to maintain the magnetic divergence-free constraint. From **Figure 8**, we can also find that the $Error(\boldsymbol{B})^{ave}$ from the composite diffusive/Powell method and diffusive method is smaller than that from the Powell method obviously. Moreover, the $Error(\boldsymbol{B})^{ave}$ from the composite diffusive/Powell method keeps on decreasing after 60 h and is significantly smaller than that from the diffusive method near 100 h. Overall, we can find that all the divergence cleaning methods can keep the related errors under control, though the divergence errors of the Powell method are larger than those of the other methods, the divergence errors shown in **Figures 6–8** are indeed small, and the largest worst number is 10^{-7},

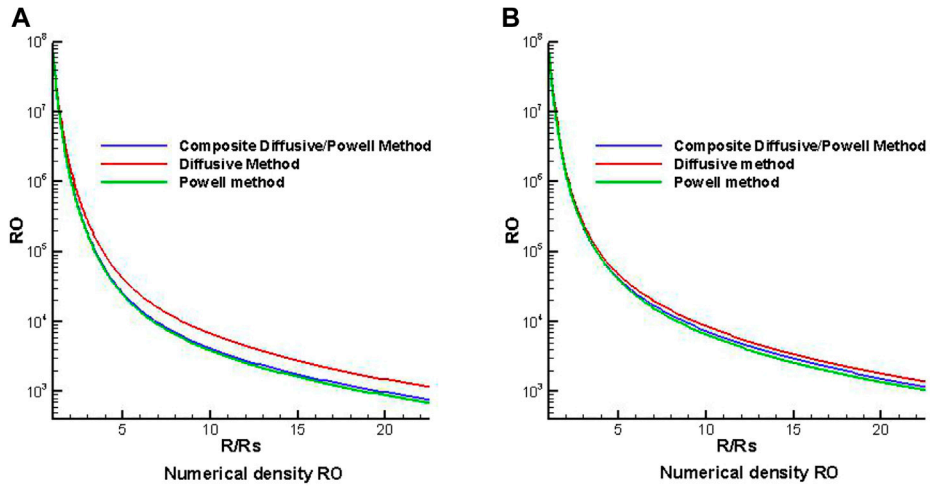

FIGURE 4 | The distribution of density *RO* (/cm^3) along heliocentric distance with different latitudes of $\theta = -80^\circ$ **(A)** and $\theta = -10^\circ$ **(B)** at the same longitude $\Phi = 0^\circ$ from three divergence methods.

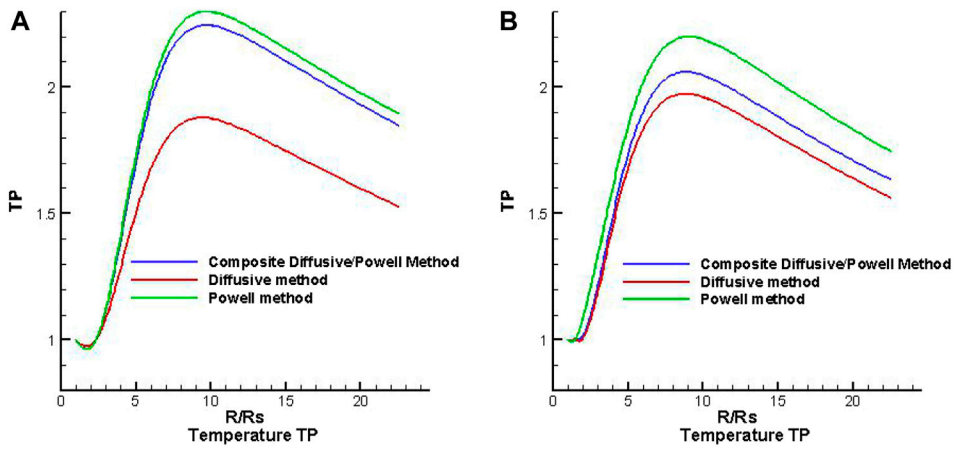

FIGURE 5 | The distribution of temperature $TP \times 10^6$ (K) along heliocentric distance with different latitudes of $\theta = -80^\circ$ **(A)** and $\theta = -10^\circ$ **(B)** at the same longitude $\Phi = 0^\circ$ from three divergence methods.

shown as the orange and red colors in **Figures 6**,**7**. The $Error(\boldsymbol{B})^{ave}$ from the Powell method is about $10^{-7.3}$, from the diffusive method is $10^{-8.4}$, and from the composite diffusive/Powell method is $10^{-8.7}$ near 100 h. The composite diffusive/Powell method is the best method to reduce the error of magnetic divergence among the three methods in this research.

CONCLUSIONS AND DISCUSSIONS

In this study, by using the 3D COIN-TVD MHD model, we simulate the solar wind in the coronal region, in which the divergence cleaning and coronal heating/acceleration methods are included. The volume heating method is an effective way for coronal heating, in which the parameters can be adjusted according to the WSA model in the simulation of the coronal solar wind. In the COIN-TVD MHD model, increasing the parameters S_0 and Q_0 of the energy and momentum source terms can make the solar wind accelerate more obviously.

For the divergence cleaning methods, here we choose the diffusive method, the Powell method and the composite diffusive/Powell method. We compared the numerical characteristics of the combination of each method for handling the divergence of the magnetic field and the COIN-TVD MHD model in the solar coronal simulation. The numerical results show that all of them can produce large-scale structured solar wind and reduce the divergence of the magnetic field more or less. The difference between the three divergence cleaning methods is summarized as follows:

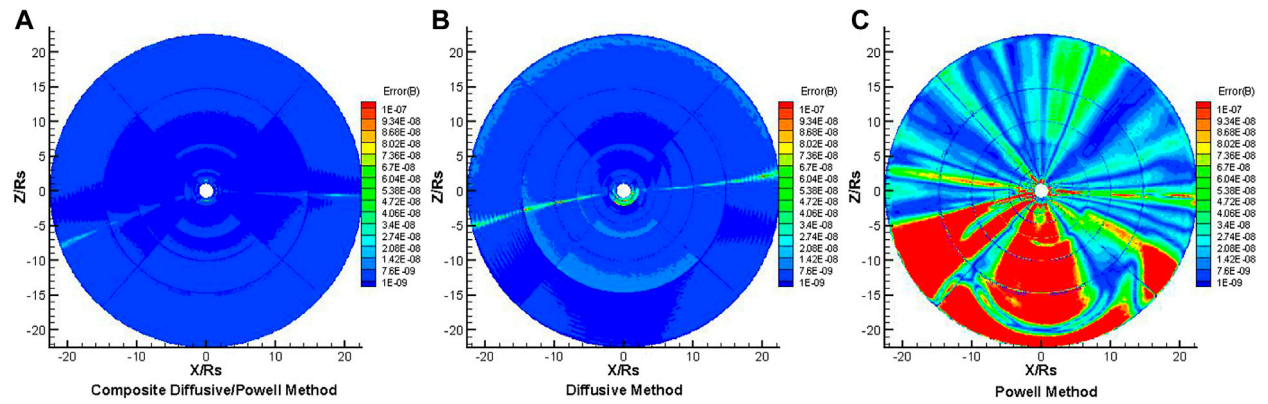

FIGURE 6 | The distribution of *Error*(*B*) on the meridional plane of $\Phi = 180^{\circ}$–0° from 1 to 22.5R_S, from composite diffusive/Powell method **(A)**, diffusive method **(B)**, and Powell method **(C)**, respectively.

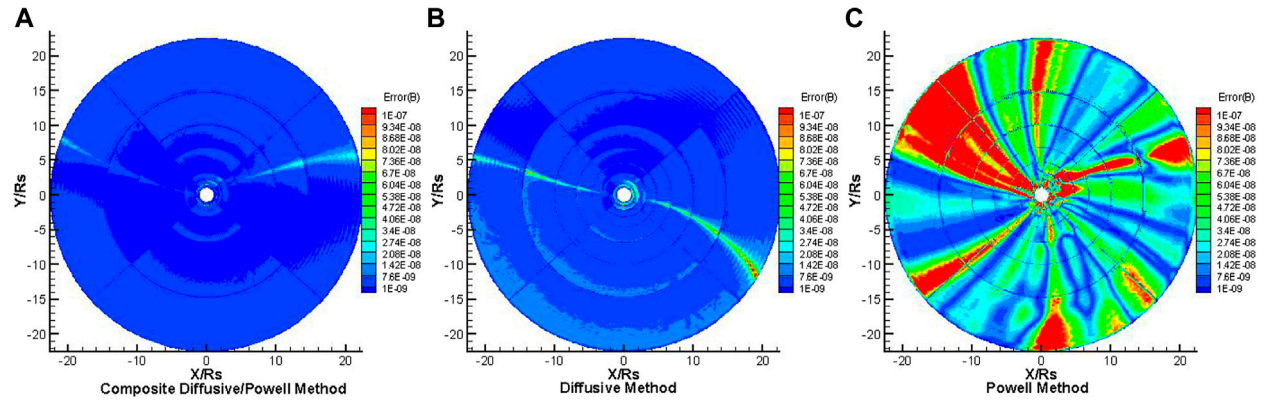

FIGURE 7 | The distribution of *Error*(*B*) on the meridional plane of $\Phi = 270^{\circ}$–90° from 1 to 22.5R_S, the results from composite diffusive/Powell method **(A)**, diffusive method **(B)** and Powell method **(C)**, respectively.

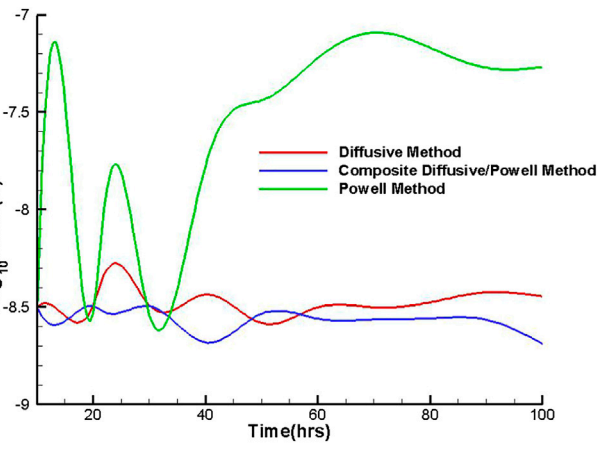

FIGURE 8 | The temporal evolution of the $\mathrm{Log}_{10}Error(B)^{ave}$ from the three divergence cleaning methods.

1) The Powell method is relatively simple to apply. It only needs to add two items to the source term of the MHD equations. In this study, the Powell method can reduce the error of the relative magnetic field divergence, but it is less effective than the other two methods in dealing with magnetic divergence.
2) The diffusive method also has a good effect on reducing magnetic field divergence error in this study. It reduces the error of divergence by adding a source term in the induction equation and the $\nabla \cdot \boldsymbol{B}$ error is diffused away by iterating $\boldsymbol{B}^{k+1} = \boldsymbol{B}^{k} + \mu(\Delta x)^2 \nabla \nabla \cdot \boldsymbol{B}^{k}$. If it is coupled with different numerical schemes, the effects of controlling divergence error are different. In this study, the diffusive method is not as good as the composite diffusive/Powell method in controlling the divergence of the magnetic field, but better than the Powell method.
3) The composite diffusive/Powell method is a preliminary new try in this study, and it combines the Powell method and the diffusive method during the simulation. It has been proven

that this composite method is the most efficient way to reduce the relative divergence errors among the three methods we used. Moreover, it also ensures the conservation of the MHD equations during the simulation.

In addition to the methods we mentioned, there are many other methods to simulate the coronal heating and the solar wind acceleration process and to control the divergence of the magnetic field. For example, both the Alfvén wave heating method and the turbulent heating method are effective for coronal heating. The Powell method can also company with other methods to control the magnetic divergence, which may be implemented in the future. Moreover, although these simulations are performed for the background solar corona, these methods can also be used for the simulation of CME initiation and propagation in the interplanetary space.

DATA AVAILABILITY STATEMENT

The original contributions presented in the study are included in the article/supplementary files, further inquiries can be directed to the corresponding author/s.

AUTHOR CONTRIBUTIONS

FS provided the thesis research topic, FS and YL provided the code for the three-dimensional solar wind numerical simulation. CL modified the code, ran the program code, and drew pictures based on the data. FS, CL, and MZ participated in the analysis of the results and the writing of the manuscript. XL modified the manuscript.

FUNDING

This work was jointly supported by the Strategic Priority Research Program of the Chinese Academy of Sciences, Grant no. XDB 41000000, National Natural Science Foundation of China (Grant nos 41774184 and 41974202), and State Key Laboratory of Special Research Fund Project.

ACKNOWLEDGMENTS

We acknowledge the use of synoptic magnetogram from the Global Oscillation Network Group (GONG). The numerical simulation of the model uses Tianhe-1A supercomputing machine.

REFERENCES

1. Feng X, Wu ST, Wei F, and Fan Q. A Class of Tvd Type Combined Numerical Scheme for Mhd Equations and its Application to Mhd Numerical Simulation. *Chin J Space Sci* (2002) 22(4):300–8. doi:10.3969/j.issn.0254-6124.2002.04.002
2. Feng X, Wu ST, Wei F, and Fan Q. A Class of TVD Type Combined Numerical Scheme for MHD Equations with a Survey about Numerical Methods in Solar Wind Simulations. *Space Sci Rev* (2003) 107:43–53. doi:10.1023/A:1025547016708
3. Feng X, Xiang CQ, Zhong DK, and Fan QL. A Comparative Study on 3-D Solar Wind Structure Observed by Ulysses and MHD Simulation. *Chin Sci Bull* (2005) 50:672–8. doi:10.1360/982004-293
4. Shen F, Feng XS, Wang Y, Wu ST, Song WB, Guo JP, et al. Three-dimensional MHD Simulation of Two Coronal Mass Ejections' Propagation and Interaction Using a Successive Magnetized Plasma Blobs Model. *J Geophys Res* (2011) 116:A9. doi:10.1029/2011JA016584
5. Shen F, Feng XS, Wu ST, Xiang CQ, and Song WB. Three-dimensional MHD Simulation of the Evolution of the April 2000 CME Event and its Induced Shocks Using a Magnetized Plasma Blob Model. *J Geophys Res* (2011) 116:A4. doi:10.1029/2010JA015809
6. Shen F, Wu ST, Feng X, and Wu C-C. Acceleration and Deceleration of Coronal Mass Ejections during Propagation and Interaction. *J Geophys Res* (2012) 117:A11. doi:10.1029/2012JA017776
7. Shen F, Shen C, Zhang J, Hess P, Wang Y, Feng X, et al. Evolution of the 12 July 2012 CME from the Sun to the Earth: Data-Constrained Three-Dimensional MHD Simulations. *J Geophys Res Space Phys* (2014) 119:7128–41. doi:10.1002/2014JA020365
8. Shen F, Yang Z, Zhang J, Wei W, and Feng X. Three-dimensional MHD Simulation of Solar Wind Using a New Boundary Treatment: Comparison with *In Situ* Data at Earth. *ApJ* (2018) 866:18. doi:10.3847/1538-4357/aad806
9. Aschwanden MJ, Burlaga LF, Kaiser ML, Ng CK, Reames DV, Reiner MJ, et al. Theoretical Modeling for the Stereo mission. *Space Sci Rev* (2008) 136:565–604. doi:10.1007/s11214-006-9027-8
10. Usmanov AV, Goldstein ML, Besser BP, and Fritzer JM. A Global MHD Solar Wind Model with WKB Alfvén Waves: Comparison with Ulysses Data. *J Geophys Res* (2000) 105:12675–95. doi:10.1029/1999JA000233
11. Zel'Dovich YB, Raizer YP, Hayes WD, Probstein RF, and Gill SP. Physics of Shock Waves and High-Temperature Hydrodynamic Phenomena. *J Appl Mech* (1967)(4) 34. doi:10.1016/B978-0-12-395672-9.X5001-2
12. Roussev II, Gombosi TI, Sokolov IV, Velli M, Manchester W, DeZeeuw DL, et al. A Three-Dimensional Model of the Solar Wind Incorporating Solar Magnetogram 15 Observations. *Astrophysical J Lett* (2003) L57(61):595. doi:10.1086/378878
13. Cohen O, Sokolov IV, Roussev II, Arge CN, Manchester WB, Gombosi TI, et al. A Semiempirical Magnetohydrodynamical Model of the Solar Wind. *ApJ* (2006) 654:L163–L166. doi:10.1086/511154
14. Cohen O, Sokolov IV, Roussev II, and Gombosi TI. Validation of a Synoptic Solar Wind Model. *J Geophys Res* (2008) 113:A3. doi:10.1029/2007JA012797
15. Suess ST, Poletto G, Wang A-H, Wu ST, and Cuseri I. The Geometric Spreading of Coronal Plumes and Coronal Holes. *Solar Phys* (1998) 180:231–46. doi:10.1023/A:1005001618698
16. Hansen KC, Gombosi TI, DeZeeuw DL, Groth CPT, and Powell KG. A 3D Global MHD Simulation of Saturn's Magnetosphere. *Adv Space Res* (2000) 26:1681–90. doi:10.1016/S0273-1177(00)00078-8
17. Parker EN. Dynamics of the Interplanetary Gas and Magnetic Fields. *ApJ* (1958) 128:664. doi:10.1086/146579
18. Parker EN. Interplanetary Dynamical Processes. *Phys Today* (1963) 17(3):72.
19. Parker EN. Dynamical Properties of Stellar Coronas and Stellar Winds. III. The Dynamics of Coronal Streamers. *ApJ* (1964) 139(8):690. doi:10.1086/147795
20. Feng X, Yang L, Xiang C, Wu ST, Zhou Y, and Zhong D. Three-dimensional Solarwindmodeling from the Sun to Earth by a Sip-Cese Mhd Model with a Six-Component Grid. *ApJ* (2010) 723:300–19. doi:10.1088/0004-637X/723/1/300
21. Feng X, Zhang M, and Zhou Y. A New Three-Dimensional Solar Wind Model in Spherical Coordinates with a Six-Component Grid. *ApJS* (2014) 214:6. doi:10.1088/0067-0049/214/1/6
22. Dedner A, Kemm F, Kröner D, Munz C-D, Schnitzer T, and Wesenberg M. Hyperbolic Divergence Cleaning for the MHD Equations. *J Comput Phys* (2002) 175:645–73. doi:10.1006/jcph.2001.6961
23. Dedner A, Rohde C, and Wesenberg M. A New Approach to Divergence Cleaning in Magnetohydrodynamic Simulations. In: TY Hou and E Tadmor, editors. *Hyperbolic Problems: Theory, Numerics, Applications*. Berlin;

Heidelberg: Spring-Verlag (2003). p. 509–18. doi:10.1007/978-3-642-55711-8-4710.1007/978-3-642-55711-8_47
24. Susanto A, Ivan L, De Sterck H, and Groth CPT. High-order central ENO Finite-Volume Scheme for Ideal MHD. *J Comput Phys* (2013) 250:141–64. doi:10.1016/j.jcp.2013.04.040
25. Evans CR, and Hawley JF. Simulation of Magnetohydrodynamic Flows - A Constrained Transport Method. *ApJ* (1988) 332:659–77. doi:10.1086/166684
26. Ziegler U. A Semi-discrete central Scheme for Magnetohydrodynamics on Orthogonal-Curvilinear Grids. *J Comput Phys* (2011) 230:1035–63. doi:10.1016/j.jcp.2010.10.022
27. Ziegler U. Block-Structured Adaptive Mesh Refinement on Curvilinear-Orthogonal Grids. *SIAM J Sci Comput* (2012) 34:C102–C121. doi:10.1137/110843940
28. Brackbill JU, and Barnes DC. The Effect of Nonzero ∇ · B on the Numerical Solution of the Magnetohydrodynamic Equations. *J Comput Phys* (1980) 35:426–30. doi:10.1016/0021-9991(80)90079-0
29. Brandenburg A, Rädler KH, Rheinhardt M, and Käpylä PJ. Magnetic Diffusivity Tensor and Dynamo Effects in Rotating and Shearing Turbulence. *ApJ* (2008) 676:740–51. doi:10.1086/527373
30. Manabu Y, Kanako S, and Yosuke M. Development of a Magnetohydrodynamic Simulation Code Satisfying the Solenoidal Magnetic Field Condition. *Comput Phys Commun* (2009) 180:1550–7. doi:10.1016/j.cpc.2009.04.010
31. Powell KG, Roe PL, Linde TJ, Gombosi TI, and De Zeeuw DL. A Solution-Adaptive Upwind Scheme for Ideal Magnetohydrodynamics. *J Comput Phys* (1999) 154:284–309. doi:10.1006/jcph.1999.6299
32. Hayashi K. Magnetohydrodynamic Simulations of the Solar Corona and Solar Wind Using a Boundary Treatment to Limit Solar Wind Mass Flux. *Astrophys J Suppl S* (2005) 161:480–94. doi:10.1086/491791
33. Feng X, Liu X, Xiang C, Li H, and Wei F. A New MHD Model with a Rotated-Hybrid Scheme and Solenoidality-Preserving Approach. *ApJ* (2019) 871:226. doi:10.3847/1538-4357/aafacf
34. Feng X, Zhang S, Xiang C, Yang L, Jiang C, and Wu ST. A Hybrid Solar Wind Model of the Cese+hll Method with a Yin-Yang Overset Grid and an Amr Grid. *ApJ* (2011) 734:50. doi:10.1088/0004-637X/734/1/50
35. Schatten KH, Wilcox JM, and Ness NF. A Model of Interplanetary and Coronal Magnetic fields. *Sol Phys* (1969) 6(3):442–55. doi:10.1007/BF00146478
36. Altschuler MD, and Newkirk G. Magnetic fields and the Structure of the Solar corona. *Solar Phys* (1969) 9(1):131–49. doi:10.1007/BF00145734
37. Lee CO, Arge CN, Odstrčil D, Millward G, Pizzo V, Quinn JM, et al. Ensemble Modeling of CME Propagation. *Sol Phys* (2013) 285:349–68. doi:10.1007/s11207-012-9980-1
38. Moguen Y, Bruel P, Perrier V, and Dick E. Non-reflective Inlet Conditions for the Calculation of Unsteady Turbulent Compressible Flows at Low Mach Number. *Mech Industry* (2014) 15(3):179–89. doi:10.1051/meca/2014027
39. Nakamizo A, Tanaka T, Kubo Y, Kamei S, Shimazu H, and Shinagawa H. Development of the 3-D MHD Model of the Solar corona-solar Wind Combining System. *J Geophys Res* (2009) 114:A7. doi:10.1029/2008JA013844
40. Feng X, Jiang C, Xiang C, Zhao X, and Wu ST. A Data-Driven Model for the Global Coronal Evolution. *ApJ* (2012) 758:62. doi:10.1088/0004-637X/758/1/62
41. Feng X, Yang L, Xiang C, Jiang C, Ma X, Wu ST, et al. Validation of the 3D AMR SIP-CESE Solar Wind Model for Four Carrington Rotations. *Sol Phys* (2012) 279:207–29. doi:10.1007/s11207-012-9969-9
42. Arge CN, and Pizzo VJ. Improvement in the Prediction of Solar Wind Conditions Using Near-Real Time Solar Magnetic Field Updates. *J Geophys Res* (2000) 105(A5):10465–79. doi:10.1029/1999ja000262
43. Arge CN, Luhmann JG, Odstrcil D, Schrijver CJ, and Li Y. Stream Structure and Coronal Sources of the Solar Wind during the May 12th, 1997 CME. *J Atmos Solar-Terrestrial Phys* (2004) 66:1295–309. doi:10.1016/j.jastp.2004.03.018
44. Suess ST, Wang A-H, and Wu ST. Volumetric Heating in Coronal Streamers. *J Geophys Res* (1996) 101(A9):19957–66. doi:10.1029/96JA01458
45. Yang L, Feng X, Xiang C, Zhang S, and Wu ST. Simulation of the Unusual Solar Minimum with 3D SIP-CESE MHD Model by Comparison with Multi-Satellite Observations. *Sol Phys* (2011) 271:91–110. doi:10.1007/s11207-011-9785-7
46. Spitzer L. *Physics of Fully Ionized Gases*. 2nd ed., 359. New York: Interscience (1962). 3559. doi:10.1126/science.139.3559.1045
47. Zhang M, and Feng X. A Comparative Study of Divergence Cleaning Methods of Magnetic Field in the Solar Coronal Numerical Simulation. *Front Astron Space Sci* (2016) 3:6. doi:10.3389/fspas.2016.00006
48. Pakmor R, and Springel V. Simulations of Magnetic fields in Isolated Disc Galaxies. *Month Notices R Astron Soc* (2013) 432:176–93. doi:10.1093/mnras/stt428
49. Gilchrist SA, Leka KD, Barnes G, Wheatland MS, and DeRosa ML. On Measuring Divergence for Magnetic Field Modeling. *ApJ* (2020) 900:136. doi:10.3847/1538-4357/aba752

Conflict of Interest: The authors declare that the research was conducted in the absence of any commercial or financial relationships that could be construed as a potential conflict of interest.

Publisher's Note: All claims expressed in this article are solely those of the authors and do not necessarily represent those of their affiliated organizations, or those of the publisher, the editors and the reviewers. Any product that may be evaluated in this article, or claim that may be made by its manufacturer, is not guaranteed or endorsed by the publisher.

frontiers in Physics

ORIGINAL RESEARCH
published: 01 September 2021
doi: 10.3389/fphy.2021.646556

Auto Recognition of Solar Radio Bursts Using the C-DCGAN Method

Weidan Zhang[1], *Fabao Yan*[1,2]*, *Fuyun Han*[2], *Ruopu He*[2], *Enze Li*[2], *Zhao Wu*[1] *and Yao Chen*[1]

[1]*Laboratory for ElectromAgnetic Detection (LEAD), Institute of Space Sciences, Shandong University, Weihai, China,* [2]*School of Mechanical, Electrical & Information Engineering, Shandong University, Weihai, China*

Solar radio bursts can be used to study the properties of solar activities and the underlying coronal conditions on the basis of the present understanding of their emission mechanisms. With the construction of observational instruments, around the world, a vast volume of solar radio observational data has been obtained. Manual classifications of these data require significant efforts and human labor in addition to necessary expertise in the field. Misclassifications are unavoidable due to subjective judgments of various types of radio bursts and strong radio interference in some events. It is therefore timely and demanding to develop techniques of auto-classification or recognition of solar radio bursts. The latest advances in deep learning technology provide an opportunity along this line of research. In this study, we develop a deep convolutional generative adversarial network model with conditional information (C-DCGAN) to auto-classify various types of solar radio bursts, using the solar radio spectral data from the Culgoora Observatory (1995, 2015) and the Learmonth Observatory (2001, 2019), in the metric decametric wavelengths. The technique generates pseudo images based on available data inputs, by modifying the layers of the generator and discriminator of the deep convolutional generative adversarial network. It is demonstrated that the C-DCGAN method can reach a high-level accuracy of auto-recognition of various types of solar radio bursts. And the issue caused by inadequate numbers of data samples and the consequent over-fitting issue has been partly resolved.

Keywords: deep learning, deep convolution generation confrontation network, image reconstruction, convolutional neural networks, space weather

OPEN ACCESS

Edited by:
Qiang Hu,
University of Alabama in Huntsville, United States

Reviewed by:
Jiajia Liu,
Queen's University Belfast, United Kingdom
Sijie Yu,
New Jersey Institute of Technology, United States

***Correspondence:**
Fabao Yan
hjc-8555@sdu.edu.cn

Specialty section:
This article was submitted to Stellar and Solar Physics, a section of the journal Frontiers in Physics

Received: *27 December 2020*
Accepted: *19 July 2021*
Published: *01 September 2021*

Citation:
Zhang W, Yan F, Han F, He R, Li E, Wu Z and Chen Y (2021) Auto Recognition of Solar Radio Bursts Using the C-DCGAN Method. Front. Phys. 9:646556. doi: 10.3389/fphy.2021.646556

INTRODUCTION

Solar radio bursts are emission enhancements at radio wavelengths released during solar activities such as flares and coronal mass ejections (CMEs) [1]. They can be used to diagnose the properties of the associated solar activities and the underlying coronal conditions on the basis of the present understanding of emission mechanisms. For instance, many solar radio bursts observed in the metric wavelengths have been attributed to the plasma emission mechanism, according to which the emission frequency represents the fundamental or harmonic of plasma oscillation frequencies which are given by the plasma electron density. Thus, the radio data can be used to infer the plasma density in the corona [2, 3] and of the emission source such as coronal shocks.

Solar radio bursts in the metric wavelengths are classified into various types, including type I to V, according to their manifestation on the dynamic spectrum which presents the temporal variation of spectral intensities [4]. In **Figure 1**, we present examples of these five types of solar radio bursts observed by the Culgoora Observatory. The type I burst consists of two components, including the

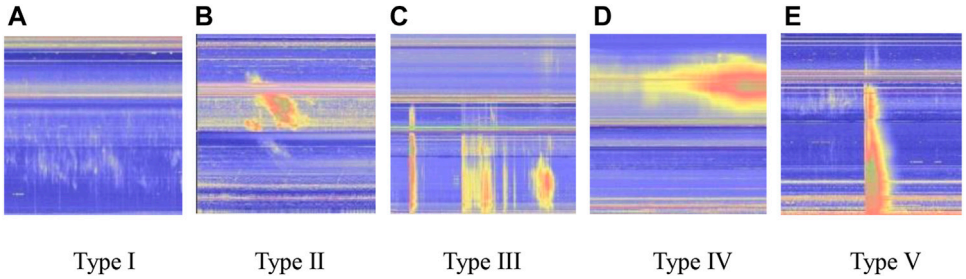

FIGURE 1 | Examples of type I–type V solar radio bursts observed in the metric decametric wavelengths **(A–E)**. The spectra used in this study are obtained from the Australian Bureau of Meteorology's Culgoora Observatory and Learmonth Observatory (http://www.sws.bom.gov.au/World_Data_Centre/1/9). The Culgoora Observatory monitors solar radio bursts in the frequency range 18–1800 MHz, and the Learmonth Observatory radio observatory monitors solar radio bursts in the range 25–180 MHz.

background continuum and short-term radio enhancements (called type I storm). The type II burst represents narrow-band drifting structures in the dynamic spectrum, generally attributed to energetic electrons accelerated around coronal shocks. The type III burst has fast-drifting features on the dynamic spectrum, usually attributed to fast, energetic electrons releasing from the flare reconnection site and escaping outward (or inwards) along field lines. They are called as the type III storm if they occur in groups over an extended interval. The type IV burst represents a wideband continuum on the dynamic spectrum, which can be further classified into two subgroups, including stationary ones and moving ones. The type V burst occurs immediately after the type III burst while occupying a wider spectral regime than the type III burst; it is generally attributed to energetic electrons that are strongly scattered by coronal waves.

Radio spectral data with high temporal and spectral resolutions are important for scientific research of solar radio bursts. To demonstrate the present status of the field using such data, in the following, we just present two examples of studies on the temporal delay of solar spikes. Using the spectral data (with a temporal resolution of 10 ms and a spectral resolution of 100 kHz) from the Chashan Solar Observatory (CSO) operated by Shandong University, Feng et al. [5] found that the time delay between harmonics of solar radio spikes could be as small as the temporal resolution of the data (~10 ms), while in an earlier study, Bouratzis et al. (2016) found that the duration of metric radio spikes is ~60 ms according to an analysis of 12,000 events [6] (see Chernov et al. [7] for more studies on radio fine structures using high-resolution spectral data).

In addition to the increased resolution of the data, the number of solar radio observatories also increased around the world. For example, the Expanded Owens Valley Solar Array (EOVSA) [8] is operating in the frequency range of 1–18 GHz. Mingantu Spectral Radioheliograph (MUSER) [9] generates nearly 3.5 TB data per day. Chashan Solar Observatory (CSO) [6] operated by Shandong University obtains up to 300 GB of data per day. This results in a rapid increase of data volume waiting to be classified and analyzed.

Similar to many other data-intensive scientific research works, solar astronomy has benefited from interdisciplinary study with computer science and information technology. In particular, the rapid development of deep learning technology has provided new avenues in astronomical research.

The deep neural network (DNN) [10], as a functional unit of the deep learning technology, has been designed to learn how human beings think and recognize objects on the basis of hierarchical layer structures. It represents one of the most important advancements in the developments of machine-learning algorithms and has been applied to many research fields when processing a large amount of data. In the field of image processing and computer vision, the convolutional neural network (CNN) [11] becomes the most popular deep-learning method, which is composed of convolution filters to extract information from the input datasets automatically without any human intervention, while traditional machine-learning algorithms require researchers to manually select and construct these extractors [12]. This great advantage is very useful, especially when being applied to research problems without sufficient knowledge or the problems are just too complex to build a "good" simplified model.

Deep learning technology has been applied to the classification of solar radio bursts in the last decade. For example, Gu et al. [13] used a combination of principal component analysis (PCA) and support vector machine (SVM) for the mentioned purpose, yet the obtained accuracy of recognition needs to be improved. To do this, Chen et al. [14] applied the multimodal network to auto-classify types of radio bursts, and later, they also tried the method of the deep belief network (DBN) [15] and the convolutional neural network (CNN) [16]. In addition, Yu et al. [17] classified the solar radio data by using the long short-term memory network (LSTM) and obtained some improvement of the classification accuracy.

Nevertheless, to train a neural network model to a satisfactory level, a large amount of data is needed along with manual labeling and the input of the classifying information. This is usually very time-consuming. In addition, the occurrence numbers of different types of radio bursts are very different from each other. For example, the numbers of type IV and V bursts are significantly less than the other types of radio bursts. The main aim of this study is to utilize a proper deep learning algorithm to

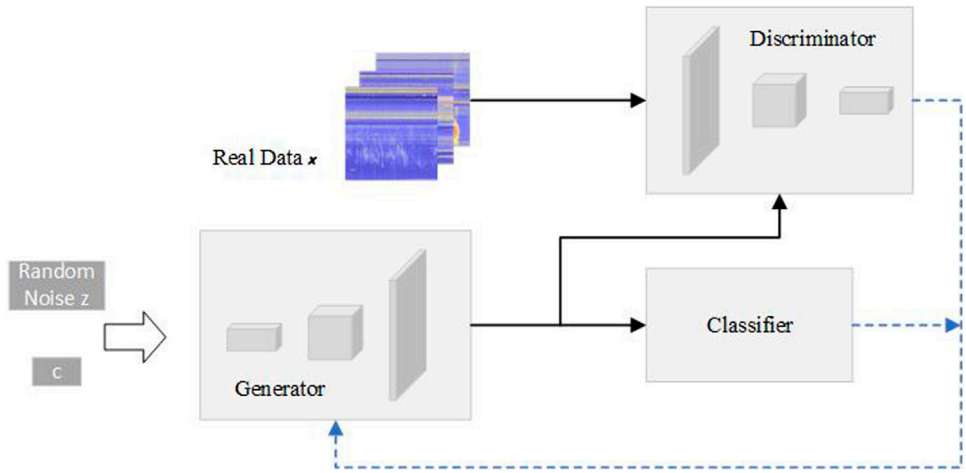

FIGURE 2 | Structure of the C-DCGAN model, including three major modules: the classifier, the discriminator (D), and the generator (G) (see text for details).

resolve the issue caused by an insufficient dataset. This is achieved by applying the method of the generative adversarial network (GAN) [18].

GAN has received a lot of attention since its emergence. It [11] introduces the idea of game theory into the training process, in which generator and discriminator are trained alternatively to learn the major characteristics of the data. Its neural network structure greatly enhances the capability in generating samples to provide more dataset when training the classification network.

GAN can be further extended to a conditional model (CGAN) if both the generator and discriminator are conditioned on some extra information (c). Condition c can be fed into both the discriminator and generator as additional input information [19]. In addition, the GAN model is further improved as the deep convolutional generative adversarial network (DCGAN) to increase the quality of image fitting through the confrontation learning of the generating model and the discriminating model [20]. This potentially increases the number of samples. These generated samples are then used together with the original dataset for training purpose.

In this study, we develop a novel machine-learning program, the conditional deep convolutional generative adversarial network (C-DCGAN) model, on the basis of the DCGAN model, to automatically classify solar radio bursts observed by the Culgoora Observatory from 1995 to 2015 and the Learmonth Observatory from 2001 to 2019. The model has been tested using the MNIST dataset. The results demonstrate that the C-DCGAN method can capture the major characteristics of each type of solar radio bursts and yield a satisfactory level of recognition accuracy of these bursts. The following section presents the details of the model and the dataset. Section *Results of Automatic Identification of Solar Radio Bursts With C-DCGAN* shows the classification results with the C-DCGAN method. The Discussion and Conclusions are given in the last section.

THE C-DCGAN MODEL AND THE DATASET OF SOLAR RADIO BURSTS

In this section, we present the technical details of the C-DCGAN model, the dataset of solar radio bursts, and how we use the data to train our model for the purpose of auto-recognition of the types of bursts.

C-DCGAN Model

The C-DCGAN model is a combination of two networks, CGAN and DCGAN. In comparison to the initial GAN model, CGAN performs better in generating categories of images, while DCGAN is better in generating artificial images. Specific conditions, for example, types of radio bursts of the sample spectra, are supplied to the C-DCGAN model during the training process. This allows the model to generate images representative of any type of radio bursts, which will be used in the deep learning process.

In **Figure 2**, we present the basic structure of the network. It can be seen that the C-DCGAN includes three major modules including the classifier which is a convolutional neural network used to classify and identify the different types of solar radio bursts, the generator (G), and the discriminator (D). G and D are trained in an adversarial manner; in other words, G is designed to generate artificial images as real as possible, while D tries to differentiate the real and fake inputs. And the classifier tries to classify all available datasets including real data and those generated by G, designed to get the most optimized outputs. Through their competition, D can proceed effectively, and the over-fitting issue caused by insufficient dataset can be largely avoided, while the classification accuracy can be improved, as shown by the following results.

The distribution of the real data (x) is taken to be $P_{data(x)}$, which is unknown. Yet the discriminator has a known noise of $P_{z(z)}$. Through G, the model learns this distribution and outputs artificial image data ($G(z|c)$) on condition c. To generate an artificial data image ($P_{data(x)}$), the data noise $P_{z(z)}$ should be

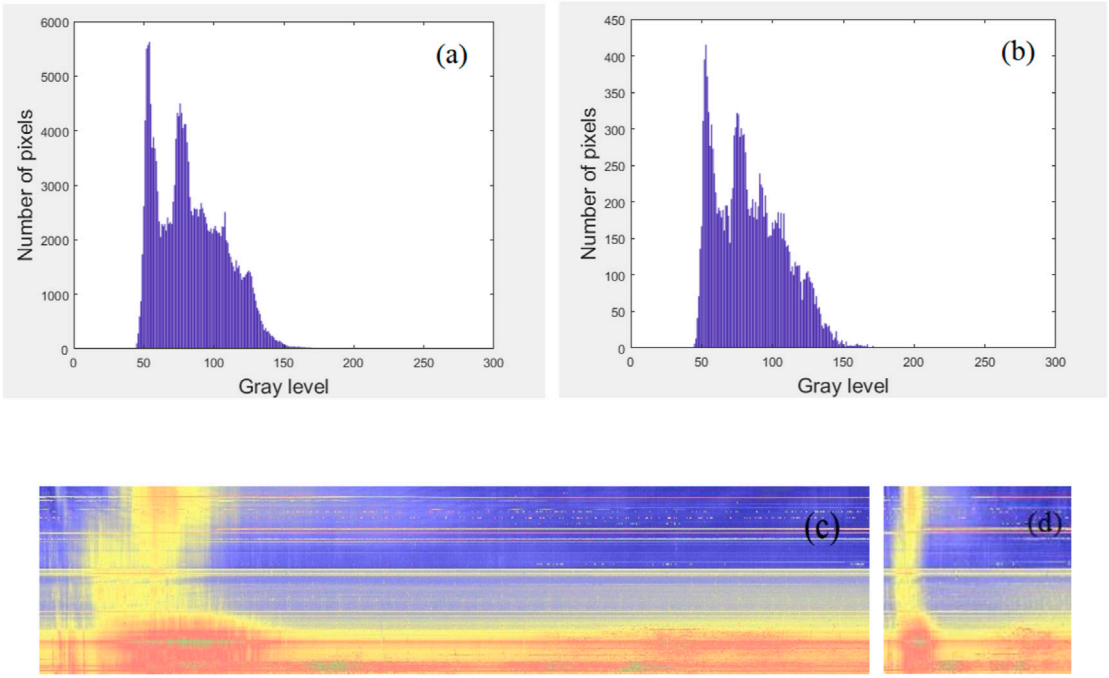

FIGURE 3 | Solar radio spectrograms and histograms before and after downsampling for the event of 2005 August 22 observed by the Learmonth. (A) Histogram before downsampling, **(B)** histogram after downsampling, **(C)** original solar radio image, and **(D)** downsampled solar radio image.

added by the generator G. This is achieved with the following cross-entropy loss function:

$$\min_G \max_D V(D,G) = E_{x\sim P_{data(x)}}[\log D(x)] + E_{z\sim P_{z(z)}}[\log(1-D(G(z|c)))],$$

where V (D, G) represents the loss functions of G and D, and E represents the expected value. And x represents the real sample, D (x) represents the probability of discriminating x as a real sample with the discriminator D, G(z) is the sample generated from noise z by the generator G, $E_{x\sim P_{data}(x)}$ represents the real data sample extracted from the training data x, and $E_{z\sim P_{z}(z)}$ the generated image; D (x) and $D(G(z|c))$ are outputs of discriminator D to determine how close the included dataset to the "real" data. In ideal situations, both parameters should be close to 1.

Dataset of Solar Radio Bursts

The dynamic spectral data of solar radio bursts recorded by the Culgoora Observatory from 1995 to 2015 and the Learmonth Observatory from 2001 to 2019 are used to train the C-DCGAN model. The horizontal axis and vertical axis of a map of the dynamic spectrum are time and frequency, respectively. The online data are represented with JPEG format of images with different dimensions in pixels that are 600 × 1750 for Culgoora and 300 × 1700 for Learmonth. These spectral data should be preprocessed before inputting them into the model.

First, we rebind both datasets into the resolution of 128 × 128. The event lasting longer than 60 min will be downsampled to 128 × 128, and the event shorter than 60 min will be upsampled to 128 × 128. This does not affect the statistical properties of the data significantly [16], according to **Figure 3**, which presents the comparison before and after the rebinding, in particular, the downsampling process. The comparison of the histogram of the original and the downsampled images indicates that the data preprocessing does not change their statistical properties significantly.

To increase the recognition accuracy, we further remove events that are incomplete and with mixing types of bursts according to the online log files of the data. We end up with a data sample including 36,005 burst images, of which 7,201 are used in the testing process (see **Table 1** for a list of the numbers of various types of radio bursts used here). It can be seen that type III burst has the largest sample numbers, while type I burst from Learmonth and type V burst from Culgoora have the least number of samples. Note that only 4 events are included for type V burst for Culgoora. This affects the performance of our model, as will be discussed later.

The Training Process

The model was run on GPU arrays of the NVIDIA GeForce quadro RTX 8000; the training process lasts up to 43 h. When the training data are not enough to provide a good estimate of the distribution of the entire data, in other words, the model is overtrained and leads to over-fitting of the data; we employ the dropout method. Typically, the outputs of neurons are set to zero with a probability of p in the training stage and

TABLE 1 | Event number of solar radio bursts used in the training process from the two stations.

Type	Occurrence number (Leamonth)	Occurrence number (Culgoora)
Type I	139	1,144
Type II	519	1,070
Type III	10,143	22,273
Type IV	288	74
Type V	351	4

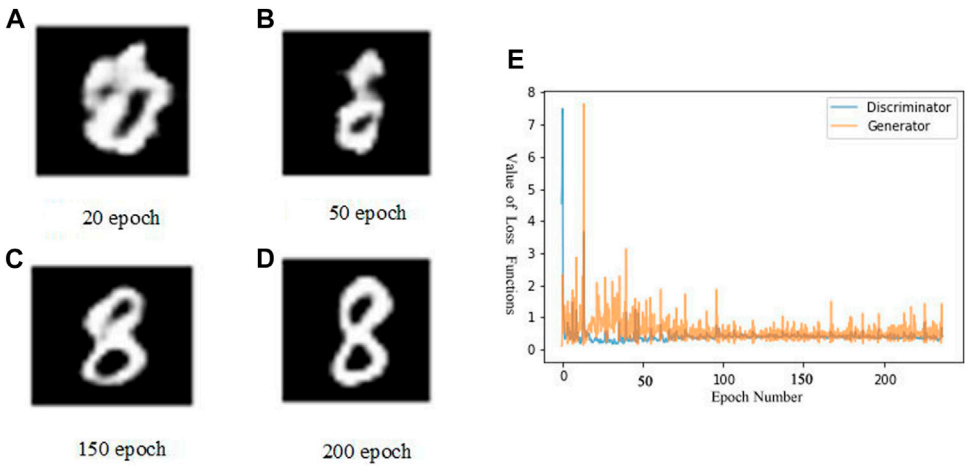

FIGURE 4 | Testing the C-DCGAN model with the MNIST dataset. **(A–D)** shows the C-DCGAN generated data at Epochs 20, 50, 150, and 200. **(E)** The values of the loss functions *versus* epoch number for D and G.

multiplied with $1 - p$ in the test stage [21]. By randomly taking out the neurons, in other words, dropout is an efficient approximation of training many different networks with shared weights of some neurons. In our experiments, we applied the dropout to all the layers, and the probability is set as $p = 0.5$.

We use the MNIST (Modified National Institute of Standards and Technology) dataset to evaluate the performance of the model, which is a large database of handwritten digits commonly used for similar training purpose. It has 60,000 training samples and 10,000 test samples. **Figures 4A–D** show the variation of the generated image samples with training epochs. **Figure 4E** shows the variety of the loss functions of both D and G. It can be seen that the original data image can be well replicated within 200 epochs, while at the earlier epochs (<100), the loss values show large oscillations. And the loss values after Epoch 100 remain below 0.5.

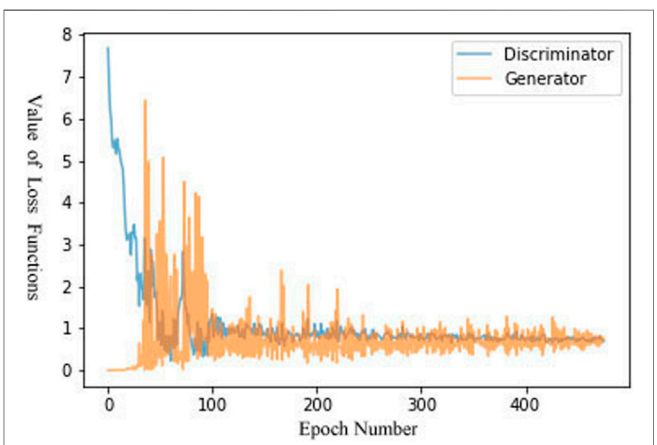

FIGURE 5 | Variations of the loss function with epoch number, blue for D and orange for G.

The Recognition Process

The process of image recognition is done through the following steps: 1) we fix the parameters of G while keeping the accuracy of D as high as possible, 2) the parameters of D are fixed while optimizing the output of G so that the discrepancies between the generated data and the real data are sufficiently small, 3) the above two steps are conducted repeatedly until the model achieves high-enough accuracy of image recognition, and 4) the discriminator is extracted from the trained C-DCGAN model to form a new structure of recognition. Both the samples generated by G and the real samples are taken as inputs to the classifier.

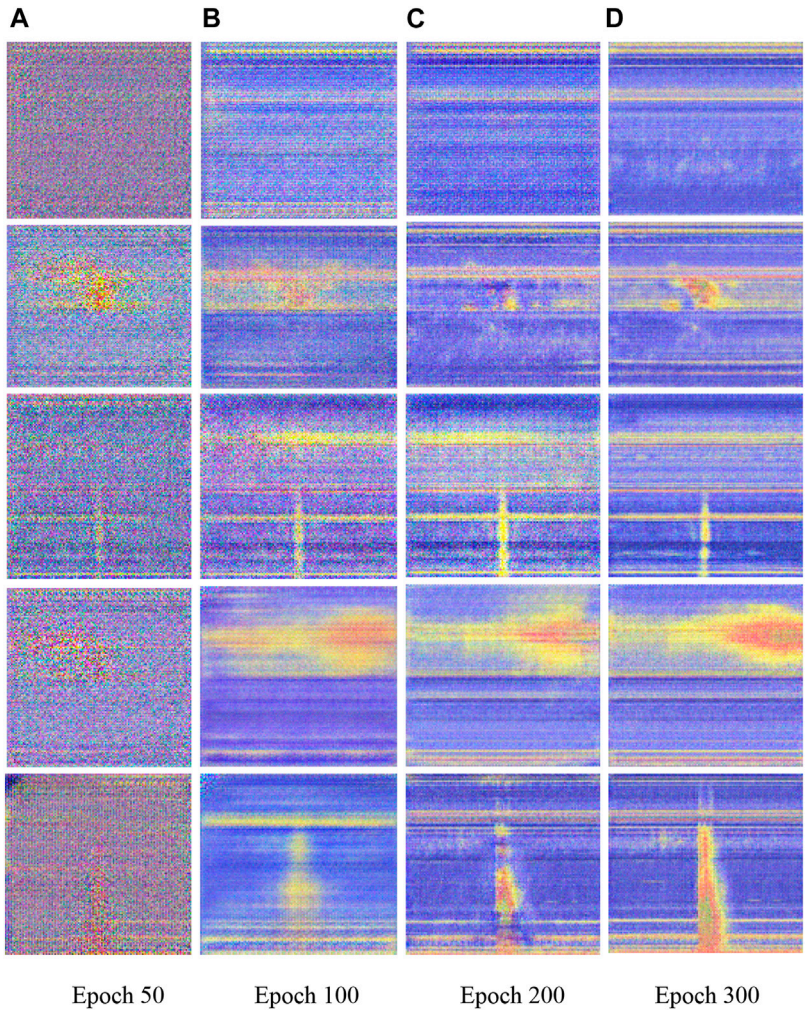

FIGURE 6 | C-GCGAN generated data images of the five types of solar radio bursts at different epoch numbers (50–300). Panels from top to bottom correspond to type I to type V bursts.

RESULTS OF AUTOMATIC IDENTIFICATION OF SOLAR RADIO BURSTS WITH C-DCGAN

In total, 28,804 solar radio spectral data images were used as the "real part" of the training sample; those images of data generated by the generator were also used. The loss functions of both D (the discriminator) and G (the generator) are plotted in **Figure 5** as a function of the epoch number of the training process. It can be seen that the value of the loss function of G is rather small at the start while that of D is rather large. With increasing the epoch number, say, after Epoch 30, the two values manifest strong oscillations, indicating the occurrence of confrontation. After Epoch 100, both values of loss function remain mostly below 1, indicating the gradual stabilization of the two networks. They remain largely below 0.8 after Epoch 250, indicating the data generated by G can be hardly discriminated from real data by D; in other words, these generated data contain most, if not all, essential features of the real data.

TABLE 2 | Accuracy of identification of different types of radio bursts according to the C-DCGAN model.

Type	Accuracy (Leamonth) (%)	Accuracy (Culgoora) (%)
Type I	85.82	86.01
Type II	85.43	85.30
Type III	91.97	91.06
Type IV	89.32	89.16
Type V	84.79	81.43

Examples of the generated data images, at different numbers of epochs from 50 to 300, for the five types of solar radio bursts observed in the metric decametric wavelengths are shown in **Figure 6**. At the early stage of the training (before Epoch 100), the generated images are rather blurred; with increasing numbers of epoch (after Epoch 200), the generated images become very similar to those observed for the same type of radio burst, indicating the success of the data-generating process. This

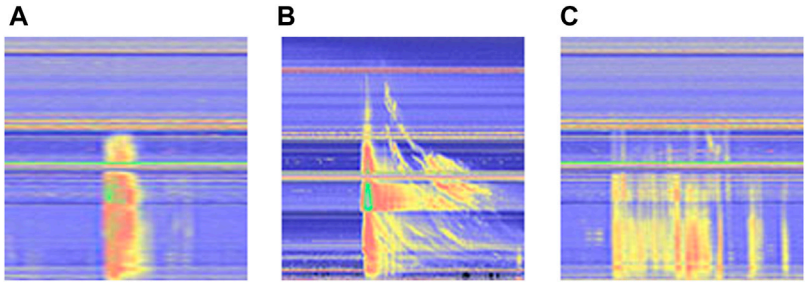

FIGURE 7 | Three cases that have been misidentified as type V by C-GCGAN. According to the online data log file, **(A)** has been classified as type III, **(B)** as type III, and **(C)** as type III.

mostly resolves the issue of insufficient data sample and the consequent over-fitting problem of earlier network models and improves the performance of our model as will be demonstrated soon.

Table 2 presents the identification accuracy of different types of metric decametric solar radio bursts. It can be seen that the accuracy of type III identification is the highest, reaching above 91% for both datasets (91.97% for Learmonth and 91.06% for Culgoora). The accuracy for type IV also has a high rate of 89.32% for Learmonth and 89.16% for Culgoora. This is likely due to the easy-to-identify features of the two bursts, in comparison to others. For example, type III is a very rapidly drifting feature with high brightness, while type IV is a long-duration wideband continuum. In addition, type III bursts usually last for less than 60 min; thus, they are not affected much by the downsampling preprocessing. The recognition accuracy of type I and type II bursts is relatively low, around 85%, while that for type V bursts are the lowest (84.79% for Learmonth and 81.43% for Culgoora). This is likely due to the smaller number of events in the sample for these bursts. Note that only 4 spectra are available for type V bursts from Culgoora; thus, C-DCGAN cannot catch the full features of the burst. This indicates that although C-DCGAN can largely resolve the inadequate data problem, its performance is yet to improve when the number of samples is too low. The average identification accuracy for the five types of radio bursts for Learmonth is higher than that for Culgoora, mainly because the sample data from Learmonth are more balanced among different types of bursts than those from Culgoora.

To further look into the causes of false recognition, we present three such examples in **Figure 7**. They were all misidentified as type V bursts. The event in **Figure 7A** was classified as a type III event according to the online log file of the Learmonth Observatory (yet it could be classified as a type V event from our perspective); the event in **Figure 7B** was classified as a type II event, according to the online log file (yet it should be classified as a mixing-type event with both type III and type II bursts), and the last event is a type III burst (should be classified as a type III storm event). Since type V usually takes place after type III burst, in this case, they coexist as mixing events in one spectral data. In addition, due to their similar morphology, type V could be easily misidentified as type III, or the two bursts are not separable in many events. According to our method of data selection, we have removed the events of mixing types of bursts. This contributes to the insufficient number of type V bursts used in the training process and affects the accuracy of our model.

CONCLUSION AND DISCUSSION

Observations and studies of solar radio bursts are important to our understanding of the physics of solar activities and relevant space weather science as well as the physics of plasma radiation in both astrophysics and space science. With the increasing volume of data, it becomes timely and demanding to develop techniques that can classify various types of solar radio bursts automatically.

To do this, we developed a C-DCGAN model combining two networks including the conditional generative adversarial network (CGAN) and the deep convolutional generative adversarial network (DCGAN). The main motivation is to resolve the issue caused by inadequate numbers of data samples and the consequent over-fitting issue. The database of solar radio bursts recorded by the Learmonth and the Culggora observatories consists of 36,005 events. We concluded that the C-DCGAN performs well for type III and IV bursts, reaching identification accuracy as high as 89–92%; for type I and type II bursts, the accuracy reaches around 85%, while for type V burst, the accuracy is the lowest, being below 85%.

The results show that our C-DCGAN model can satisfactorily generate artificial data images from a small set of data and potentially expand the size of the data sample. This is important for the better performance of our model over others published earlier [16] and represents a novel way in the auto-classification of solar radio bursts using the deep learning technology.

There exist two major limitations of the present model that should be overcome in the future: 1) downsampling of the data may lose some critical information of the original data and thus affect the accuracy of the recognition; 2) the strong signal of radio interference may become the major features of a radio spectrum in some cases; thus, further studies should consider either to remove these signals from the spectra or learn their major characteristics so as to identify them.

DATA AVAILABILITY STATEMENT

The original contributions presented in the study are included in the article/Supplementary Material; further inquiries can be directed to the corresponding author.

AUTHOR CONTRIBUTIONS

WZ was the experimental designer and conductor of the experimental study, completed the data analysis, and wrote the first draft of the article. FH, RH, and EL were involved in the experimental design and analysis of the results. FY and YC were the conceptualizers and leaders of the project, directing the experimental design, and data analysis. WZ is responsible for the revision and improvement of the thesis. All authors have read and agreed to the final text.

FUNDING

This project was supported by the National Natural Science Foundation of China (41774180, 11803017), Shandong postdoctoral innovation project (202002004), the China Postdoctoral Science Foundation (2019M652385), and Young Scholars Program of Shandong University, Weihai (20820201005).

REFERENCES

1. Bouratzis C, Hillaris A, Alissandrakis CE, Preka-Papadema P, Moussas X, Caroubalos C, et al. Fine Structure of Metric Type IV Radio Bursts Observed with the ARTEMIS-IV Radio-Spectrograph: Association with Flares and Coronal Mass Ejections. *Sol Phys* (2015) 290:219–86. doi:10.1007/s11207-014-0562-2
2. Chen Y. A Review of Recent Studies on Coronal Dynamics: Streamers, Coronal Mass Ejections, and Their Interactions. *Chin Sci Bull* (2013) 5(14):1599. doi:10.1007/s11434-013-5669-6
3. Chen Y, Du G, Feng L, Feng S, Kong X, Guo F, et al. A Solar Type Ii Radio Burst from Coronal Mass Ejection-Coronal Ray Interaction: Simultaneous Radio and Extreme Ultraviolet Imaging. *Astrophysical. J.* (2014) 787:59. doi:10.1088/0004-637x/787/1/59
4. Gary DE, and Keller CU. *Solar, and Space Weather Radiophysics—Current Status and Future Developments*, 314. Dordrecht: Astrophysics and Space Science LibraryKluwer Academic (2004).
5. Feng SW, Chen Y, Kong XL, Li G, Song HQ, Feng XS, et al. Diagnostics on the Source Properties of a Type Ii Radio Burst with Spectral Bumps. *Astrophysical. J.* (2013) 767:29. doi:10.1088/0004-637x/767/1/29
6. Feng SW, Chen Y, and Li CY. Harmonics of Solar Radio Spikes at Metric Wavelengths. *Solar Phys* (2018) 293:39. doi:10.1007/s11207-018-1263-z
7. Chernov PG. *Fine Structure of Solar Radio Bursts*. Springer Berlin Heidelberg (2011). doi:10.1007/978-3-642-20015-1
8. Gary D. E, Chen B, Dennis B. R. G. D, Hurford GJ, Krucker S, McTiernan JM, et al. Microwave and Hard X-Ray Observations of the 2017 September 10 Solar Limb Flare [J]. *Astrophysical J* 863:83. doi:10.3847/1538-4357/aad0ef
9. Yan Y, Chen L, and Yu S. First Radio Burst Imaging Observation from Mingantu Ultrawide Spectral Radioheliograph. *Proc IAU* (2015) 11:427–35. doi:10.1017/s174392131600051x
10. Tang X-L, Yi-Ming D, Liu Y-W, Jia-Xin LI, and Ma Y-W. Image Recognition with Conditional Deep Convolutional Generative Adversarial Networks. *Acta Automatica. Sinica* (2018) 44(5):855–64. doi:10.16383/j.aas.2018.c170470
11. He K, Zhang X, and Ren S. "Deep Residual Learning for Image Recognition [J]." in 2016 IEEE Conference on Computer Vision and Pattern Recognition (CVPR) (2016) 770–8. doi:10.1109/CVPR.2016.90
12. Jin LW, Zhong ZY, Yang Z, Yang WX, Xie ZC, and Sun J. Applications of Deep Learning for Handwritten Chinese Character Recognition [J]: a Review. *Acta Automatica Sinica* (2016) 42(8):1125–41. doi:10.16383/j.aas.2016.c150725
13. Gu B, Sheng VS, Tay KY, Romano W, and Li S. Incremental Support Vector Learning for Ordinal Regression. *IEEE Trans Neural Netw Learn Syst.* (2015) 26(7):1403–16. doi:10.1109/tnnls.2014.2342533
14. Chen Z, Ma L, Xu L, Tan C, and Yan Y. Imaging and Representation Learning of Solar Radio Spectrums for Classification. *Multimed Tools Appl* (2016) 75(5):2859–75. doi:10.1007/s11042-015-2528-2
15. Chen Z, Ma L, Xu L, Weng Y, and Yan Y. Multimodal Learning for Classification of Solar Radio Spectrum [C]. *IEEE Int Conf Syst Man, Cybernetics* (2015) 1035–40. doi:10.1109/SMC.2015.187
16. Xu L, Yan Y-H, Yu X-X, Zhang W-Q, Chen J, and Duan L-Y. LSTM Neural Network for Solar Radio Spectrum Classification. *Res Astron Astrophys* (2019) 19(9):135. doi:10.1088/1674–4527/19/9/135
17. Yu X, Xu L, and Ma L. Solar Radio Spectrum Classification with LSTM [C]. IEEE International Conference on Multimedia & Expo Workshops. IEEE (2017). p. 519–24.
18. Goodfellow I, Pouget-Abadie J, Warde-Farley D, Ozair S, Courville A, and Bengio Y. Generative Adversarial Nets [C]. Advances in Neural Information Processing Systems (2014). p. 2672–80.
19. Mirza M, and Osindero S. *Conditional Generative Adversarial Nets [J]*. arXiv preprint arXiv:1411.1784 (2014). Available at: https://ui.adsabs.harvard.edu/abs/2014arXiv1411.1784M/abstract.
20. Radford A, Metz L, and Chintala S. *Unsupervised Representation Learning with Deep Convolutional Generative Adversarial Networks [J]*. arXiv preprint arXiv:1511.06434 (2015). Available at: https://ui.adsabs.harvard.edu/abs/2015arXiv151106434R/abstract.
21. Srivastava N, Hinton G, and Krizhevsky A. Dropout: a Simple Way to Prevent Neural Networks from Overfitting [J]. *J Machine Learn Res* (2014) 15(1):1929–58.

Conflict of Interest: The authors declare that the research was conducted in the absence of any commercial or financial relationships that could be construed as a potential conflict of interest.

Publisher's Note: All claims expressed in this article are solely those of the authors and do not necessarily represent those of their affiliated organizations, or those of the publisher, the editors, and the reviewers. Any product that may be evaluated in this article, or claim that may be made by its manufacturer, is not guaranteed or endorsed by the publisher.

frontiers in Physics

ORIGINAL RESEARCH
published: 21 September 2021
doi: 10.3389/fphy.2021.750097

Spectral Evolution of an Eruptive Polar Crown Prominence With IRIS Observations

Jianchao Xue [1], *Hui Li* [1,2]* *and Yang Su* [1,2]

[1]*Key Laboratory of Dark Matter and Space Astronomy, Purple Mountain Observatory, Chinese Academy of Sciences, Nanjing, China,* [2]*School of Astronomy and Space Science, University of Science and Technology of China, Hefei, China*

Prominence eruption is closely related to coronal mass ejections and is an important topic in solar physics. Spectroscopic observation is an effective way to explore the plasma properties, but the spectral observations of eruptive prominences are rare. In this paper we will introduce an eruptive polar crown prominence with spectral observations from the Interface Region Imaging Spectrograph (IRIS), and try to explain some phenomena that are rarely reported in previous works. The eruptive prominence experiences a slow-rise and fast-rise phase, while the line-of-sight motions of the prominence plasma could be divided into three periods: 2 hours before the fast-rise phase, opposite Doppler shifts are found at the two sides of the prominence axis; then, red shifts dominate the prominence gradually; in the fast-rise phase, the prominence gets to be blue-shifted. During the second period, a faint component appears in Mg II k window with a narrow line width and a large red shift. A faint region is also found in AIA 304 Å images along the prominence spine, and the faint region gets darker during the expansion of the spine. We propose that the opposite Doppler shifts in the first period is a feature of the polar crown prominence that we studied. The red shifts in the second period are possibly due to mass drainage during the elevation of the prominence spine, which could accelerate the eruption in return. The blue shifts in the third period are due to that the prominence erupts toward the observer. We suggest that the faint component appears due to the decreasing of the plasma density, and the latter results from the expansion of the prominence spine.

Keywords: Sun: corona, Sun: coronal mass ejections (CMEs), Sun: filaments, prominences, Sun: UV radiation, techniques: spectroscopic

OPEN ACCESS

Edited by:
HengQiang Feng,
Luoyang Normal University, China

Reviewed by:
Leping Li,
National Astronomical Observatories (CAS), China
Pavol Schwartz,
Astronomical Institute of Slovak Academy of Sciences, Slovakia

***Correspondence:**
Hui Li
nj.lihui@pmo.ac.cn

Specialty section:
This article was submitted to Stellar and Solar Physics, a section of the journal Frontiers in Physics

Received: *30 July 2021*
Accepted: *06 September 2021*
Published: *21 September 2021*

Citation:
Xue J, Li H and Su Y (2021) Spectral Evolution of an Eruptive Polar Crown Prominence With IRIS Observations. Front. Phys. 9:750097. doi: 10.3389/fphy.2021.750097

1 INTRODUCTION

Solar prominences are composed of cold and dense plasma suspended in the hot corona [1–4]. Prominence eruptions have a close relationship with flares and coronal mass ejections (CMEs), and the latter two phenomena are main causes of the space weather storms. Hence studying the triggering mechanism and evolution of prominence eruptions are important topics in solar physics. Spectroscopic observation is an effective way to reveal plasma properties and line-of-sight (LOS) motions. However, high-quality spectral data of eruptive prominences are rare due to limited field of view (FOV) of general spectroscopic observations and randomness of prominence eruptions.

The Interface Region Imaging Spectrograph (IRIS [5]), is a small explorer spacecraft launched in 2013 June. It provides simultaneous high-resolution spectral and imaging data from the photosphere to the corona. The IRIS especially has an advantage of observing chromosphere and transition region

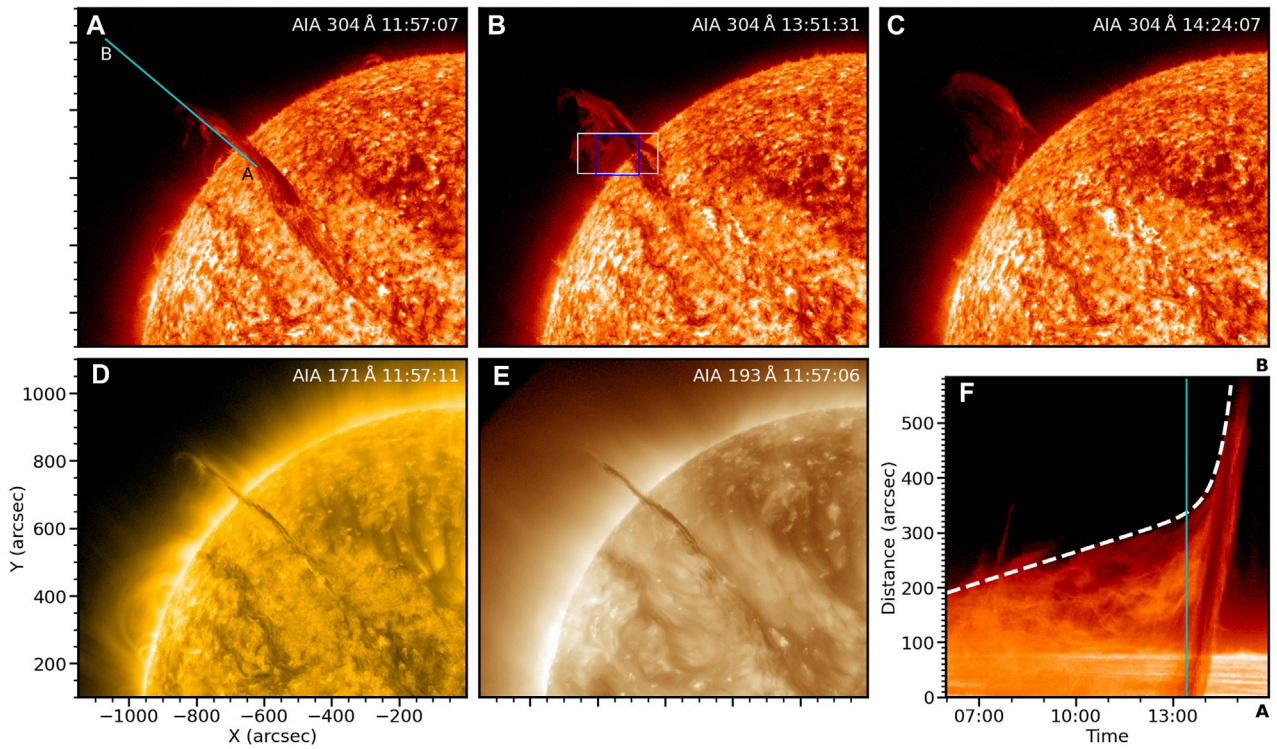

FIGURE 1 | Evolution of the eruptive prominence in EUV images. **(A–C)** AIA 304 Å images. The cyan slice AB in **(A)** is the position of the time-distance diagram in panel **(F)**. The white box in **(B)** represents the FOV of IRIS SJI observations, and the blue box marks the FOV of spectroscopic observations. **(D–E)** AIA 171 and 193 Å images, respectively. **(F)** Time-distance diagram along the slice AB in panel **(A)** from AIA 304 Å images. The cyan line marks the onset of the fast-rise phase.

with some strong resonance lines of Mg II (temperature of formation of log T [K] ~ 4.0), C II (log T [K] ~ 4.3), and Si IV (log T [K] ~ 4.8). The prominence core has a chromospheric temperature, and prominence also has a prominence-corona transition region (PCTR). So the IRIS is also suitable to observe prominences and filaments. The IRIS has been widely used to study the dynamics of quiescent prominences [6–9], but the spectroscopic observations of eruptive prominences are still rare. Among the few works [10], reported an erupting prominence in active region using IRIS observations; the authors found a faint component with **a** LOS velocity up to 460 km s^{-1}, and revealed the unwinding motions during the prominence eruption [11]. studied an eruptive prominence in quiet region with radiative transfer computations; they derived the electron densities of the prominence between 1.3×10^9 and 6.0×10^{10} cm^{-3}, the mean temperature around 1.1×10^4 K, and the total hydrogen mass between 1.3×10^{14} and 3.2×10^{14} g.

In this work, we focus on the spectral evolution of an eruptive polar crown prominence (the prominence located at high latitude) on 2015 April 28th, which erupts successfully with a CME. The high-quality IRIS observations reveal some phenomena that have not been reported, and we try to give reasonable explanations on them. This event was studied by Reference [12] using extreme ultraviolet (EUV) images, who were interested in the outflows within the dimming region and proposed that the outflows are the origin of CME-induced solar wind. Dai et al. (submitted) used EUV images to explore the eruption mechanism of this event, and thought that the eruption is related to the prominence oscillation and mass drainage. Our paper is organized as follows: **Section 2** introduces the observations and data reduction; **Section 3** shows the prominence eruption process and **its** spectral features; we give our explanations on some observed phenomena in **Section 4**, which is followed by conclusion in **Section 5**.

2 OBSERVATIONS AND DATA REDUCTION

An eruption of a polar crown prominence on 2015 April 28th was well observed by the IRIS. **Figure 1A-E** show the snapshots of the eruptive prominence in EUV images from the Atmospheric Imaging Assembly (AIA [13]), onboard the Solar Dynamics Observatory (SDO [14]). The observational channels and times are denoted in each panel. The IRIS observations were carried out between 10:59–14:54 UT with 24 large coarse raster scans, and each scan had 64 × 2″ raster steps. The binned pixel size along the raster slit is 0.33″, the same as the slit width. The resulting FOV is 126″ × 119″ centered at – 742″ east and 666″ north (see the blue rectangle in **Figure 1B**). In the snapshot of **a** slit-jaw image (SJI) **at** 2796 Å in **Figure 2A**, the dashed white lines mark the slit position No.30 (left), upper boundary of the FOV of the Mg II raster

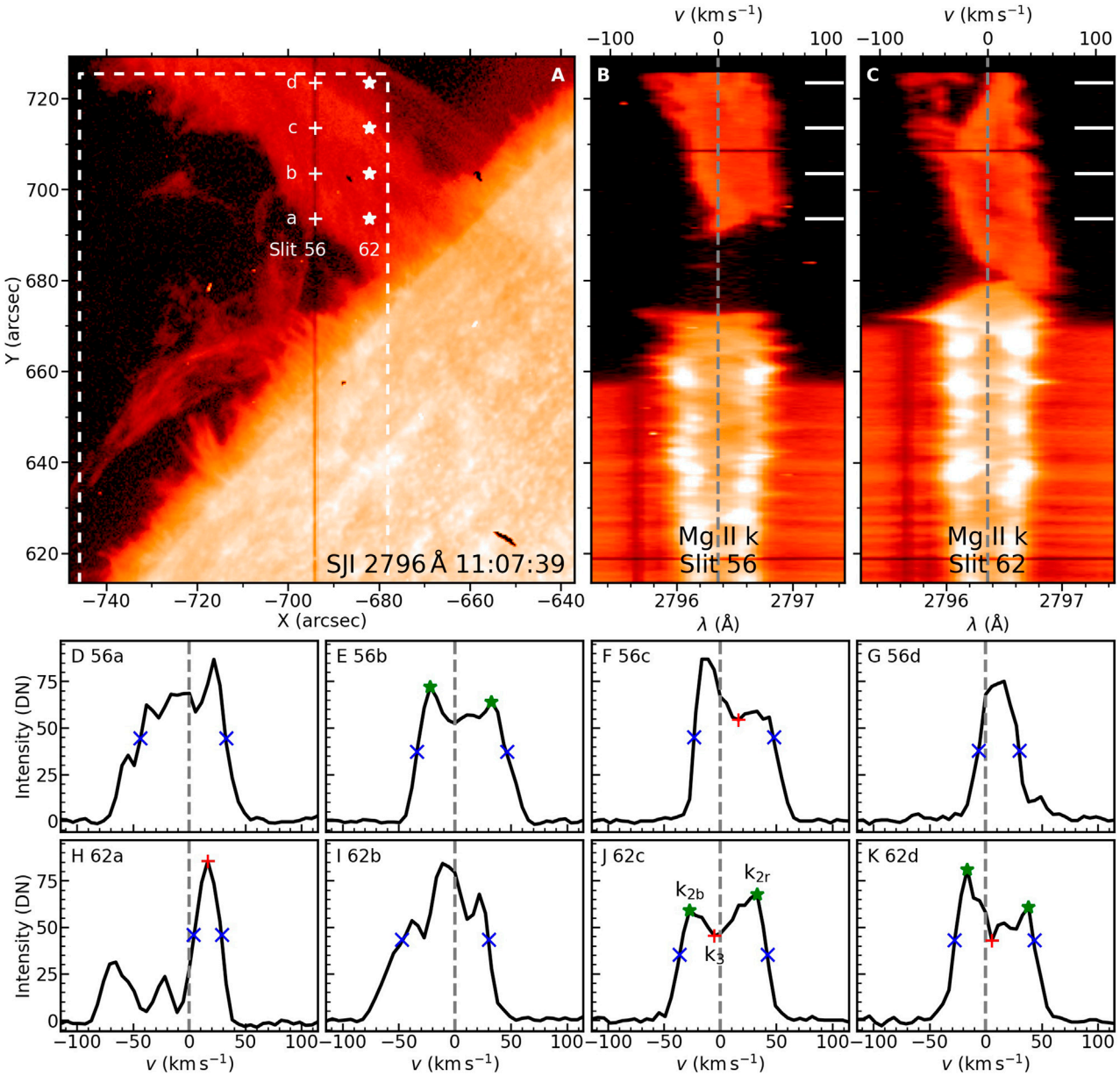

FIGURE 2 | Estimation of LOS velocities from Mg II k line profiles. **(A)** SJI 2796 Å. The dashed white lines mark the slit position No.30 **(left)**, upper boundary of the FOV of Mg II raster **(top)**, and the slit position No.64 **(right)**. Eight points marked by plus or star symbols are chosen for analysis in panels **(D–K)**. **(B–C)** Images of the Mg II k spectra along the **slit** positions No.56 (at 11:07:39 UT) and 62 (at 11:08:44 UT), respectively. The short white lines mark the positions of the spectra in panels **(D–K)**. The vertical dashed lines represent the rest wavelength of the Mg II k line. **(D–K)** Mg II k profiles at the positions marked in panels **(A–C)**. The red pluses represent the positions of k_3, the green stars represent k_2, and the blue × symbols represent the positions of half maximum.

(top), and the slit position No.64 (right). The exposure time of each raster is 8 s and the step cadence is 9.2 s. The spectral resolution is ~ 5.5 km s^{-1} with binned pixels. The slit occurs at the center of SJIs in Solar-X direction. The FOV of each SJI is 117″ × 119″, and FOV of SJI observations is marked in **Figure 1B** with the white rectangle. The SJIs at 2796, 1400, and 1330 Å are available, which have a cadence of ~ 37 s and the binned pixel size is 0.333 arcsec in each channel. We mainly use SJIs 2796 Å and 1400 Å, the former has a passband of 4 Å centered at 2796 Å, mainly contributed by the Mg II k line; the latter has a passband of 55 Å centered at 1390 Å, mainly contributed by Si IV lines but also including O IV lines, etc.

IRIS level 2 data are used, for which dark current and offsets are removed, flat field is corrected, and geometric and wavelength calibrations (for spectrograph channels) are done. The FOV of SJIs is checked by comparing them with the AIA 304 Å images. The spatial position of spectra is shifted along Solar-Y slightly "using the fiducial marks on the slit" as suggested by the referee.

(see **Figure 2B** at 618″ and 708″, respectively). The wavelength calibrations are checked using lines Ni I 2799.474 Å in the Mg II window and Fe II 1392.82 Å in the Si IV window radiated from the solar disk; the wavelength errors are expected to be within 2 km s^{-1}. For images of the Si IV 1394 Å line spectra, bright and isolated pixels are identified as spikes, and their values are replaced by their surrounding mean values. Errors of spectral intensities from signal uncertainty and readout noise are considered. The former is set to be square root of photon number, and the conversion coefficient from digital number (DN) to photons is 18 for near ultraviolet (NUV, including the Mg II k line), and 4 for far ultraviolet (FUV, including the Si IV 1394 Å line). The readout noise is related to dark current uncertainty, which is set to be 1.8 DN for NUV (from the negative values in data) and 3.3 DN for FUV [5].

EUV images from the SDO/AIA and LOS magnetograms from the SDO/HMI (Helioseismic and Magnetic Imager [15]), are used. The former has pixel size of 0.6″ and temporal resolution of 12 s; the latter has pixel size of 0.5″. Both AIA and HMI images are processed to level 1.5.

2.1 Estimation of Prominence LOS Velocity

It is almost impossible to describe LOS (Doppler) velocities of a prominence strictly, due to that a prominence consists of many threads with different velocities [6, 8]. For optically thin lines, such as Si IV 1394 Å, double Gaussian fitting could give two averaged LOS velocities. For optically thick lines, such as Mg II k/h and H I Lyman series, the profiles are often centrally reversed due to self-absorption, and effects of non-LTE (departure from the local thermodynamic equilibrium) should be considered [16–19]. Despite these difficulties, we could still obtain some information of LOS velocities from the optically thick lines Reference [20]. proposed that for reversed profiles of Mg II k/h lines, the Doppler shift of the central minimum (or the maximum for a purely emission profile, called k_3 for the k line, see **Figure 2J**) correlates strongly with the LOS velocity at the $\tau = 1$ height of the line core (τ represents the optical thickness), and the average Doppler shift of the peaks (called k_{2b} and k_{2r} for the blue and red sides of the peaks, respectively) correlates with the LOS velocity at the average $\tau = 1$ height of the peaks (deeper than the formation height of the line core). LOS velocity also affects the asymmetry of the peaks [18]. However, it is often difficult to identify the positions of k_{2b}, k_{2r}, and k_3 for complex profiles.

The center of gravity (COG) method can be used to derive the Doppler shifts of purely absorption (photospheric lines [21]) or purely emission lines. When there are multi-velocity components in a spectral profile, the COG method gives a weighted average result. However, the COG method is physically wrong for the emission profiles with central reversals, although this method is sometimes still useful in such case [11]. The COG method is expressed as

$$v_D = \frac{\sum_i (I(v_i) - C)v_i}{\sum_i (I(v_i) - C)}, \quad (1)$$

TABLE 1 | Estimation of LOS velocities of the eight profiles shown in **Figure 2D–K** using different methods: shift of k_3, average shift of k_{2b} and k_{2r}, average shift at half maximum, and COG. The velocities are in the unit of "km s^{-1}".

Method	56a	56b	56c	56d	62a	62b	62c	62d
k_3	-	-	16	-	16	-	–5	6
k_3	-	6	-	-	-	-	3	11
Half maximum	–6	6	12	11	16	–9	3	8
COG	–7.1	6.9	11.3	13.4	–11.6	–10.8	3.6	6.1

NOTE–The given accuracies of the calculated velocities using the shift of k_3, average shift of k_2, and average shift at half maximum are 1 km s^{-1} due to that the spectral resolution is ≈5.5 km s^{-1}, and the accuracies using the COG method are 0.1 km s^{-1} because around 40 pixels are considered.

where v_D is Doppler velocity, I is intensity, C is continuum, and wavelength λ is converted into velocity (v) in the unit of "km s^{-1}" using

$$v_i = \frac{\lambda_i - \lambda_0}{\lambda_0} c, \quad (2)$$

in which λ_0 is the rest wavelength and c is the light speed.

To check the reliability of the COG method, we compare it with the methods proposed by Ref. [20]. **Figure 2A** is a slit-jaw 2796 Å image during the first scan, and **Figures 2B,C** show the images of the Mg II k line spectra along slit positions No.56 (at 11:07:39 UT) and No.62 (at 11:08:44 UT), respectively. Four points along the slit position No.56 and four along the No.62 are chosen (denoted with "a", "b", "c", "d" for different heights in panel (A)), and their Mg II k line profiles are plotted in **Figures 2D-K** sequentially. Positions of k_3 (marked with the red plus symbols) and k_2 (marked with the green stars) are identified when there is no much confusion. We also calculate the average shift at half maximum for each profile (marked with the blue × symbols). The results are listed in **Table 1**. From the images of the spectra in **Figure 2B-C**, it is intuitive that the top part along the slit position No.56 is slightly blue-shifted and the lower part of the prominence is red-shifted; along the slit position No.62, the top part has multi-velocity components and the lower part is also red-shifted. Among the eight line profiles in **Figure 2D-K**, the positions of k_3 are only identified in four profiles, and three of them are even questionable (56c, 62c, and 62d). So the LOS velocities derived from k_3 are also questionable. The positions of k_{2b} and k_{2r} are determined in three profiles relatively precisely. The average shift at half maximum is calculated for each profile, and the results are consistent with what we see in the image of the spectra. However, this method may not include weak components as in case of the profiles from Positions 56a and 62a (**Figures 2D,H**). The LOS velocities derived from the COG method have the same signs as those derived from the average shifts of peaks or at half maximum except the 62a profile due to the aforementioned reason. The results of the COG method are also consistent with the images of the spectra, which means that this method is not influenced by occurrence of central reversals for the chosen profiles.

We will see that some Mg II k line profiles are reversed deeply during the prominence eruption. In most cases, the signs of LOS

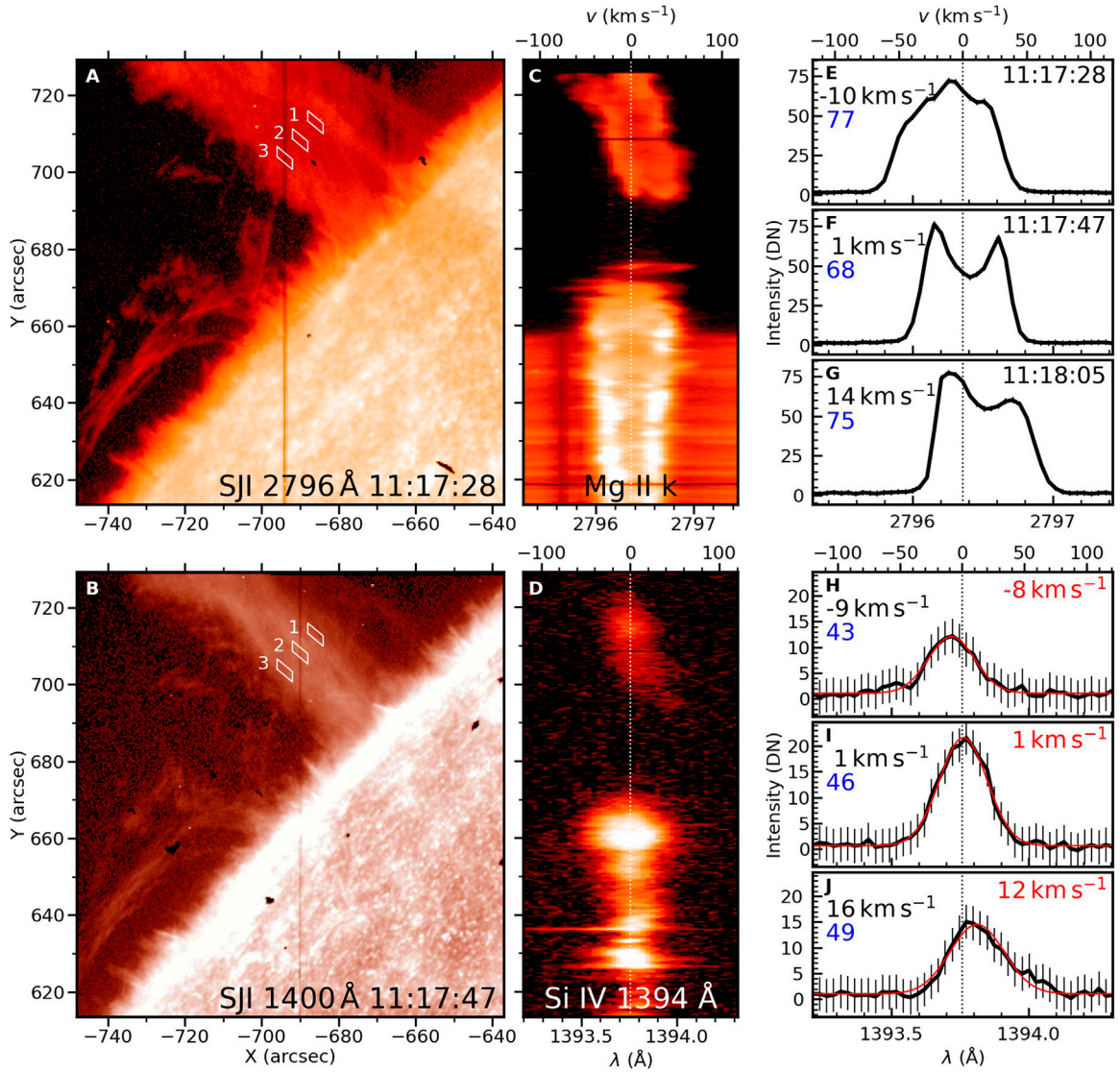

FIGURE 3 | Spectral observations around 11:17 UT. First column: IRIS SJIs. Second column: images of the spectra at the slit position as shown in panel **(A)**. Third column: average spectral profiles from boxes 1-3tbox1-3 in panels **(A–B)**, sequentially. The first row is for **Mg II** observations and the second row is for the Si iv window. The vertical dotted lines in **(C–J)** mark the positions of rest wavelengths. In panels **(E–J)**, Doppler velocities derived from the COG method (black fonts) and FWHMs in the units of "km s^{-1}" (blue fonts) are noted in left. In panels **(H–J)**, the Doppler velocities derived from Gaussian fitting (red curves) are marked in right (red fonts).

velocities derived from the COG method are generally consistent with the images of the spectra. We will give quantitative results using Gaussian fitting or directly from the images of the spectra, and use the COG method to derive LOS velocities statistically (not physically for profiles with self-absorption) and qualitatively.

3 RESULTS

3.1 Eruption Overview

The long filament, when the prominence is seen against the solar disk, extends from nearly solar disk center to beyond the northeastern solar limb on 2015 April 28th. **Figure 1A–E** show its EUV images, including the eruption process in AIA 304 Å. When seen in AIA 171 and 193 Å (**Figure 1D–E**), the prominence is thinner than that seen in AIA 304 Å (**Figure 1A**) due to lower opacities. A part of the prominence is blocked by itself before the prominence eruption (**Figure 1A**), and LOS is mainly along the prominence axis for IRIS observations. In **Figure 1B**, the prominence is erupting; a dark region along the filament spine and two bright ribbons on the solar disk can be seen. In **Figure 1C**, the prominence erupts further, and its spine inclines toward the solar equator. We synthesize a time-distance diagram in AIA 304 Å along the slice AB in **Figure 1A**, and the result is shown in **Figure 1F**. We fit the prominence height in **Figure 1F** with a slow-rise phase (linear function) and a fast-rise phase (exponential function) using the approximation [22, 23].

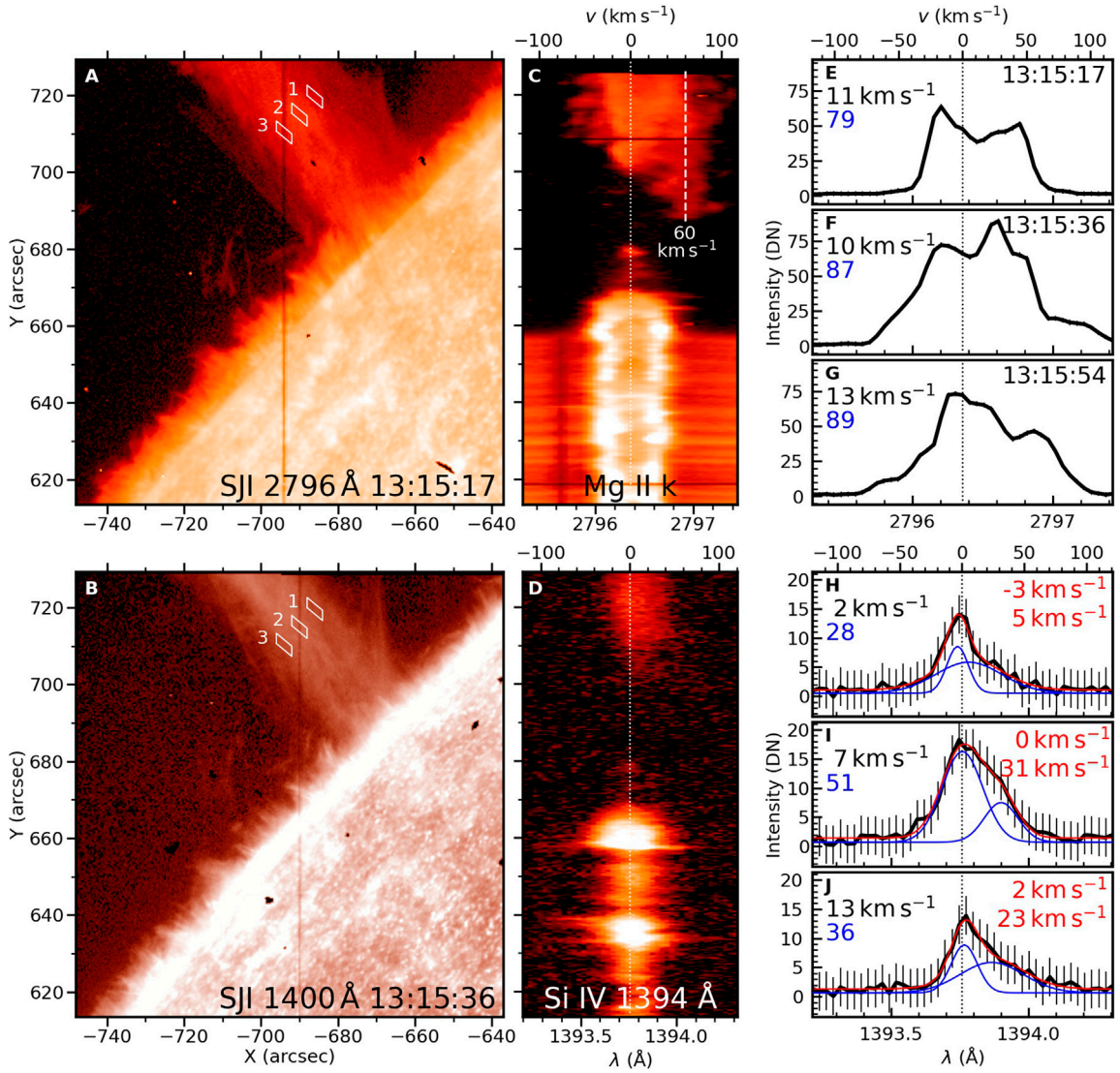

FIGURE 4 | Spectral observations around 13:15 UT. The layout is similar to **Figure 3** but double Gaussian fitting is used for Si IV 1394 Å line profiles in panels **(H–J)**, where blue curves show separate Gaussian components.

$$h(t) = c_0 e^{(t-t_0)/\tau} + c_1 (t - t_0) + c_2, \tag{3}$$

where h represents height, t is time, t_0 is arbitrary, and τ, c_0, c_1, c_2 are parameters obtained by fitting. The obtained initial rise speed is $c_1 = 3.78\ \mathrm{km\ s^{-1}}$, and the erupting speed at the end of our tracking is ~ 103 km s^{-1}. Onset of the fast-rise phase is defined by

$$t_{\mathrm{onset}} = \tau \ln\left(\frac{c_1 \tau}{c_0}\right) + t_0, \tag{4}$$

which is calculated to be 13:25:30 UT (the cyan vertical line in **Figure 1F**).

3.2 Spectral Evolution

We have seen in **Figure 2** around 11:07 UT that the top part of the raster is slightly blue-shifted and the lower part of the prominence is red-shifted. In this section, we will introduce the spectral evolution, especially the variations of LOS velocities of the erupting prominence in detail. **Figure 3** shows IRIS observations around 11:17 UT (the second raster scan), including SJI snapshots (**Figure 3** left column), images of the spectra along the dark slit in **Figure 3A** (middle), and spectral profiles (right) of the Mg II k line (upper part) and the Si IV line (lower part), respectively. Comparing the prominence images in the two wavelengths, SJI 1400 Å has a narrower bright core with faint prominence edges (**Figure 3B**) than SJI 2796 Å (**Figure 3A**), and the Si IV 1394 Å line profiles (**Figure 3H–J**) are weaker with lower signal-to-noise ratios (S/N) than the Mg II k line (**Figure 3E–G**). Mg II k line **profiles** are sometimes reversed (**Figure 3F–G**), while Si IV 1394 Å line profiles can be fitted using a Gaussian profile (red curves in **Figure 3H–J**). Besides, the Mg II k line has a larger line width than the Si IV 1394 Å, despite that the latter is formed at a higher temperature. These performances are

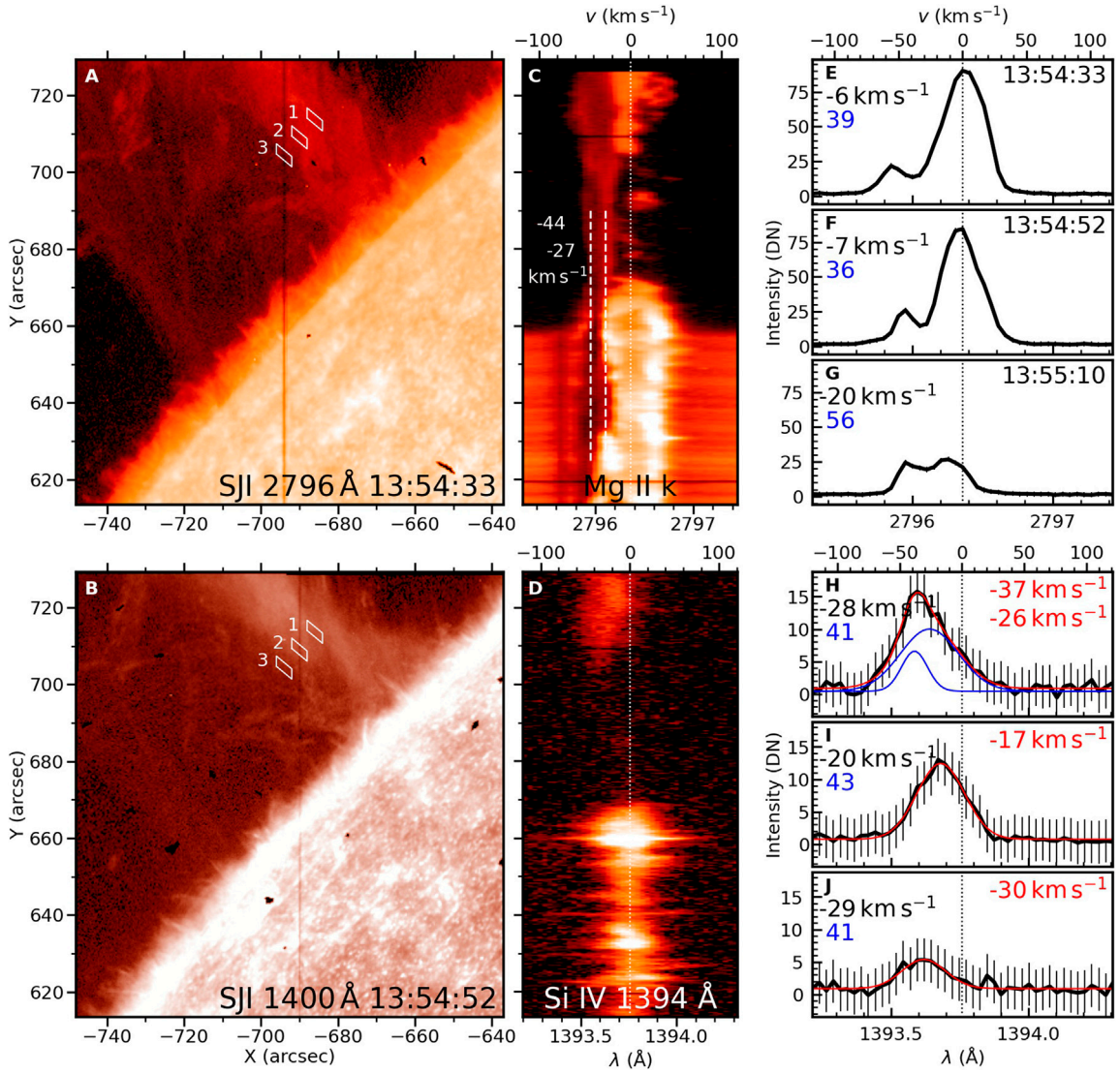

FIGURE 5 | Spectral observations around 13:54 UT, similar to **Figures 3**, **4**.

mainly due to that the Mg II k line has a larger opacity than the Si IV 1394 Å.

In both of the images of the Mg II k and Si IV 1394 Å spectra in **Figure 3C, D**, the blue-shifted top part and red-shifted lower part are visible. We choose three regions in **Figure 3A, B** from right to left with respect to the prominence axis, and their average spectral profiles are plotted in **Figure 3E–J**. In these panels, the Doppler velocities derived from the COG method (black fonts) and the full widths at half maximum (FWHMs, blue fonts, in the unit of "km s^{-1}") are denoted at the left. In **Figure 3H–J** for the Si IV 1394 Å line profiles, the Doppler velocities from Gaussian fitting are denoted at the right (red fonts). Both Mg II k and Si IV 1394 Å lines show that the right part of the prominence is blue-shifted, with the Doppler velocity of −8.4 ± 0.7 km s^{-1} (**Figure 3H** using single Gaussian fitting); the left part is red-shifted, with the Doppler velocity of 11.7 ± 0.8 km s^{-1} (**Figure 3J**).

The prominence spectra vary obviously when the prominence approaches eruption. The layout of **Figure 4** is similar to **Figure 3** but observed at ~13:15 UT, about 10 min before the onset of the fast-rise phase. In **Figures 4C,** a red-shifted (around 60 km s^{-1}) faint component appears, which can be seen in SJI at the prominence edges (**Figure 4A, B**). The Mg II k line profiles in **Figure 4E–G** are red-asymmetry with multi-velocity components, and another red Gaussian profile is necessary to fit the Si IV 1394 Å line profiles in **Figure 4H–J**. With more velocity components, the line widths get wider, and FWHM of the Mg II k line is nearly 90 km s^{-1} (**Figure 4F, G**), and that of the Si IV 1394 Å line is around 50 km s^{-1} (**Figure 4I**). However, the Mg II k line of the faint component has a narrower width around 30 km s^{-1} (**Figure 4C**).

During the fast-rise phase in **Figure 5**, the faint components changes to be blue-shifted, with two main Doppler velocities

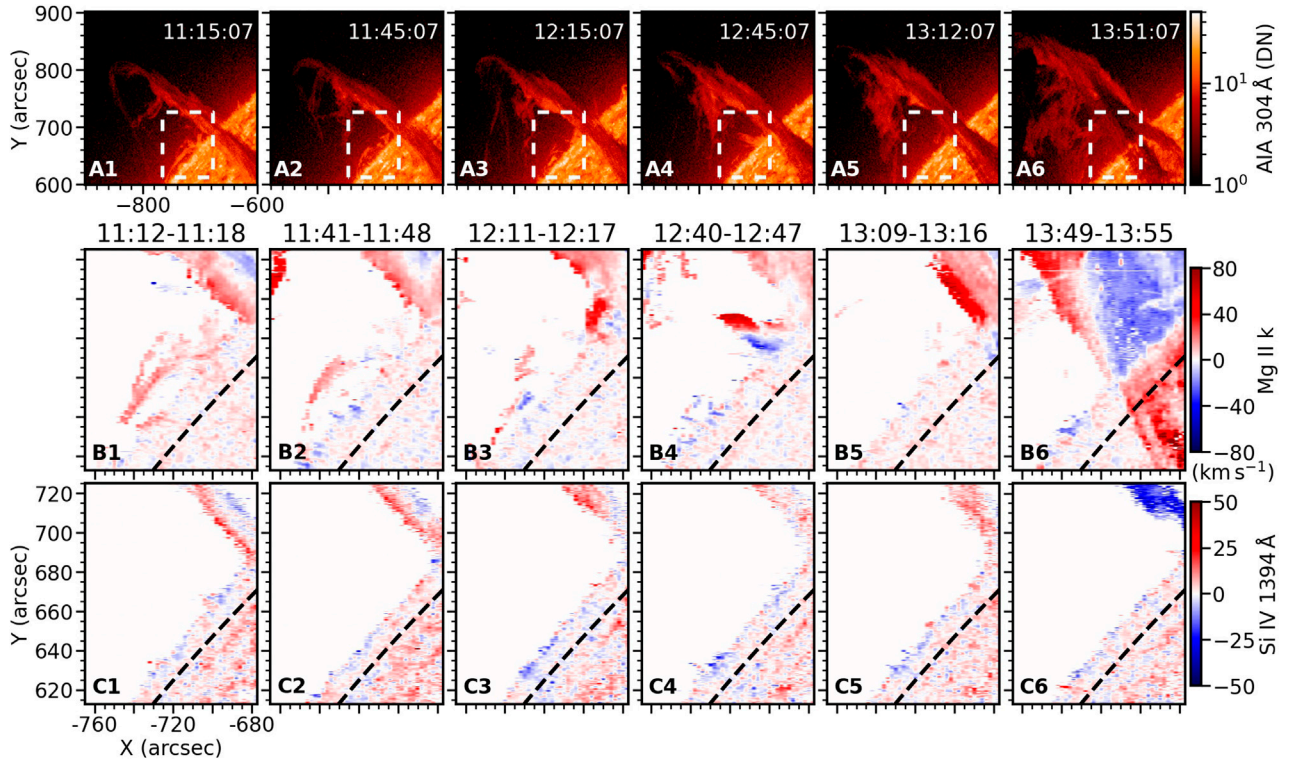

FIGURE 6 | Doppler images derived from the spectra of Mg II k (first row) and Si IV 1394 Å (second row) using the COG method. First row: the AIA 304 Å images. Second and third rows: Doppler images from the Mg II k and the Si IV 1394 Å lines, respectively. Each Doppler image is composed of 44 raster steps from the slit position No.21 **(left)** to the slit position No.64 **(right)**, and the observation times of the two slits are denoted above. The dashed black lines represent the solar limb. Color bars are shown at the right for each row.

shown in the image of the Mg II k line spectra (**Figure 5C**): -44 and −27 km s^{-1}. In the image of Si IV 1394 Å spectra in **Figure 5D**, the bright component is also obviously blue-shifted, and the Gaussian fitting results show that the Doppler velocity is at least −17 km s^{-1} (**Figure 5I**). However, the bright component in Mg II k has no obvious shift (**Figure 5C**), and the line widths are small (**Figure 5E, F**). We will see in next section that it is due to the absorption by the faint component. The emission of the box 3 in the SJI 2796 Å (**Figure 5A**) is mainly from the faint component, which is identified from the weak emission of the Mg II k line with blue shifts (**Figure 5G**). The weak emission of the Si IV 1394 Å line from the box 3 (**Figure 5J**) with the similar blue shift suggests that the Si IV line has a contribution to the brightness of the faint component in SJI 1400 Å.

To analyze the evolution of the prominence LOS velocities in detail, we calculate Doppler images from both the Mg II k and Si IV 1394 Å lines using the COG method. After the calculations, isolated noises in the Doppler images are further removed.

The obtained Doppler images are shown in **Figure 6**, where the first row shows AIA 304 Å images and the dashed boxes mark the FOV of the Doppler images in the lower two rows. Initially (the first column in **Figure 6**), the left part of the prominence is red-shifted and the right part is mainly blue-shifted with a boundary near the prominence axis; the maximum red-shifted velocity is ~ 30 km s^{-1}, and the maximum blue-shifted velocity is ~ 20 km s^{-1} from both Mg II k and Si IV 1394 Å Doppler images (the difference is < 2 km s^{-1}). Then, red shifts dominate the prominence gradually, and the largest Doppler shifts always occur at the left edge. At around 13:15 (**Figure 6**B5), there is a largely red-shifted region corresponding with the faint component as shown in **Figure 4A, B**. About 25 min after the onset of the fast-rise phase (the rightmost column in **Figure 6**), the erupting prominence is mainly blue-shifted, and the average and maximum LOS velocities in Si IV 1394 Å window are 22 and 47 km s^{-1}, respectively. The blue-shifted velocities in Mg II k window are smaller, and red shifts can still be seen at the left edge. Note that in the Mg II k Doppler image in **Figure 6**B6, the positive values along the filament on the solar disk result from the fact that part of the blue wing of the Mg II k line, which is radiated from the solar disc, is absorbed by the erupting filament (see **Figure 5C**).

3.3 Faint Component

A detailed view on the evolution of the faint component is shown in **Figure 7**, where the AIA 304 Å images at different times are shown in the first row, the slit-jaw 2796 Å images are shown in the second row, the third row shows images of the Mg II k line spectra along the slit positions in **Figure 7B**, and the remaining two rows show Mg II k profiles at the positions marked in **Figure 7C**. Panels C-E share the same abscissa but in different units. At 12:55:39 UT (the first column in **Figure 7**), the regions

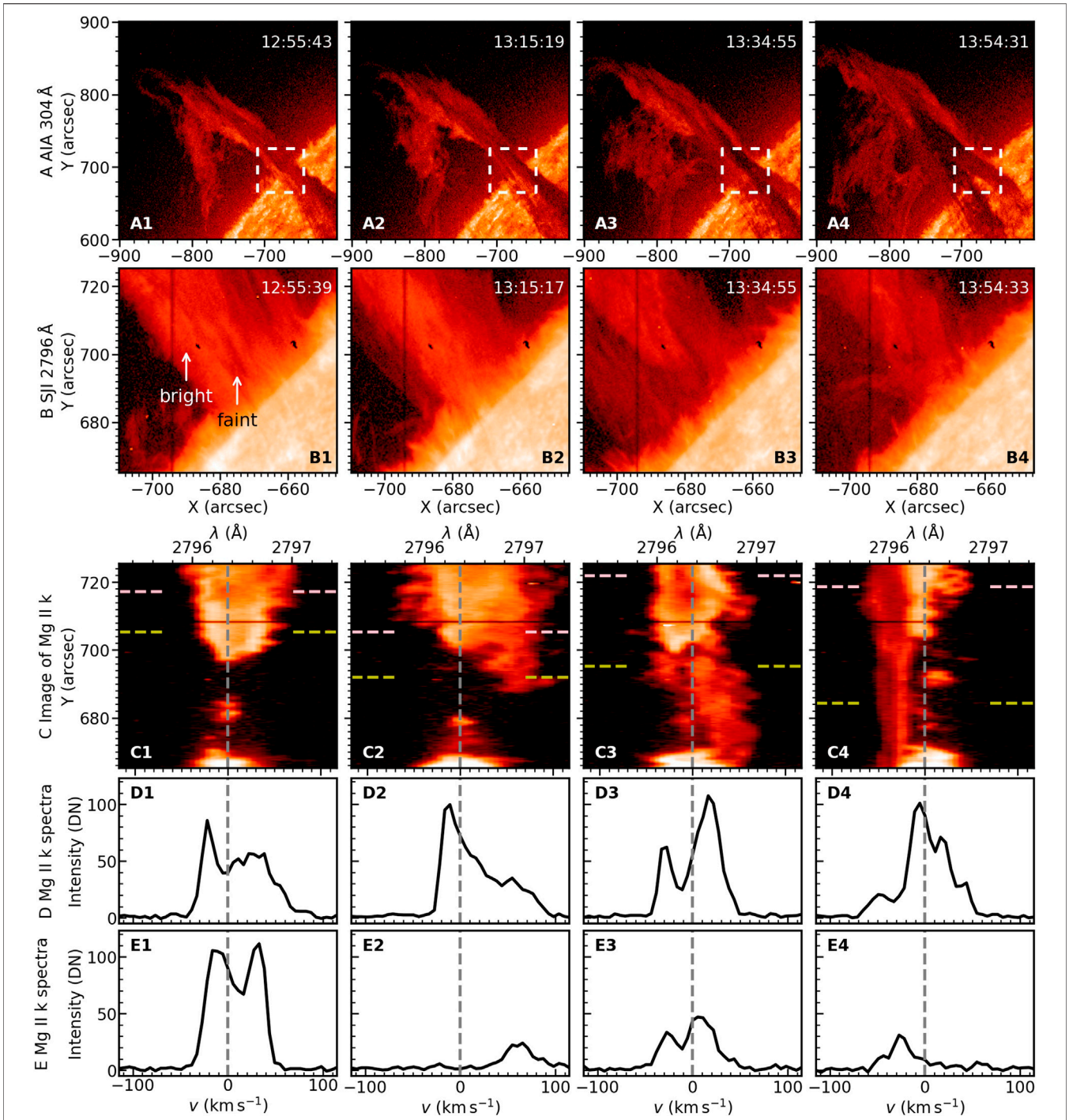

FIGURE 7 | AIA 304 Å and Mg II k observations focusing on faint components. **(A)** The AIA 304 Å images. The dashed boxes represent the FOV of the snapshots in panels **(B)**. **(B)** The slit-jaw 2796 Å images. **(C)** Images of the Mg II k spectra at the slit positions as shown in images in panels **(B)**. **(D)** Mg II k profiles from the positions marked with dashed pink lines in panels **(C)**. **(E)** Mg II k profiles from the positions marked with dashed yellow lines in panels **(C)**.

with or without the faint components can be differed in both AIA 304 Å and SJI 2796 Å. In **Figure 7**C1, the lower part of prominence spectrum is not blended by the faint component, which is reversed with two clear peaks (**Figure 7**(e1)); but the upper part is overlaid with the faint component and the peak at the red wing is absorbed with some weak peaks (**Figure 7**(d1)). Twenty min later (the second column in **Figure 7**, the same time as **Figure 4**), the faint component is significantly red-shifted. From **Figure 7**C2, we can see that the largest Doppler velocity of red-shifted component is beyond 100 km s^{-1}. The Mg II k line in

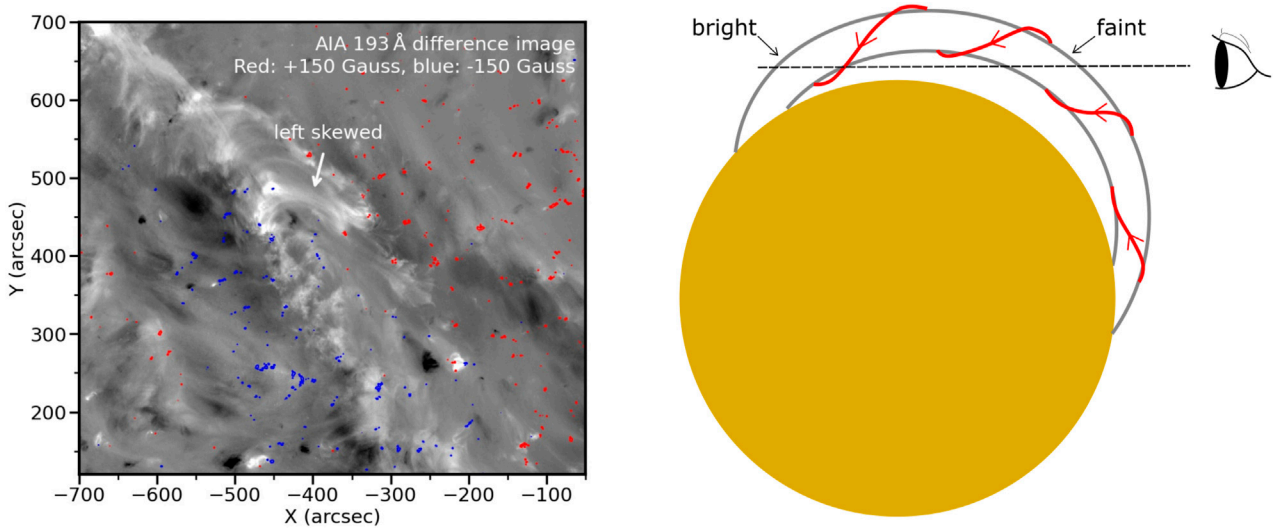

FIGURE 8 | Prominence chirality and view. **(A)** AIA 193 Å difference image by the image observed at 16:00:06 UT subtracting the one at 11:57:06 UT. The red and blue contours mark LOS magnetic field ±150 Gauss, respectively, from HMI observed at 15:59:05 UT. **(B)** Cartoon showing the prominence viewing angle. The red arrows represent the magnetic helicity with exaggerated twist number.

Figure 7D2 includes information of both bright and faint components; it also peaks at blue wing and the red wing is absorbed. At 13:34:55 UT, about 10 min after the onset of fast-rise phase (the third column in **Figure 7**), the sign of Doppler shifts of the faint component is changing: the lower part is mainly red-shifted but the upper part is blue-shifted (**Figure 7**C3). The Mg II k line in **Figure 7**D3 is seriously reversed, and the ratio of line peak to central minimum is 4.5. As a comparison, the ratio of the profile in **Figure 7**E1 is 1.7. At 13:54:33 UT (the fourth column in **Figure 7**, the same time as **Figure 5**), the faint component is blue-shifted, and the blue wing of the bright component is absorbed. When focusing on the AIA 304 Å images, we can see the darkening of the faint region during the eruption process. The expansion of the faint prominence spine is visible in both AIA 304 Å and SJI 2796 Å.

4 DISCUSSION

The prominence eruption in the FOV of SDO/AIA can be divided into slow- and fast-rise phases, and the onset of the fast-rise phase is around 13:25 UT. However, The prominence Doppler shifts experience three periods: 1) 2 hours before the fast-rise phase, the left part of prominence, with respect to the prominence axis, is red-shifted and the right part is mainly blue-shifted (first column in **Figure 6**); 2) then, red-shifted area increases, and almost the whole prominence (in IRIS FOV) is red-shifted at 10 min before the fast-rise phase; 3) during the fast-rise phase, the prominence gets to be blue-shifted. A faint component is clearly identified at 12:55:39 UT (first column in **Figure 7**). The faint component in Mg II k window has a narrow line width (~ 30 km s^{-1}, **Figure 4**) and significant variations of Doppler shifts. Besides, the faint component can absorb the radiation from the bright part, which leaves a single profile peak when the faint component has a significant Doppler shift, or results in a deep central reversal when the shift is slight. In Si IV window, the faint component can still be identified in SJI despite the lower S/N; two Gaussian profiles are necessary to fit the Si IV 1394 Å line profiles when the bright component is overlapped with the faint component in LOS. The faint region along the prominence spine in AIA 304 Å images is spatially related to the faint component. The darkening and expansion of the faint region during the prominence eruption are visible. The faint component is also red-shifted before the fast-rise phase, with a larger LOS velocity than the bright component. In the fast-rise phase, the faint component gets to be blue-shifted, too. In the following sections, we will give our explanations on these phenomena.

4.1 Magnetic Configuration and View of the Prominence

A knowledge about the magnetic configuration and viewing angle of the prominence is helpful for understanding its observational features. The left image in **Figure 8** is a AIA 193 Å difference image overlaid with LOS magnetogram contours of ±150 Gauss. The post-eruption loops is left skewed, which suggests that the filament channel has a negative magnetic helicity [24]. Hence, we plot the cartoon of the filament as a flux rope [25] with an exaggerated twist number for a clear view (the right image in **Figure 8**). Due to the fact that the faint component can absorb Mg II k radiation from the bright component, the faint component should be in front, which could also be seen in AIA 304 Å images (**Figure 7A**).

4.2 Causes of Doppler Evolutions

Opposite Doppler shifts observed in a same prominence are generally explained as counter-streaming. In previous observations of counter-streaming, bidirectional flows were seen thread by thread [26], or blue- and red-wing images showed different directional flows [27]. Some of counter-streaming observations could be explained by local motions of plasma, such as small-scale oscillations [28] or magnetic reconnection [29]. In our event, the opposite Doppler shifts are found from the beginning of IRIS observations, and are possibly a property of the polar crown prominence that we studied. A major difference from previous observations is that the opposite Doppler shifts are distributed much regularly, i.e., the left half is red-shifted and the right part is mainly blue-shifted. This phenomenon reveals large-scale flows along the prominence spine, and cannot be explained by the local plasma motions.

Unidirectional flows along the flux rope could also cause opposite Doppler shifts when the LOS is perpendicular to the flux rope axis [24, 30–32]. Despite that the LOS is mainly along the prominence spine in the FOV of the IRIS in our case, we assume that the opposite Doppler shifts are caused by the flows within the spine. In this case, in the cartoon of **Figure 8**, the flows of the part marked with "bright" should move toward the observer, or the flows marked with "faint" should move away from the observer, or both, to cause the left being red-shifted and the right being blue-shifted with respect to the prominence axis. In the following period, the spine is dominantly red-shifted, but the blue shifts are not enhanced. The different evolutions of the red and blue shifts makes this assumption questionable.

During the fast-rise phase in the third column in **Figure 7**, the faint component shows opposite Doppler shift along the slit, which is possibly caused by untwisting motion of the erupting prominence [10], which could be seen in AIA 304 Å images by tracking the faint region (**Figure 7**).

When approaching the fast-rise phase, red shifts dominate the prominence, and the faint component has a large LOS velocity. In the Mg II k window, the LOS velocity of the bright component is not clear due to the fact that its emission is absorbed partly by the faint component. But from the Si IV window, the results of the double Gaussian fitting (**Figure 4H–J**) suggest that the Doppler shift of the bright component is not obvious. The red shifts could be explained by the mass drainage during the elevation of the prominence spine, which could accelerate the prominence eruption in return [33]. In our case, if the prominence mass moves toward the prominence footpoint behind the solar disk, the direction of LOS velocity is consistent with the red shifts (see the cartoon in **Figure 8**). The large Doppler velocity of the faint component suggests that the mass near the spine center moves faster than the mass near the footpoint, which is possibly due to more significant elevation of the prominence spine center, and that the large density near the footpoint may slow down the flows.

During the fast-rise phase, the prominence gets to be blue-shifted, which reveals the overall movement of the erupting prominence away from the solar disk and toward the observer.

4.3 Formation of the Faint Component

Reference [10] did also observe a faint and narrow component with a large Doppler velocity up to 460 km s^{-1} in an erupting active region prominence. The authors proposed that the two components with different Doppler velocities suggest that the erupting material is distributed in a hollow cone shape. The faint component in our observations share most of features as reported by Reference [10]; despite that the Doppler velocity is relatively small. In addition, there are some phenomena only seen in our observations. Firstly, we could see the faint component in AIA 304 Å images and SJIs directly, hence we observed darkening and expansion of the faint component during the prominence eruption (**Figure 7A, B**). Besides, we observed that the faint component can absorb the Mg II k radiation from the bright component. On the basis of these phenomena, we suspect that the Mg II k line from the faint component has a lower opacity than that from the bright component, and the faint component is composed of low-density and cold plasma due to the expansion of the prominence spine.

The intensity ratio of Mg II k and h lines is widely used to check the opacity [7, 10, 11, 20]: the ratio is generally in the range of 1–2, and approaches 2 under the optically thin assumption and gets small with the increase of opacity. **Figure 9** shows the images of Mg II k integrated intensity (panels A,B) and k/h ratio (panels C,D) from spectral observations. Continuum intensity is subtracted when calculating the images. The left column in **Figure 9** is observed between 11:13 UT and 13:19 UT before the occurrence of the faint component, and the k/h ratio is relatively homogeneous. A region is selected in **Figure 9C** with yellow box, and the mean k/h ratio is 1.25. The right column in **Figure 9** is observed between 13:11 UT and 13:17 UT, and a faint region is seen at the prominence left edge (**Figure 9B**). The k/h ratio image in **Figure 9D** shows that the faint component has a larger k/h ratio (1.40) than the bright prominence (mainly between 1.2 and 1.3), which suggests that the faint component has a lower opacity. It should be noticed that the k/h ratios vary for different prominences with different viewing angles Reference [11]. reported the k/h value around 1.4 in the main body of an eruptive prominence in quiet region, but in the erupting prominence studied by Reference [10]; the intensity ratio of the primary bright component varies from 1.4 to 1.9.

Prominence Mg II k radiation is partly from the emission of local plasma, and partly from the scattering of the chromospheric radiation [7, 34]. In our observations, the faint component can absorb or scatter the light from the bright part behind. Using non-LTE radiative transfer techniques Reference [20], simulated emergent Mg II k and h lines in solar disk; the authors found that Mg II k core intensity is weak if the line core forms at a high position due to a low density and three-dimensional scattering, although temperature increases along height in the chromosphere. In our observations, the low emission (**Figure 7E2-E4**) and deep central reversal (**Figure 7D3**) of the faint component possibly result from the scattering of low-density plasma. In addition, line width is mainly determined by plasma temperature and micro-turbulence. The narrow Mg II k line profiles suggest that the faint component is mainly prominence core, whose temperature is lower than the PCTR.

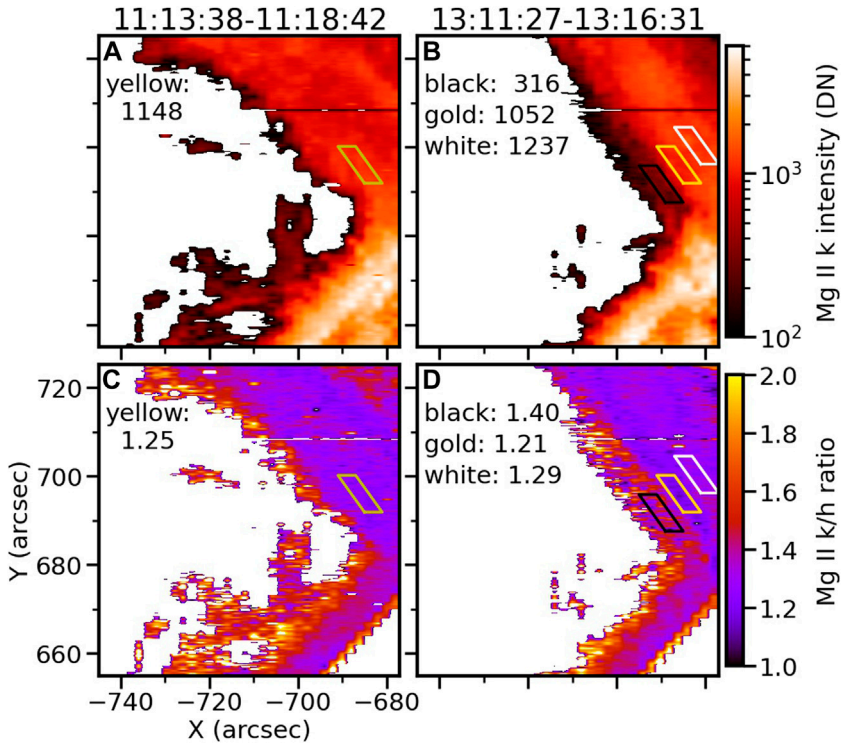

FIGURE 9 | Images of integrated uncalibrated intensity of the Mg II k line **(A–B)** and the Mg II k/h intensity ratio **(C–D)**. Mean values of the marked regions are noted in each panel.

TABLE 2 | Main observational results of this work.

Prominence eruption	(1) Slow-rise phase (2) Fast-rise phase
Evolution of spectra	(1) Opposite Doppler shifts with respect to the prominence axis in slow-rise phase (2) Dominantly red-shifted around the onset of fast-rise phase (3) Dominantly blue-shifted during prominence eruption
Faint component	Faint and narrow features in the Mg II k line Large red shifts (~ 60 km s^{-1}) around the onset of fast-rise phase Darkening and expansion in AIA 304 Å

Therefore, we propose that the faint component consists of low-density and cold plasma, which appear due to the expansion of the prominence core during the prominence eruption. In this process, the flows move fast along the prominence spine and result in significant Doppler shifts. However, non-LTE modeling is necessary to give a strict explanation on the characteristics of the AIA 304 Å and IRIS Mg II k observations.

5 CONCLUSION

We studied spectral evolution of an eruptive polar crown prominence using its IRIS observations in the Mg ii and Si iv lines and AIA EUV images. The main observational results of this work are listed in **Table 2**. The AIA observations suggest that the prominence experiences a slow- and fast-rise phase before **it** leaves the FOV of AIA. Simultaneously, the variation of Doppler shifts of the erupting prominence could be divided into three periods. In the first period, more than 2 h before the onset of the fast-rise phase, opposite Doppler shifts at the two sides of the prominence axis are found with maximum LOS velocity between 20–30 km s^{-1}. In the second period, around the onset of the fast-rise phase, the whole prominence gets to be red-shifted gradually. In the third period, the prominence is dominantly blue-shifted. The possible cause of the opposite Doppler shifts in the first period is large-scale counter-streaming, or unidirectional flows along the prominence spine (as a flux rope). More observations are necessary to determine which mechanism results in the opposite shifts, then reveal the mode of flows within the prominence spine. Besides, the opposite Doppler shifts of the

faint component during the fast-rise phase may result from the untwisting motion of the erupting prominence. The obvious red shifts in the second period may reveal mass drainage along the prominence spine due to the elevation of the prominence, and the mass drainage might accelerate the prominence eruption in return. The blue shifts in the last period is likely to result from the eruption of the prominence toward the observer.

During the second period, a faint component appears in AIA 304 Å, SJI 2796 and 1400 Å. The faint component has a narrow line profile, is initially red-shifted with a typical LOS velocity of 60 km s^{-1}. The Mg II k/h ratio of the faint component (~ 1.40) is larger than that of the bright component (between 1.2 and 1.3), which suggests that the faint component has a lower opacity. We also observed the darkening and expansion of the faint component in AIA 304 Å images. On the basis of these characteristics, we propose that the faint component is composed of low-density and cold plasma due to the expansion of the prominence during eruption.

Hence we can relate the evolution of the spectra and the formation of the faint component to the prominence eruption. The opposite Doppler shifts are properties of the polar crown prominence that we studied. When the prominence approaches eruption, the prominence spine elevates and expands, and the acceleration of the mass drainage causes the obvious red shifts. Simultaneously, a faint region along the prominence spine forms and gets darker due to the decreasing of the plasma density during the spine expansion. Finally, the acceleration of the prominence eruption results in the blue shifts. Despite the consistence of above explanations, however, non-LTE radiative transfer simulations in future are necessary to interpret the observational characteristics of the Mg II k line and AIA 304 Å images.

DATA AVAILABILITY STATEMENT

Publicly available datasets were analyzed in this study. This data can be found here: https://iris.lmsal.com/search.

AUTHOR CONTRIBUTIONS

JX processed the observational data, decided the main content of the paper, plotted figures, and wrote the article. HL selected the topic, joined discussion, and modified the article. YS joined discussion, offered ideas about the explanation on the observed phenomena, and modified the article.

FUNDING

This work is supported by the NSFC grants (11427803, U1731241, U1631242, 11820101002) and by CAS Strategic Pioneer Program on Space Science, grant Nos. XDA15052200, XDA15320103, XDA15320300, and XDA15320301.

ACKNOWLEDGMENTS

The authors thank the reviewers for their suggestions, some findings and ideas in this paper are proposed by them. JX thanks Jean-Claude Vial, Yingna Su, and Ping Zhang for discussion, thanks Ying Li and Hui Tian for a guidance on processing IRIS data. We thank the IRIS, AIA, and HMI teams for providing the data. YS acknowledges the Jiangsu Double Innovation Plan.

REFERENCES

1. Labrosse N, Heinzel P, Vial JC, Kucera T, Parenti S, Gunár S, et al. Physics of Solar Prominences: I—Spectral Diagnostics and Non-LTE Modelling. *Space Sci Rev* (2010) 151:243–332. doi:10.1007/s11214-010-9630-6
2. Parenti S. Solar Prominences: Observations. *Living Rev Solar Phys* (2014) 11:1. doi:10.12942/lrsp-2014-1
3. Vial J-C, and Engvold O. *Solar Prominences* (2015) 415.
4. Chen P-F, Xu A-A, and Ding M-D. Some Interesting Topics Provoked by the Solar Filament Research in the Past Decade. *Res Astron Astrophys* (2020) 20: 166. doi:10.1088/1674-4527/20/10/166
5. De Pontieu B, Title AM, Lemen JR, Kushner GD, Akin DJ, Allard B, et al. The Interface Region Imaging Spectrograph (IRIS). *Sol Phys* (2014) 289:2733–79. doi:10.1007/s11207-014-0485-y
6. Schmieder B, Tian H, Kucera T, López Ariste A, Mein N, Mein P, et al. Open Questions on Prominences from Coordinated Observations by IRIS, Hinode, SDO/AIA, THEMIS, and the Meudon/MSDP. *A&A* (2014) 569:A85. doi:10.1051/0004-6361/201423922
7. Vial J-C, Pelouze G, Heinzel P, Kleint L, and Anzer U. Observed IRIS Profiles of the H and K Doublet of Mg Ii and Comparison with Profiles from Quiescent Prominence NLTE Models. *Sol Phys* (2016) 291:67–87. doi:10.1007/s11207-015-0820-y
8. Okamoto TJ, Liu W, and Tsuneta S. Helical Motions of Fine-structure Prominence Threads Observed by Hinode and IRIS. *ApJ* (2016) 831:126. doi:10.3847/0004–637X/831/2/126
9. Ruan G, Schmieder B, Mein P, Mein N, Labrosse N, Gunár S, et al. On the Dynamic Nature of a Quiescent Prominence Observed by IRIS and MSDP Spectrographs. *ApJ* (2018) 865:123. doi:10.3847/1538-4357/aada08
10. Liu W, De Pontieu B, Vial J-C, Title AM, Carlsson M, Uitenbroek H, et al. First High-Resolution Spectroscopic Observations of an Erupting Prominence within a Coronal Mass Ejection by the Interface Region Imaging Spectrograph (IRIS). *ApJ* (2015) 803:85. doi:10.1088/0004-637X/803/2/85
11. Zhang P, Buchlin É, and Vial JC. Launch of a CME-Associated Eruptive Prominence as Observed with IRIS and Ancillary Instruments. *A&A* (2019) 624:A72. doi:10.1051/0004-6361/201834259
12. Lörinčík J, Dudík J, Aulanier G, Schmieder B, and Golub L. Imaging Evidence for Solar Wind Outflows Originating from a Coronal Mass Ejection Footpoint. *ApJ* (2021) 906:62. doi:10.3847/1538-4357/abc8f6
13. Lemen JR, Title AM, Akin DJ, Boerner PF, Chou C, Drake JF, et al. The Atmospheric Imaging Assembly (AIA) on the Solar Dynamics Observatory (SDO). *Sol. Phys.* (2012) 275:17–40. doi:10.1007/s11207-011-9776-8
14. Pesnell WD, Thompson BJ, and Chamberlin PC. The Solar Dynamics Observatory (SDO). *Sol Phys* (2012) 275:3–15. doi:10.1007/s11207-011-9841-3
15. Scherrer PH, Schou J, Bush RI, Kosovichev AG, Bogart RS, Hoeksema JT, et al. The Helioseismic and Magnetic Imager (HMI) Investigation for the Solar Dynamics Observatory (SDO). *Sol Phys* (2012) 275:207–27. doi:10.1007/s11207-011-9834-2
16. Schwartz P, Heinzel P, Schmieder B, and Anzer U. Study of an Extended EUV Filament Using SoHO/SUMER Observations of the Hydrogen Lyman Lines. *A&A* (2006) 459:651–61. doi:10.1051/0004-6361:20065619

17. Schwartz P, Gunár S, and Curdt W. Non-LTE Modelling of Prominence fine Structures Using Hydrogen Lyman-line Profiles. *A&A* (2015) 577:A92. doi:10.1051/0004-6361/201425138
18. Gunár S, Heinzel P, Anzer U, and Schmieder B. On Lyman-line Asymmetries in Quiescent Prominences. *A&A* (2008) 490:307–13. doi:10.1051/0004-6361:200810127
19. Gunár S, Schwartz P, Schmieder B, Heinzel P, and Anzer U. Statistical Comparison of the Observed and Synthetic Hydrogen Lyman Line Profiles in Solar Prominences. *A&A* (2010) 514:A43. doi:10.1051/0004-6361/200913411
20. Leenaarts J, Pereira TMD, Carlsson M, Uitenbroek H, and De Pontieu B. The Formation of IRIS Diagnostics. II. The Formation of the Mg II H&k Lines in the Solar Atmosphere. *ApJ* (2013) 772:90. doi:10.1088/0004-637X/772/2/90
21. Uitenbroek H. The Accuracy of the Center-of-Gravity Method for Measuring Velocity and Magnetic Field Strength in the Solar Photosphere. *ApJ* (2003) 592:1225–33. doi:10.1086/375736
22. Cheng X, Zhang J, Ding MD, Olmedo O, Sun XD, and Guo Y. Investigating Two Successive Flux Rope Eruptions in a Solar Active Region. *ApJ* (2013) 769:L25. doi:10.1088/2041-8205/769/2/L25
23. Su Y, van Ballegooijen A, McCauley P, Ji H, Reeves KK, and DeLuca EE. Magnetic Structure and Dynamics of the Erupting Solar Polar Crown Prominence on 2012 March 12. *ApJ* (2015) 807:144. doi:10.1088/0004-637X/807/2/144
24. Chen PF, Harra LK, and Fang C. Imaging and Spectroscopic Observations of a Filament Channel and the Implications for the Nature of Counter-streamings. *ApJ* (2014) 784:50. doi:10.1088/0004-637X/784/1/50
25. Ouyang Y, Zhou YH, Chen PF, and Fang C. Chirality and Magnetic Configurations of Solar Filaments. *ApJ* (2017) 835:94. doi:10.3847/1538-4357/835/1/94
26. Zirker JB, Engvold O, and Martin SF. Counter-streaming Gas Flows in Solar Prominences as Evidence for Vertical Magnetic fields. *Nature* (1998) 396:440–1. doi:10.1038/24798
27. Lin Y, Engvold OR, and Wiik JE. Counterstreaming in a Large Polar Crown Filament. *Sol Phys* (2003) 216:109–20. doi:10.1023/A:1026150809598
28. Ahn K, Chae J, Cao W, and Goode PR. Patterns of Flows in an Intermediate Prominence Observed Byhinode. *ApJ* (2010) 721:74–9. doi:10.1088/0004-637X/721/1/74
29. Shen Y, Liu Y, Liu YD, Chen PF, Su J, Xu Z, et al. Fine Magnetic Structure and Origin of Counter-streaming Mass Flows in a Quiescent Solar Prominence. *ApJ* (2015) 814:L17. doi:10.1088/2041-8205/814/1/L17
30. Li LP, Peter H, Chen F, and Zhang J. Conversion from Mutual Helicity to Self-Helicity Observed with IRIS. *A&A* (2014) 570:A93. doi:10.1051/0004-6361/201424377
31. Li LP, and Peter H. Plasma Injection into a Solar Coronal Loop. *A&A* (2019) 626:A98. doi:10.1051/0004-6361/201935165
32. Zou P, Fang C, Chen PF, Yang K, and Cao W. Magnetic Separatrix as the Source Region of the Plasma Supply for an Active-Region Filament. *ApJ* (2017) 836:122. doi:10.3847/1538-4357/836/1/122
33. Fan Y. Simulations of Prominence Eruption Preceded by Large-Amplitude Longitudinal Oscillations and Draining. *ApJ* (2020) 898:34. doi:10.3847/1538-4357/ab9d7f
34. Heinzel P, Vial JC, and Anzer U. On the Formation of Mg Ii H and K Lines in Solar Prominences. *A&A* (2014) 564:A132. doi:10.1051/0004-6361/201322886

Conflict of Interest: The authors declare that the research was conducted in the absence of any commercial or financial relationships that could be construed as a potential conflict of interest.

Publisher's Note: All claims expressed in this article are solely those of the authors and do not necessarily represent those of their affiliated organizations, or those of the publisher, the editors and the reviewers. Any product that may be evaluated in this article, or claim that may be made by its manufacturer, is not guaranteed or endorsed by the publisher.

frontiers in Physics

ORIGINAL RESEARCH
published: 30 September 2021
doi: 10.3389/fphy.2021.736319

Observations of a Quickly Flapping Interplanetary Magnetic Reconnection Exhaust

Jiemin Wang[1,2] *and Yan Zhao*[1,2]*

[1]Institute of Space Physics, Luoyang Normal University, Luoyang, China, [2]Henan Key Laboratory of Electromagnetic Transformation and Detection, Luoyang, China

On the basis of the Petschek reconnection model and the characteristics of reconnection, hundreds of reconnection exhausts were reported in the solar wind. Many multi-spacecraft observations also indicated that interplanetary magnetic reconnection is a quasi–steady-state plasma process and the reconnection X-line can extend hundreds of Earth radii. In this study, we report an interplanetary flapping reconnection exhaust observed by Wind on April 1, 2003 at one AU. The magnetic reconnection event has two adjacent accelerated flows. We compared the plasma and magnetic characteristics of the two accelerated flows and found that the second accelerated flow was due to the back-and-forth movement of the reconnection exhaust. Our observations reveal that not all interplanetary reconnections operate in a quasi–steady-state manner; some reconnection current sheets can move rapidly back and forth.

Keywords: interplanetary magnetic structure, interplanetary current sheet, magnetic reconnection, solar wind, reconnection exhaust

OPEN ACCESS

Edited by:
Hongqiang Song,
Shandong University, China

Reviewed by:
Chenglong Shen,
University of Science and Technology of China, China
Pingbing Zuo,
Harbin Institute of Technology, China

***Correspondence:**
Yan Zhao
zhaoyan201707@163.com

Specialty section:
This article was submitted to Stellar and Solar Physics, a section of the journal Frontiers in Physics

Received: *05 July 2021*
Accepted: *23 August 2021*
Published: *30 September 2021*

Citation:
Wang J and Zhao Y (2021) Observations of a Quickly Flapping Interplanetary Magnetic Reconnection Exhaust. Front. Phys. 9:736319. doi: 10.3389/fphy.2021.736319

KEY POINTS:

1: A magnetic reconnection event with two adjacent accelerated flows was studied.
2: The detection of the second accelerated flow was due to the back-and-forth movement of the reconnection exhaust.
3: The observations indicate some interplanetary reconnections operate in an unsteady manner with reconnection current sheets flapping rapidly.

INTRODUCTION

Magnetic reconnection is a universal plasma process that not only converts magnetic field energy into plasma kinetic and thermal energies but also breaks and reconnects oppositely directed frozen-in field lines from different plasma regions. This process is implicated in various contexts, including space physics, solar physics, and laboratory plasma physics. The authors in reference [1,2] first established the Sweet–Parker model to describe magnetic reconnection using observations from solar flare activity. One of the model's limitations however is that the reconnection rate is much slower than necessary for flare eruption. In 1964, the authors in reference [3] proposed a new reconnection model and pointed out that the magnetic reconnection is a topological process, and the field lines need not reconnect resistively along the entire length of the boundary layer but could merge over a short length. The key feature of the Petschek model is its assumed separation between the small length scale of the non-ideal electric field, which is

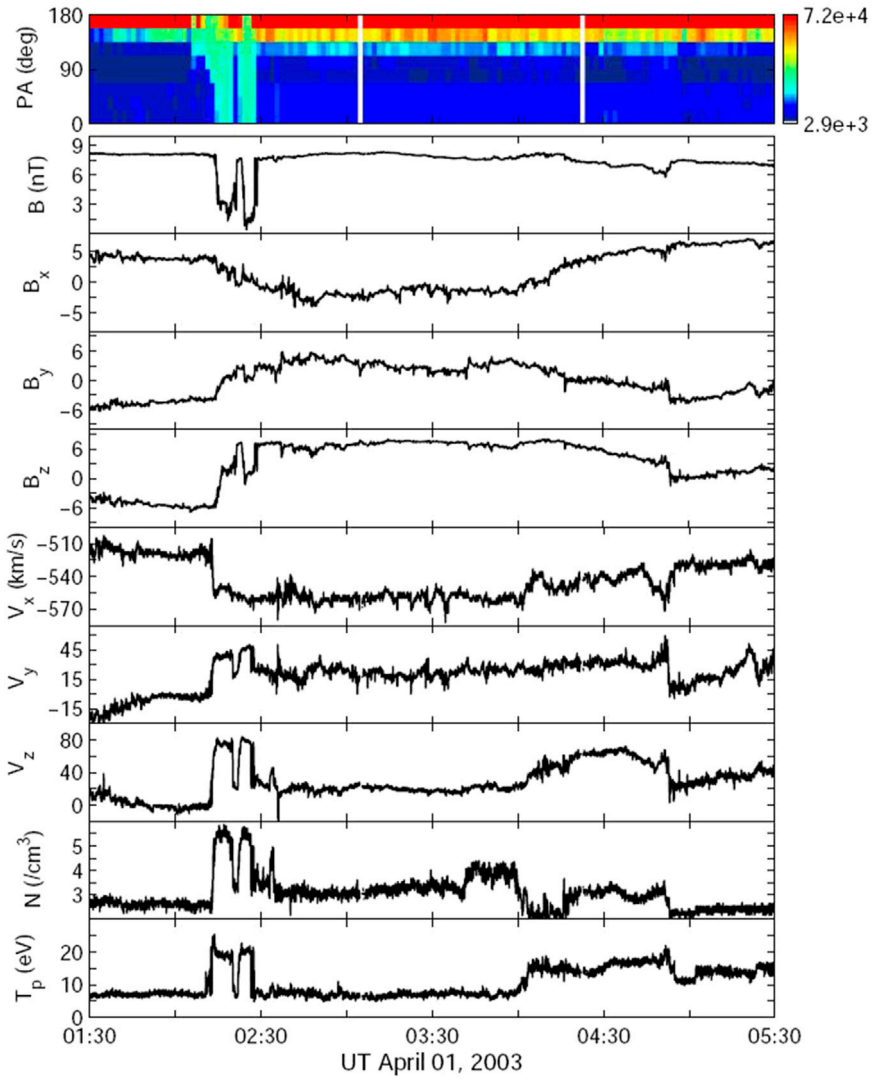

FIGURE 1 | Suprathermal electron pitch angle spectrogram of 165.0 eV, magnetic field, and proton temperature data measured by Wind on April 1, 2003 on the basis of the magnetic reconnection exhaust and the following faster flow.

responsible for breaking magnetic field lines, and the large length scales on which energy is released and dissipated [4]. The Petschek model yields a sufficiently fast reconnection rate by virtue of the localized diffusion region and the extended slow shocks. Reconnection is also characterized by the acceleration of plasma away from the reconnection site in a pair of oppositely directed exhaust regions. The authors in reference [5] proposed a quasi-stationary reconnection exhaust criteria based on the Petschek reconnection model and the characteristic feature of the reconnection process. The requirements to identify reconnection exhausts mainly include 1) a roughly Alfvénic accelerated flow, 2) the enhancements of proton density and temperature, and 3) depression of the magnetic field strength. In accordance with the reconnection exhaust criteria, a large member of observed solar wind reconnection events has been identified and reported (e.g., [5–18]). Multi-spacecraft observations also indicated that the magnetic reconnections in the solar wind are quasi-steady plasma processes, reconnecting current sheets are roughly planar, and the reconnection X-lines can extend hundreds of Earth radii [6,12,19–21]. Although most reconnection observations revealed that exhausts have quasi-steady, roughly planar structures, several reported exhausts were re-entered one or two times by the same spacecraft after the main exhaust encounter [11,22–26]. Since these re-entry durations were all short, the reported narrow re-entry was interpreted as that exhaust boundaries were non-planar due to their local small-scale folds, even the folds can be orthogonal to the reconnection plane [26]. In addition, the quick flapping of reconnection exhaust may also cause that exhausts were re-entered by one spacecraft. Here, a possible swinging reconnection exhaust observed by Wind on April 1, 2003 was presented.

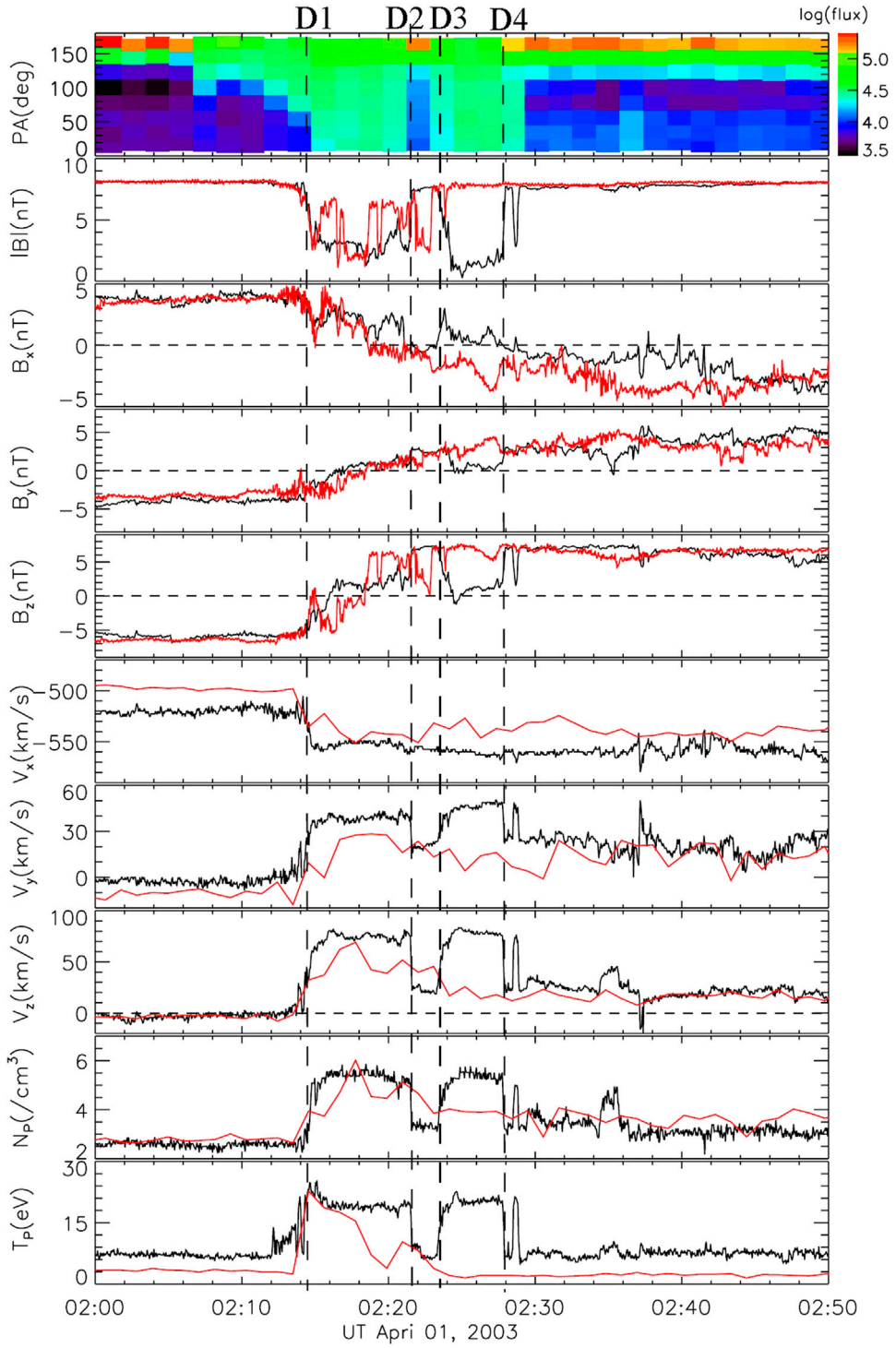

FIGURE 2 | Magnified images of the suprathermal electron spectrogram, magnetic field, and plasma data of the magnetic reconnection exhaust on April 1, 2003. The red cures indicate observations of ACE. Note that observations of ACE are shifted toward 22 min in time.

OBSERVATIONS

Figure 1 illustrates the suprathermal electron pitch angle spectrogram, magnetic field, and plasma data of the magnetic reconnection event, and the following short, fast magnetic structure, which has been identified as a small flux rope in a small-scale magnetic flux rope database in reference [27], measured by Wind at (228.06, 83.01, 10.58) R_E

(R_E = 6,378 km) in the GSE coordinate system. The top plot displays the suprathermal electron pitch angle spectrograms of 165.0 eV. The subsequent plots show the strength of the magnetic field (B); the x, y, and z components of the magnetic field (B_x, B_y, B_z); the x, y, and z components of the proton speed (V_x, V_y, V_z); proton density (N); and the proton temperature (T_p), respectively. The suprathermal electron data were obtained by using a 3D plasma (3DP) analyzer, and the time resolution was approximately 97 s (Lin et al. 1995). The resolution of the plasma and magnetic field data is 3 s. **Figure 1** also indicates that the magnetic reconnection event occurred at the interface between a faster magnetic structure and its slower frontal background solar wind. The faster magnetic structure lasts less than 3 h, and it exhibits smooth rotations along the magnetic field directions. Similar to a magnetic cloud, the faster magnetic structure may have a closed magnetic configuration because of its smooth field rotations. Magnetic reconnection may occur because of the compression of the following faster closed magnetic structure. **Figure 2** provides the magnified images of the suprathermal electron spectrogram, magnetic field, and plasma curves of the magnetic reconnection event. The authors in reference [13] first identified and reported the magnetic reconnection event, and they also determined the leading boundary of the exhaust at around 02:14:19 UT and found that the duration of the exhaust is 34 min, that is, their identified rear boundary is at around 02:48:19 UT. They also obtained a field shear angle of 153° across the exhaust. **Figure 2** also reveals that the accelerated plasma flow and enhanced proton temperature and proton density regions are mainly at 02:14:19-02:27:52 UT, where the magnetic strength exhibits an apparent depression. In addition, the phase space densities of suprathermal electrons display an apparent enhancement in the region, and these suprathermal electrons may be heated by the reconnection event. In **Figure 2**, it seems that the reconnection event involves two adjacent exhausts, whose boundaries were denoted by four magnetic field directional discontinuities (DDs). The first possible exhaust event is about within 02:14:19-02:21:34 UT, and the second possible exhaust event is from 02:23:31 UT to 02:27:52 UT. Both events have apparent exhaust signatures: the accelerated plasma flow, the enhanced density and temperature, and the depressed magnetic field strength. However, for the first event, the changes between velocity and magnetic field components are correlated with one another at the front boundary of the event and are anticorrelated at the rear boundary, but the changes in velocity and magnetic field are anticorrelated at both sides of the second one. That is to say, only the first event can be identified as a reconnection exhaust according to the reconnection exhaust criteria of Gosling et al. (2005a). Comparing observed features of the two accelerated flow events, we can find that the two events have some similar characteristics. This may indicate that the two accelerated flow events were just one exhaust, which was detected twice in a short time by the Wind spacecraft. As mentioned before, both folds of exhaust boundaries and flapping of reconnection exhausts can cause that exhausts were re-entered by one spacecraft. In the following, we will analyze and discuss the cause of the re-entered reconnection exhaust.

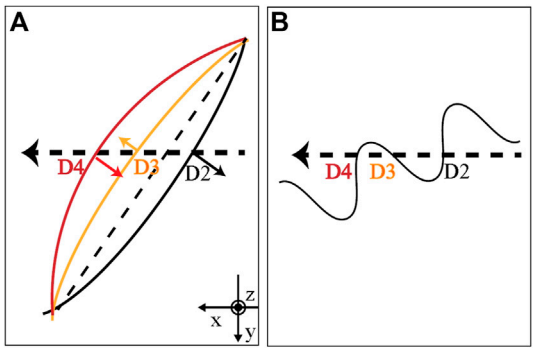

FIGURE 3 | Illustration of motion of the rear boundary of the reconnection exhaust in the *x-y* plane. The thick black arrowed line denotes the trajectory of the spacecraft passing through the rear boundary. **(A)** The flapping motion of the rear boundary. The black curve indicates the position and shape of the rear boundary at D2 time. The orange and magenta solid curves denote the position and shape of the rear boundary at D3 and D4 time, respectively. The arrowed line indicates the direction of the flap, and its length denotes the speed. The thin black dashed line denotes the undisturbed rear boundary of the reconnection exhaust. **(B)** The fold of the rear boundary.

The spacecraft will detect different signals under different scenarios. For the scenario of flapping reconnection exhaust, the spacecraft detects the rear partial exhaust repeatedly, namely, the spacecraft passes through the same plasma environment twice. Therefore, the observed plasma and magnetic features of the partial re-entered exhaust should be similar to that of the rear part of the main exhaust. In addition, the rear boundary of the main exhaust and the both boundaries of the partial re-entered exhaust should have the same DD, which was crossed three times by the spacecraft. Although the DD moved back and forth with the exhaust, it may keep the roughly planar structure. For the scenario of folds in the rear boundary, the trajectory of the spacecraft should be close to the warping rear boundary so that it can cross its rear boundary more than two times. The spacecraft detects different plasma environments at every turn. Therefore, partial of observed plasma features of two accelerated (or decelerated) plasma flows may be similar, such as proton density and the proton temperature for the two scenarios. But the observations of the magnetic field directions and the proton velocities should be different for the two scenarios [26]. Especially, the rear boundary of the first accelerated flow and both boundaries of the second accelerated flow should be not planar in the fold scenario. The main differences between the two scenarios are illustrated in **Figure 3**.

Now, we examine the two adjacent accelerated flows observed by Wind in more detail. **Figure 2** reveals that the plasma and magnetic characteristics of the two intervals 02:14:19-02:21:34 UT and 02:23:31-02:27:52 UT are approximately consistent, and these characteristics include magnetic field strength, the magnetic field direction, the proton velocity, proton density, and the proton temperature. Especially their profiles of velocity components are almost unanimous. In addition, the profiles of the magnetic field and solar wind speed are symmetric at about 02:22:28 UT. Therefore, we infer that two adjacent accelerated flows only

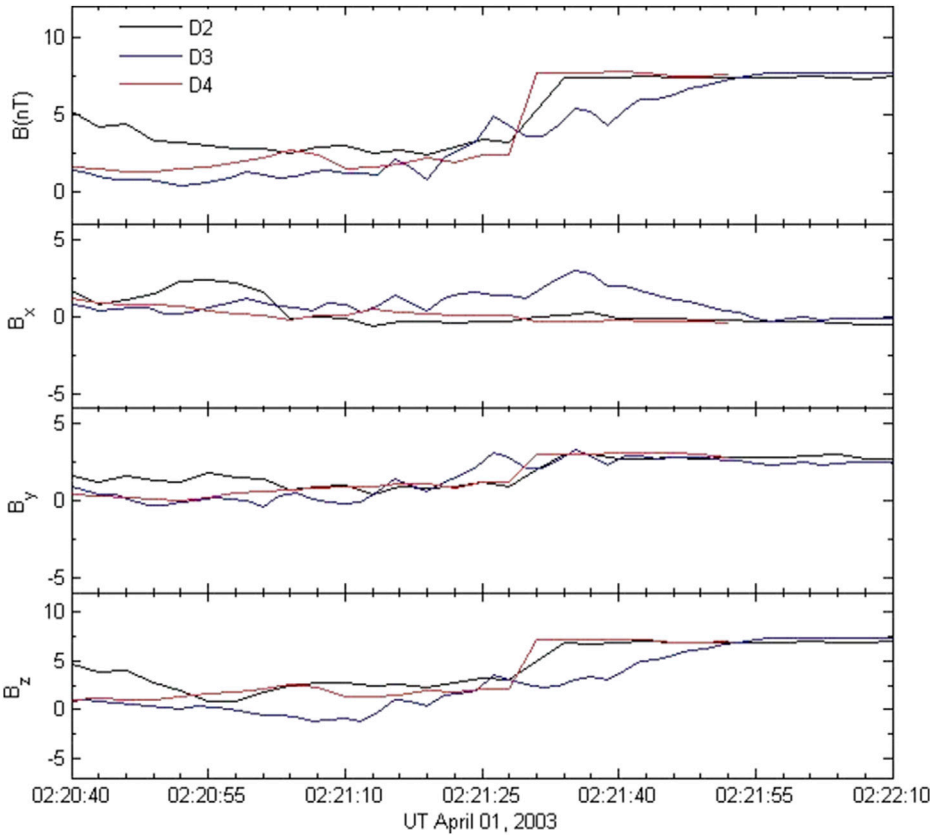

FIGURE 4 | Magnetic field data around the directional discontinuities D2, D3, and D4; D3 and D4 were shifted forward in time by 135 and 378 s, and the time series of D3 are reversed.

TABLE 1 | Normal vectors of the DDs in the GSE coordinate.

	X	Y	Z
D2	−0.611	0.732	−0.301
D3	−0.576	0.750	−0.327
D4	−0.539	0.799	−0.264

represent one exhaust detected twice simply due to its back-and-forth movement. If so, all the directional discontinuities D2, D3, and D4 are the rear boundary of the exhaust, but D3 is crossed by Wind from the outside. All the three directional discontinuities should have consistent variation characteristics. **Figure 4** gives the overlay of time-shifted magnetic field data around the three directional discontinuities. The data of D3 and D4 were shifted forward in time by 135 and 378 s, respectively, the time series of D3 are reversed. **Figure 4** demonstrates that three sets of curves have a similar changing trend, but jump curves of D2 and D4 are steeper than those of D3. This indicates that the Wind spacecraft took more time to cross D3 than to cross D2 and D4. The delayed effect of D3 can be explained with back-and-forth movement of the exhaust. After Wind passed through the rear boundary the first time, flapping reconnection exhaust with the solar wind departs from the Wind satellite quickly. For the second encounter, the rear boundary needs to come back to scan the Wind satellite. Thus, the second traversing speed must be lower, and correspondingly, its traversing duration was longer. Now that D2, D3, and D4 represent that the rear boundary was crossed at different time, the three DDs should have similar normal directions. A minimum variance analysis (MVA) technique is frequently used to estimate DD normal; here, we also estimated the normals of the three DDs with the MVA technique, and **Table 1** lists their normal vectors in the GSE coordinate. From **Table 1**, one can find that the three normal directions are coincident, and the angles between two of the three normal vectors are in the range of 2.72° and 6.06°. In conclusion, our findings suggest that the reconnection current sheet was quickly moving back and forth when the Wind spacecraft crossed the reconnection exhaust.

SUMMARY AND DISCUSSION

In this study, we report an interplanetary magnetic reconnection event, which was detected by the Wind spacecraft on April 1, 2003. Wind's observations show that the magnetic reconnection event has two discrete accelerated flows, and there is an about 2-min interval between the accelerated flows. The second accelerated flow

indicates that Wind re-entered the main exhaust. But the cause of the re-entered exhaust is different from previously reported re-entered exhaust [11,22–26]. A previous work suggests that the re-entered parts result from the folded local exhaust boundaries. However, the analysis of the reconnection event presented here indicated that the re-entered parts resulted from quickly flapping of reconnection exhaust. The traversing times of D2 and D3 were about 30 and 60˚s, respectively. The speed of the solar wind in the normal direction of the rear boundary was about 313 km/s. Taking this speed as the traversing speed of D2, the traversing speed of D3 should be 156.5 km/s. Such a traversing speed was very likely to be overestimated since D2 was probably moving in a slower speed due to the flapping motion. However, the flapping speed could not be smaller than 313 km/s; otherwise, the observations by spacecraft may not be able to reveal the flapping movement. The duration between D2 and D4 was ~330˚s. Therefore, the amplitude of the flapping motion was at least 16 R_E (taking the flapping speed as 313 km/s). This reconnection exhaust was also detected by ACE at (−5, −29, −65) R_E relative to the position of Wind 22 min later [13]. The observations of ACE are shown in red curves in **Figure 2** (shifted toward 22 min in time for clarity). The rear boundary of the reconnection exhaust at ACE was thought to be at ~02:18:20 (corresponding to a steep and strong change in Bz). Therefore, the duration of the reconnection exhaust at ACE was 260˚s, which was less than that of 450˚s at Wind. The normal direction of the reconnection exhaust was estimated to be (−0.32, −0.93, 0.20) at ACE and (−0.45, −0.85, 0.27) at Wind by applying the hybrid minimum variance analysis [28] method to the whole exhaust. The angle between the two normal was ~8˚. Therefore, the scale of the reconnection exhaust in the normal direction was ~4.5 R_E at ACE and 10.5 R_E at Wind. At ~02:22:50, ACE detected another steep and strong change in Bz. However, it is hard to decide if this steep variation in Bz was caused by re-enter the rear boundary of the reconnection exhaust, due to the low time resolution of the plasma data from ACE. Besides, one can see that the magnetic field was more fluctuating at ACE, which indicates that some explosive event was ongoing. This event may be the cause of the flapping motion of the reconnection current. In conclusion, for many reported reconnection exhausts, their exhaust geometries, the wedge angles, and dimensionless reconnection rates were calculated based on the quasi-stationary reconnection hypothesis (e.g., [28–31]). If reconnection current sheets were flapping when the spacecraft crossed reconnection exhausts, all the estimated values will be unreliable.

DATA AVAILABILITY STATEMENT

Publicly available datasets were analyzed in this study. This data can be found here: http://cdaweb.gsfc.nasa.gov/cdaweb/istp_public/.

AUTHOR CONTRIBUTIONS

JW drafted the manuscript and led the observational analysis. YZ provided heuristic advice and revised the manuscript. All authors contributed to the interpretation of the results and helped draft the manuscript.

ACKNOWLEDGMENTS

The authors thank Q. M. Lu and D. J. Wu for their helpful discussions. The authors acknowledge support from NSFC (Grant Nos. 41974197, 41804162, and 42104158). The authors thank NASA/GSFC for the use of data from the Wind and ACE; these data can obtain freely from the Coordinated Data Analysis Web (http://cdaweb.gsfc.nasa.gov/cdaweb/istp_public/).

REFERENCES

1. Sweet PA. 14. The Neutral point Theory of Solar Flares. *Symp - Int Astron Union* (1958) 6:123–34. doi:10.1017/s0074180900237704
2. Parker EN. Sweet's Mechanism for Merging Magnetic fields in Conducting Fluids. *J Geophys Res* (1957) 62:509–20. doi:10.1029/jz062i004p00509
3. Petschek HE. Magnetic Field Annihilation. In: WN Hess, editor. *The Physics of Solar Flares*. Washington D C: NASA Special Publication (1964). p. 425–39.
4. Longcope DW, and Klimchuk JA. How Gas-Dynamic Flare Models Powered by Petschek Reconnection Differ from Those with Ad Hoc Energy Sources. *ApJ* (2015) 813:131. doi:10.1088/0004-637x/813/2/131
5. Gosling JT, Skoug RM, McComas DJ, and Smith CW. Direct Evidence for Magnetic Reconnection in the Solar Wind Near 1 AU. *J Geophys Res* (2005) 110:A01107. doi:10.1029/2004JA010809
6. Davis MS, Phan TD, Gosling JT, and Skoug RM. Detection of Oppositely Directed Reconnection Jets in a Solar Wind Current Sheet. *Geophys Res Lett* (2006) 33:L19102. doi:10.1029/2006GL026735
7. Feng H, and Wang J. Magnetic-reconnection Exhausts in the Sheath of Magnetic Clouds. *A&A* (2013) 559:A92. doi:10.1051/0004-6361/201322522
8. Feng H, and Wang J. Magnetic Reconnection as a Possible Heating Mechanism of the Local High Temperature Protons within Magnetic Clouds. *Sci China Earth Sci Earth Sci* (2014) 57:1979–85. doi:10.1007/s11430-013-4816-x
9. Gosling JT, Skoug RM, Haggerty DK, and McComas DJ. Absence of Energetic Particle Effects Associated with Magnetic Reconnection Exhausts in the Solar Wind. *Geophys Res Lett* (2005) 32:a–n. doi:10.1029/2005GL023357
10. Gosling JT, Eriksson S, Skoug RM, McComas DJ, and Forsyth RJ. Petschek-Type Reconnection Exhausts in the Solar Wind Well beyond 1 AU:Ulysses. *ApJ* (2006) 644:613–21. doi:10.1086/503544
11. Gosling JT, Eriksson S, Phan TD, Larson DE, Skoug RM, and McComas DJ. Direct Evidence for Prolonged Magnetic Reconnection at a Continuous X-Line within the Heliospheric Current Sheet. *Geophys Res Lett* (2007) 34:L06102. doi:10.1029/2006GL029033
12. Gosling JT, Eriksson S, McComas DJ, Phan TD, and Skoug RM. Multiple Magnetic Reconnection Sites Associated with a Coronal Mass Ejection in the Solar Wind. *J Geophys Res* (2007) 112:a–n. doi:10.1029/2007JA012418
13. Phan TD, Gosling JT, and Davis MS. Prevalence of Extended Reconnection X-Lines in the Solar Wind at 1 AU. *Geophys Res Lett* (2009) 36:L09108. doi:10.1029/2009GL037713
14. Phan TD, Gosling JT, Paschmann G, Pasma C, Drake JF, Øieroset M, et al. THE DEPENDENCE OF MAGNETIC RECONNECTION ON PLASMA β AND MAGNETIC SHEAR: EVIDENCE FROM SOLAR WIND OBSERVATIONS. *ApJ* (2010) 719:L199–L203. doi:10.1088/2041-8205/719/2/l199
15. Feng HQ, Wu DJ, Wang JM, and Chao JW. Magnetic Reconnection Exhausts at the Boundaries of Small Interplanetary Magnetic Flux Ropes. *A&A* (2011) 527:A67. doi:10.1051/0004-6361/201014473

16. Feng H, Zhao Y, Zhao G, Liu Q, and Wu D. Observations on a Series of Merging Magnetic Flux Ropes within an Interplanetary Coronal Mass Ejection. *Geophys Res Lett* (2019) 46:5–10. doi:10.1029/2018GL080063
17. Feng H, Zhao G, and Wang J. Small Interplanetary Magnetic Flux Rope. *Sci China Technol Sci* (2019) 63:183–94. doi:10.1007/s11431-018-9481-1
18. Feng H, Zhao Y, Wang J, Liu Q, and Zhao G. Observations of Magnetic Flux Ropes Opened or Disconnected from the Sun by Magnetic Reconnection in Interplanetary Space. *Front Phys* (2021) 9:679780. doi:10.3389/fphy.2021.679780
19. Phan TD, Gosling JT, Davis MS, Skoug RM, Øieroset M, Lin RP, et al. A Magnetic Reconnection X-Line Extending More Than 390 Earth Radii in the Solar Wind. *Nature* (2006) 439(7073):175–8. doi:10.1038/nature04393
20. Mistry R, Eastwood JP, Phan TD, and Hietala H. Development of Bifurcated Current Sheets in Solar Wind Reconnection Exhausts. *Geophys Res Lett* (2015) 42:513–520. doi:10.1002/2015GL066820
21. Zhao Y, Feng H, Liu Q, and Zhao G. Coalescence of Magnetic Flux Ropes within Interplanetary Coronal Mass Ejections: Multi-Cases Studies. *Front Phys* (2019) 7:151. doi:10.3389/fphy.2019.00151
22. Gosling JT, Eriksson S, Blush LM, Phan TD, Luhmann JG, McComas DJ, et al. Five Spacecraft Observations of Oppositely Directed Exhaust Jets from a Magnetic Reconnection X-Line Extending > 4.26 × 106km in the Solar Wind at 1 AU. *Geophys Res Lett* (2007) 34:L20108. doi:10.1029/2007GL031492
23. Gosling JT. Magnetic Reconnection in the Heliosphere: New Insights from Observations in the Solar Wind. *Universal Heliophysical Process* (2009) 257:367.
24. Lin CC, Feng HQ, Wu DJ, Chao JK, Lee LC, and Lyu LH. Two-spacecraft Observations of an Interplanetary Slow Shock. *J Geophys Res* (2009) 114:a–n. doi:10.1029/2008JA013154
25. Eriksson S, Gosling JT, Phan TD, Blush LM, Simunac KDC, Krauss-Varban D, et al. Asymmetric Shear Flow Effects on Magnetic Field Configuration within Oppositely Directed Solar Wind Reconnection Exhausts. *J Geophys Res* (2009) 114:a–n. doi:10.1029/2008JA013990
26. Mistry R, Eastwood JP, and Hietala H. Detection of Small-scale Folds at a Solar Wind Reconnection Exhaust. *J Geophys Res Space Phys* (2015) 120:30–42. doi:10.1002/2014JA020465
27. Hu Q, Zheng J, Chen Y, le Roux J, and Zhao L. Automated Detection of Small-Scale Magnetic Flux Ropes in the Solar Wind: First Results from the Wind Spacecraft Measurements. *ApJS* (2018) 239(1):12. doi:10.3847/1538-4365/aae57d
28. Gosling JT, and Phan TD. Magnetic Reconnection in the Solar Wind at Current Sheets Associated with Extremely Small Field Shear Angles. *ApJ* (2013) 763(2):L39. doi:10.1088/2041-8205/763/2/l39
29. Xu X, Wei F, and Feng X. Observations of Reconnection Exhausts Associated with Large-Scale Current Sheets within a Complex ICME at 1 AU. *J Geophys Res* (2011) 116:A05105. doi:10.1029/2010JA016159
30. Teh W-L, Sonnerup BUÖ, Hu Q, and Farrugia CJ. Reconstruction of a Large-Scale Reconnection Exhaust Structure in the Solar Wind. *Ann Geophys* (2009) 27:807–22. doi:10.5194/angeo-27-807-2009
31. Lavraud B, Gosling JT, Rouillard AP, Fedorov A, Opitz A, Sauvaud J-A, et al. Observation of a Complex Solar Wind Reconnection Exhaust from Spacecraft Separated by over 1800 R E. *Sol Phys* (2009) 256(1–2):379–92. doi:10.1007/s11207-009-9341-x

Conflict of Interest: The authors declare that the research was conducted in the absence of any commercial or financial relationships that could be construed as a potential conflict of interest.

frontiers in Physics

ORIGINAL RESEARCH
published: 01 October 2021
doi: 10.3389/fphy.2021.746576

Formation of Magnetic Flux Rope During Solar Eruption. I. Evolution of Toroidal Flux and Reconnection Flux

Chaowei Jiang[1], Jun Chen[2,3], Aiying Duan[4], Xinkai Bian[1], Xinyi Wang[5], Jiaying Li[1], Peng Zou[1] and Xueshang Feng[1,5]*

[1]Institute of Space Science and Applied Technology, Harbin Institute of Technology, Shenzhen, China, [2]School of Astronomy and Space Science, Nanjing University, Nanjing, China, [3]CAS Key Laboratory of Geospace Environment, School of Earth and Space Sciences, University of Science and Technology of China, Hefei, China, [4]School of Atmospheric Sciences, Sun Yat-sen University, Zhuhai, China, [5]State Key Laboratory for Space Weather, Center for Space Science and Applied Research, Chinese Academy of Sciences, Beijing, China

Magnetic flux ropes (MFRs) constitute the core structure of coronal mass ejections (CMEs), but hot debates remain on whether the MFR forms before or during solar eruptions. Furthermore, how flare reconnection shapes the erupting MFR is still elusive in three dimensions. Here we studied a new MHD simulation of CME initiation by tether-cutting magnetic reconnection in a single magnetic arcade. The simulation follows the whole life, including the birth and subsequent evolution, of an MFR during eruption. In the early phase, the MFR is partially separated from its ambient field by a magnetic quasi-separatrix layer (QSL) that has a double-J shaped footprint on the bottom surface. With the ongoing of the reconnection, the arms of the two J-shaped footprints continually separate from each other, and the hooks of the J shaped footprints expand and eventually become closed almost at the eruption peak time, and thereafter the MFR is fully separated from the un-reconnected field by the QSL. We further studied the evolution of the toroidal flux in the MFR and compared it with that of the reconnected flux. Our simulation reproduced an evolution pattern of increase-to-decrease of the toroidal flux, which is reported recently in observations of variations in flare ribbons and transient coronal dimming. The increase of toroidal flux is owing to the flare reconnection in the early phase that transforms the sheared arcade to twisted field lines, while its decrease is a result of reconnection between field lines in the interior of the MFR in the later phase.

Keywords: magnetic fields, magnetohydrodynamics (MHD), methods: numerical, sun: corona, sun: flares

OPEN ACCESS

Edited by:
Hongqiang Song,
Shandong University, China

Reviewed by:
Jiong Qiu,
Montana State University, United States
Guiping Zhou,
National Astronomical Observatories (CAS), China

****Correspondence:***
Chaowei Jiang
chaowei@hit.edu.cn

Specialty section:
This article was submitted to Stellar and Solar Physics, a section of the journal Frontiers in Physics

Received: *24 July 2021*
Accepted: *16 September 2021*
Published: *01 October 2021*

Citation:
Jiang C, Chen J, Duan A, Bian X, Wang X, Li J, Zou P and Feng X (2021) Formation of Magnetic Flux Rope During Solar Eruption. I. Evolution of Toroidal Flux and Reconnection Flux. Front. Phys. 9:746576. doi: 10.3389/fphy.2021.746576

1 INTRODUCTION

Solar eruptions are spectacular manifestation of explosive release of magnetic energy in the Sun's atmosphere, i.e., the solar corona, and therefore, unveiling the relevant magnetic field structures and their evolution holds a central position in the study of solar eruptions. Magnetic flux rope (MFR), a bundle of twisted magnetic field lines winding around a common axis with the same sign, is believed to be a fundamental structure in solar eruptions [1–3], especially in those which successfully produce coronal mass ejections (CMEs). By reconstruction of the cross section of ICME (i.e., CMEs that evolves into the inter-planetary space) from the *in-situ* data obtained by satellites passing through the ICME, it has been well established that typical ICMEs have structure of highly twisted MFR (e.g., [4,5]).

Although there is little doubt that MFR constitutes the core structure of CMEs, whether MFR exists in the solar corona before CME initiation is still in intense debates [6,7]. Currently, there are two different opinions; one is that MFR does not exist before solar eruption, and it is the latter that creates MFR through magnetic reconnection; the other is that MFR should exist prior to eruption and it is the ideal magnetohydrodynamic (MHD) instability of the MFR that initiates the eruption. The typical scenarios for the first opinion include the runaway tether-cutting reconnection model [8–10] and the magnetic breakout model [11–14]. In these models, the coronal magnetic field before eruption is strongly sheared and eruption is triggered by magnetic reconnection, internally within the sheared arcade (i.e., tether-cutting), or above it (i.e., breakout), while MFR is built up during the eruption through reconnection which transforms the sheared arcade into the rope. For the models assuming the pre-existence of MFR, such as the catastrophe model [15,16], the torus instability and kink instability models [17–21], an MFR is proposed to either emerge from below the photosphere (i.e., in the convective zone, where the turbulent convection can create thin, twisted magnetic tubes [22,23]), or forms slowly by reconnection in the lower atmosphere [24] through the so-called flux cancellation process [25]. Observations seem to indicate that both opinions are possible. For example, on one hand, Song et al [26] presented a good observation that an MFR can formed during a CME. On the other hand, an MFR characterized by a hot sigmoid structure may pre-exist before eruption, as manifested by precursor oscillation [27] or precursor external magnetic reconnection between the top of the MFR and ambient magnetic field [28].

Regardless of which model is relevant to the real case in the corona, it is commonly agreed that flare reconnection (i.e., the main reconnection that occurs below the erupting MFR) can shape substantially the on-the-fly MFR. In the purely two-dimensional (2D) standard flare model, a plasmoid (corresponding to the cross section of MFR in 3D) rises from the top of the flare current sheet, and reconnection in the current sheet continuously adds poloidal flux to the MFR, which thus grows and expands during the eruption. As a result, the observed double flare ribbons, which indicate the locations of the reconnecting field-line footpoints in the opposite magnetic polarities, are continuously separated with each other. However, in a fully 3D case, it is not that straightforward how the reconnection shapes the MFR. Numerical simulations of the simplest magnetic configuration (i.e., a bipolar magnetic field), aided with accurate analysis of magnetic topology evolution, have been developed to study how an MFR evolves with reconnection during eruption [20,29], and the findings are becoming known as the standard flare model in 3D [29–31], although it is still an over-simplified version of the realistic cases as demonstrated in recent data-constrained and data-driven simulations (e.g., [32–34]).

In the standard 3D model, the erupting MFR is separated from the ambient field by a quasi-separatrix layer (QSL [35]), and in more details, this QSL intersects with itself below the MFR, forming a hyperbolic flux tube (HFT, [36]), and the flare reconnection occurs mainly in the HFT. The footprints of this QSL at the bottom surface, i.e., the photosphere, forms two thin strips of J shape on each side of the main polarity inversion line (PIL), and the legs of the MFR are anchored within the hooked parts of the J-shaped strips. Thus, the observed flare ribbons usually exhibit double-J pattern, and the transient coronal holes [37], i.e., post-eruptive twin coronal dimmings, are naturally suggested to map the feet of erupting MFRs, along which mass leakage into interplanetary space could take place [38–40], and the boundaries of such twin coronal dimmings are outlined by the hooks of flare ribbons. With the ongoing of reconnection, the arms of the double-J ribbons separate, and their hooks gradually extends outwards. In such process, the flare reconnection, which occurs between the pre-reconnection sheared arcade (as shown in the classic cartoon of tether-cutting model, i.e., Figure 1 of [10]), should increase the toroidal (axial) flux by increasing the number of field lines within the MFR.

However, such a "standard" type of flare reconnection in 3D still cannot explain fully the observations of "standard" two-ribbon flares. A well-known, unexplained fact is that the feet of the erupting flux rope, as manifested by twin coronal dimmings and also by the hook ends of double-J flare ribbons, are found to be drifting progressively away from the main PIL during eruption [37], even though the photosphere can be regarded as motionless during the short time scale of eruption. To this end, Aulanier and Dudík [41] analyzed in more details the reconnection process in their simulation of flux rope eruption and showed that the flare reconnection actually occurs in three different types of events according to their different effect in building up the flux rope. The first one is named as *aa-rf reconnection*, which is the standard 3D flare reconnection that occurs between two arcades and results in a long field line joining the flux rope and a short one as a flare loop. The second one is the so-called *rr-rf reconnection*, which occurs within the flux rope by reconnecting two flux-rope field lines with each other and generates a new multi-turn flux-rope field line and a flare loop. The third one is *ar-rf reconnection*, in which an inclined arcade reconnects with the leg of a flux-rope field line, and it generates new flux-rope field line rooted far away from the PIL and a flare loop. Thus, it is the *ar-rf reconnection* that actually leads to gradual drifting of the MFR footpoints.

Observations show even more features not explained (or not mentioned) in the "advanced" standard model of [41]. For instance, using high-resolution observations, [42] found two closed-ring-shaped flare ribbons in the case of a buildup of highly twisted MFRs with the development of a flare reconnection. During the separation of the main flare ribbons, the flare rings expand significantly, starting from almost point-like brightening. Note that such closed circular shape flare ribbons have different nature from those formed by null-point topology which also produce circular ribbon due to reconnection in the null's spine-fan separatrix [32]. It is predicted by theoretical models [35] that if the MFR grows to sufficiently twisted, the hooks of the double-J shaped footprints of the QSL can indeed close onto themselves, becoming two closed rings, although this is not reproduced by the numerical model of [20], possibly because their simulation run is stopped before the MFR grows to such a high degree of twist.

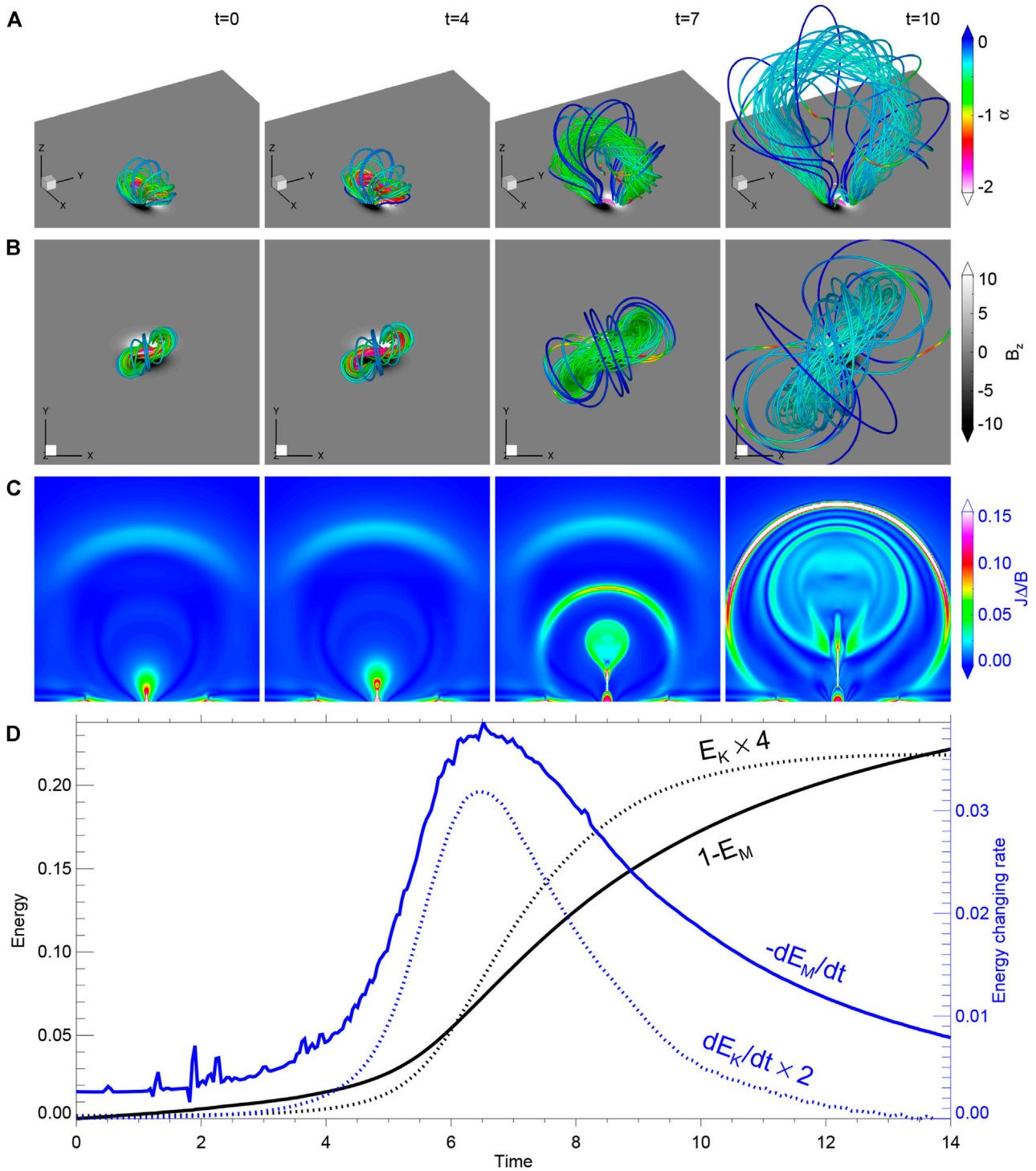

FIGURE 1 | Structural evolution of the eruption. **(A)** 3D prospective view of magnetic field lines colored by the force-free factor. Here the field lines are traced at fixed footpoints on the bottom surface, and they represent the core structure of the pre-eruption field. **(B)** Top view of the structure shown in (a). **(C)** Evolution of the dimensionless current density $J\Delta/B$ on the central cross section (i.e., the $x = 0$ slice). **(D)** Evolution of magnetic and kinetic energies and their temporal changing rate. The energies are all normalized by the magnetic energy at $t = 0$ and the unit of time is 105 s. Also see **Supplementary Movie S1** for a high-cadence evolution of the eruption process.

Very recently, a few papers reported that there is a systematic decrease of the toroidal flux of erupting MFR after its fast increase (e.g., [40,42,43]). In particular, Xing et al [40] developed a practical method for estimation of the toroidal flux of MFR during eruption by combining twin coronal dimmings and the hooks of flare ribbons. They found that the toroidal flux of the CME flux rope for all four studied events shows a two-phase evolution: a rapid increasing phase followed by a decreasing phase, and moreover, the evolution is well synchronous in time with that of the flare soft X-ray flux. The increase of MFR's toroidal flux can be easily understood by the *aa-rf reconnection* while the subsequent decrease remains unclear. Although Xing et al [40] invoked the *rr-rf reconnection* as the mechanism responsible for such decrease, it is still unknown whether the increase-to-decrease evolution of toroidal flux can self-consistently be reproduced in any MHD simulation.

This series of papers are devoted to a comprehensive analysis of a new MHD simulation of eruption [44], focusing on the formation of MFR during eruption. That simulation demonstrated in fully 3D that solar eruption can be initiated from a single magnetic arcade without the formation of MFR before the triggering of eruption. This is different from the aforementioned simulations [20,41], in which the eruption is initiated by torus instability (which is a kind of ideal MHD instability [17]) of an MFR formed well before the eruption. With the new MHD simulation, one can follow whole life, i.e., the birth and subsequent evolution, of an MFR during the eruption. As the first paper of this series, here we show, for the first time, that both the closing of the hook ends of the QSLs at the MFR's feet and the increase-to-decrease evolution of the toroidal magnetic flux can be self-consistently reproduced by the simulation, suggesting that they are genuine features of erupting MFRs. We further quantified the evolution of reconnection flux during the eruption, and found that the evolution of QSLs is rather complex within the MFR. In the second article of this series, we will illustrate the 3D configuration of the different types of magnetic reconnection in building up the MFR and disclose why the QSLs evolve in such a complex way, following the pioneering work by [41].

2 MHD SIMULATION AND ANALYSIS METHOD

Recently, Jiang et al [44] performed an ultra-high accuracy, fully 3D MHD simulation and demonstrated that solar eruptions can be initiated in a single sheared arcade with no additional special topology. Their simulation shows that, "through photospheric shearing motion alone, an electric current sheet forms in the highly sheared core field of the magnetic arcade during its quasi-static evolution. Once magnetic reconnection sets in, the whole arcade is expelled impulsively, forming a fast-expanding twisted flux rope with a highly turbulent reconnecting region underneath". They further found that the high-speed reconnection jet plays the key role in driving the eruption. The simplicity and efficacy of this scenario, in the theoretical point of view, argue strongly for its fundamental importance in the initiation of solar eruptions. Since the model do not need a pre-existing MFR, the MFR itself comes into being *after* the eruption initiation.

Here we focus on the formation and evolution of MFR during the eruption by using a simulation run like the one in [44], but with a lower resolution than the original ones. Such simulation solves the full set of MHD equations and starts from a bipolar potential magnetic field and a hydrostatic plasma stratified by solar gravity with typical coronal temperature. Then shearing flows along the PIL, which are implemented by rotating the two magnetic polarities at the photosphere in the same count-clockwise direction, are applied on the bottom boundary to energize the coronal field until an eruption is triggered, and after then the surface flow is stopped. The whole computational box extends as $(-32, -32, 0) < (x, y, z) < (32, 32, 64)$ with length unit of 11.5 Mm. We solve a full MHD equation with both solar gravity and plasma pressure included, but with the energy equation simplified as an isothermal process. The time unit of the model is $\tau = 105$ s, and the shearing motion is applied by approximately 120τ before the onset of the eruption, during which a current sheet is gradually built up. Since no explicit resistivity is used in the MHD model, magnetic reconnection is triggered when the current sheet is sufficiently thin such that its width is close to the grid resolution. For more details of the simulation settings, the readers are referred to [44]. In that paper, the simulation is managed to be of very high resolutions with Lundquist number achieving $\sim 10^5$ for a length unit. Therefore, the secondary tearing instability (or plasmoid instability) is triggered in the current sheet and the magnetic topology becomes extremely complicated in small scales along with formation of the large-scale MFR. Such a complexity substantially complicates our analysis of the large-scale magnetic topology evolution associated with the erupting MFR, thus in this paper we used a lower-resolution run (corresponding to a Lundquist number of $\sim 10^3$). In the lower-resolution run, the basic evolution of the MFR during the eruption is not changed as compared to the high-resolution run, except that the small-scale structure will not arise, and thus the QSLs are computed in a cleaner pattern. Moreover, with the lower resolution, we can run the simulation longer and thus follow a longer evolution of MFR.

To help revealing the variation of the magnetic topology, we study the distribution and evolution of two parameters, the magnetic squashing degree and the magnetic twist number, which are commonly used for the study of 3D magnetic fields and their dynamics [2,29,30,45–47]. The magnetic squashing degree Q quantifies the gradient of magnetic field-line mapping with respect to their footpoints, and it is helpful for searching QSLs (and true separatries) of magnetic fields [36], which can have extremely large values of Q (e.g., $\geq 10^5$) and are preferential sites of magnetic reconnection. By locating the QSLs from the high values of Q we can see how the magnetic topology is evolved by the magnetic reconnection. Specifically, for a field line starting at one footpoint (x, y) and ending at the other footpoint (X, Y) where X and Y are both functions of x and y, the squashing degree Q associated with this field line is given by [36]

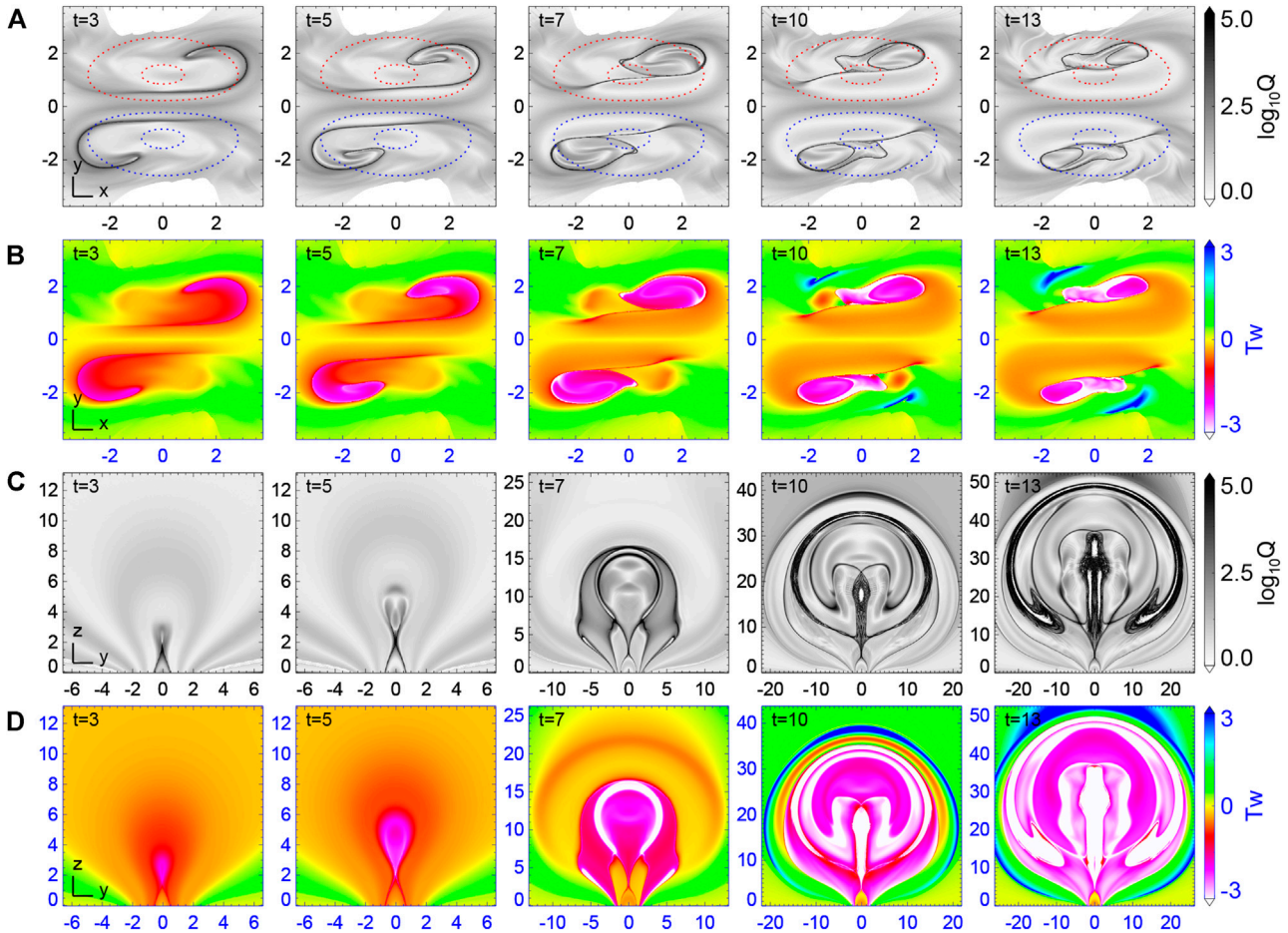

FIGURE 2 | Magnetic topology evolution and formation of MFR during the eruption. (A) Magnetic squashing degree Q on the bottom surface. The dashed lines are contours of B_z = −5, −10 (blue) and 5, 10 (red). **(B)** Magnetic twist number T_w on the bottom surface. **(C)** and **(D)** show the two parameters Q and T_w on the central vertical cross section (i.e., x = 0 plane). Also see **Supplementary Movie S2** for a high-cadence evolution.

$$Q = \frac{a^2 + b^2 + c^2 + d^2}{|ad - bc|} \tag{1}$$

where

$$a = \frac{\partial X}{\partial x}, \quad b = \frac{\partial X}{\partial y}, \quad c = \frac{\partial Y}{\partial x}, \quad d = \frac{\partial Y}{\partial y}. \tag{2}$$

The magnetic twist number T_w [48] is defined for a given (closed) field line by taking integration of $T_w = \int_L \mathbf{J}\cdot\mathbf{B}/B^2 dl/(4\pi)$ along the length L of the field line between two conjugated footpoints on the photosphere. Note that T_w is not identical to the classic winding number of field lines about a common axis, but an approximation of the number of turns that two infinitesimally close field lines wind about each other [47].

3 RESULTS

3.1 Overview of the Eruption

Figure 1 (and **Supplementary Movie S1**) shows the magnetic field lines, current density, and energies evolution from slightly before the eruption onset to a time well after the eruption peak time (that is, the peak time of energy conversion rate, which is t = 6.5). As can be seen, our simulation demonstrates a typical coronal eruption leading to a CME, as seen in observations as well as many previous numerical simulations with different scenarios [49–51]. The core magnetic field changes from the pre-eruptive sheared arcades to a inverse S-shaped MFR structure that subsequently exhibits a huge growth in size. From the top view, the MFR axis shows a significant anti-clockwise rotation during the eruption. **Figure 1C** shows a dimensionless current density, defined as $J\Delta/B$ (where J is the current density, Δ is the grid resolution and B is the magnetic field strength), on the central cross section, i.e., the x = 0 slice of the 3D volume. One can see a picture of the 2D standard flare model: a plasmoid rises and leaves behind a cusp structure corresponding to the edge of post-flare loop, and connecting them is a long CS in which magnetic reconnection occurs continuously. This reconnection results in high-speed bi-directional (up and down) plasma jets due to the "slingshot" effect, and the upward jet flow continuously pushes outward the newly reconnected

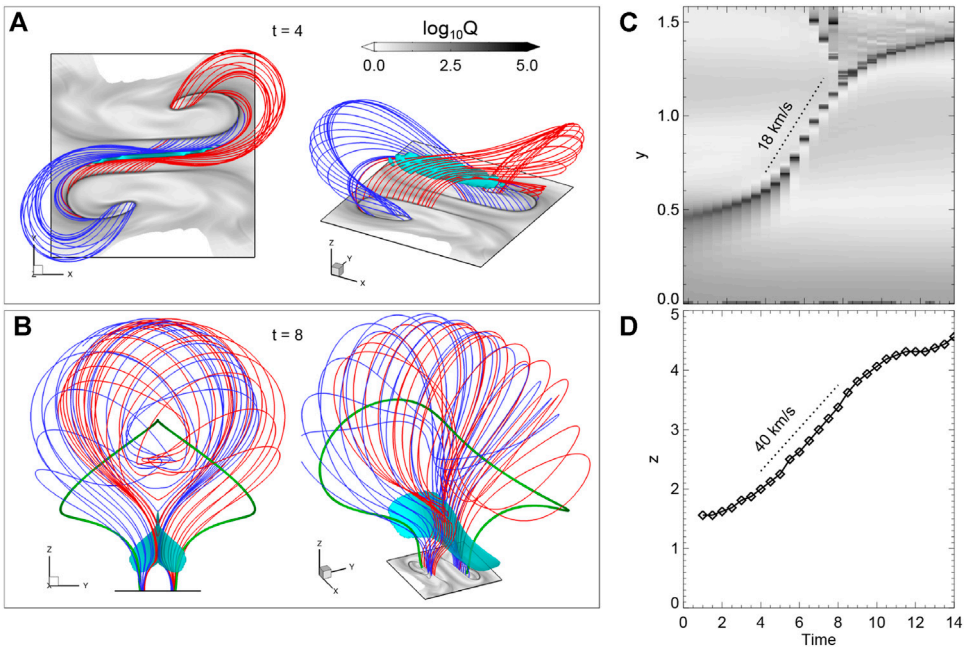

FIGURE 3 | Details of reconnection. (A) Structure of the reconnecting field lines at t = 4. The field lines are colored in red and blue. The cyan object is the iso-surface of $J\Delta/B$ = 0.2, i.e., the reconnection CS. The magnetic field lines are traced from the QSLs shown on the bottom surface, and as can be seen, they all contact the CS as these field lines are undergoing reconnection. **(B)** Sample of reconnecting field lines at t = 8. The thick green lines represent the axis of the newly formed MFR. Note that the actual sizes of the bottom surfaces shown in (a) and (b) are identical. **(C)** A stacked time sequence of the bottom Q map in y-direction and centred at x = 0, which shows the separation motion of the two J-shaped QSLs shown in **Figure 2A**. The sloped, dashed line denotes the largest separation speed. **(D)** Time evolution of the height of X point of the hyperbolic flux tube, i.e., the apex of the cusp structure, shown in **Figure 2C**. The slopped, dashed line denotes the largest rising speed.

magnetic flux. Eventually, it produces a CME and drives an arc-shaped fast magnetosonic shock enclosing the erupting structure.

3.2 Evolution of Magnetic Squashing Factor and Twist Number

To analyze the evolution of magnetic topology, in particular the formation of MFR, during the simulated eruption, we calculate the magnetic squashing factor Q and magnetic twist number T_w at the bottom surface and at a vertical central cross section of the 3D volume. The results are shown in **Figure 2** for a few snapshots and **Supplementary Movie S2** for the whole evolution. At the bottom surface, initially there are two thin strips of high Q, i.e., QSLs (or more precisely, the footprints of QSLs), forming two J shapes on either side of the PIL. With onset of the eruption, the two J-shaped QSLs on the bottom surface begin to evolve rapidly (see **Figure 2A** and the high-cadence evolution in **Supplementary Movie S2**). In **Figures 3A,B**, we show the field lines traced from the bottom QSLs at two different times, and the 3D structure of the reconnection current sheet by an iso-surface of extremely strong current density. As can be seen, all the field lines pass through the reconnection current sheet, which demonstrates clearly that the field lines in the QSLs are undergoing reconnection. Consequently, the motion of the bottom QSLs corresponds to the apparent motion of footpoints of the field lines that were undergoing reconnection. Furthermore, from **Figure 3**, one can see that in the early phase the reconnection is a fully 3D manner with a strong guide field component (i.e., B_x) because joining in the reconnection is mainly the strongly sheared, low-lying flux. While in the later phase, as the sheared flux has been reconnected, the reconnection transfers into a quasi-2D manner, which consumes mainly the large-scale, overlying flux that is barely sheared.

On the central cross section (**Figure 2C**), the QSLs intersect with each other, developing into an X shape, i.e., an HFT [36], and the intersection X point is essentially the reconnection site (in analogy to the null point in a 2D X-shaped reconnection configuration). As the eruption proceeds, more and more magnetic fluxes reconnect, and consequently, the two J-shaped QSLs on the bottom surface continuously separate with each other (see also **Figure 3C**, in which the separation speed is estimated). In the end of the simulation, they have swept to the center of each magnetic polarity (which is analogous to the umbra of sunspot). Meanwhile, the X point of the HFT rises upward progressively (see also **Figure 3D**, in which the rising speed is estimated) with the cusp region expanding below. Such two QSLs with their separation should be manifested as two separating flare ribbons in observations [33,46], while the rise of the X point corresponds to the apparent rising of the apex of post-flare arcades.

Figures 2B,D present the T_w distribution on the bottom surface and the central cross section, respectively. Starting from the hooks of the J-shaped QSLs, magnetic flux with high

twist (as denoted by large absolute values of T_w) begins to form owing to the tether-cutting reconnection, which creates long field lines connecting the far ends of the two pre-reconnection sheared arcades. With the twisted flux accumulated through the continuation of reconnection, the areas occupied by the footpoints of the highly twisted field lines at the hooks expand. Consequently, the hook of each J-shaped QSL continuously extends inward until its end reaches the arm, forming a closed curve encircling the highly twisted flux (see the QSL at $t = 7$). Such a transition of QSLs reproduces the evolution of flare ribbons that gradually forms close rings at their ends [42]. With this, the MFR is *fully* separated with its surroundings by the QSLs. Consistently, as can be seen in the vertical cross section at $t = 7$, the QSL form a closed tear-drop shape connecting the HFT, within which the twisted flux of the MFR has twist number T_w mostly below −2.

The evolution speed of the QSLs is related to the rate of reconnection. As shown in **Figure 3C**, at the beginning of the eruption, the distance of the two QSLs is about 10 Mm, and it reaches ~ 30 Mm at the end of the simulation. The separation speed first increases and then decreases, with its largest value of about 18 km s^{-1} at the time of around $t = 6.5$, which is also the time the plasma acceleration reaches its maximum (see **Figure 1**). Meanwhile, the rising speed of the X point, i.e., the apex of the cusp structure reaches a maximum of about 40 km s^{-1}. Our simulated flare-ribbon distances, their separation speed as well as the rising speed of the cusp are all comparable to typical observed ones [52–55].

Nearly at the same time when the hook ends of the J-shaped QSLs close, there is even a new QSL forms within the closed QSLs (see $t = 10$ and $t = 13$ in **Figure 2A**). In the positive polarity, for example, this new QSL is bifurcated from the hook end and moves to the right. As a result, the region bounded by the closed QSL, i.e., the foot of the MFR, is divided into two regions separated by the newly formed QSL, and the region after swept by the new QSL shows even stronger magnetic twist than before. This indicates that there must be internal reconnection between different field lines of the MFR. Another noticeable change is the decrease of the area in the closed QSLs, i.e., the feet of the MFR, which is quantified below.

3.3 Evolution of MFR's Toroidal Flux

The toroidal flux of the MFR, i.e., the content of the rope's flux that connects the bottom surface, can be quantified by using the distributions of twist number T_w and squashing factor Q at the bottom surface. Before the full closing of the hook ends of the QSLs, the feet of the MFR are characterized by the high T_w areas, while after the closing of the hooked QSLs, they can be identified more accurately by the area within the closed QSLs, but the T_w is still a good indicator since the QSL-enclosed region has a distinctly strong twist number (compare T_w and Q in **Figure 2**). We thus directly use the distribution of T_w to locate the MFR's feet in the whole evolution. However, it should be noted that the T_w provides only an approximation of the classic definition of the winding number around a common axis, and that there is no consensus on the definition of MFR based on either the winding number or the twist number T_w, although it is generally agreed that the winding of field lines in an MFR should be at least one turn. Therefore, we use two different thresholds for T_w to locate the MFR, and two values of the toroidal flux of the MFR are calculated by summing the magnetic flux with T_w exceeding the two thresholds, respectively. One is $T_w \leq -1$, which is also used by Duan et al [2] for searching MFRs in coronal field extrapolations, and the other is $T_w \leq -1.5$, which is properly chosen such that the MFR can be clearly differentiated from the background flux that has moderate twist number of $T_w \sim -1$ but without reconnection during the eruption (thus remains non-flux-rope field lines during the eruption). We also compute the areas of the MFR foot using the two thresholds, as well as the average twist number of the toroidal flux. The results are present in **Figures 4A,B**, which clearly show that the toroidal flux (as computed by either thresholds) first increases, reaching its peak value fast, and then decrease slowly. Such an evolution pattern also applies to that of the MFR foot area. This increase-to-decrease pattern of toroidal flux reproduces the observed variations of magnetic flux in erupting MFR's foot as identified by flare ribbons and transient coronal dimming [40]. On the other hand, the mean twist number shows a systematic increase to a value close to 3.5 at the end of simulation.

3.4 Evolution of Reconnection Flux

We further quantify how much of the magnetic flux is reconnected during the eruption. In principle, the total reconnected flux is simply the flux (by a factor of two) that is swept by the QSLs at the bottom surface in magnetic polarities of the same sign. This is analogous to counting the photospheric magnetic flux swept by flare ribbons to measure reconnection rate from direct observations [52,56]. However, this requires a very high time cadence of simulated data to capture the fast motion of the QSLs, such that the combination of all the QSLs at different times can seamlessly form the whole area that experiences reconnection. Furthermore, the geometry of QSLs is rather complex, and it is not straightforward to compute the areas swept by the QSLs. For instance, in **Figure 5A**, the QSLs at two consecutive times ($t = 6$ and 6.5) are over-plotted. As can be seen, there are clearly a margin between them, and this margin area is exactly the region swept by the QSL in the time increment (i.e., from $t = 6$ to 6.5). It is not easy to calculate the flux in this bounded area owing to its very irregular shape.

Thus, we proposed an alternative way to calculate the reconnected flux by taking advantage of the fast-slipping motion of the footpoints of the reconnected field lines. In our simulation the bottom surface is fixed without any motion, thus for any field line without reconnection, it will be perfectly frozen with the plasma, and its two footpoints will not change with time. So, if tracing from a fixed footpoint of a field line to the other end, the conjugate footpoint will also be a fixed point at different times. If the field line undergoes reconnection, the conjugate footpoint will slip to a different location in the time step, and thus by the displacement one can easily find whether the field line reconnects or not during the time step. By this approach, the region between the two QSLs at the two consecutive times is clearly enhanced, as shown in **Figures 5B,C**, and then we can calculate the reconnected flux in the time step. In **Figure 5D** all the QSLs

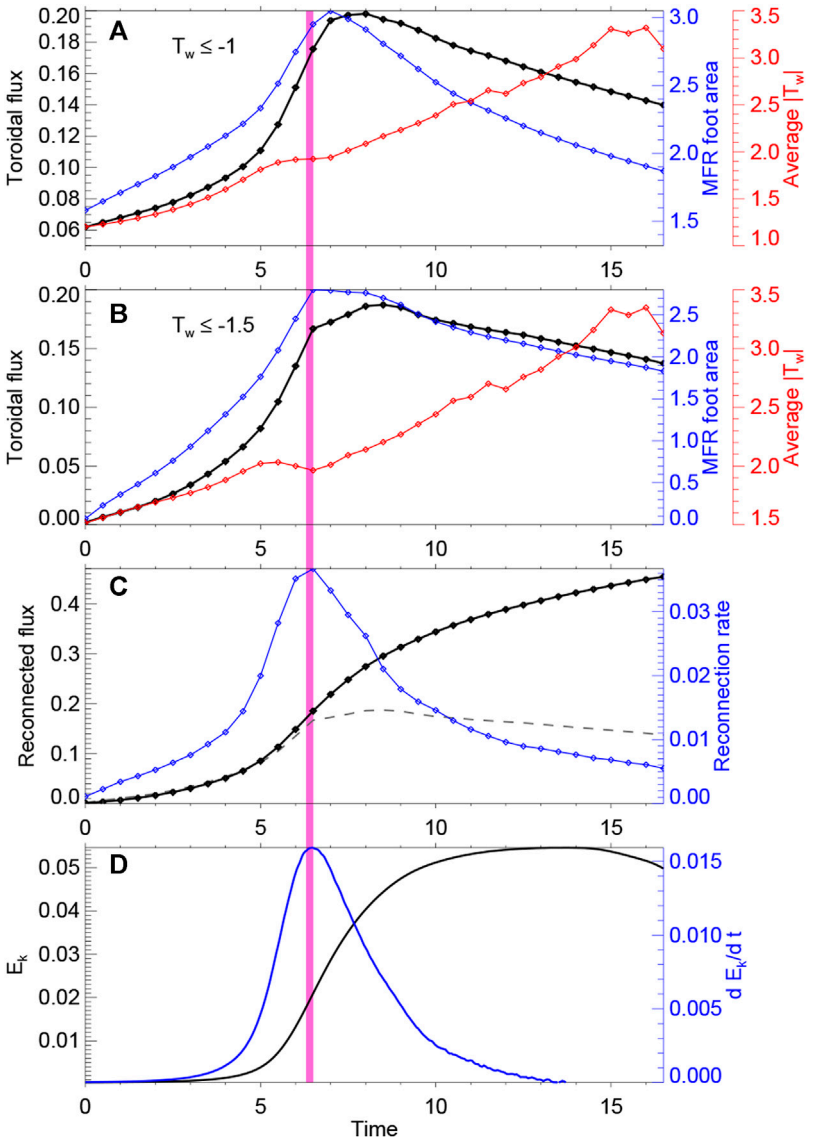

FIGURE 4 | Temporal evolution of different parameters in the eruption. **(A)** Toroidal flux (black line), foot area (blue line) and average twist number (red line) of the MFR as calculated with $T_w \le -1$. They are defined as, respectively, $\int_S B_z ds$, area of S and $\int_S B_z T_w ds / \int_S B_z ds$, in which S is the region of $T_w \le -1$ at the bottom surface. **(B)** Same as **(A)** but with $T_w \le -1.5$. **(C)** Magnetic reconnected flux and its increasing rate. The dashed line shows the toroidal flux with $T_w \le -1.5$. **(D)** Kinetic energy and its changing rate. The pink vertical bar denotes the peak time of the increasing rate of kinetic energy.

at different times (in one polarity) are overlaid, and in **Figure 5E** all the regions swept by the moving QSL are shown. We note that a large portion of the polarity is swept and therefore reconnects during the eruption, and an evident drift of the MFR foot can be seen. Interestingly, there are some regions that are swept by the QSL with more than one time, some even reaching 4 times, suggesting a rather complex internal reconnection in the erupting MFR.

The reconnection flux and its changing rate are shown in **Figure 4C**. The total reconnected flux increases monotonically, attaining nearly half of AR's total flux content at the end of the simulation. The reconnection rate, i.e., the increasing rate of the reconnected flux, shows an evolution pattern (i.e., fast increase and then slow decrease) like the changing rate of the kinetic and magnetic energies (see also **Figure 1**), and all of them reach the peak at the same time. Such temporal correlation between reconnection rate (or flare emission) and CME acceleration has been well revealed in observation studies [57,58], stressing the central role and fundamental importance of magnetic reconnection in producing flare and CME [59].

It is interesting to compare evolution of the MFR's toroidal flux and that of the reconnected flux. In **Figure 4C**, the dashed line shows the toroidal flux as present in **Figure 4B**. In the early stage, i.e., before the reconnection rate reaches its peak, the reconnected flux almost equals to the toroidal flux, meaning that the reconnection builds up the MFR by transferring the same

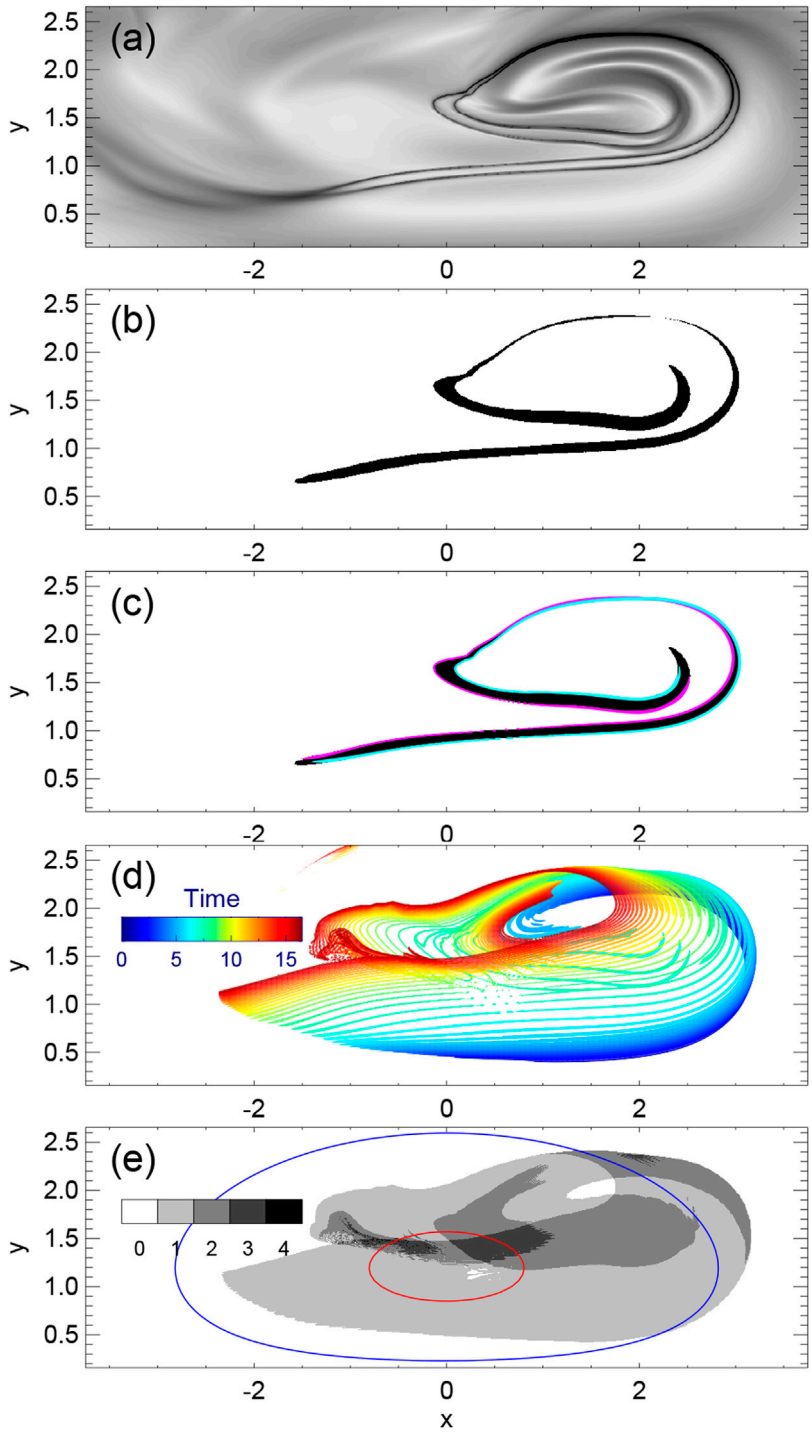

FIGURE 5 | Areas swept by the QSLs at the bottom surface. **(A)** A overlaid image of Q at two consecutive times t = 8 and 8.5. **(B)** The reconnected region (shown in black) as calculated by using the slipping of the field line footpoints. **(C)** Same as **(B)** and overlaid with the QSLs at t = 8 (colored in cyan) and t = 8.5 (colored in pink). **(D)** Overlaid plot of the QSLs at all the different times from t = 0 to 16.5. The QSLs at different times are color coded by time. **(E)** All the regions swept by the QSL. Note that some regions are swept by the QSL with more than one time, and the swept times are denoted by gray color. Two contours of B_z, 10 (red) and 5 (blue), are overlaid for showing the location of the magnetic polarity.

amount of sheared arcade flux into the same amount of flux in the rope. However, after the peak time, although the reconnected flux continues to increase, the toroidal flux in the rope decreases, and this suggesting that there must be reconnection within the MFR, by the so-called *rr-rf* reconnection [41]. We note that, interestingly, the peak time of reconnection rate (at t = 6.5) also coincides with the time of the closing of the QSLs, and immediately afterward, the toroidal flux also reaches it maximum.

4 SUMMARY

In this paper, we have studied the magnetic evolution of an MFR formed during the eruption in an MHD simulation. The MFR is generated absolutely by tether-cutting reconnection of the pre-eruption, strongly sheared arcade. In the early phase, the MFR is partially separated from its ambient field by a QSL that has a double-J shaped footprint on the bottom surface. With the ongoing of the reconnection, the arms (i.e., the straight parts) of the two J-shaped footprints continually separate from each other, which eventually pass through the centers of each polarity. Meanwhile, the hooks of the J shaped footprints expand and eventually become closed almost at the eruption peak time, and thereafter the MFR is fully separated with the un-reconnected field by a QSL. The reconnection substantially shapes the MFR by first increasing quickly and then decreasing gradually its total toroidal flux, which explains a recent observation of magnetic flux variation in erupting MFR's foot. In the whole eruption, nearly half of the AR's flux is reconnected, and the reconnection rate, as measured by the increasing rate of the reconnection flux, synchronizes well with the energy conversion rate (i.e., magnetic energy releasing rate and the kinetic energy increasing rate). In the early stage, i.e., before the reconnection rate reaches its peak, the reconnected flux almost equals to the toroidal flux in the MFR, whereas after the peak time the toroidal flux in the MFR decreases despite that the reconnected flux continues to increase. The increase of toroidal flux is owing to the flare reconnection in the early phase that transforms the sheared arcade to twisted field lines, while its decrease should be a result of reconnection between field lines in the interior of the MFR in the later phase, as first disclosed in [41].

Our simulation shows that the QSLs associated with the MFR in the later phase become more complex than expected, since there are new QSLs formed within the MFR, while the flux associated with these new QSLs becomes extremely highly twisted. This is due to a fast expansion of the MFR as well as its complex 3D nature, and thus at certain locations field lines reconnect with others in the MFR or themselves. Such reconnection may happen multiple times for field lines rooted at the same locations, even making some of field lines self-closed in the corona, which might be an important way for a CME flux to be totally detached from the Sun. The details of such complexity and the involved reconnection, and whether such complexity is hinted in observation, are to be elaborated in future works.

DATA AVAILABILITY STATEMENT

The original contributions presented in the study are included in the article/**Supplementary Material**, further inquiries can be directed to the corresponding author.

AUTHOR CONTRIBUTIONS

CJ leads this work and all contribute to the study.

ACKNOWLEDGMENTS

This work is jointly supported by National Natural Science Foundation of China (NSFC 4217040250, 41822404, 41731067) and Shenzhen Technology Project JCYJ20180306171748011. The computational work was carried out on TianHe-1(A), National Supercomputer Center in Tianjin, China.

SUPPLEMENTARY MATERIAL

The Supplementary Material for this article can be found online at: https://www.frontiersin.org/articles/10.3389/fphy.2021.746576/full#supplementary-material

REFERENCES

1. Cheng X, Guo Y, and Ding M. Origin and Structures of Solar Eruptions I: Magnetic Flux Rope. *Sci China Earth Sci* (2017) 60:1383–407. doi:10.1007/s11430-017-9074-6
2. Duan A, Jiang C, He W, Feng X, Zou P, and Cui J. A Study of Pre-flare Solar Coronal Magnetic Fields: Magnetic Flux Ropes. *ApJ* (2019) 884:73. doi:10.3847/1538-4357/ab3e33
3. Liu R. Magnetic Flux Ropes in the Solar corona: Structure and Evolution toward Eruption. *Res Astron Astrophys* (2020) 20:165. doi:10.1088/1674-4527/20/10/165
4. Wang Y, Zhuang B, Hu Q, Liu R, Shen C, and Chi Y. On the Twists of Interplanetary Magnetic Flux Ropes Observed at 1 AU. *J Geophys Res Space Phys* (2016) 121:9316–39. doi:10.1002/2016ja023075
5. Hu Q. The Grad-Shafranov Reconstruction in Twenty Years: 1996-2016. *Sci China Earth Sci* (2017) 60:1466–94. doi:10.1007/s11430-017-9067-2
6. Chen PF. Coronal Mass Ejections: Models and Their Observational Basis. *Living Rev Solar Phys* (2011) 8:1. doi:10.12942/lrsp-2011-1
7. Patsourakos S, Vourlidas A, Török T, Kliem B, Antiochos SK, Archontis V, et al. Decoding the Pre-eruptive Magnetic Field Configurations of Coronal Mass Ejections. *Space Sci Rev* (2020) 216:131. doi:10.1007/s11214-020-00757-9
8. Moore RL, and Labonte BJ. In: M Dryer and E Tandberg-Hanssen, editors. *IAU Symposium, Vol. 91, Solar and Interplanetary Dynamics* (1980). p. 207–10.
9. Moore RL, and Roumeliotis G. Lecture Notes in Physics. In: Z Svestka and BV Jackson, editors. *IAU Colloq. 133: Eruptive Solar Flares*, 399. Berlin Springer Verlag& M. E. Machado (1992). p. 69.
10. Moore RL, Sterling AC, Hudson HS, and Lemen JR. Onset of the Magnetic Explosion in Solar Flares and Coronal Mass Ejections. *ApJ* (2001) 552:833–48. doi:10.1086/320559
11. Antiochos SK, DeVore CR, and Klimchuk JA. A Model for Solar Coronal Mass Ejections. *ApJ* (1999) 510:485–93. doi:10.1086/306563

12. Aulanier G, DeLuca EE, Antiochos SK, McMullen RA, and Golub L. The Topology and Evolution of the Bastille Day Flare. *ApJ* (2000) 540:1126–42. doi:10.1086/309376
13. Lynch BJ, Antiochos SK, DeVore CR, Luhmann JG, and Zurbuchen TH. Topological Evolution of a Fast Magnetic Breakout CME in Three Dimensions. *ApJ* (2008) 683:1192–206. doi:10.1086/589738
14. Wyper PF, Antiochos SK, and DeVore CR. A Universal Model for Solar Eruptions. *Nature* (2017) 544:452–5. doi:10.1038/nature22050
15. Forbes TG, and Isenberg PA. A Catastrophe Mechanism for Coronal Mass Ejections. *ApJ* (1991) 373:294. doi:10.1086/170051
16. Lin J, Forbes TG, and Isenberg PA. Prominence Eruptions and Coronal Mass Ejections Triggered by Newly Emerging Flux. *J Geophys Res* (2001) 106: 25053–73. doi:10.1029/2001ja000046
17. Kliem B, and Török T. Torus Instability. *Phys Rev Lett* (2006) 96:255002. doi:10.1103/physrevlett.96.255002
18. Török T, and Kliem B. Confined and Ejective Eruptions of Kink-Unstable Flux Ropes. *ApJ* (2005) 630:L97–L100. doi:10.1086/462412
19. Fan Y, and Gibson SE. Onset of Coronal Mass Ejections Due to Loss of Confinement of Coronal Flux Ropes. *ApJ* (2007) 668:1232–45. doi:10.1086/521335
20. Aulanier G, Török T, Démoulin P, and DeLuca EE. Formation of Torus-Unstable Flux Ropes and Electric Currents in Erupting Sigmoids. *ApJ* (2010) 708:314–33. doi:10.1088/0004-637x/708/1/314
21. Amari T, Canou A, Aly J-J, Delyon F, and Alauzet F. Magnetic Cage and Rope as the Key for Solar Eruptions. *Nature* (2018) 554:211–5. doi:10.1038/nature24671
22. Fan Y. The Emergence of a Twisted Ω-Tube into the Solar Atmosphere. *ApJL* (2001) 554:L111–L114. doi:10.1086/320935
23. Cheung MCM, and Isobe H. Flux Emergence (Theory). *Living Rev Solar Phys* (2014) 11. doi:10.12942/lrsp-2014-3
24. Green LM, Kliem B, and Wallace AJ. Photospheric Flux Cancellation and Associated Flux Rope Formation and Eruption. *A&A* (2011) 526:A2. doi:10.1051/0004-6361/201015146
25. van Ballegooijen AA, and Martens PCH. Formation and Eruption of Solar Prominences. *ApJ* (1989) 343:971. doi:10.1086/167766
26. Song HQ, Zhang J, Chen Y, and Cheng X. Direct Observations of Magnetic Flux Rope Formation during a Solar Coronal Mass Ejection. *ApJ* (2014) 792: L40. doi:10.1088/2041-8205/792/2/l40
27. Zhou GP, Zhang J, and Wang JX. Observations of Magnetic Flux-Rope Oscillation during the Precursor Phase of a Solar Eruption. *ApJ* (2016) 823: L19. doi:10.3847/2041-8205/823/1/l19
28. Zhou GP, Tan CM, Su YN, Shen CL, Tan BL, Jin CL, et al. Multiple Magnetic Reconnections Driven by a Large-Scale Magnetic Flux Rope. *ApJ* (2019) 873: 23. doi:10.3847/1538-4357/ab01cf
29. Aulanier G, Janvier M, and Schmieder B. The Standard Flare Model in Three Dimensions. *A&A* (2012) 543:A110. doi:10.1051/0004-6361/201219311
30. Janvier M, Aulanier G, Pariat E, and Démoulin P. The Standard Flare Model in Three Dimensions. *A&A* (2013) 555:A77. doi:10.1051/0004-6361/201321164
31. Janvier M, Aulanier G, Bommier V, Schmieder B, Démoulin P, and Pariat E. Electric Currents in Flare Ribbons: Observations and Three-Dimensional Standard Model. *ApJ* (2014) 788:60. doi:10.1088/0004-637x/788/1/60
32. Jiang C, Feng X, and Hu Q. Formation and Eruption of an Active Region Sigmoid. II. Magnetohydrodynamic Simulation of a Multistage Eruption. *ApJ* (2018) 866:96. doi:10.3847/1538-4357/aadd08
33. Jiang C, Zou P, Feng X, Hu Q, Liu R, Vemareddy P, et al. Magnetohydrodynamic Simulation of the X9.3 Flare on 2017 September 6: Evolving Magnetic Topology. *ApJ* (2018) 869:13. doi:10.3847/1538-4357/aaeacc
34. Zhong Z, Guo Y, and Ding MD. The Role of Non-Axisymmetry of Magnetic Flux Rope in Constraining Solar Eruptions. *Nat Commun* (2021) 12:2734. doi:10.1038/s41467-021-24745-x
35. Demoulin P, Henoux JC, Priest ER, and Mandrini CH. Quasi-Separatrix Layers in Solar Flares. I. Method. *A&A* (1996) 308:643.
36. Titov VS, Hornig G, and Démoulin P. Theory of Magnetic Connectivity in the Solar Corona. *J Geophys Res* (2002) 107:1164. doi:10.1029/2001ja000278
37. Kahler SW, and Hudson HS. Origin and Development of Transient Coronal Holes. *J Geophys Res* (2001) 106:29239–47. doi:10.1029/2001ja000127
38. Webb DF, Lepping RP, Burlaga LF, DeForest CE, Larson DE, Martin SF, et al. The Origin and Development of the May 1997 Magnetic Cloud. *J Geophys Res* (2000) 105:27251–9. doi:10.1029/2000ja000021
39. Qiu J, Hu Q, Howard TA, and Yurchyshyn VB. On the Magnetic Flux Budget in Low-Corona Magnetic Reconnection and Interplanetary Coronal Mass Ejections. *ApJ* (2007) 659:758–72. doi:10.1086/512060
40. Xing C, Cheng X, and Ding M. Evolution of the Toroidal Flux of CME Flux Ropes during Eruption. *The Innovation* (2020) 1:100059. doi:10.1016/j.xinn.2020.100059
41. Aulanier G, and Dudík J. Drifting of the Line-Tied Footpoints of CME Flux-Ropes. *A&A* (2019) 621:A72. doi:10.1051/0004-6361/201834221
42. Wang W, Liu R, Wang Y, Hu Q, Shen C, Jiang C, et al. Buildup of a Highly Twisted Magnetic Flux Rope during a Solar Eruption. *Nat Commun* (2017) 8: 1330. doi:10.1038/s41467-017-01207-x
43. Chen H, Yang J, Ji K, and Duan Y. Observational Analysis on the Early Evolution of a CME Flux Rope: Preflare Reconnection and Flux Rope's Footpoint Drift. *ApJ* (2019) 887:118. doi:10.3847/1538-4357/ab527e
44. Jiang C, Feng X, Liu R, Yan X, Hu Q, Moore RL, et al. A Fundamental Mechanism of Solar Eruption Initiation. *Nat Astron* (2021). doi:10.1038/s41550-021-01414-z
45. Inoue S, Hayashi K, Shiota D, Magara T, and Choe GS. Magnetic Structure Producing X- and M-Class Solar Flares in Solar Active Region 11158. *ApJ* (2013) 770:79. doi:10.1088/0004-637x/770/1/79
46. Savcheva A, Pariat E, McKillop S, McCauley P, Hanson E, Su Y, et al. The Relation between Solar Eruption Topologies and Observed Flare Features. Ii. Dynamical Evolution. *ApJ* (2016) 817:43. doi:10.3847/0004-637x/817/1/43
47. Liu R, Kliem B, Titov VS, Chen J, Wang Y, Wang H, et al. Structure, Stability, and Evolution of Magnetic Flux Ropes from the Perspective of Magnetic Twist. *ApJ* (2016) 818:148. doi:10.3847/0004-637x/818/2/148
48. Berger MA, and Prior C. The Writhe of Open and Closed Curves. *J Phys A: Math Gen* (2006) 39:8321–48. doi:10.1088/0305-4470/39/26/005
49. Linker JA, Mikić Z, Lionello R, Riley P, Amari T, and Odstrcil D. Flux Cancellation and Coronal Mass Ejections. *Phys Plasmas* (2003) 10:1971–8. doi:10.1063/1.1563668
50. Amari T, Luciani JF, Aly JJ, Mikic Z, and Linker J. Coronal Mass Ejection: Initiation, Magnetic Helicity, and Flux Ropes. I. Boundary Motion-Driven Evolution. *ApJ* (2003) 585:1073–86. doi:10.1086/345501
51. Török T, Downs C, Linker JA, Lionello R, Titov VS, Mikić Z, et al. Sun-to-Earth MHD Simulation of the 2000 July 14 "Bastille Day" Eruption. *ApJ* (2018) 856:75. doi:10.3847/1538-4357/aab36d
52. Wang H, Qiu J, Jing J, and Zhang H. Study of Ribbon Separation of a Flare Associated with a Quiescent Filament Eruption. *ApJ* (2003) 593:564–70. doi:10.1086/376360
53. Qiu J, Gary DE, and Fleishman GD. Evaluating Mean Magnetic Field in Flare Loops. *Sol Phys* (2009) 255:107–18. doi:10.1007/s11207-009-9316-y
54. Hinterreiter J, Veronig AM, Thalmann JK, Tschernitz J, and Pötzi W. Statistical Properties of Ribbon Evolution and Reconnection Electric Fields in Eruptive and Confined Flares. *Sol Phys* (2018) 293:38. doi:10.1007/s11207-018-1253-1
55. Yan XL, Wang JC, Pan GM, Kong DF, Xue ZK, Yang LH, et al. Successive X-Class Flares and Coronal Mass Ejections Driven by Shearing Motion and Sunspot Rotation in Active Region NOAA 12673. *ApJ* (2018) 856:79. doi:10.3847/1538-4357/aab153
56. Qiu J, Lee J, Gary DE, and Wang H. Motion of Flare Footpoint Emission and Inferred Electric Field in Reconnecting Current Sheets. *ApJ* (2002) 565: 1335–47. doi:10.1086/324706
57. Zhang J, Dere KP, Howard RA, Kundu MR, and White SM. On the Temporal Relationship between Coronal Mass Ejections and Flares. *ApJ* (2001) 559: 452–62. doi:10.1086/322405
58. Qiu J, Wang H, Cheng CZ, and Gary DE. Magnetic Reconnection and Mass Acceleration in Flare-Coronal Mass Ejection Events. *ApJ* (2004) 604:900–5. doi:10.1086/382122
59. Zhu C, Qiu J, Liewer P, Vourlidas A, Spiegel M, and Hu Q. How Does Magnetic Reconnection Drive the Early-Stage Evolution of Coronal Mass

Ejections. *ApJ* (2020) 893:141, 2020 . arXiv: 2003.11134. doi:10.3847/1538-4357/ab838a

Conflict of Interest: The authors declare that the research was conducted in the absence of any commercial or financial relationships that could be construed as a potential conflict of interest.

Publisher's Note: All claims expressed in this article are solely those of the authors and do not necessarily represent those of their affiliated organizations, or those of the publisher, the editors and the reviewers. Any product that may be evaluated in this article, or claim that may be made by its manufacturer, is not guaranteed or endorsed by the publisher.

frontiers in Physics

ORIGINAL RESEARCH
published: 15 October 2021
doi: 10.3389/fphy.2021.749479

Magnetic Structure in Successively Erupting Active Regions: Comparison of Flare-Ribbons With Quasi-Separatrix Layers

P. Vemareddy *

Indian Institute of Astrophysics, Bengaluru, India

This paper studies the magnetic topology of successively erupting active regions (ARs) 11,429 and 12,371. Employing vector magnetic field observations from Helioseismic and Magnetic Imager, the pre-eruptive magnetic structure is reconstructed by a model of non-linear force-free field (NLFFF). For all the five CMEs from these ARs, the pre-eruptive magnetic structure identifies an inverse-S sigmoid consistent with the coronal plasma tracers in EUV observations. In all the eruption cases, the quasi-separatrix layers (QSLs) of large Q values are continuously enclosing core field bipolar regions in which inverse-S shaped flare ribbons are observed. These QSLs essentially represent the large connectivity gradients between the domains of twisted core flux within the inner bipolar region and the surrounding potential like arcade. It is consistent with the observed field structure largely with the sheared arcade. The QSL maps in the chromosphere are compared with the flare-ribbons observed at the peak time of the flares. The flare ribbons are largely inverse-S shape morphology with their continuity of visibility is missing in the observations. For the CMEs in the AR 12371, the QSLs outline the flare ribbons as a combination of two inverse J-shape sections with their straight parts being separated. These QSLs are typical with the weakly twisted flux rope. Similarly, for the CMEs in the AR 11429, the QSLs are co-spatial with the flare ribbons both in the middle of the PIL and in the hook sections. In the frame work of standard model of eruptions, the observed flare ribbons are the characteristic of the pre-eruptive magnetic structure being sigmoid which is reproduced by the NLFFF model with a weakly twisted flux rope at the core.

Keywords: Sun: CMEs, Sun: magnetic flux ropes, Sun: magnetic fields, Sun: flares, Sun: active region

OPEN ACCESS

Edited by:
HengQiang Feng,
Luoyang Normal University, China

Reviewed by:
Hongqiang Song,
Shandong University, China
Yang Guo,
Nanjing University, China

****Correspondence:***
P. Vemareddy
vemareddy@iiap.res.in

Specialty section:
This article was submitted to Stellar and Solar Physics, a section of the journal Frontiers in Physics

Received: *29 July 2021*
Accepted: *27 September 2021*
Published: *15 October 2021*

Citation:
Vemareddy P (2021) Magnetic Structure in Successively Erupting Active Regions: Comparison of Flare-Ribbons With Quasi-Separatrix Layers. Front. Phys. 9:749479. doi: 10.3389/fphy.2021.749479

1 INTRODUCTION

Most often the coronal mass ejections are seen to launch from magnetically concentrated regions called active regions (ARs). In soft X-rays or in EUV images, the ARs that precede CMEs are seen with the observational features of S- and J-shaped loops situated over along the polarity inversion line (PIL). Owing to this specific S- or inverted S-shape, [1] termed these regions as sigmoids and are considered to be one of the most important precursor structures for the solar eruptions [2–4].

The shape of the sigmoid indicates the loops composed of non-potential magnetic field configuration characterised by sheared and/or twisted magnetic field lines. As a reason, the magnetic structure of the sigmoids are described by two competing configurations that are sheared arcade and magnetic flux rope (MFR). In the sheared arcade model, the two magnetic

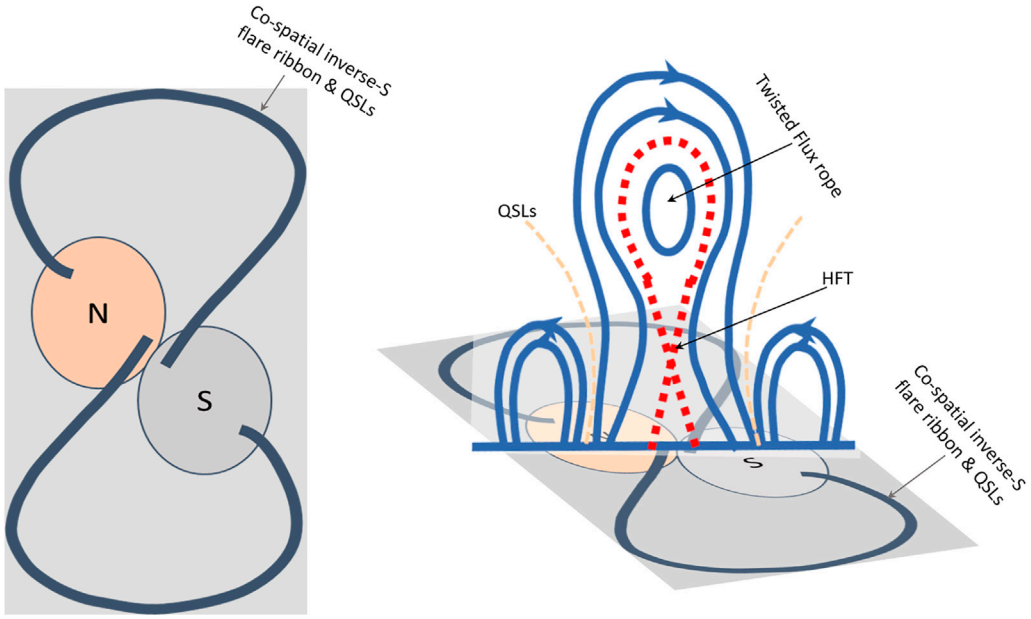

FIGURE 1 | Schematic of the 3D standard model for eruptive flares. **left panel:** Black thick curves indicate the inverse-S QSL footprints at the photosphere. "N" ("S") refers to north (south) polarity magnetic flux distribution. These inverse-S QSLs are regarded as the combination of two inverse-J shaped sections with straight parts lying in the opposite polarities about the PIL. **right panel:** Perspective view of the erupting flux rope structure and HFT underneath in a vertical plane across the MFR. Erupting MFRs form flare ribbons which trace these photospheric QSL footpoints.

elbows sheared past each other are situated at the opposite ends of the PIL with a central sheared core at the middle section of the PIL [5,6]. And in the MFR scenario, a magnetic MFR is embedded in a stabilizing potential envelope field [1,7,8]. Because of the non-potential nature of the magnetic field, the magnetic structure in the sigmoid is approximated with a non-linear force-free field (NLFFF) which allows different twist parameter for individual field lines. The force-free modeling is justified by the low-β corona with a slowly evolving field compared to the Alfven crossing time.

To understand the eruptive nature of sigmoidal regions, it is important to study their magnetic structure and evolution both theoretically and observationally. Observations showed that the magnetic flux ropes have frequently been associated with sigmoidal regions [1,9–13] and the modelled NLFFF magnetic configuration that describes the observed shape of sigmoids is a weakly twisted flux rope embedded in potential arcade [14–18]. The flux rope structure constructed from analytical configurations [4,19,20] exhibits current sheets in the magnetic interface layers called quasi-separatrix layers (QSLs) where the connectivity of the field lines changes drastically just like separatrix layers. In the process of emerging, such a MFR develops a separatrix surface touching the photosphere along the PIL section [21,22]. These sections of the PIL are called bald-patches (BPs) and the separatrix surface at the BP appears as an S-shape from top view similar to sigmoid shape. After the emergence phase, the S-shaped bald-patch separatrix surface (BPSS) bifurcates into a double J-shaped QSL with the main body of the MFR lifted off. From this BPSS topology, the QSL structure underneath the rising flux rope develops an X-line configuration referred to as hyperbolic flux tube (HFT), where the reconnection sets in for the onset of the eruption. Therefore, the HFT topology is the predicted site for flare reconnection and CME eruption [23]. Further, the topological analysis of the MFR configurations, both models and observations, recommends the extension of the standard CHSHK flare model [24–27] to 3D. In the 2D flare model two flare ribbons are observed on either side of the PIL, whereas MFR eruptions found co-spatial flare ribbons with hook-shaped QSLs [15,28–30]. **Figure 1** displays the schematic of the 3D standard model for eruptive flares as interpreted from simulations of eruptive MFRs [21,28,31]. In the left panel, the hook-shape inverse-S shaped QSLs in the photosphere are shown in thick black curves. The HFT underneath the uplifting MFR is depicted in the right panel as seen from perspective view. The photospheric QSL footpoints are co-spatial with flare ribbons in the 3D-eruptive flare models which is a signature of the MFR topology.

Motivated by the above topological studies of the erupting regions, in this paper, we study the pre-eruptive magnetic structure of five CMEs from two successively erupting ARs. The coronal field is constructed by NLFFF [32], then we computed the chromospheric QSLs to compare their spatial locations with the geometry of the observed flare ribbons. By this comparison, one can ascertain the model predictions of the topological features with the observations, and then also validate the extent of the invoked NLFFF model to reproduce the actual coronal field. The paper is organized as follows. In **Section 2**, an overview of the CME events with a brief description of results presented in the previous reports. Reconstruction of the magnetic

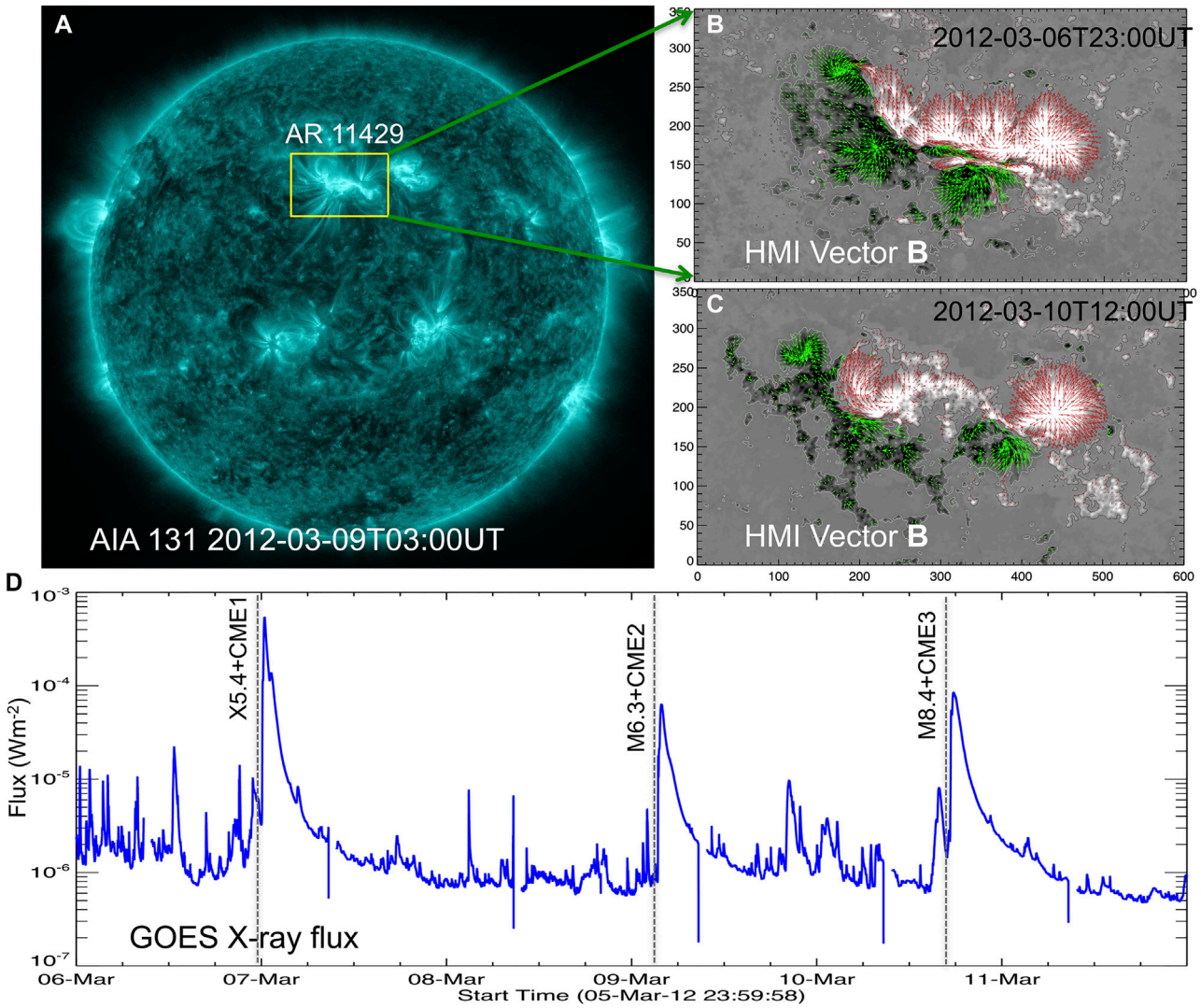

FIGURE 2 | Observations of the successively erupting AR 11429 **(A)** Full disk observation of AIA 131 Å. The structured emission from AR 11429 is outlined with yellow rectangular box, **(B-C)** HMI vector magnetogram observations of the AR 11429 at the onset of CME eruptions on March 6 and 10 respectively. The background image is vertical magnetic field with contours at ±120 G. Green/red arrows denote horizontal field with their length being proportional to the magnitude $B_h = \sqrt{(B_x^2 + B_y^2)}$. *Axis* units are pixels of 0.5 arc-second, **(D)** Disk integrated GOES X-ray flux in 1–8 Å band during the disk transit time of the AR 11429. Text near the X-rays peaks refers to the CMEs and associated X, M-class flares from the AR 11429.

structure by NLFFF modeling is presented in **Section 3**. Comparison of the QSLs with the flare-ribbons is made in **Section 4** and concluded with a summarized discussion in **Section 5**.

2 OVERVIEW OF THE OBSERVATIONS

Observations of the successive eruptions from the ARs 11429 and 12371 are obtained from the Atmospheric Imaging Assembly (AIA [33]) and Helioseismic Magnetic Imager (HMI [34]) on board NASA's space-based Solar Dynamics Observatory (SDO). The AIA instrument captures the full disc images of the solar corona in 10 wavelengths at 0.6 arcsec pixel^{-1} resolution. The HMI provides photospheric line of sight and vector magnetic field observations at 0.5 arcsec pixel^{-1} resolution in Fe I 6,173 Å wavelength. The pipeline procedures of deriving the vector magnetic fields from the Stokes filter images are documented in [35] and [36]. We used vector magnetic field data product `hmi.sharp_cea_720s` at a cadence of 720s. Additional information of the CME eruptions is obtained from web portals like CME catalog[1], and solar monitor[2].

The AR 11429 was a pre-emerged one probably on far-side of the Sun. **Figure 2** demonstrates the eruption scenario in this AR 11429. In panel 2a. the full disk image of AIA 131 Å shows the

[1]https://cdaw.gsfc.nasa.gov/CME_list/
[2]https://www.solarmonitor.org

TABLE 1 | Information of CME eruptions and associated flares from the studied ARs.

Event	Flare peak time [UT]	Location	Associated flare [UT]	CME speed [Km/s]
		AR NOAA 11429		
CME1	SOL2012-03–07T00:24	N17°E31°	X5.4 (00:24)	1825
CME2	SOL2012-03–09T03:53	N15°W03°	M6.3 (03:53)	950
CME3	SOL2012-03–10T17:44	N17°W24°	M8.4 (17:44)	1,296
		AR NOAA 12371		
CME1	SOL2015-06–18T17:35	N10°E50°	M3.1 (17:35)	1,305
CME2	SOL2015-06–21T02:36	N12°E16°	M2.2 M2.7 (02:36)	1,366
CME3	SOL2015-06–22T18:23	N13°W06°	M6.5 (18:23)	1,209
CME4	SOL2015-06–25T08:16	N12°W40°	M7.9 (08:16)	1,627

The bold values refer to the events in the AR by name 11429 and 12371.

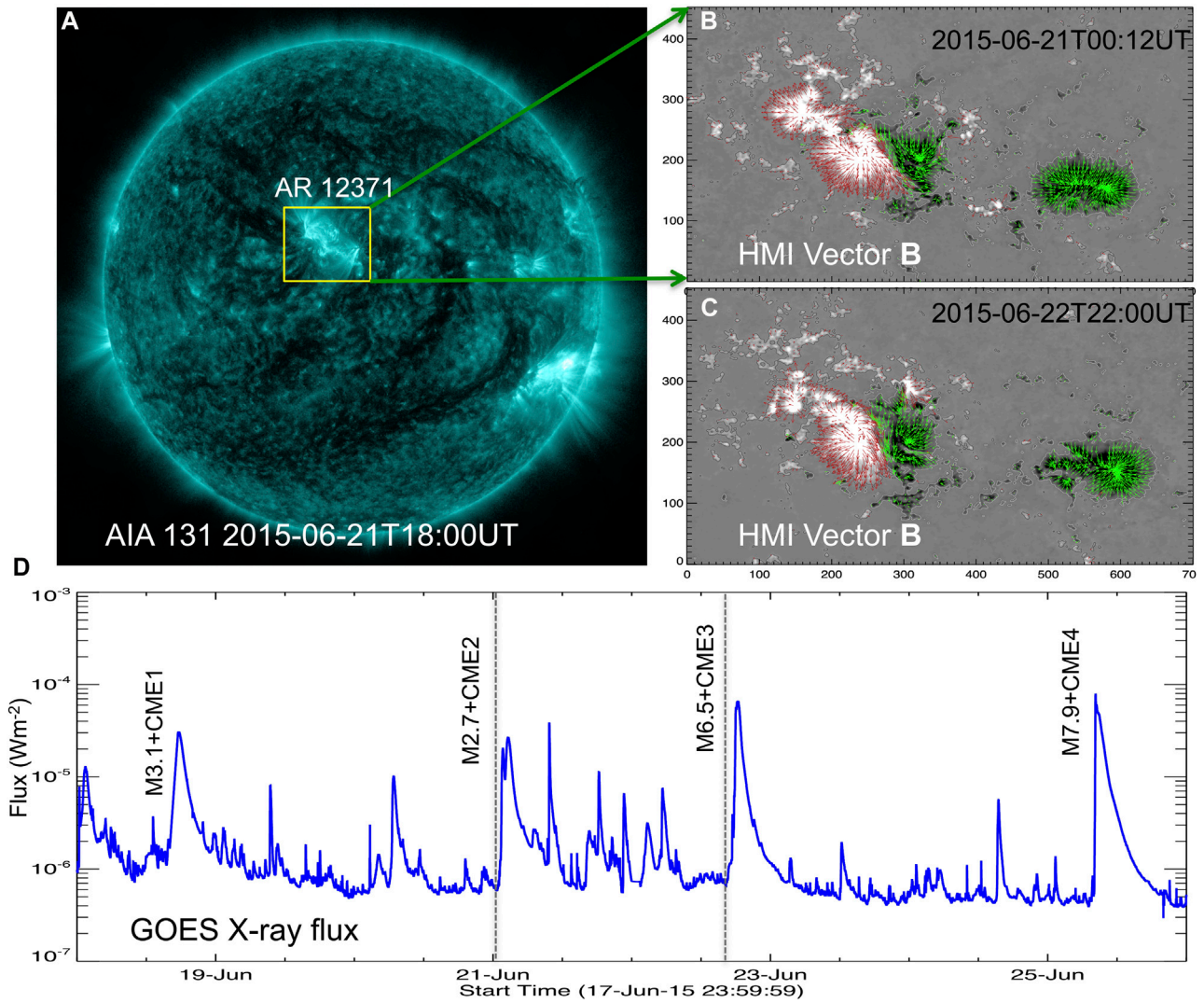

FIGURE 3 | Observations of the successively erupting AR 12371 **(A)** Full disk observation of AIA 131 Å. The structured emission from AR 12371 is outlined with yellow rectangular box, **(B-C)** HMI vector magnetogram observations of the AR 12371 at the onset of CME eruptions on June 21 and 22 respectively. The background image is vertical magnetic field with contours at ±120 G. Green/red arrows denote horizontal field vector whose length is proportional to magnitude $B_h = \sqrt{(B_x^2 + B_y^2)}$. *Axis* units are pixels of 0.5 arc-second units, **(D)** Disk integrated GOES X-ray flux in 1–8 Å band during the disk transit time of the AR 12371. Text near the X-ray peaks refers to the CMEs and associated M-class flares from the AR 12371. The events marked with vertical lines are studied in this work.

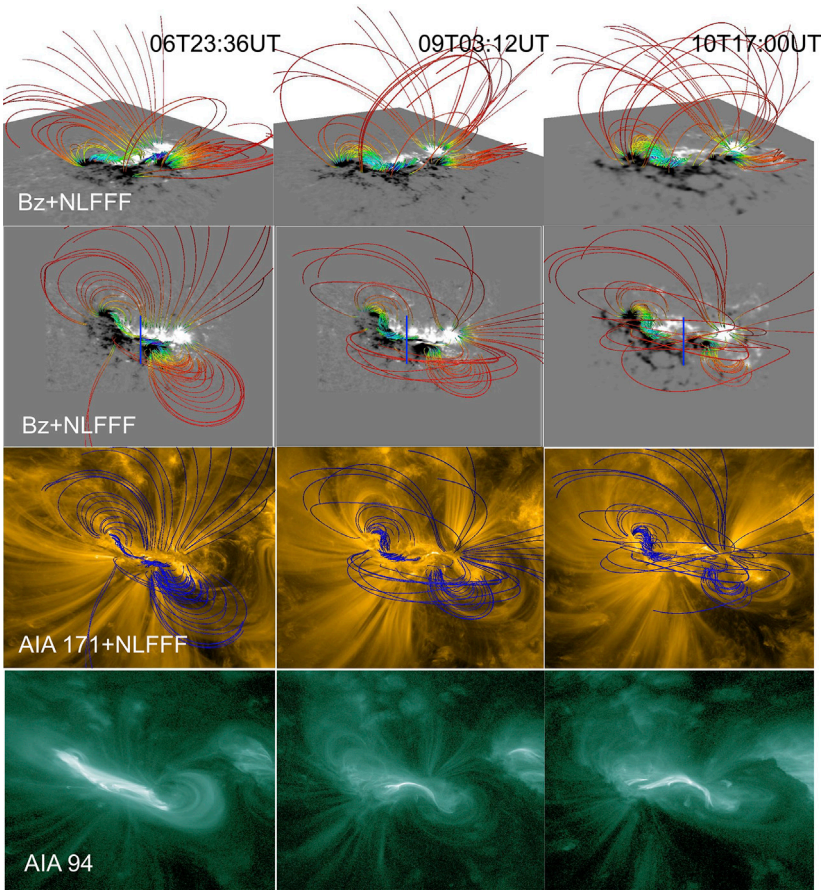

FIGURE 4 | Pre-eruptive magnetic structure modeled by NLFFF in the AR 11429 for the three CME events. **First row:** Perspective view of the field-line rendering. Bottom image is photospheric magnetogram (B_z). Twisted structure along the PIL is overlaid by the less sheared field lines **Second row:** field lines plotted on top of the photospheric magnetogram (Bz). The global structure is a sigmoid with two opposite-J-shaped loops and an inner core of highly twisted field. Vertical blue lines indicate the location of the slice plane for QSL analysis. **Third row:** same field lines on AIA 171 Å images, **Fourth row:** AIA 94 Å images at the same time. Hot plasma emission is mainly co-spatial with the strongly sheared core along the PIL. To a good approximation, the modeled structure resembles the coronal plasma loops in the EUV images. Field lines are color coded (blue (red): 1,200 (2)G) with the horizontal field strength in height in first and second rows.

structured coronal emission from the AR 11429 (yellow rectangular box) located in the north (N17°) hemisphere. HMI observations of the photospheric vector magnetograms at the pre-eruption time on two different days are displayed in panels 2 (b-c). The AR presents a large interface opposite polarities known as polarity inversion line (PIL). These magnetic polarities evolve with persistent shearing and converging motions which led to continuous flux cancellation as observed with the decay of the magnetic flux regions. Such regions are favorable to form stored energy configurations of sheared magnetic fields along the PIL. As a result, the AR evolved to a much more complex magnetic configuration ($\beta/\gamma/\delta$) producing severe flare/CME activity during its disk transit. In Panel 2(c), GOES X-ray flux (1–8 Å band) displays the peaks of one X and two M-class flares associated with the CME eruptions from the AR 11429. Because of recurrent eruptions from the same region under a continuous physical process, these eruptions are referred to as homologous eruptions [37,38]. Study of this AR by [39] suggests that the shearing motion and magnetic flux cancellation by converging fluxes were key processes to recurrently form the erupting structure and then its eruption. Details of the CME eruptions from this AR are listed in **Table 1**.

Another recurrent CME producing AR was NOAA 12371, which was also a pre-emerged region that passes the visible solar disk 12°N on June 16, 2015. **Figure 3** presents the eruption scenario of this AR. A representative AIA 131 Å full disk image is displayed in panel 3a, which shows the sigmoidal morphology of AR corona (yellow rectangular box). Panels 3 (b-c) display the HMI vector magnetograms at the pre-eruption time on June 21 and 22. The AR essentially consists of a leading negative flux region with the following interacting opposite polarity regions. From these magnetic field observations, the AR's disk passage reveals that the following bipolar region was seen with large shear and converging motion as a result the flux distribution becomes diffused and disintegrated in successive days. As in the earlier AR, such an evolution of magnetic polarities leads to formation of the twisted flux along the PIL, which indeed is revealed by the sigmoidal loop structure in the EUV images. Four major CME

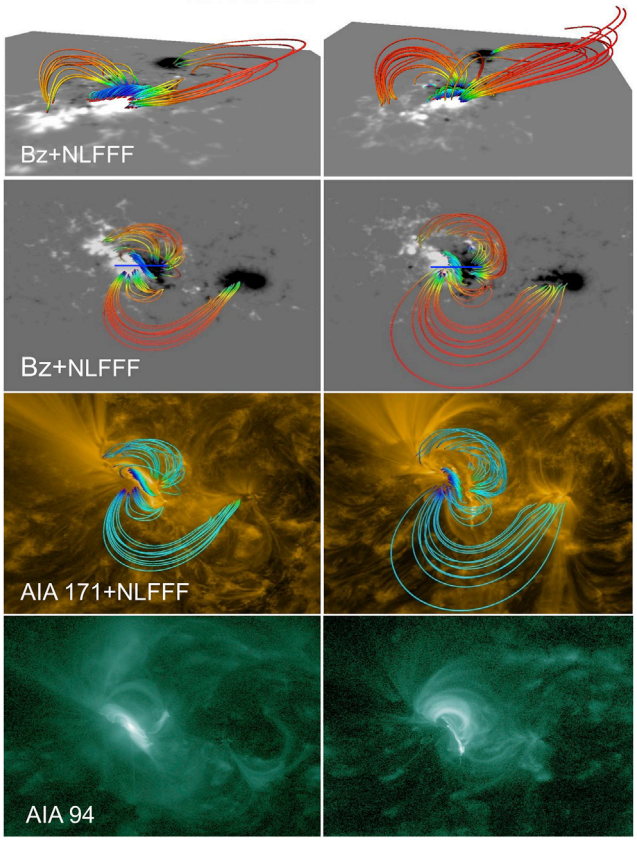

FIGURE 5 | Pre-eruptive magnetic structure modeled by NLFFF in the AR 12371 for the CME2 and CME3 events. **First row:** Perspective view of the field-line rendering. Bottom image is photospheric magnetogram (B_z). Twisted structure along the PIL is overlaid by the less sheared field lines **Second row:** field lines plotted on top of the photospheric magnetogram (B_z). The global structure is a sigmoid with two opposite-J-shaped sections and an inner core of highly twisted field. Horizontal blue lines indicate the location of the slice plane for QSL analysis. **Third row:** same field lines on AIA 171 Å images, **Fourth row:** AIA 94 Å images at the same time. Hot plasma emission is mainly co-spatial with the strongly sheared core along the PIL. To a good approximation, the modeled structure resembles the coronal plasma loops in the EUV images. Field lines are color coded (blue (red): 1,200 (2)G) with the horizontal field strength in height in first and second rows.

eruptions occurred associated with M-class flares from this AR as shown by the peaks in the GOES X-ray flux plot of panel 3c. A detailed study of this AR by [40] interprets the successive eruptions by the cyclic process of energy and helicity storage over a time scale of a day or two and then its release by the CME eruptions. **Table 1** lists the CME eruptions and associated flares from this AR.

3 MODELLED MAGNETIC STRUCTURE: NON-LINEAR FORCE-FREE FIELD

The AR magnetic structure in 3D is modelled by applying the NLFFF extrapolation [32,41,42]. The NLFFF algorithm involves minimization of the functional

$$L = \int_V \left(w \frac{|(\nabla \times \mathbf{B}) \times \mathbf{B}|^2}{B^2} + w|\nabla \bullet \mathbf{B}|^2 \right) dV + \nu \int_S (\mathbf{B} - \mathbf{B}_{\rm obs}) \cdot W \cdot (\mathbf{B} - \mathbf{B}_{\rm obs})\, dS. \quad (1)$$

In the above equation, the first integral includes quadratic forms of the force-free and solenoidal conditions and w is a weighting function toward the lateral and top boundaries. Second term is surface integral to take into account measurement errors and allows a slow injection of the boundary data controlled by the Lagrangian multiplier ν (see [42], for more details). $W(x, y)$ is a diagonal matrix, which is chosen inversely proportional to the transverse magnetic field strength.

The observed photospheric vector magnetic field from the HMI is used as the lower boundary condition, for which the field has to satisfy flux balance, force-free conditions. When the vector magnetic field has full coverage of the AR, the flux balance condition is normally satisfied within 10% deviation. To keep this value as small as possible, we multiply the positive polarity region with a relative flux factor defined by the ratio of positive and negative flux. The force-free conditions are further satisfied by applying a pre-processing procedure on the magnetic field components [43]. To facilitate tracing field lines in a large extent of volume comparable to EUV field-of-view, the boundary magnetic field observations are inserted in an extended field of view and then rebinned to 1 arcsec pixel^{-1}. With the normal field component of magnetic field, we reconstructed the 3D potential field (PF) which is then used as the initial condition and also to prescribe the top and side boundaries for the NLFFF algorithm.

In **Figure 4**, we show the NLFFF magnetic structure of AR 11429 just before the CME events on March 6, 9 and 10. The NLFFF is constructed on a grid of 450 × 450 × 201 representing the physical dimensions of 328 × 328 × 146 Mm^3 AR corona. Similarly in **Figure 5**, we show the NLFFF magnetic structure of AR 12371 just before the CME events on June 21 and 22. In this case, the NLFFF field is constructed on a grid of 512 × 512 × 256 representing the physical dimensions of 373 × 373 × 186 Mm^3 AR corona. For all of the cases, the NLFFF relaxation converges to an average field divergence of the order 10^{-4} and an average field-aligned current defined by θ_J to an extent 9–12°.

To capture the most sheared structure, the field lines are rendered according to total current density (|J|) and horizontal field component (B_h) at the bottom boundary. The field line rendering is shown in perspective and top views in first and second rows respectively of **Figures 4**, **5**. In these panels, the bottom plane is an observed B_z map. The field rendering in these panels comprise two inverse J-shaped field lines sheared past each other about the main PIL, which together reveal the shape of the inverse S-sigmoid. Owing to shearing motions of the foot points, the field lines near PIL are strongly stressed, manifesting low lying twisted core of the sigmoid, which is regarded as flux rope with helical field lines. During the onset of the eruption, this flux rope builds up further by the reconnection of oppositely sheared field, and therefore is the central structure of the solar eruptions [5,44].

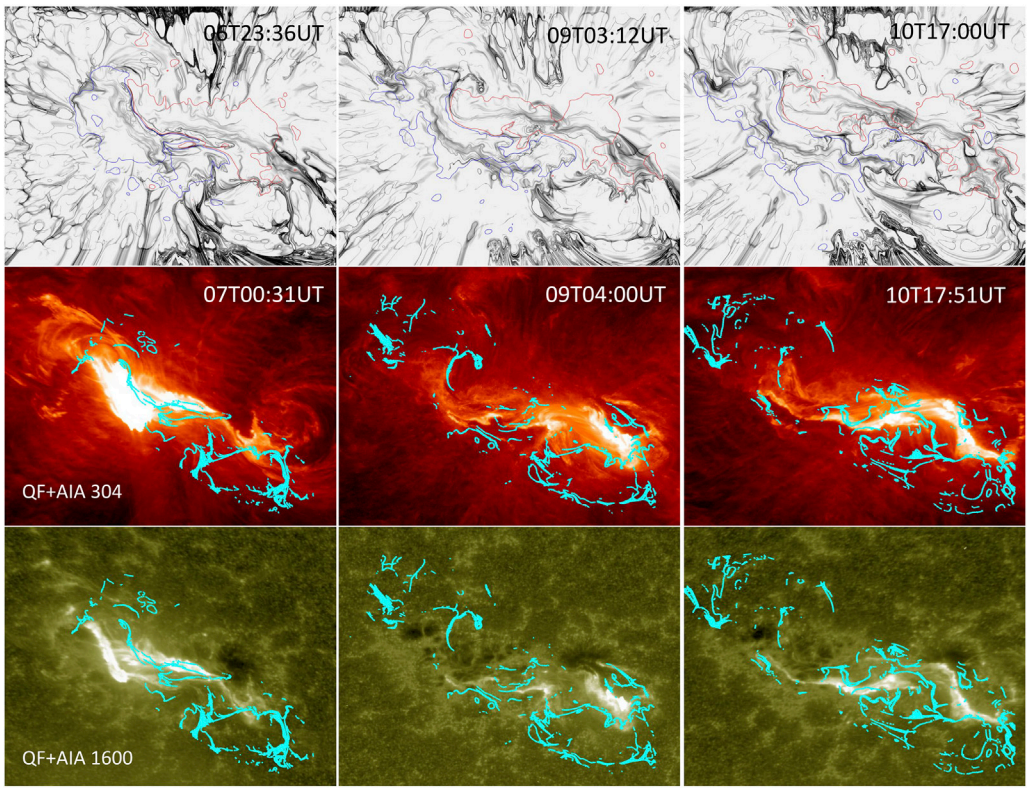

FIGURE 6 | Comparison of QSLs and flare ribbons for the pre-eruptive magnetic structure of CME1 (first column), CME2 (second column), CME3 (third column) in the AR 11429. **First row:** Inverse maps of Log(Q) obtained at $z = 1.5$ *Mm*. B_z-contours at ±120 G are overdrawn (red/blue curves). QSLs with large Q values are identified by intense black traces in strong field region. All maps are scaled within $1 < \text{Log}(Q) < 7$. QSLs of large Q-values separate the sheared/twisted core field from the surrounding less sheared field in the following bipolar region. Also higher Q-values in quiet regions are due to noisy transverse field and have no relevance to the magnetic structure of interest. **Second and third rows:** Co-spatiality of QSLs and flare ribbons. Contours of Log(Q)=[4,5,6] (in cyan color) on AIA 304 Å (second row) and AIA 1600 Å (third row) snapshots taken at around the peak flare time. QSLs are co-spatial with the flare ribbons including the hooked shape.

In order to judge the NLFFF model to the coronal magnetic field, the modeled magnetic structure is compared to EUV coronal observations. To this end, we ensure that the EUV images are co-aligned to the magnetic field with the same field-of-view. The same field line rendering is over-plotted on EUV observations of corona captured in AIA 171 Å images (second row panels) which delineates a good global resemblance of the field lines with the plasma tracers. Because of the strong volume currents, the intense hot emission in AIA 94 Å images is mostly co-spatial with the NLFFF twisted core along the PIL.

4 QUASI-SEPARATRIX LAYERS AND FLARE RIBBONS

QSLs are the regions of the magnetic volume where the field line connectivity experiences dramatic but continuous variations, including possible discontinuities in the mapping, so are the generalized features to the separatrices [45]. From the constructed 3D coronal fields, the change in magnetic field line linkage in the volume is measured by the strength of QSLs which is defined by squashing factor Q [22,46]. Q describes the gradients in the field line mapping whose larger values correspond to the cross section of QSLs in any plane. It is computed by tracing two consecutive field lines with foot points at an extremely small distance and then measuring the distance between the respective conjugate foot points as given by the following mathematical expression

$$Q = \frac{\sum_{i,j=1}^{2} \left(\frac{\partial X_i}{\partial x_j}\right)^2}{|B_{z,0}/B_{z,1}|}, \tag{2}$$

where X_i (i = 1, 2) is the coordinates of the conjugate foot point in the Cartesian system and $B_{z,0}$ and $B_{z,1}$ are vertical field components at the starting and ending footpoints of a field line. From the 3D NLFFF, we calculate Q using the code developed by [47] according to formalism prescribed in [28]. The field lines are traced by integrating the first order differential equations by fourth order Runge-Kutta solver with the help of tri-linear interpolation scheme. To have a smooth and dense distribution of Q, these computations are performed on a finer grid of resolution increased by eight times that of the extrapolation grid.

The complexity in the QSL maps of the NLFFF model is intrinsic to the large amount of fragmentation in the observed

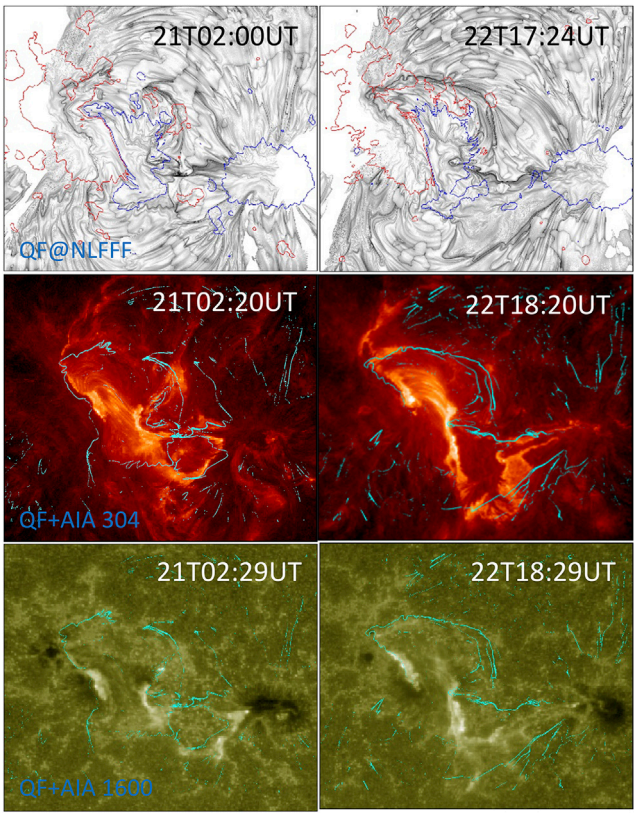

FIGURE 7 | Comparison of QSLs and flare ribbons for the pre-eruptive magnetic structure of CME2 (first column) and CME3 (second column) in the AR 12371. **First row:** Inverse maps of Log(*Q*) obtained at z =1.5 *Mm*. B_z-contours at ±120 G are overdrawn (red/blue curves). QSLs with large Q values are identified by intense black traces in strong field region. All maps are scaled within 1< Log(*Q*)<7. QSLs of large Q-values separate the sheared/twisted core field from the surrounding less sheared field in the following bipolar region. Also higher Q-values in quiet regions are due to noisy transverse field and have no relevance to the magnetic structure of interest. **Second and third rows:** Relation between QSLs and flare ribbons. Contours of Log(*Q*)=[5,6] (in cyan color) on AIA 304 Å (second row) and AIA 1600 Å (third row) snapshots taken at around the peak flare time. The contours constitute two inverse-J sections, qualitatively outlining the inverse-S flare ribbons.

photospheric magnetic-field distribution. It has been shown that the complexity of QSL maps decreases with the height [14]. This is a consequence of the magnetic field being progressively smoother with height. Therefore, to determine important QSLs, Q maps are computed at 1.5 Mm height above the photosphere, which we refer chromospheric QSLs in this manuscript discussion.

In the first row panels of **Figures 6**, **7**, we plot log Q maps at z = 1.5 *Mm* with inverse sign, so the darker parts correspond to higher Q values. For a reference, B_z contours of ±120G are over-plotted. Due to noisy transverse field, the Q maps of NLFFF are more fragmented in weak field regions. The relevant QSLs are having large Q values (>10^7) located in the stronger magnetic polarities related to the sigmoid structure. In panel of 23:36UT on March 6, the relevant QSLs traces the PIL in addition to the QSLs in the hooked sections in the top and bottom of the sigmoid. A similar distribution is presented in other panels. As seen in the 02:00 UT map on June 21, the QSL of high-Q values have two sections each falling in the opposite polarity regions of inner bipolar regions, both of which extends towards leading negative polarity. These two sections joined at the top in positive polarity. Although lower part have smaller values of Q, this overall QSL is continuous and encloses an inverse S-shaped region filled with lower Q-values. Essentially, these QSL highlights the difference between the twisted core flux within the region and the surrounding potential like arcade outside.

This picture is even clearer in the vertical cross-section map of Q obtained across the sigmoid. These are shown in **Figures 8**, **9**. B_z-contours (±80G, red for positive, blue for negative), obtained in the same cut-plane, are over-plotted. Different from horizontal maps, the vertical Q maps are smooth with an obvious relevance with the magnetic polarities about the PIL. In these maps, the QSLs of large Q values well distinguish two closed domains belonging to largely sheared sections on either side of the PIL and the surrounding potential like arcade. Importantly the QSLs intersect the magnetic polarities at the middle in the NLFFF, whereas they cover the entire polarity region in the PF. This is clearly an indication of a sheared core being surrounded by less-sheared/potential arcade in the AR. Given the twisted flux (flux rope) at the core, the QSLs in its cross section mimics a inverse tear-drop shape as predicted by the theoretical models quoted in the Introduction. Depending on the degree of the twist, the identification of such QSLs varies due to observational and modeling difficulties (see for example **Figure 8** in [48] and **Figure 4** in [15]). In our NLFFF structures of the five CMEs, it is mildly visible as shown in **Figures 8**, **9**. For a comparison with flare ribbons, the corresponding AIA 304 Å 1,600 Å observations are displayed in the second and third row panels of **Figures 6**, **7** respectively. On these maps, contours of Q for the corresponding event at 10^5, 10^6 levels are over-plotted in cyan-color. Note that we are comparing pre-eruptive Q-maps with the ribbons at around peak time of the flare of each eruption. Owing to noisy transverse field, and the discontinuous field distribution, the Q maps have patchy structure and we further apply a small threshold $|B_z| < 15$ G to remove non-relevant QSLs. In addition, irrelevant QSLs are removed by applying a mask on the computed Q-maps.

The correspondence between the photospheric QSLs and flare ribbons has been shown in several studies. Theoretical studies predict that the flare ribbons are the photospheric foot prints of QSLs that encloses a twisted MFR [30,45]. The extremities of the ribbons are hook shaped for weakly twisted MFRs and are spiral shaped for highly twisted MFRs, as depicted in the cartoon of the 3D-model for eruptive flares in **Figure 1**. Moreover, the characteristic 3D shape of QSLs associated with a twisted MFR depends on the height of the horizontal cut plane [15,23,46,49]. The QSL is S-shaped if the horizontal cut plane is at HFT and the cut planes lies below HFT, the QSL will appear as 2 (inverse) J-shaped with straight parts of J parallel to each other along the PIL. From this point of view of the MFR topology, the panels in **Figure 6** for the CME events from AR 11429, the QSLs are broadly spread over the flare ribbons especially the hook sections

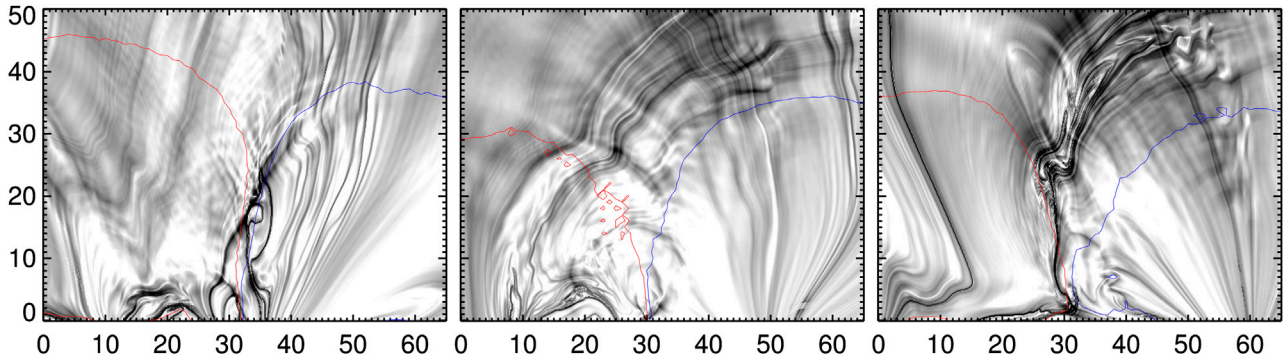

FIGURE 8 | Inverse maps of Log(*Q*) in the vertical slice placed across the sigmoid in the AR 11429 as shown in **Figure 4**. Contours of B_z (±80 G, red/blue curves) are over plotted. QSLs of large Q-values (black) are boundaries of magnetic domains enclosing the twisted-sheared core about the PIL.

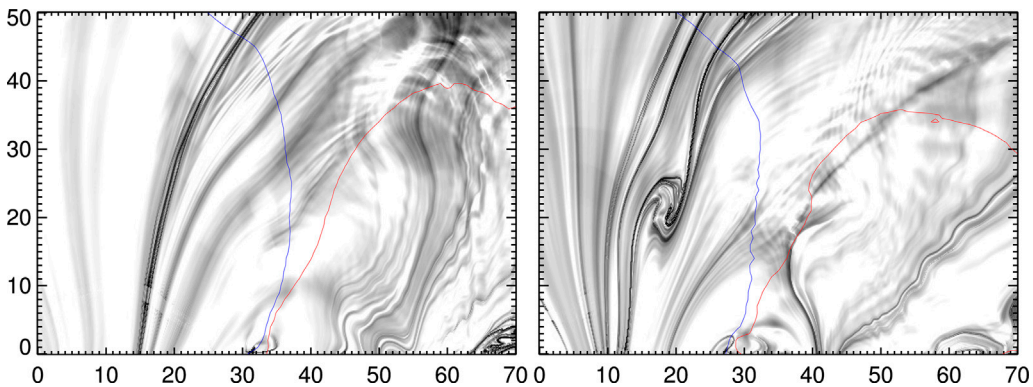

FIGURE 9 | Inverse maps of Log(*Q*) in the vertical slice placed across the sigmoid in the AR 12371 as shown in **Figure 5**. Contours of B_z (±80 G, red/blue curves) are over plotted. QSLs of large Q-values (black) are boundaries of magnetic domains enclosing the twisted-flux core about the PIL.

of the QSLs are in good morphological agreement. Such a remarkable match is an indication of the NLFFF models being capable of capturing hooked shape QSLs co-spatial with the observed flare ribbons, and was first reported by [15] in the topological analysis of AR 12158 employing the Grad-Rubin based NLFFF model.

From the above described MFR topology, the QSLs in the AR 12371 are also qualitatively match with the observed flare ribbons. The inverse-S ribbon exactly falls in the region outlined by QSLs of large Q-values. In fact, these QSLs can be regarded as a combination of 2 inverse-J shaped with a significant separation distance between the straight parts along PIL. We interpret the observed shape of the QSLs in the AR 12371 due to large part of sheared arcade surrounding the PIL, embedding the small-scale MFR. The sheared arcade becomes a large-scale twisted MFR only during onset of eruption by tether-cutting reconnection. The process of sheared arcade becoming large scale MFR is a dynamic process and may not be captured in vector magnetograms. Therefore, the static extrapolation results in a configuration with QSLs outlining the sheared arcade. Then the QSLs represents the boundaries of two connectivity domains separating the sheared arcade and the surrounding potential arcade.

Another factor that could also contribute to capture the observed shape of QSL is the amount of twist in the magnetic configuration [14,28]. A more twisted MFR will present a more pronounced hook such that the it appears as spiral in shape. In our cases, the separation distance between the straight parts of QSL J-sections and their hook shape are very likely due to insufficient or weak twist. Moreover, the twist of these field lines increases as a consequence of the eruption. Meeting this twist criteria, in particular during the dynamic phase of the eruption, the QSL foot prints would be co-spatial precisely with the observed flare ribbons.

5 SUMMARY AND DISCUSSION

Topological study of magnetic connectivity gradients provides more insights on the relation of magnetic structure of the sigmoid

and flare ribbons in the frame work of standard model of eruptions. We studied the pre-eruptive magnetic structure of five CMEs launched from two successively erupting ARs. The modelled magnetic structure is largely resembles an inverse-S sigmoid in good agreement with the coronal plasma tracers in EUV observations. In all the eruption cases, the QSLs of large Q values are continuous enclosing core field bipolar region in which inverse-S shaped flare ribbon is observed. These QSLs essentially represent the large connectivity gradients between the domains of twisted core flux within the inner bipolar region and the surrounding potential like arcade outside. It is consistent with the observed field structure largely with the sheared arcade.

The QSL maps in the chromosphere are compared with the flare ribbons observed at the peak time of the flares. The flare ribbons are largely with inverse-S shape morphology with their continuity of visibility is missing in the observations. For the CMEs in the AR 12371, the QSLs outline the flare ribbons as a combination of two inverse J-shape sections but their straight sections being separated at the middle of the PIL. These QSLs are typically associated with the weakly twisted flux rope topology. Similarly, for the CMEs in the AR 11429, the QSLs are co-spatial with the flare ribbons both in the middle of the PIL and in the hook sections. This overall match of the observed flare ribbons with the photospheric QSLs is an indication that the NLFFF model of optimization approach reproduces the pre-eruptive magnetic structure to a very good extent. Earlier Grad-Rubin implementation of NLFFF model was reported to capture the hook shaped QSLs co-spatial with the flare ribbons [15].

However, we can notice that the co-spatiality is not precise to the predicted extent in the theoretical models of the MFRs. In the tether-cutting scenario, the MFR forms only during eruption dynamically at which time we expect hook shaped, two inverse-J sections of QSLs that are co-spatial with the observed flare ribbons [15,30,50]. As per the view that the sheared arcades are weakly twisted MFRs in the sense that the magnetic field is dominated by the axial component [51], we can regard the observed QSL shape in the AR 12371 as the combination of two inverse-J sections with significant separation distance between the straight parts along the PIL. Therefore, the QSLs outlining the flare ribbons in the AR 12371 and less compact QSL hooks in the AR 11429 are likely due to the weakly twisted flux rope system. Additionally, difficulties related to input observations, construction of actual magnetic structure with the NLFFF modeling could also contribute to this discrepancy in the expected inverse-S (or two J-shaped ones) QSLs exactly co-spatial with the observed flare ribbons.

DATA AVAILABILITY STATEMENT

Publicly available datasets were analyzed in this study. This data can be found here: http://jsoc.stanford.edu/.

AUTHOR CONTRIBUTIONS

The author confirms being the sole contributor of this work and has approved it for publication.

ACKNOWLEDGMENTS

SDO is a mission of NASA's Living With a Star Program. The NLFFF code was developed by T. Wiegelmann of Max Planck Institute for Solar System. 3D field line rendering is due to VAPOR (www.vapor.ucar.edu) software. We acknowledge an extensive usage of the multi-node, multi-processor high performance computing facility at the Indian Institute of Astrophysics. I thank the reviewers for their generous comments and suggestions which improved the clarity of the text.

REFERENCES

1. Rust DM, and Kumar A. Evidence for Helically Kinked Magnetic Flux Ropes in Solar Eruptions. *Astrophys J Lett* (1996) 464:L199–L202. doi:10.1086/310118
2. Hudson HS, Lemen JR, St. Cyr OC, Sterling AC, and Webb DF. X-ray Coronal Changes during Halo CMEs. *Geophys Res Lett* (1998) 25:2481–4. doi:10.1029/98GL01303
3. Canfield RC, Hudson HS, and McKenzie DE. Sigmoidal Morphology and Eruptive Solar Activity. *Geophys Res Lett* (1999) 26:627–30. doi:10.1029/1999gl900105
4. Canfield RC, Kazachenko MD, Acton LW, Mackay DH, Son J, and Freeman TL. Yohkoh SXT Full-Resolution Observations of Sigmoids: Structure, Formation, and Eruption. *ApJ* (2007) 671:L81–L84. doi:10.1086/524729
5. Moore RL, Sterling AC, Hudson HS, and Lemen JR. Onset of the Magnetic Explosion in Solar Flares and Coronal Mass Ejections. *ApJ* (2001) 552:833–48. doi:10.1086/320559
6. Moore RL, and Sterling AC. Initiation of Coronal Mass Ejections. *Solar Eruptions Energetic Particles Geophys Monogr Ser* (2006) 165:43–57. doi:10.1029/165gm07
7. Moore RL, and Roumeliotis G. Triggering of Eruptive Flares - Destabilization of the Preflare Magnetic Field Configuration. Eruptive Solar Flares. Proceedings of Colloquium #133 of the International Astronomical Union, Iguazu, Argentina, August 2-6, 1991. In: Z Svestka, BV Jackson, and ME Machado, editors. *IAU Colloq. 133: Eruptive Solar Flares*, Vol. 399. New York, NY: Berlin Springer Verlag (1992) p. 69, 1992 . Lecture Notes in Physics. doi:10.1007/3-540-55246-4
8. Hood AW, and Priest ER. Kink Instability of Solar Coronal Loops as the Cause of Solar Flares. *Sol Phys* (1979) 64:303–21. doi:10.1007/BF00151441
9. Gibson SE, Fan Y, Török T, and Kliem B. The Evolving Sigmoid: Evidence for Magnetic Flux Ropes in the Corona before, during, and after CMES. *Space Sci Rev* (2007) 124:131–44. doi:10.1007/s11214-006-9101-2
10. Green LM, Kliem B, Török T, van Driel-Gesztelyi L, and Attrill GDR. Transient Coronal Sigmoids and Rotating Erupting Flux Ropes. *Sol Phys* (2007) 246:365–91. doi:10.1007/s11207-007-9061-z
11. Song HQ, Chen Y, Zhang J, Cheng X, Wang B, Hu Q, et al. Evidence of the Solar EUV Hot Channel as a Magnetic Flux Rope from Remote-Sensing and *In Situ* Observations. *ApJ* (2015) 808:L15. doi:10.1088/2041-8205/808/1/L15
12. Vemareddy P, and Mishra W. A Full Study on the Sun-Earth Connection of an Earth-Directed Cme Magnetic Flux Rope. *ApJ* (2015) 814:59. doi:10.1088/0004-637x/814/1/59
13. Song HQ, Chen Y, Qiu J, Chen CX, Zhang J, Cheng X, et al. The Acceleration Process of a Solar Quiescent Filament in the Inner Corona. *ApJ* (2018) 857:L21. doi:10.3847/2041-8213/aabcc3

14. Savcheva AS, Green LM, van Ballegooijen AA, and DeLuca EE. Photospheric Flux Cancellation and the Build-Up of Sigmoidal Flux Ropes on the Sun. *ApJ* (2012) 759:105. doi:10.1088/0004-637X/759/2/105
15. Zhao J, A. Gilchrist S, Aulanier G, Schmieder B, Pariat E, and Li H. Hooked Flare Ribbons and Flux-Rope-Related QSL Footprints. *ApJ* (2016) 823:62. doi:10.3847/0004-637X/823/1/62
16. Guo Y, Ding MD, Cheng X, Zhao J, and Pariat E. Twist Accumulation and Topology Structure of a Solar Magnetic Flux Rope. *ApJ* (2013) 779:157. doi:10.1088/0004-637X/779/2/157
17. Vemareddy P, Cheng X, and Ravindra B. Sunspot Rotation as a Driver of Major Solar Eruptions in the NOAA Active Region 12158. *ApJ* (2016) 829:24. doi:10.3847/0004-637X/829/1/24
18. Vemareddy P, and Demóulin P. Study of Three-Dimensional Magnetic Structure and the Successive Eruptive Nature of Active Region 12371. *ApJ* (2018) 857:90. doi:10.3847/1538-4357/aab6b7
19. Démoulin P. Extending the Concept of Separatrices to QSLs for Magnetic Reconnection. *Adv Space Res* (2006) 37:1269–82. doi:10.1016/j.asr.2005.03.085
20. Démoulin P. Where Will Efficient Energy Release Occur in 3-D Magnetic Configurations?. *Adv Space Res* (2007) 39:1367–77. doi:10.1016/j.asr.2007.02.046
21. Titov VS, and Démoulin P. Basic Topology of Twisted Magnetic Configurations in Solar Flares. *Astron Astrophys* (1999) 351:707–20.
22. Titov VS, Hornig G, and Démoulin P. Theory of Magnetic Connectivity in the Solar corona. *J Geophys Res* (2002) 107:3–1. doi:10.1029/2001JA000278
23. Savcheva AS, van Ballegooijen AA, and DeLuca EE. Field Topology Analysis of a Long-Lasting Coronal Sigmoid. *ApJ* (2012) 744:78. doi:10.1088/0004-637x/744/1/78
24. Carmichael H. *A Process for Flares*, 50. NASA Special Publication (1964). p. 451.
25. Sturrock PA. Model of the High-Energy Phase of Solar Flares. *Nature* (1966) 211:695–7. doi:10.1038/211695a0
26. Hirayama T. Theoretical Model of Flares and Prominences. *Sol Phys* (1974) 34:323–38. doi:10.1007/BF00153671
27. Kopp RA, and Pneuman GW. Magnetic Reconnection in the corona and the Loop Prominence Phenomenon. *Sol Phys* (1976) 50:85–98. doi:10.1007/BF00206193
28. Pariat E, and Démoulin P. Estimation of the Squashing Degree within a Three-Dimensional Domain. *A&A* (2012) 541:A78. doi:10.1051/0004-6361/201118515
29. Janvier M, Aulanier G, Pariat E, and Démoulin P. The Standard Flare Model in Three Dimensions. *A&A* (2013) 555:A77. doi:10.1051/0004-6361/201321164
30. Janvier M, Aulanier G, and Démoulin P. From Coronal Observations to MHD Simulations, the Building Blocks for 3D Models of Solar Flares (Invited Review). *Sol Phys* (2015) 290:3425–56. doi:10.1007/s11207-015-0710-3
31. Chen P, Su J, Guo Y, and Deng Y. Where Do Flare Ribbons Stop?. *Chin Sci Bull* (2012) 57:1393–6. doi:10.1007/s11434-011-4829-9
32. Wiegelmann T. Optimization Code with Weighting Function for the Reconstruction of Coronal Magnetic fields. *Solar Phys* (2004) 219:87–108. doi:10.1023/b:sola.0000021799.39465.36
33. Lemen JR, Title AM, Akin DJ, Boerner PF, Chou C, Drake JF, et al. The Atmospheric Imaging Assembly (AIA) on the Solar Dynamics Observatory (SDO). *Solar Phys* (2012) 275:17–40. doi:10.1007/s11207-011-9776-8
34. Schou J, Scherrer PH, Bush RI, Wachter R, Couvidat S, Rabello-Soares MC, et al. Design and Ground Calibration of the Helioseismic and Magnetic Imager (HMI) Instrument on the Solar Dynamics Observatory (SDO). *Solar Phys* (2012) 275:229–59. doi:10.1007/s11207-010-9639-8
35. Bobra MG, Sun X, Hoeksema JT, Turmon M, Liu Y, Hayashi K, et al. The Helioseismic and Magnetic Imager (HMI) Vector Magnetic Field Pipeline: SHARPs - Space-Weather HMI Active Region Patches. *Sol Phys* (2014) 289:3549–78. doi:10.1007/s11207-014-0529-3
36. Hoeksema JT, Liu Y, Hayashi K, Sun X, Schou J, Couvidat S, et al. The Helioseismic and Magnetic Imager (HMI) Vector Magnetic Field Pipeline: Overview and Performance. *Sol Phys* (2014) 289:3483–530. doi:10.1007/s11207-014-0516-8
37. Nitta NV, and Hudson HS. Recurrent Flare/CME Events from an Emerging Flux Region. *Geophys Res Lett* (2001) 28:3801–4. doi:10.1029/2001GL013261
38. Zhang J, and Wang J. Are Homologous Flare-Coronal Mass Ejection Events Triggered by Moving Magnetic Features? *Astrophys J Lett* (2002) 566:L117–L120. doi:10.1086/339660
39. Dhakal SK, Zhang J, Vemareddy P, and Karna N. Recurring Homologous Solar Eruptions in NOAA AR 11429. *ApJ* (2020) 901:40. doi:10.3847/1538-4357/abacbc
40. Vemareddy P. Successive Homologous Coronal Mass Ejections Driven by Shearing and Converging Motions in Solar Active Region Noaa 12371. *ApJ* (2017) 845:59. doi:10.3847/1538-4357/aa7ff4
41. Wheatland MS, Sturrock PA, and Roumeliotis G. An Optimization Approach to Reconstructing Force-free Fields. *ApJ* (2000) 540:1150–5. doi:10.1086/309355
42. Wiegelmann T, and Inhester B. How to deal with Measurement Errors and Lacking Data in Nonlinear Force-free Coronal Magnetic Field Modelling?. *A&A* (2010) 516:A107. doi:10.1051/0004-6361/201014391
43. Wiegelmann T, Inhester B, and Sakurai T. Preprocessing of Vector Magnetograph Data for a Nonlinear Force-free Magnetic Field Reconstruction. *Sol Phys* (2006) 233:215–32. doi:10.1007/s11207-006-2092-z
44. Duan A, Jiang C, He W, Feng X, Zou P, and Cui J. A Study of Pre-flare Solar Coronal Magnetic Fields: Magnetic Flux Ropes. *ApJ* (2019) 884:73. doi:10.3847/1538-4357/ab3e33
45. Demoulin P, Henoux JC, Priest ER, and Mandrini CH. Quasi-Separatrix Layers in Solar Flares. *Method Astron Astrophys* (1996) 308:643–55.
46. Titov VS. Generalized Squashing Factors for Covariant Description of Magnetic Connectivity in the Solar Corona. *ApJ* (2007) 660:863–73. doi:10.1086/512671
47. Liu R, Kliem B, Titov VS, Chen J, Wang Y, Wang H, et al. Structure, Stability, and Evolution of Magnetic Flux Ropes from the Perspective of Magnetic Twist. *ApJ* (2016) 818:148. doi:10.3847/0004-637X/818/2/148
48. Vemareddy P. Very Fast Helicity Injection Leading to Critically Stable State and Large Eruptive Activity in Solar Active Region NOAA 12673. *ApJ* (2019) 872:182. doi:10.3847/1538-4357/ab0200
49. Savcheva A, Pariat E, McKillop S, McCauley P, Hanson E, Su Y, et al. The Relation between Solar Eruption Topologies and Observed Flare Features. I. Flare Ribbons. *ApJ* (2015) 810:96. doi:10.1088/0004-637X/810/2/96
50. Savcheva A, Pariat E, van Ballegooijen A, Aulanier G, and DeLuca E. Sigmoidal Active Region on the Sun: Comparison of a Magnetohydrodynamical Simulation and a Nonlinear Force-free Field Model. *ApJ* (2012) 750:15. doi:10.1088/0004-637x/750/1/15
51. Mackay DH, Karpen JT, Ballester JL, Schmieder B, and Aulanier G. Physics of Solar Prominences: II-Magnetic Structure and Dynamics. *Space Sci Rev* (2010) 151:333–99. doi:10.1007/s11214-010-9628-0

Conflict of Interest: The author declares that the research was conducted in the absence of any commercial or financial relationships that could be construed as a potential conflict of interest.

frontiers in Physics

ORIGINAL RESEARCH
published: 20 October 2021
doi: 10.3389/fphy.2021.712599

Magnetic Field Intensity Modification to Force Free Model of Magnetic Clouds: Website of *Wind* Examples From Launch to July of 2015

Chin-Chun Wu[1]*, *R. P. Lepping*[2,3] and *D. B. Berdichevsky*[4,5]

[1]Naval Research Laboratory, Washington, DC, United States, [2]UMBC, Baltimore, MD, United States, [3]Heliophysics Science Division, NASA/Goddard Space Flight Center, Greenbelt, MD, United States, [4]MC 672, GSFC/NASA, Greenbelt, MD, United States, [5]IFIR/UNR-CONICET, Rosario, Argentina

OPEN ACCESS

Edited by:
Hongqiang Song,
Shandong University, China

Reviewed by:
Miguel A. Hidalgo,
University of Alcalá, Spain
Simon Good,
University of Helsinki, Finland
Yutian Chi,
University of Science and Technology of China, China

***Correspondence:**
Chin-Chun Wu
chin-chun.wu@nrl.navy.mil

Specialty section:
This article was submitted to Stellar and Solar Physics, a section of the journal Frontiers in Physics

Received: 20 May 2021
Accepted: 19 July 2021
Published: 20 October 2021

Citation:
Wu C-C, Lepping RP and Berdichevsky DB (2021) Magnetic Field Intensity Modification to Force Free Model of Magnetic Clouds: Website of Wind Examples From Launch to July of 2015. Front. Phys. 9:712599. doi: 10.3389/fphy.2021.712599

We describe a new NASA website that shows normalized magnetic field (***B***) magnitude profiles within *Wind* magnetic clouds (MCs) (i.e., observations *versus* basic model *versus* modified model) for 209 MCs observed from launch in late 1994 to July of 2015, where model modification is based on the studies of Lepping et al. (Solar Phys, 2017, 292:27) and Lepping et al. (Solar Phys, 2018, 293:162); the basic force free magnetic cloud parameter fitting model employing Bessel functions (Lepping et al., J. Geophys. Res., 1990, 95: 11957) is called the LJB model here. The fundamental principles should be applicable to the ***B***-data from any spacecraft at 1 AU. Earlier (in the LJB study), we justified why the field magnitude can be thought of as decoupled from the field direction within an MC, and further, we justified this idea in terms of actual observations seen over a few decades with examples of MCs from *Wind* data. The model modification is achieved by adding a correction ("Quad") value to the LJB model (Bessel function) value in the following manner: B (est)/B_0 ≈ [LJB Model + Quad (CA,u)], where B_0 is the LJB-estimated field magnitude value on the MC's axis, CA is the relative closest approach (See **Supplementary Appendix A**), and u is the distance that the spacecraft travels through the MC from its entrance point. In an average sense, the Quad technique is shown to be successful for 82% of the past modeled MCs, when Quality (Q_0) is good or excellent (see **Supplementary Appendix A**). The Quad technique is successful for 78% of MCs when all cases are considered. So Q_0 of the MC LJB-fit is not a big factor when the success of the Quad scheme is considered. In addition, it is found that the Quad technique does not work better for MC events with higher solar wind speed. Yearly occurrence frequency of all MC events (N_{Yearly}) and those MC events with $\Delta\sigma_N/\sigma_{N2} \geq 0.5$ ($N_{\Delta\sigma N/\sigma N2 \geq 0.5}$) are well correlated, but there is no solar cycle dependence for normalizing $N_{\Delta\sigma N/\sigma N2 \geq 0.5}$ with N_{Yearly}.

Keywords: magnetic cloud, force free model, magnetic field intensity, solar wind, *Wind*-MC

1 INTRODUCTION AND BACKGROUND

A magnetic cloud (MC) is a solar wind region with the following features: enhanced magnetic field strength, a smooth change in magnetic field direction as observed by a spacecraft passing through the MC, low proton temperature compared to the ambient proton temperature, and low proton plasma beta (e.g., [1–3]). Also, we must require that the duration of the MC be 5 h or more, based on numerous observations. Many MC lists are available (e.g., [4–11]). Enhanced southward magnetic field of an MC will cause geomagnetic activity while the MC is passing by the Earth. Here, we call attention to a method of modifying a normalized magnetic field (**B**) magnitude profile within a *Wind* magnetic cloud (MC) (or for any spacecraft at 1 AU) by describing a new website that shows B-profiles (observations vs. model vs. modified model) for 209 cases of *Wind* MCs from launch (late 1994) to the end of 2015. The model modification is based on the studies of Lepping et al. [12] and Lepping et al. [10]; the basic MC parameter fitting (force free) model is that of Lepping et al. [13] (henceforth called the LJB model). The modification is based on the statistics of many actual MCs observed in the past by the *Wind* spacecraft. (For articles on the discovery of MCs and other relevant aspects see [1–3].)

The justification for separating the magnitude of $\boldsymbol{B}$ from its direction in the implementation of the LJB model results from the manner in which the model was posed in the first place and in what was shown to be the characteristics of hundreds of actual MCs from many different spacecraft. That is, the model always operated on the fundamental assumption that we could unit-normalize $\boldsymbol{B}$ (i.e., create $\boldsymbol{B}/|\boldsymbol{B}|$ at all points) within the MC and carry out the least-square fitting of the model to the resulting data, being the unit normalized-$\boldsymbol{B}$—not on the actual $\boldsymbol{B}$. And only later do we adjust the B (model) profile to the average value of B across the MC; this leads to providing an appropriate B_0, which is the estimated value for the magnetic field magnitude on the axis of the MC. In particular, this treatment for over 200 *Wind* MCs has generally provided a faithful reproduction of the profile of the direction of $\boldsymbol{B}$ within a MC for most cases (i.e., at least at 1 AU) and especially when considering the lower frequency components of $\boldsymbol{B}$, that is, excluding what may be considered "noise." But the model rarely gives a very good reproduction of the actual profile of the *magnitude* of $\boldsymbol{B}$. The study by Lepping et al. [10] attempts to statistically correct for this shortcoming of the LJB model, as described below.

2 THE QUAD SCHEME FOR MODIFYING THE *B*-INTENSITY WITHIN THE MAGNETIC CLOUD

Recently, a scheme was developed by Lepping et al. [10] to provide a more realistic B/B_0 profile of an MC, than that used in the LJB model, based on the results of 21 years of MCs studied from the *Wind* spacecraft (also, see Lepping et al. [10,12] for more detail on the foundation of the scheme). It was shown statistically that this scheme should improve MC profiles by about 82% of the time, when the highest quality (Q_0) MCs are considered. Q_0 can take one of three possible values: 1 (excellent), 2 (good/fair), and 3 (poor) (see **Supplementary Appendix A**, for a strict definition of Q_0). To provide differing examples, **Figure 1** shows plots of B/B_0 *versus* %-of-time through the MC for three MCs (cases of #s 70, 71, and 62, all of $Q_0 = 1$), in terms of actual observations (101 averages across each MC, i.e., data averaged into 100 bins across each MC shown by the dot-dot-dashed curve; called the Obs curve), the original Bessel function model profile (the black solid-line curve, described by LJB), and the new statistically modified version (the red dashed curve, described generically by Lepping et al., 2018). MC #70 starts on 2002-03-24, #71 starts on 2002-04-18, and #62 starts on 2001-04-12; these dates are shown on the first line at the top of each panel of **Figure 1**. Also, within each panel of the figure are the start time (also on the first line at the top), and then the value of the relative closest approach in percentage ($CA \equiv |Y_0|/R_0$ in %), Q_0, the MC duration (τ), the average plasma speed within the MC ($<V_{MC}>$), and the estimated B_0, where Y_0 is the closest approach and R_0 is the estimated radius of the MC. Below the curves is the quantity $\Delta\sigma_N/\sigma_{N2}$ described by Lepping et al. [10] as a good measure of how well the scheme is performing; when $\Delta\sigma_N/\sigma_{N2}$ is above 0.5, it is doing very well (or exceptional when it approaches or exceeds 1.0); when it is between 0.0 and 0.5, it is acceptable; when it is negative, it is a failure. We give an abbreviated interpretation of $\Delta\sigma_N/\sigma_{N2}$ here as follows:

The ratio $\Delta\sigma_N/\sigma_{N2}$ is a relative measure of the improvement in the B/B_0 fit to the MC's profile by using a so-called Quad (CA,u) formula weighted by the "accuracy" of the final fit, for the LJB model, where σ_{N2} is a quantitative measure of how well the Quad equations fit the difference-profile between the observations and the model values; u is the distance measured as the spacecraft travels through the MC. $\Delta\sigma_N$ is a quantitative measure of the improvement in the fit of B/B_0 after adding in the Quad modification (and $\Delta\sigma_N$ must be greater than or equal to 0.0 for a success), where B (est)/$B_0 \approx$ [LJB Model + Quad (CA,u)], developed for four possible CAs (in%), 12.5, 37.5, 62.5, and 87.5 (these are the center points of four equally spaced segments of the full span of CA (0–100%)). Quad is a quadratic fit to the difference-quantity [B/B_0(Observations)-LJB Model] for each point in the MC carried out statistically from 124 averaged (good quality, i.e., Q_0 = 1,2) MCs using *Wind* B-data (see Lepping et al. [10] for a more detailed explanation of the ratio $\Delta\sigma_N/\sigma_{N2}$).

Concerning specifics of the three examples of **Figure 1**, we note the following:

- For case #70, we have a $\Delta\sigma_N/\sigma_{N2} = -0.443$, a poor (negative) case, with a CA of 8% and a long duration of 43.0 h. Since the Quad technique usually works best when B/B_0(Observations) is higher than the Bessel force free field in the early hours of the MC, which is not the case here, the "correction" field (red dashed curve in **Figure 1**) is too high in this case. This is a somewhat unusual case because of the low intensity field in these early hours, and therefore, it violates the assumptions on which the Quad technique was based and not surprisingly gives poor results, that is, the negative ratio for $\Delta\sigma_N/\sigma_{N2}$ of -0.443, even though $Q_0 = 1$. In fact, there usually is not a good correlation between $\Delta\sigma_N/\sigma_{N2}$ and Q_0 (see **Figure 2** and related

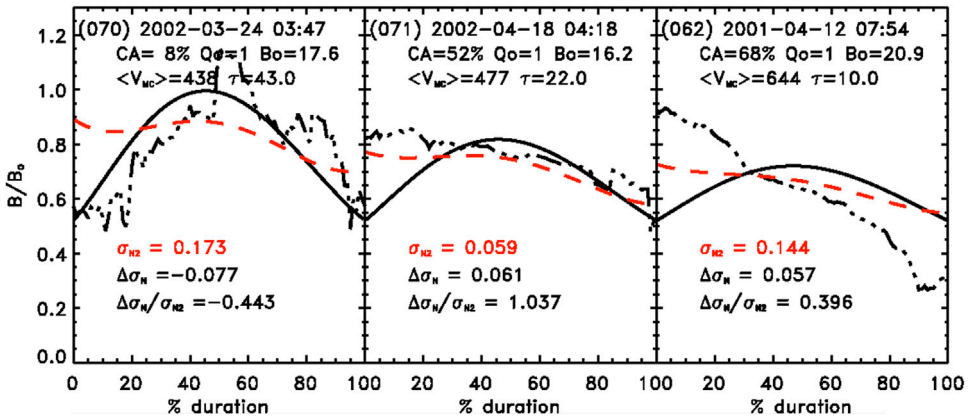

FIGURE 1 | Three examples (the cases of #s 70, 71, and 62 of *Wind* MCs; see the associated starting dates of these MCs on the first line at the top of each panel) of plots of B/B_0-profiles: B_0-normalized *B observations* (black dash-dot-dot), force free model values (black solid curve) and modified-model values (red dashed curve from Lepping et al. [10]—all as a function of percent passage through the MC (i.e., *u* in %); each profile has 101 points across. In each panel the following are shown: TOP OF EACH PANEL: the start time (year-month-day of month) hour:minute (UT), *CA* (= $|Y_0|/R_0$ in %), Quality (Q_0), B_0 (in nT), average plasma speed within the MC ($<V_{MC}>$, in km s^{-1}), and duration (τ, in hours), BOTTOM OF EACH PANEL: the values of the quantities $\Delta\sigma_N$,σ_{N2}, and $\Delta\sigma_N/\sigma_{N2}$ (see text) that are described by Lepping et al. [10]. The ratio $\Delta\sigma_N/\sigma_{N2}$ in particular is shown to be a good measure of how well the scheme is performing in general.

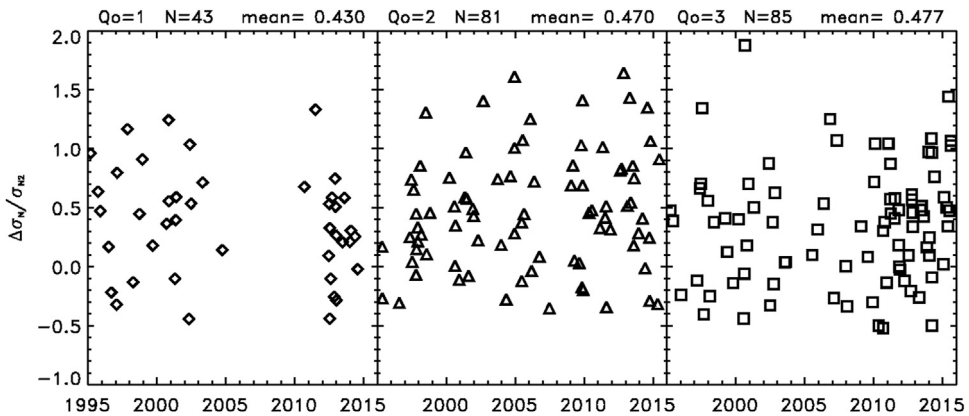

FIGURE 2 | A plot of $\Delta\sigma_N/\sigma_{N2}$ *versus* time for the family of Q_0, showing almost the same average of $\Delta\sigma_N/\sigma_{N2}$ for each Q_0 (the averages are given above each panel), where Q_0 = 1 set is represented by diamonds, Q_0 = 2 by triangles, and Q_0 = 3 by squares, with a large spread in values in each case.

text (**Section 5**) concerning this issue). And finally, notice that B_o is 17.6 nT, a typical value for B_o, and $<V>$ = 438 km s^{-1}.

- For case #71 we have a $\Delta\sigma_N/\sigma_{N2}$ = 1.037, an excellent case, with a *CA* of 52% and a fairly typical duration of 22.0 h. Here the observations are *higher* than the Bessel force free field (red dashed curve in **Figure 1**) in the early hours, which, as stated above is typical, and, in fact, this is an excellent example of such front-end enhancement in the field. Also Q_0 = 1. B_o is 16.2 nT, another typical value for B_o, and finally, $<V>$ = 477 km s^{-1}.
- For case #62 with a $\Delta\sigma_N/\sigma_{N2}$ = 0.396, we have an acceptable (intermediate) case, that is, a positive ratio but less than 0.500—and a short duration of the MC of 10 h. Here *CA* was moderately large (68%) and again Q_0 = 1. B_o is 20.9 nT, a somewhat high value for B_o, and finally, a moderately high $<V>$ = 644 km s^{-1}.

All three cases were deliberately chosen to be in the Q_0 = 1 category so that Quality would not be an obvious determinate in the value of the ratio $\Delta\sigma_N/\sigma_{N2}$ (see comments in the Conclusions and Discussion (**Section 5**) about $\Delta\sigma_N/\sigma_{N2}$ *versus* Q_0).

3 *WIND* WEBSITE TO OBTAIN THE FULL SET OF FIELD INTENSITY PLOTS

The Website to obtain the MC B/B_o profiles is within the *Wind*/MFI Website, which is https://wind.nasa.gov/mfi/mag_cloud_pub1.html.

The link at that Website to the Field Intensity plots, based on the Quad scheme, is http://lepmfi.gsfc.nasa.gov/mfi/mag_cloud_B_magnitude.html.

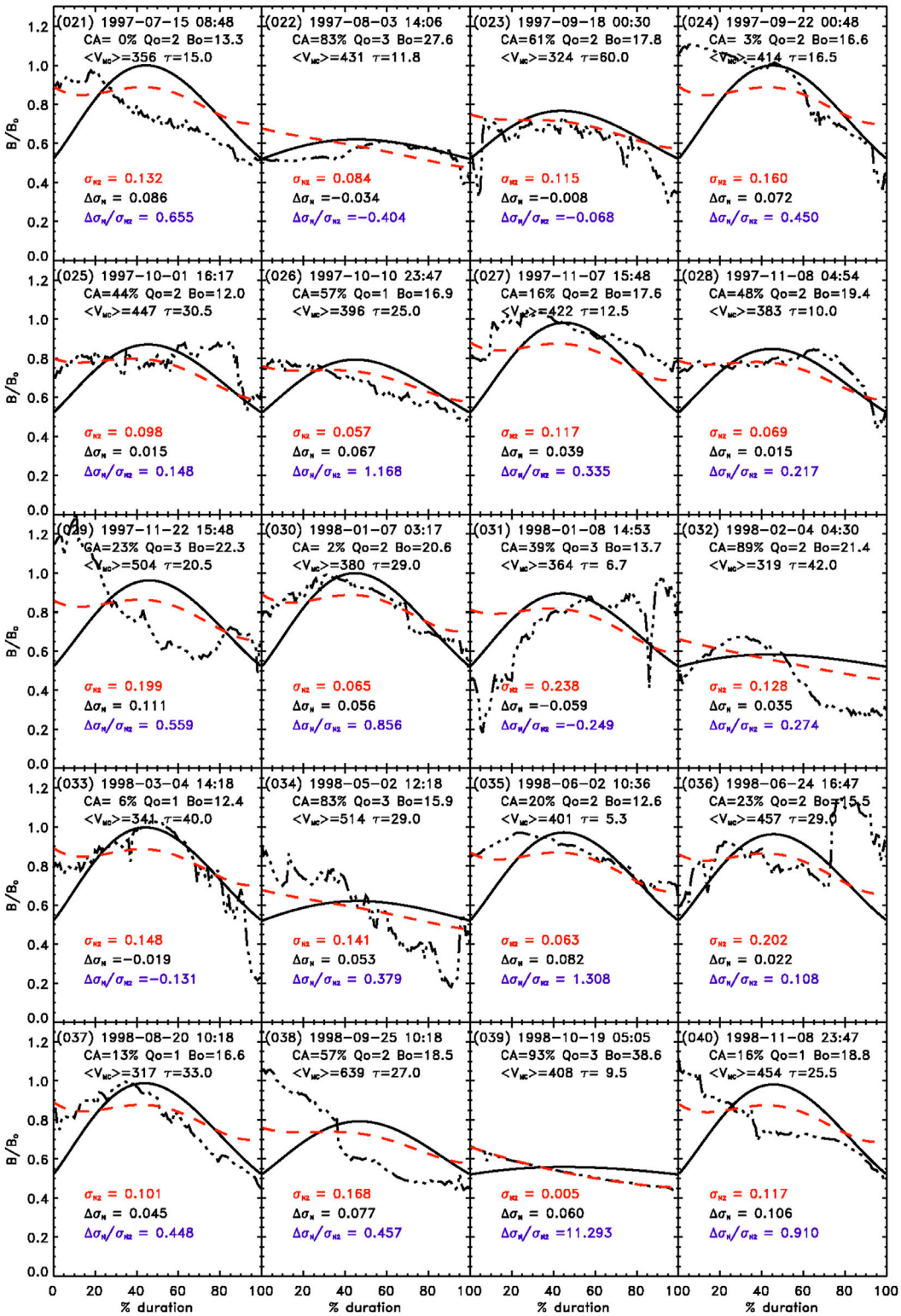

FIGURE 3 | Example page (p. 2) of set of 11 pages (20 panels each) of the same quantities as shown in **Figure 1**, and in the same format, of *Wind* MCs from launch to July of 2015.

TABLE 1 | Summary of number of MC failures and number of those with $\Delta\sigma_N/\sigma_{N2} \geq 0.5$

Page No.[a]	No. of failures	No. of $\Delta\sigma_N/\sigma_{N2} \geq 0.5$
1	6[b] (1)[c]	7[b] (4)[c]
2	4 (2)	7 (5)
3	5 (2)	7 (4)
4	4 (2)	10 (8)
5	3 (3)	7 (7)
6	6 (3)	9 (5)
7	3 (0)	8 (5)
8	6 (3)	6 (4)
9	3 (2)	10 (9)
10	5 (3)	6 (2)
11	1 (1)	7 (1)
Sum [%]	46 [22%][b] (22 {18%})[c]	84 [40%][b] (54 {44%})[c]

[a]*Page number out of 11 pages (initially) of 20 MCs each, except for page 11 which has 9 events.*

[b]*For all cases, that is, MCs of Q_0 = 1, 2, and 3. There were a total of 209 such cases for the mission.*

[c]*Numbers in parentheses are for the better quality cases, that is, where the MCs are of quality Q_0 = 1 or 2 only. There were a total of 124 such cases for the mission.*

Each MC has a case number (#) that is given (in parentheses) in the upper left-hand corner of each panel, as we saw in the three examples of **Figure 1**. We give below an example of a single page in the initial set.

4 EXAMPLE OF A PAGE OF 20 CASES OF WIND MCS

Figure 3 shows a single example page, that is, page 2, of a set of pages (20 panels each page, with one MC per panel) of the same quantities as shown in **Figure 1** of *Wind* MCs from launch to July of 2015. A full set of 11 figures is shown in **Supplementary Appendix B**. Initially, there are 11 such pages in the Website described above, to cover the 209 MCs that are believed to exist over that period. Notice that the figure shows that the force free Bessel fields (solid black lines) at the start and end times, for all cases, give the same B/B_o value of about 0.52, as expected. The upper left-hand corner of each panel shows the case number (#) of the MC.

First, case #039 shows a value of $\Delta\sigma_N/\sigma_{N2}$ of 11.29, which is unusually high (indicating a good result, even though Q_0 = 3), because the value of σ_{N2} = 0.005 is unusually small. We will not see many odd cases like this. Now consider good cases like #035 and #040, where $\Delta\sigma_N/\sigma_{N2}$ is 1.31 (with Q_0 = 2) and 0.91 (with Q_0 = 1), respectively; both are well above 0.5. In both cases, we see the dramatic difference between the ability of the Quad scheme (dashed curve) to almost reproduce the observed values in the early part of the MC and the inability of the Bessel function (solid black curve) to do so in that part of the MC. Notice that #026 is similar to #035 in that they give similar values of $\Delta\sigma_N/\sigma_{N2}$ (1.17 and 1.31, respectively) even though the first one has a somewhat long duration of 25.0 h and the second one has a rather short duration of only 5.3 h, and both of a quality that differs from Q_0 = 3. Now we consider a very poor case, #022, that is, where $\Delta\sigma_N/\sigma_{N2}$ is negative and rather large in the absolute value, where $\Delta\sigma_N/\sigma_{N2}$ is −0.40 (with Q_0 = 3). Case #033 is interesting in that the Quad scheme does well in the early part of the MC but not in the middle or latter regions, i.e. not as well as the Bessel field, so $\Delta\sigma_N/\sigma_{N2}$ is negative, −0.13; notice that this is a very long duration MC of 40.0 h, and Q_0 = 1. Those cases where the observed field is significantly lower in relative intensity than the Bessel function field, early in the MC, will usually produce the poorest results, such as in cases #022 and #031. This does not occur very frequently.

5 CONCLUSION AND DISCUSSION

Here, we describe a new NASA Website (see **Section 3**) that provides normalized magnetic field (B/B_o) magnitude profiles within *Wind* MCs in terms of observations *versus* the basic-LJB model *versus* the Quad-modified model for 209 MCs that cover the period from launch (late 1994) to July of 2015. The model-modification is based on the studies of Lepping et al. [12] and Lepping et al. [10]. The basic force free MC parameter fitting model that is modified is that of LJB. The statistics of both the number of MC-modified failures and the number of (very good) cases where $\Delta\sigma_N/\sigma_{N2} \geq 0.5$ given by this new website to this point (July 2021) is provided in **Table 1**.

For all cases (i.e., MCs of Q_0 = 1, 2, and 3), **Table 1** shows that the percentage of failures is 22%, and for the cases where Q_0 = 1 and 2, only (values in parentheses) the percentage slightly improves to 18%. However, considering all cases, we find that 40% have $\Delta\sigma_N/\sigma_{N2} \geq 0.5$, but the percentage slightly increases to 44% when the cases are restricted to Q_0 = 1 and 2 only.

Figure 4 gives a histogram (called f (obs) and shown by a solid black curve) representing the frequency of occurrence of the observed ratio $\Delta\sigma_N/\sigma_{N2}$ for the full *Wind* mission (i.e., from launch to July 2015), and for Q_0 = 1, 2, and 3, and showing some key features, such as having a peak at about 0.5, a relatively

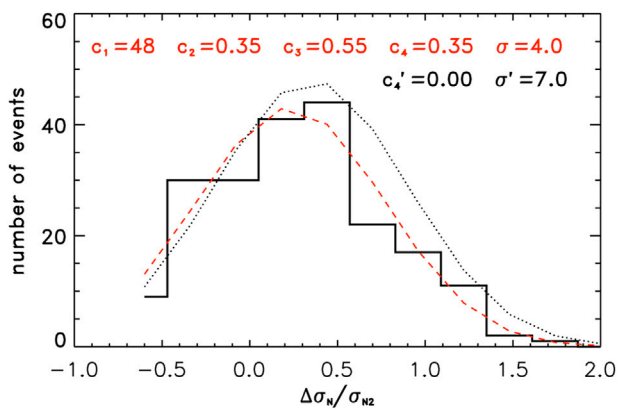

FIGURE 4 | A histogram of frequency of occurrence of the observed ratio $\Delta\sigma_N/\sigma_{N2}$ (black solid curve) with a superimposed skewed normal (Gaussian)-distribution, f(Z) (red dashed curve), where $Z \equiv \Delta\sigma_N/\sigma_{N2}$; c_1, c_2, c_3, and c_4 are the coefficients shown in **Eq. 1**. The black dotted curve is for the same Gaussian (i.e., the same values of c_1, c_2, and c_3), except now c_4 is set equal to zero. σ gives a measure of how well the fit-curve approximates the observed histogram and is given by **Eq. 2**. The red coefficients hold for the red dashed skewed Gaussian and the black coefficients are for the simple Gaussian (second line at the top), where c_1, c_2, and c_3 are the same in both cases. Note that both black and red curves are approximately Gaussian.

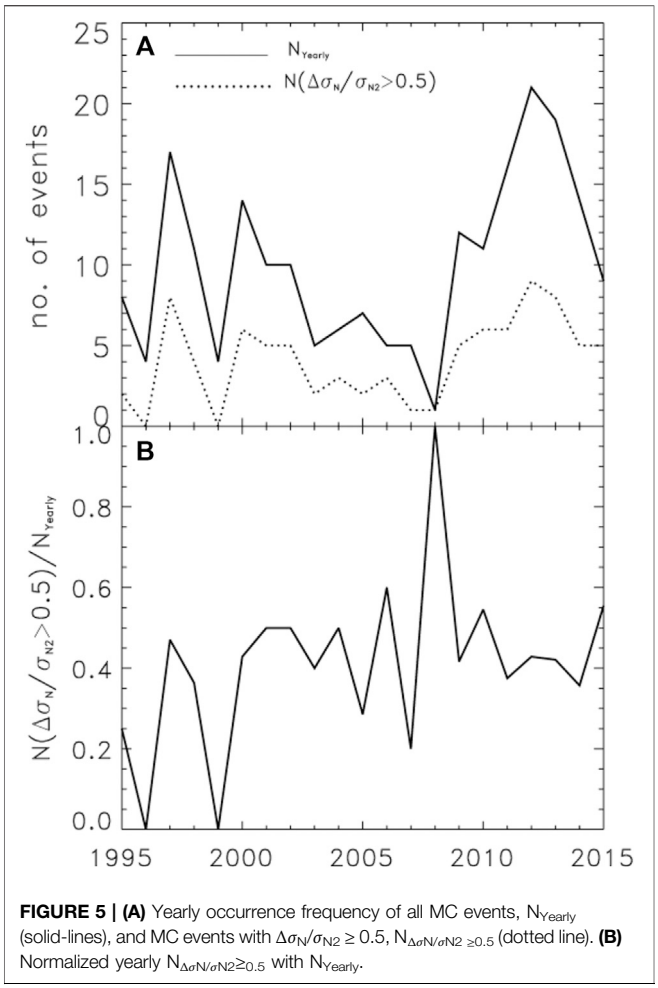

FIGURE 5 | (A) Yearly occurrence frequency of all MC events, N_{Yearly} (solid-lines), and MC events with $\Delta\sigma_N/\sigma_{N2} \geq 0.5$, $N_{\Delta\sigma N/\sigma N2 \geq 0.5}$ (dotted line). **(B)** Normalized yearly $N_{\Delta\sigma N/\sigma N2 \geq 0.5}$ with N_{Yearly}.

small number of events greater than 1.0. It appears to be a slightly modified normal distribution. Since the histogram peaks near $\Delta\sigma_N/\sigma_{N2} = 0.5$, we choose it as a separator of "acceptable" from "very good" values of $\Delta\sigma_N/\sigma_{N2}$. In fact, the curve f (obs) appears to be quite well fitted with a simple skewed Gaussian distribution (called f(Z) here):

$$\text{Freq of occurrence} = f(Z) = c_1 \times (1 - c_4 Z) \times \exp\left[(-1/2)(Z - c_2)^2/c_3^2\right], \quad (1)$$

where $Z \equiv \Delta\sigma_N/\sigma_{N2}$, for $c_1 = 48$, $c_2 = 0.35$, and $c_3 = 0.55$ (see [14]); the skewness factor is (1—c_4Z), where $c_4 = 0.35$. f(Z) is shown in **Figure 4** as the red dashed curve. For a measure of how well this modified normal distribution fits the actual histogram, we define a σ as follows:

$$\sigma = \sqrt{\left(\sum_i \left[f(\text{obs})_i - f(Z)_i\right]^2/N\right)}, \quad (2)$$

where i goes from 1 to 11, and therefore, N in this case is 11 (but recall that the total number of MCs employed in this analysis is 209). The value of σ = 4.0 is shown in the upper right-hand corner (first line in red) of **Figure 4**. For comparison, for the same set of coefficients, except with no skewness (i.e., $c_4' = 0.0$), we get a larger σ′ = 7.0 seen on the second line; this simple Gaussian is the black dotted curve in **Figure 4**. And for a set of coefficients of $c_1 = 45$, $c_2 = 0.35$, $c_3 = 0.55$, and $c_4 = 0.0$, we get an intermediate value for σ′′ = 6.0 (not shown in **Figure 4**); this is an attempt to lower the peak in the black dotted curve in the figure. The set of coefficients giving σ = 4.0, where only two-place accuracy is needed, is probably the best set possible, or very close to it. As new MCs are found in future *Wind* data, they will be added to this website, and, of course, they may alter the optimum f(Z) fit curve.

Finally, we discuss **Figure 2** which is a plot of $\Delta\sigma_N/\sigma_{N2}$ *versus* time for a family of Q_0 (1, 2, and 3) showing almost the same average of $\Delta\sigma_N/\sigma_{N2}$ (which goes from 0.43 to 0.48) regardless of the value of Q_0, but with large scatter in each case. This means that there is a very poor correlation between $\Delta\sigma_N/\sigma_{N2}$ and Q_0. In other words, better values of $\Delta\sigma_N/\sigma_{N2}$ should not necessarily be expected, just because the MCs are of better Quality (based on the LJB model). However, as **Table 1** shows, the better Q_0 is we might expect statistically slightly better results in both the success rate and in the degree of excellence, that is, in the percentage of cases where $\Delta\sigma_N/\sigma_{N2} \geq 0.5$.

Concerning the issue of solar cycle dependence, solid and dotted lines of **Figure 5A** show yearly occurrence frequency of all MC events, N_{Yearly} and MC events with $\Delta\sigma_N/\sigma_{N2} \geq 0.5$, and $N_{\Delta\sigma N/\sigma N2 \geq 0.5}$. The correlation coefficient between them is 0.94; that is, they correlate very well. Both N_{Yearly} and $N_{\Delta\sigma N/\sigma N2 \geq 0.5}$ vary with solar activity. **Figure 5B** shows clearly that there is no solar cycle dependence for normalized $N_{\Delta\sigma N/\sigma N2 \geq 0.5}$ with N_{Yearly}.

Speed is also an important input parameter for the LJB model. We separate 209 MCs into two groups: 1) $\Delta\sigma_N/\sigma_{N2} < 0.5$ and 2) $\Delta\sigma_N/\sigma_{N2} \geq 0.5$. There are 123 MCs with $\Delta\sigma_N/\sigma_{N2} < 0.5$ and 86 MCs with $\Delta\sigma_N/\sigma_{N2} \geq 0.5$. The average and median speed are 440 and 405 km/s, respectively, for group (1). The average and median speed are 433 and 408 km/s, respectively, for group (2). This implies that the Quad technique does not work better for the MC events with higher speed.

The Quad modification is derived from the difference in field magnitude between the actual field profiles and the fields derived from the LJB (Bessel function) model where many cases are considered, to develop quadratic correction functions. We have shown that in general, the LJB model with the Quad modification is expected to provide more accurate MC fitting, and it should be useful particularly for those studies where the spatial variation of the B-field magnitude across a MC is important, especially in comparison to the basic LJB model.

DATA AVAILABILITY STATEMENT

The original contributions presented in the study are included in the article/**Supplementary Material**; further inquiries can be directed to the corresponding author.

AUTHOR CONTRIBUTIONS

C-CW, RL, and DB contributed to conception and design of the study. C-CW organized the database. RL and C-CW performed

the statistical analysis. RL wrote the first draft of the manuscript. RL, C-CW, and DB wrote sections of the manuscript. All authors contributed to manuscript revision, reading, and approved the submitted version.

FUNDING

This study was partially supported by the Chief of Naval Research (CCW), NASA 80HQTR19T0062 (CCW & RPL), 80HQTR18T0023, and 80HQTR20T0067 (CCW) grants.

ACKNOWLEDGMENTS

We thank the *Wind* MFI and SWE teams for the care that they employ in producing the magnetic field and plasma data.

SUPPLEMENTARY MATERIAL

The Supplementary Material for this article can be found online at: https://www.frontiersin.org/articles/10.3389/fphy.2021.712599/full#supplementary-material

REFERENCES

1. Burlaga L, Sittler E, Jr., Mariani F, and Schwenn R Magnetic Loop Behind an Interplanetary Shock: Voyager, Helios, and IMP 8 Observations. *J Geophys Res* (1981) 86:6673–84. doi:10.1029/ja086ia08p06673
2. Burlaga LF Magnetic Clouds and Force-Free Fields with Constant Alpha. *J Geophys Res* (1988) 93:7217–24. doi:10.1029/ja093ia07p07217
3. Burlaga LF *Interplanetary Magnetohydrodynamics*. New York: Oxford Univ. Press (1995). p. 89–114.
4. Cane HV, and Richardson IG Interplanetary Coronal Mass Ejections in the Near-Earth Solar Wind during 1996–2002. *J Geophys Res* (2003) 108:1156. doi:10.1029/2002JA009817
5. Jian L, Russell CT, Luhmann JG, and Skoug RM Properties of Interplanetary Coronal Mass Ejections at One AU during 1995 – 2004. *Solar Phys* (2006) 239:393–436. doi:10.1007/s11207-006-0133-2
6. Chi Y, Shen C, Wang Y, Xu M, Ye P, Wang S, et al. Statistical Study of the Interplanetary Coronal Mass Ejections from 1995 to 2015. *Sol Phys* (2016) 291:2419–39. doi:10.1007/s11207-016-0971-5
7. Lepping RP, Berdichevsky DB, Wu C-C, Szabo A, Narock T, Mariani F, et al. A Summary of *WIND* Magnetic Clouds for Years 1995-2003: Model-Fitted Parameters, Associated Errors and Classifications. *Ann Geophys* (2006) 24:215–45. doi:10.5194/angeo-24-215-2006
8. Lepping RP, Wu C-C, Berdichevsky DB, and Szabo A Magnetic Clouds At/near the 2007 - 2009 Solar Minimum: Frequency of Occurrence and Some Unusual Properties. *Sol Phys* (2011) 274:345–60. doi:10.1007/s11207-010-9646-9
9. Lepping RP, Wu C-C, Berdichevsky DB, and Szabo A *Wind* Magnetic Clouds for 2010 - 2012: Model Parameter Fittings, Associated Shock Waves, and Comparisons to Earlier Periods. *Sol Phys* (2015) 290:2265–90. doi:10.1007/s11207-015-0755-3
10. Lepping RP, Wu C-C, Berdichevsky DB, and Kay C Magnetic Field Magnitude Modification for a Force-free Magnetic Cloud Model. *Solar Phys* (2018) 293(19):162. doi:10.1007/s11207-018-1383-5
11. Lepping RP, Wu C-C, Berdichevsky DB, and Szabo A Model Fitting of Wind Magnetic Clouds for the Period 2004 – 2006. *Solar Phys* (2020) 295:83. doi:10.1007/s11207-020-01630-2
12. Lepping RP, Berdichevsky DB, and Wu C-C Average Magnetic Field Magnitude Profiles of Wind Magnetic Clouds as a Function of Closest Approach to the Clouds' Axes and Comparison to Model. *Solar Phys* (2017) 292(2):27. doi:10.1007/s11207-016-1040-9
13. Lepping RP, Jones JA, and Burlaga LF Magnetic Field Structure of Interplanetary Magnetic Clouds at 1 AU. *J Geophys Res* (1990) 95:11957. doi:10.1029/ja095ia08p11957
14. Freund JE *Mathematical Statistics*. Englewood Cliffs, NJ: Prentice-Hall (1962). p. 127–8.

Conflict of Interest: The authors declare that the research was conducted in the absence of any commercial or financial relationships that could be construed as a potential conflict of interest.

Publisher's Note: All claims expressed in this article are solely those of the authors and do not necessarily represent those of their affiliated organizations, or those of the publisher, the editors, and the reviewers. Any product that may be evaluated in this article, or claim that may be made by its manufacturer, is not guaranteed or endorsed by the publisher.

frontiers in Physics

ORIGINAL RESEARCH
published: 11 November 2021
doi: 10.3389/fphy.2021.745152

Statistical Study of Small-Scale Interplanetary Magnetic Flux Ropes in the Vicinity of the Heliospheric Current Sheet

Qiang Liu[1,2]*, *Yan Zhao*[1,2] *and Guoqing Zhao*[1,2]

[1]Institute of Space Physics, Luoyang Normal University, Luoyang, China, [2]Henan Key Laboratory of Electromagnetic Transformation and Detection, Luoyang, China

The small-scale interplanetary magnetic flux ropes (SIMFRs) are common magnetic structures in the interplanetary space, yet their origination is still an open question. In this article, we surveyed 63 SIMFRs found within 6-day window around the heliospheric current sheet (HCS) and investigated their axial direction, as well as the local normal direction of the HCS. Results showed that the majority (48/63) of the SIMFRs were quasi-parallel to the associated HCS (i.e., the axial direction of SIMFRs was quasi-perpendicular to the normal direction of the associated HCS). They also showed that the SIMFRs quasi-parallel to the associated HCS statistically had shorter duration than the cases quasi-perpendicular. The results indicate that most of these SIMFRs may be generated in the nearby HCSs.

Keywords: interplanetary magnetic structure, interplanetary current sheet, magnetic reconnection, solar wind, reconnection exhaust

OPEN ACCESS

Edited by:
Hongqiang Song,
Shandong University, China

Reviewed by:
Mengjiao Xu,
University of Science and Technology of China, China
Emilia Kilpua,
University of Helsinki, Finland

***Correspondence:**
Qiang Liu
liuq523@163.com

Specialty section:
This article was submitted to Stellar and Solar Physics, a section of the journal Frontiers in Physics

Received: *21 July 2021*
Accepted: *07 October 2021*
Published: *11 November 2021*

Citation:
Liu Q, Zhao Y and Zhao G (2021) Statistical Study of Small-Scale Interplanetary Magnetic Flux Ropes in the Vicinity of the Heliospheric Current Sheet. Front. Phys. 9:745152. doi: 10.3389/fphy.2021.745152

HIGHLIGHTS

1 Most of the small-scale interplanetary magnetic flux ropes were parallel to the nearby heliospheric current sheet.
2 Among the ropes parallel to the nearby heliospheric current sheet, the majority of the ropes had a short duration.
3 Most of the small-scale interplanetary magnetic flux ropes were generated within the nearby heliospheric current sheet.

INTRODUCTION

Magnetic flux ropes (MFRs) are a helical magnetic structure that is very common in solar corona, the interplanetary space, planetary ionosphere, and earth magnetosphere [1]. The interplanetary MFRs (IMFRs) play an important role in connecting the earth magnetosphere and the solar atmosphere. For example, it is found that IMFRs (e.g., magnetic cloud [MCs]) usually have strong geomagnetic effect [2–5]. Therefore, the generation, evolution, and propagation of IMFRs structure are important problems in research of solar-terrestrial space physics. According to the size and duration, IMFRs can generally be divided into two categories. One is large-scale MCs, whose diameter ranges from 0.2 to 0.4 AU near the Earth [2, 6–9]. The other one is small-scale IMFR (SIMFRs). Unlike large-scale MCs, the diameters of the SIMFRs are approximately

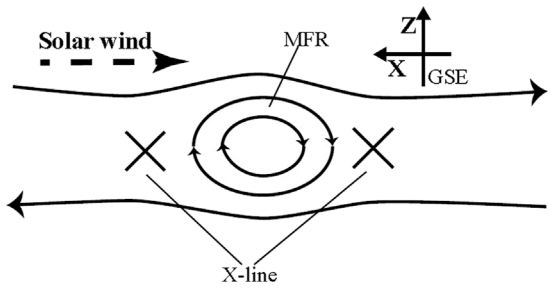

FIGURE 1 | An illustration of a magnetic flux rope (MFR) formed by multiple X-line magnetic reconnection. The dashed arrowed line indicates the direction of the movement of the solar wind.

0.02 AU, and their durations are usually less than 12 h [10, 11, 34]. Moldwin et al. [12] first reported an SIMFR detected by Ulysses spacecraft near 5 AU. From then, SIMFRs have aroused researchers' great interest. It is generally believed that the solar corona and interplanetary medium are two important source regions of SIMFRs [10, 11, 13–28, 30]. Moldwin et al. [13] found the SIMFRs and MCs had both similar and different characteristics, and they suggested that the SIMFRs and MCs are two different categories and have different source regions. Feng et al. [10] investigated the data of Wind during 1995–2005 and identified 144 IMFRs. They found that the diameters of these events showed a continuous distribution; thus, they proposed that all IMFRs had the same source regions, namely, originated from solar eruptions. Then, based on the counterstreaming suprathermal electrons (CSEs), the average ionized state distribution of iron or oxygen, and the interplanetary observational characteristics, the idea that the SIMFRs originated from the sun was adopted by many researchers [16, 19, 24]. And some researchers [29–32] have found direct observational evidence for some SIMFRs to come from solar explosive events. In addition, the view that SIMFRs could be generated by heliospheric current sheet (HCS) was also proposed by many studies based on the observational data [10, 13, 20, 33–35]. Magnetic reconnection is one of the important mechanisms forming MFRs. **Figure 1** illustrates the formation of MFRs by multiple X-line reconnection in the x-z plane of the Geocentric Solar Ecliptic (GSE) coordinate system [36]. If SIMFRs were formed by magnetic field reconnection in the HCS, these SIMFRs should lie in the plane of HCS (i.e., the axis of the SIMFRs should be perpendicular to the normal of the HCS). Besides, as solar wind and structures embedded in it mainly move in the Sun–Earth line direction, assuming that the magnetic field points from the Sun to the Earth in the upper hemisphere and points from the Earth to the Sun on the bottom hemisphere, as illustrated in **Figure 1**, the spacecraft should detect negative to positive variation of the z component of the magnetic field. In this article, we surveyed SIMFRs detected near the HCS. The results indicated that most of these SIMFRs may be generated in the HCS.

DATA AND METHODS

In this study, the high-resolution magnetic field and plasma data are provided by instruments on Wind spacecraft. We used the magnetic field data from the Magnetic Field Investigation instrument and the plasma data from the WIND 3-D Plasma instrument, both with time resolution of 3s [37]. For events during which there are no plasma data from the WIND 3-D Plasma, data with time resolution of 92s from the Solar Wind Experiment [38] are used. The GSE coordinate system is used in this article, if not specified.

The SIMFRs studied in this article were detected by Wind from 1995 to 2013 in the vicinity of HCSs. The crossing of an HCS is identified by a flip in at least one component of the magnetic field, and the polarity of the magnetic field should be kept several hours or more before and after the flip. The width of the HCS is approximately 10,000 km near 1 AU, and its surrounding plasma sheet is approximately 30 times thicker [39]. The transit of the HCS varies from several seconds to hours [39]. However, due to, for example, waves, the spacecraft could cross the HCS several times in relatively short time interval. In such cases, the center one crossing would be considered as the crossing time of the HCS. Feng et al. [2015] shows that CSEs were found in most SIMFRs, and the CSEs usually are detected within 3 days of sector boundary [19, 40]. Therefore, we investigate SIMFRs found within 6-day window around HCS [19]. The identification of SIMFRs is based on a bipolar variation of the one component of the magnetic field and enhancement of the magnitude of magnetic field near the center of the bipolar variation. Part of the studied SIMFRs is adopted from the SIMFRs in the study of Feng et al. (2015) [19]. We estimate the axial direction of flux ropes using the Grad–Shafranov (G-S) reconstruction method [41–44]. The basic idea of the G-S method is that assuming a flux rope is two-dimensional and quasi-steady, the thermal pressure and the magnitude of the axial magnetic field should be constant along one magnetic field line in the plane perpendicular to the axial direction, according to the G-S equation [41]. The normal of the HCS was obtained by applying minimum variance analysis to the magnetic field data and that the minimum variance direction is thought to be the normal direction the HCS [45–47]. As the movement of the solar wind and the magnetic structures within it is mainly in the x direction, to improve the reliability of estimation of the normal direction of HCSs, only HCSs with the angle between the normal and the y directions within the range of 30°–150° are considered. Finally, we obtained a total of 63 cases, and the properties of these flux ropes are shown in **Table 1**. In **Table 1**, the second and third columns show the front boundary and duration of SIMFRs. The fourth and fifth columns show the longitude and latitude of the axis of SIMFRs and the normal direction of HCS with respect to the ecliptic plane. The sixth column shows the time when the spacecraft crosses the HCS. The seventh column shows the time difference between the beginning of the SIMFR and the HCS crossing. The eighth column shows the angle between the axis of SIMFRs and the normal direction of the associated HCSs.

TABLE 1 | The list of SIMFR studied in this work.

No.	Start[a]	Duration (MIN)[b]	SIMFR (longitude, latitude)[c]	HCS (longitude, latitude)[c]	HCS[d]	The time interval (h)[e]	Angle[f]
001	1995/01/16 11:38	81	(113.5, −58.2)	(176.25, −13.42)	1995/01/17 04:55	17.3	64.5
002	1995/03/07 04:00	243	(160.91, 23.82)	(186.99, 52.87)	1995/03/04 11:07	7.0	35.12
003	1995/03/24 11:31	284	(14.32, 77.57)	(340.37, 36.08)	1995/03/24 04:35	8.0	43.99
004	1995/04/06 20:09	49	(283.50, −0.89)	(76.66, 83.70)	1995/04/06 13:10	10.3	96.50
005	1995/04/06 21:12	74	(324.42, 2.37)	(76.66, 83.70)	1995/04/06 13:10	14.6	90.02
006	1995/04/18 06:10	318	(81.28, 12.62)	(9.54, −57.22)	1995/04/18 16:25	55.3	91.54
007	1995/05/29 13:47	161	(65.7, 46.48)	(231.44, −3.08)	1995/05/30 04:20	41.3	134.86
008	1995/06/17 21:43	414	(231.64, −45.33)	(49.69, 13.14)	1995/06/19 08:09	38.9	147.77
009	1995/09/20 12:59	78	(48.18, −4.39)	(22.46, 72.02)	1995/09/22 20:14	16.2	78.21
010	1995/09/21 02:55	119	(282.10, 12.74)	(22.46, 72.02)	1995/09/22 20:14	23.7	81.05
011	1996/05/14 21:53	101	(42.54, −4.86)	(183.86, 10.82)	1996/05/13 01:58	1.3	141.25
012	1996/06/20 16:41	126	(181.03, 36.61)	(185.45, −34.59)	1996/06/19 01:45	8.8	71.32
013	1996/08/06 00:04	226	(117.19, −18.96)	(38.2, 30.41)	1996/08/06 16:15	64.7	90.50
014	1997/05/12 05:24	138	(55.11, −17.39)	(227.35, −66.39)	1997/05/11 05:45	12.1	96.01
015	1997/05/16 06:15	429	(236.68, −34.14)	(35.74, 37.71)	1997/05/15 00:24	0.0	162.71
016	1997/07/23 20:54	80	(58.24, −40.77)	(16.88, 19.13)	1997/07/23 22:14	20.0	71.15
017	1997/07/24 07:00	27	(269.14, 24.32)	(16.88, 19.13)	1997/07/23 22:14	61.3	97.32
018	1997/09/27 15:14	100	(122.79, −29.58)	(91.47, −72.12)	1997/09/30 07:55	0.7	45.74
019	1997/10/07 04:30	169	(140.71, −46.78)	(358.13, 57.45)	1997/10/08 04:32	23.1	155.08
020	1998/01/29 08:10	292	(84.85, −0.57)	(220.86, −21.80)	1998/01/29 20:15	47.8	131.63
021	1998/02/27 05:45	182	(275.48, −2.85)	(169.71, −15.51)	1998/02/27 05:45	42.0	104.38
022	1998/03/25 13:28	170	(313.08, 14.44)	(229.4, 50.58)	1998/03/26 09:30	3.3	74.91
023	1998/03/28 22:47	204	(291.53, −12.69)	(229.4, 50.58)	1998/03/26 09:30	72.5	83.11
024	1998/06/26 00:04	465	(142.79, −39.25)	(187.08, −31.71)	1998/06/23 23:08	4.3	36.47
025	1998/10/27 14:25	74	(294.07, 7.82)	(36.54, −18.69)	1998/10/27 13:45	40.6	104.25
026	1998/11/08 04:42	592	(140.47, 35.87)	(168.84, 31.55)	1998/11/09 15:18	69.3	23.91
027	1999/05/24 09:00	118	(217.34, −26.63)	(167.68, 8.66)	1999/05/23 09:52	44.2	59.70
028	2000/04/27 19:00	254	(232.19, 48.06)	(219.72, 10.82)	2000/04/27 08:15	30.6	38.68
029	2001/01/08 20:59	173	(296.34, −39.15)	(2.11, −6.75)	2001/01/10 20:44	1.9	67.03
030	2001/01/09 02:42	38	(30.88, 78.00)	(2.11, −6.75)	2001/01/10 20:44	41.7	86.21
031	2002/08/19 12:49	76	(290.00, −17.08)	(181.12, 7.14)	2002/08/19 09:30	12.1	110.09
032	2002/11/10 23:07	111	(312.44, 18.24)	(178.11, −19.26)	2002/11/10 07:52	3.3	136.87
033	2002/11/20 22:50	303	(102.58, 35.74)	(298.14,- 0.30)	2002/11/20 01:10	6.2	141.72
034	2003/01/14 13:10	150	(293.59, 57.73)	(31.99, 2.15)	2003/01/17 13:40	51.9	92.61
035	2003/01/17 09:22	250	(317.34, 18.94)	(31.99, 2.15)	2003/01/17 13:40	26.7	74.72
036	2003/02/11 05:25	136	(289.44, −5.54)	(219.25, 10.76)	2003/02/12 22:00	3.6	71.74
037	2005/04/22 10:49	39	(138.67, −7.57)	(24.54, −27.14)	2005/04/19 13:30	24.1	107.49
038	2005/10/16 20:14	93	(115.25, −55.69)	(200.72, 15.38)	2005/10/15 00:00	22.4	100.14
039	2005/10/25 22:55	59	(150.31, 11.37)	(36.18, 19.51)	2005/10/24 16:22	18.8	108.17
040	2005/11/11 00:11	47	(267.47, 59.25)	(212.9, 22.27)	2005/11/11 02:05	3.6	53.13
041	2006/01/22 09:52	136	(73.12, 4.63)	(54.27, 46.11)	2006/01/23 06:05	18.1	44.60
042	2006/01/24 23:47	40	(241.08, 1.87)	(54.27, 46.11)	2006/01/23 06:05	7.5	111.74
043	2006/02/19 21:47	70	(296.73, −3.43)	(41.42, 6.37)	2006/02/19 09:40	11.0	106.83
044	2006/04/13 01:23	358	(246.98, −3.9)	(315.06, −21.09)	2006/04/13 03:58	21.3	27.46
045	2006/08/27 15:19	75	(220.61, 5.64)	(319.90, −6.40)	2006/08/27 12:00	15.8	62.03
046	2007/01/01 07:52	69	(232.58, −15.69)	(4.21, −19.55)	2007/01/01 14:04	30.7	120.81
047	2007/02/10 13:13	111	(252.36, −22.8)	(161.22, 34.17)	2007/02/12 17:09	33.4	103.29
048	2007/04/10 21:18	211	(121.76, 25.72)	(34.41, −82.96)	2007/04/09 06:34	70.8	115.19
049	2007/05/22 01:53	360	(153.80, 44.94)	(18.56, 46.71)	2007/05/21 22:15	17.3	80.24
050	2007/11/08 16:44	29	(313.99, −28.18)	(19.48, −62.91)	2007/11/07 16:39	7.0	54.06
051	2008/01/13 09:18	140	(61.29, 12.15)	(62.76, 2.78)	2008/01/12 10:53	8.0	65.11
052	2008/02/07 21:10	95	(231.47, 3.01)	(122.71, 28.84)	2008/02/07 02:20	10.3	72.14
053	2008/12/05 09:19	96	(49.57, 17.94)	(300.64, −14.50)	2008/12/04 11:19	14.6	169.99
054	2009/11/02 10:18	37	(275.14, −12.78)	(150.70, −29.30)	2009/11/02 06:40	55.3	62.10
055	2010/05/26 00:15	171	(180.18, 70.83)	(175.93, 3.01)	2010/05/25 06:09	41.3	67.87
056	2010/08/09 07:33	185	(301.27, 58.47)	(29.36, −19.43)	2010/08/09 15:00	38.9	105.49
057	2010/11/12 09:27	87	(330.46, 40.53)	(51.29, −24.06)	2010/11/12 20:28	16.2	98.87
058	2011/03/10 20:56	85	(280.40, −12.59)	(40.62, −7.91)	2011/03/11 20:16	23.7	117.16
059	2011/04/29 05:54	166	(321.95, 10.57)	(328.74, −40.31)	2011/04/28 14:06	1.3	112.55
060	2012/01/27 03:41	91	(92.71, 9.5)	(143.02, 76.82)	2012/01/25 20:59	8.8	72.28
061	2012/05/31 20:52	354	(141.05, −26.55)	(157.39, 37.62)	2012/06/01 18:50	64.7	162.33
062	2013/06/30 13:56	94	(141.55, −12.24)	(145.55, 78.38)	2013/06/29 04:34	12.1	89.97
063	2013/11/11 06:32	42	(64.44, −23.00)	(333.20, 62.54)	2013/11/14 05:18	0.0	133.06

[a]*The beginning of the SIMFR (UT).*

[b]The duration of the SIMFR (MIN).
[c]The longitude and latitude of the axis of SIMFR and the normal direction of HCS with respect to the ecliptic plane.
[d]The time of HCS crossing (UT).
[e]The time between the beginning of the SIMFR and the HCS crossing.
[f]The angle between the axial direction of SIMFR and the normal direction of HCS.

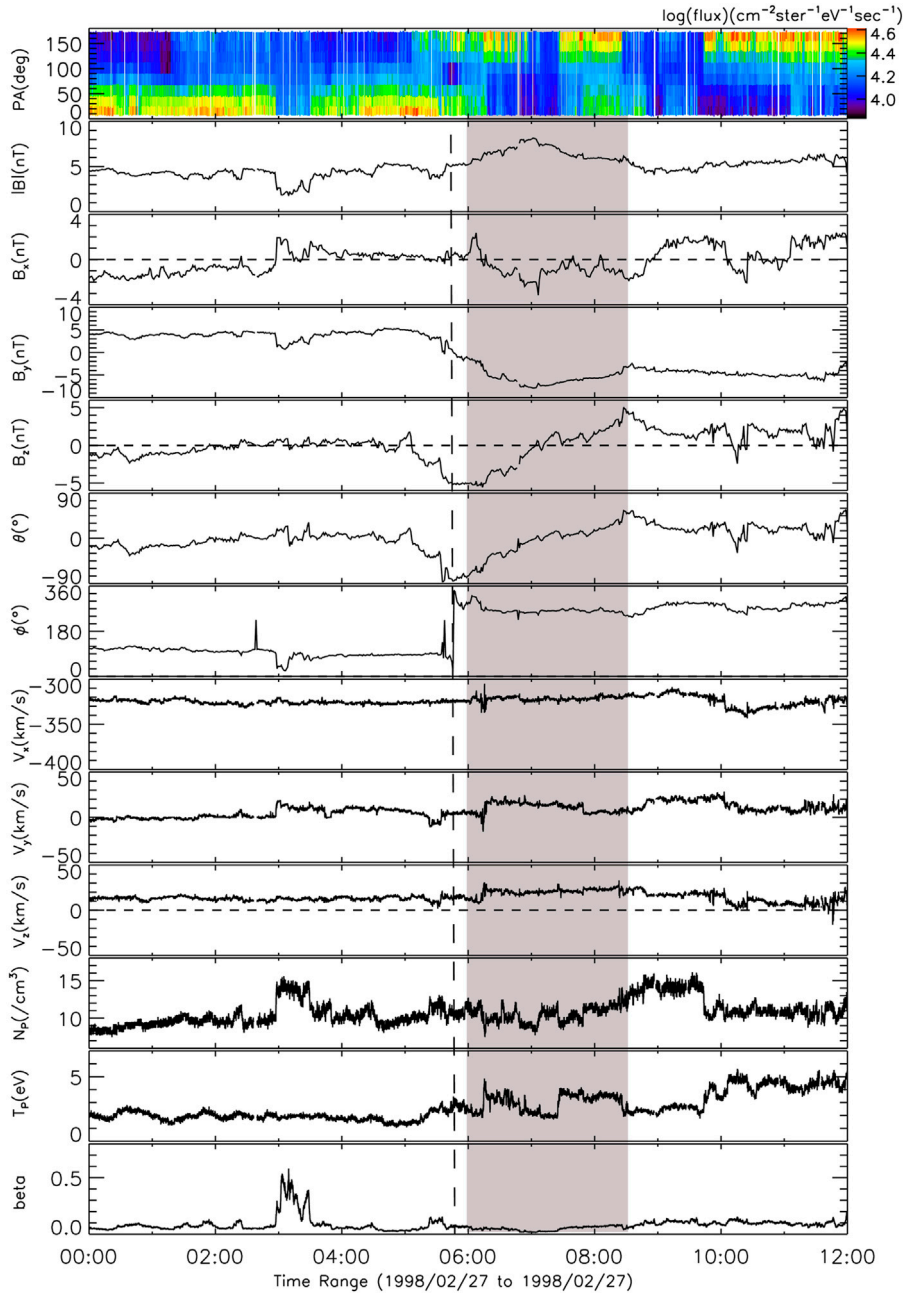

FIGURE 2 | An example of a magnetic flux rope detected in the vicinity of an HCS on February 27, 1998. From top to bottom, the pitch angle distribution of electrons with energy of 228 eV, the magnitude and the three components of the magnetic field, the angular coordinates of the magnetic field vector, the three components of velocity, the number density, the temperature of protons, and the plasma β values. The vertical dashed line indicates the crossing time of the HCS by the space craft. The shadow region indicates the magnetic flux rope.

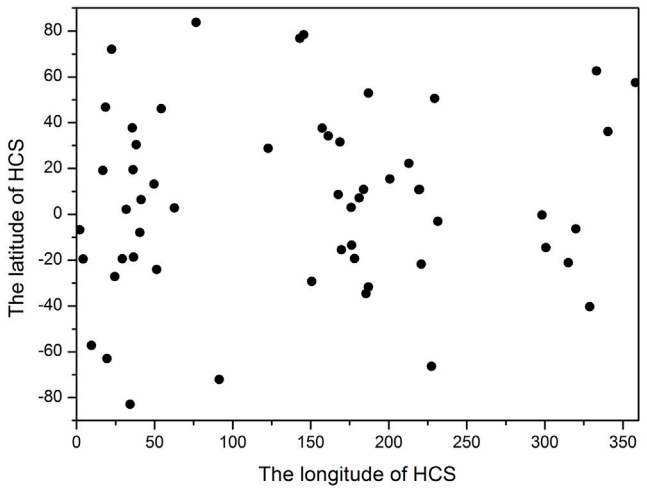

FIGURE 3 | The distribution of the latitude and longitude of the normal direction of the HCSs.

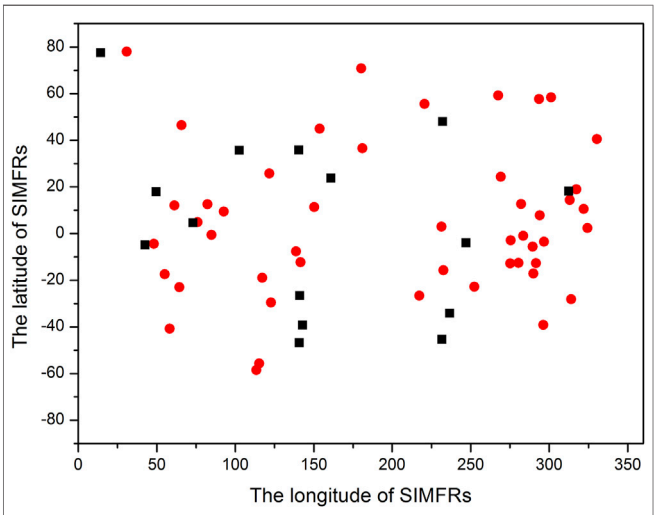

FIGURE 4 | The distribution of the latitude and longitude of the axial direction of the studied SIMFRs. The red dots represent cases that the SIMFRs quasi-parallel to the associated HCS (CAT1). The black squares represent the SMIFRs of CAT2 category.

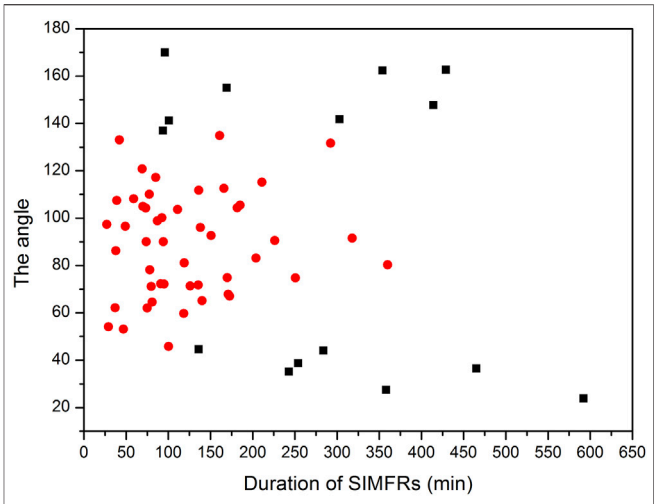

FIGURE 5 | The distribution of the angle between the axis of the rope and the normal of the associated HCS as a function of the duration of the flux ropes. The red dots represent the SIMFRs of CAT1 category. The black squares represent SIMFRs of CAT2 category.

RESULTS

Figure 2 shows an example of an SIMFR in the vicinity of an HCS on February 27, 1998. From top to bottom, **Figure 2** shows the pitch angle distribution of electrons with energy of 228 eV, the magnitude and the three components of the magnetic field, the angular coordinates of the magnetic field vector, the three components of velocity, the number density, the temperature of protons, and the plasma β values. From 04:45, the By component decreased from ~+5 nT to zero around 05:45 and then changed sign and increased in magnitude. The pitch angle of electrons also changed from 0° to 180° around 05:45. Such a variation in the magnetic field is thought to be caused by crossing of an HCS. Just after crossing the HCS, the spacecraft detected a bipolar variation in the Bz component (varied from −5 to 5 nT). In the meantime, the magnitude of the magnetic field and the By component peaked. Therefore, the bipolar signal in Bz is thought to be caused by crossing of an MFR. The direction of the axis of the flux rope is (275.48°, −2.85°). The normal direction of the HCS is (169.71°, −15.51°). The angle between the axis of the flux rope and the normal of the HCS is 104.38, which means that the flux rope almost lied in the plane of the HCS. Consider the observations were made in the increasing phase of the 23rd solar cycle, the dipolar Bz varying from −5 to 5 nT is consistent with an MFR generated by magnetic reconnection in the HCS moving to further heliosphere.

Figure 3 plots the distribution of the latitude and longitude of the normal direction of the HCSs. The distribution of the latitude is mainly in the range between −60° and 60°, which is reasonable, considering that the movement of the solar wind is mainly in the *x* direction, which make the detection of HCSs relatively difficult. The longitude of the HCS normal is mainly near 45° and 225°, which is not unexpected considering that the parker spiral angle is 135° at Earth. **Figure 4** displays the distribution of the latitude and longitude of the axial direction of the studied flux ropes. The longitude of the axis ranges from 25° to 325°, whereas the latitude mainly lies between −60° and 60°.

In order to explore the possible connection between SIMFRs and HCSs, the angle between the axis of the flux rope and the normal of the associated HCS is investigated. Based on the angle, the studied flux ropes are divided into two categories. The first category (CAT1) is for the flux ropes quasi-parallel to the HCS; that is, the angle between the axial direction of the flux ropes and the normal direction of the associated HCS are within the range of 45° and 135°. The other category (CAT2) is for ropes quasi-perpendicular to the HCS, and their angles are less than 45° or greater than 135°. A total of 48 flux ropes are found in the CAT1

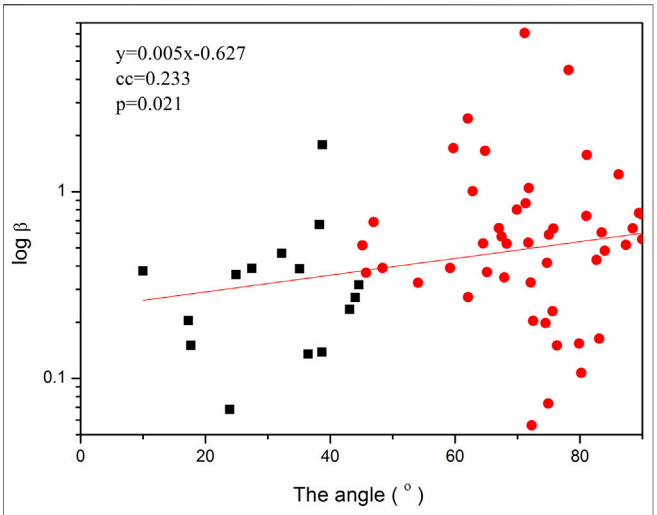

FIGURE 6 | The distribution of plasma β with the angle between the axis of the rope and the normal of the associated HCS. The red dots represent the SIMFRs of CAT1 category. The black squares represent SIMFRs of CAT2 category. The correlation coefficient (cc) and *p* value (*p*) are shown in the upper left corner.

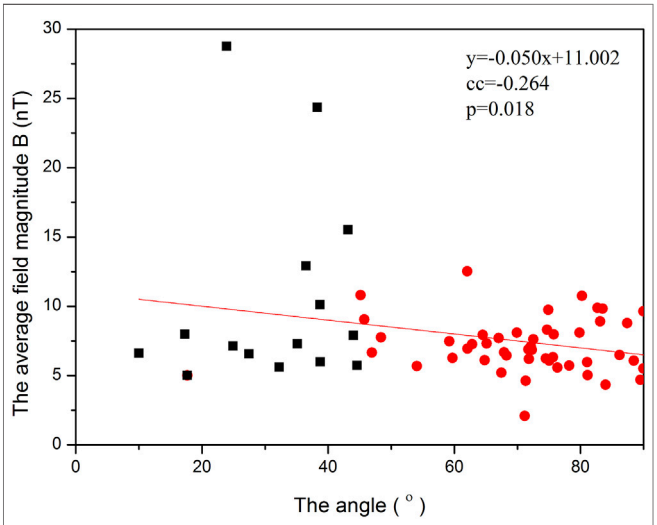

FIGURE 7 | The distribution of the average field magnitude with the angle between the axis of the rope and the normal of the associated HCS. The red dots represent the SIMFRs of CAT1 category. The black squares represent SIMFRs of CAT2 category. The correlation coefficient (cc) and *p* value (*p*) are shown in the upper right corner.

category; the percentage is 76.2%. That is, most of SIMFRs were quasi-parallel to the associated HCS.

Out results also show that, among the ropes quasi-parallel to the associated HCS, the majority of the ropes have a short duration. **Figure 5** presents the scatter plot of the angle between the axis of the rope and the normal of the associated HCS as a function of the duration of the flux ropes. The red dots represent the SIMFRs of CAT1 category, which are quasi-parallel to the HCS. The black squares represent the SMIFRs of CAT2

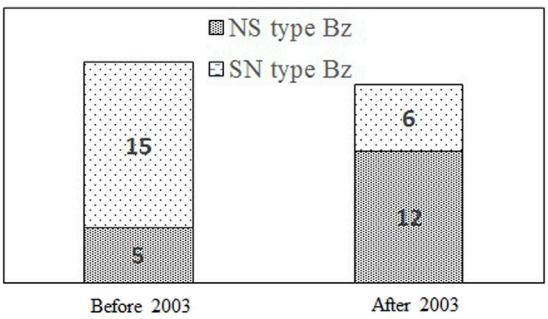

FIGURE 8 | The distribution of the Bz type of the SIMFRs with axial direction near the *y* direction. The left (right) histogram represents SIMFRs observed before (after) 2003.

category. Based on the duration, one may find that, for ropes with duration less than 350 min, the ropes of CAT1 category dominated, and the ratio is 83.9% (47 of 56 ropes). For those with duration greater than 350 min, the ropes of CAT2 category dominated, and the ratio is 85.7% (six of seven ropes).

Figures 6, **7** plot the distributions of the plasma (proton) β and the average field magnitude of SIMFRs as a function of the angle between the axis of the rope and the normal of the associated HCS, respectively, where the red dots are for the SIMFRs of CAT1 category, and the black squares are for the SMIFRs of CAT2 category. Note that we only consider the size of the angle, the direction of the angle is ignored, and the range of the angle is from 0° to 90°. It seems that there was weak but negative relation between the plasma β and the angle, whereas there was positive relation between the average field magnitude and the angle.

Assuming that one SIMFR was generated by HCS magnetic reconnection and lay in the HCS plane. The spacecraft traversing it should detect south-to-north (SN) or north-to-south (NS) variation of the z component of the magnetic field (Bz) [11]. Furthermore, as Janivier et al. [2014] pointed out that the variation of Bz depends on the globe solar dipole magnetic field [21, 48]. The change of the sign of the global solar dipole happens typically 1 year after the solar maximum (~2003 years in this work) [49]. **Figure 8** shows the distributions of the two-type variation of the Bz component of CAT1 category flux ropes with the angle range from 60°"""" to 120°. One can see that before the year of 2003, the ratio of SN to NS type was 3:1 and became 1:2 after 2003.

SUMMARY AND DISCUSSION

SIMFRs are common structures in the interplanetary space and play an important role in space weather [16]. Determining the source region of SIMFRs is important for understanding of their generation and evolution. In this article, we surveyed the axial distribution of SIMFRs detected within 6-day window around HCS and found that most of the ropes (76.2%) was quasi-parallel to the HCS. If SIMFRs are originated from HCS (e.g., generated during magnetic reconnection), then the axis of the ropes should

tend to have large angle (be perpendicular) to the normal of the associated current sheet [11]. Therefore, our result indicated that these flux ropes detected near the HCSs may be generated within the HCS. Except for the angle distribution feature, the scales of flux ropes originated in HCS should also be limited by the thickness of the HCS bearing them [11, 21]. From **Figure 4**, one can see that for most of the ropes (56 of 63 ropes) with short duration (<350 min), and most of these ropes (47 of 56 ropes) are quasi-parallel to the associated HCS. While for those with long duration (>400 min), the ropes are all quasi-perpendicular to the HCS. That is, these short-duration flux ropes are probably generated within the associated HCSs. For those long-duration ropes, the angle distribution is not consistent with those predicted by HCS magnetic reconnection. These ropes may have their source region in the solar corona.

The total average plasma β of CAT1 and CAT2 ropes was $\beta_1 = 0.84 \pm 0.17$ and $\beta_2 = 0.40 \pm 0.11$, respectively. The SIMFRs of CAT1 have higher total average plasma β and smaller average magnetic fields magnitude than CAT2 (**Figures 6**, **7**). If flux ropes of CAT1 were from HCS and flux ropes of CAT2 were from the solar corona, then the difference in the magnetic field magnitude and the plasma β seems reasonable, since the magnetic field in the solar corona is much stronger than that of the HCS.

The data studied in this work cover the whole 23rd solar cycle and the increasing phase of the 24th solar cycle. According to Janivier et al. [2014], if SIMFRs are formed in HCS, the dominate type of SIMFRs (i.e., the variation of Bz) should be different in different phase of solar cycle. We selected the variation of Bz of flux ropes with the angle range from 60° to 120° in the CAT1 category, and then comparing them before and after the time when the sign of the global solar dipole field changes (~2003 years), we found that the SN type dominated before 2003, whereas after 2003, the NS type dominated. Such a change was consistent with the magnetic topology of HCS during this period and thus consistent with the conclusion that MFRs of CAT1 may be generated in HCS. Moldwin et al. [2008] found no dependence of variation of Bz of SIMFRs on solar cycle, which is inconsistent with the result present here. The possible reason of such contrary is that unlike in the study by Moldwin et al. [2008], this article only focuses on the SIMFRs near the HCS.

In summary, we surveyed the SIMFRs detected within 6-day window around HCS. The results indicate that most of these SIMFRs may have their source region within the HCS.

DATA AVAILABILITY STATEMENT

Publicly available datasets were analyzed in this study. This data can be found here: http://cdaweb.gsfc.nasa.gov/cdaweb/istp_public/.

AUTHOR CONTRIBUTIONS

QL drafted the manuscript and led the observational analysis. YZ and GZ provided heuristic advice and revised the manuscript. All authors contributed to the interpretation of the results and helped draft the manuscript.

FUNDING

This work is also supported in part by the Plan for Scientific Innovation Talent of Henan Province (No. 174100510019).

ACKNOWLEDGMENTS

We acknowledge supports from NSFC under Grant Nos.: 41674170, 41974197, and 41874204. We thank NASA/GSFC for the use of data from the Wind spacecraft mission, which are available freely from the Coordinated Data Analysis Web (https://cdaweb.gsfc.nasa.gov/misc/NotesW.html).

REFERENCES

1. Russell CT, Priest ER, Lee L-C. *Physics of Magnetic Flux Ropes*. Washington, D.C.: American Geophysical Union (1990).
2. Burlaga LF. Magnetic Clouds and Force-free fields with Constant Alpha. *J Geophys Res* (1988) 93(A7):7217–24. doi:10.1029/JA093iA07p07217
3. Feng HQ, Chao JK, Lyu LH, Lee LC. The Relationship between Small Interplanetary Magnetic Flux Rope and the Substorm Expansion Phase. *J Geophys Res* (2010) 115:A09108. doi:10.1029/2009ja015191
4. Gonzalez WD, Tsurutani BT, Clúa de Gonzalez AL. Interplanetary Origin of Magnetic Storms. *Space Sci Rev* (1999) 88:529–62. doi:10.1023/A:1005160129098
5. Gonzalez WD, Echer E, Clua-Gonzalez AL, Tsurutani BT. Interplanetary Origin of Intense Geomagnetic Storms (Dst. *Geophys Res Lett* (2007) 34:340. doi:10.1029/2006GL028879
6. Burlaga L, Sittler E, Mariani F, Schwenn R. Magnetic Loop behind an Interplanetary Shock: Voyager, Helios, and IMP 8 Observations. *J Geophys Res* (1981) 86:6673–84. doi:10.1029/JA086iA08p06673
7. Bothmer V, Schwenn R. The Structure and Origin of Magnetic Clouds in the Solar Wind. *Ann Geophys* (1998) 16:1–24. doi:10.1007/s00585-997-0001-x
8. Goldstein H. On the Field Configuration in Magnetic Clouds. In: M Neugebauer, editor. *Solar Wind Five*, 2280. Pasadena, CA: NASA Conf. Publ. (1983). p. 731–3.
9. Lepping RP, Jones JA, Burlaga LF. Magnetic Field Structure of Interplanetary Magnetic Clouds at 1 AU. *J Geophys Res* (1990) 95(A8):11957–65. doi:10.1029/JA095iA08p11957
10. Feng HQ, Wu DJ, Chao JK. Size and Energy Distributions of Interplanetary Magnetic Flux Ropes. *J Geophys Res* (2007) 112:a–n. doi:10.1029/2006JA011962
11. Cartwright M, Moldwin M. Comparison of Small-Scale Flux Rope Magnetic Properties to Large-Scale Magnetic Clouds: Evidence for Reconnection across the HCS? *J Geophys Res Space Phys* (2008) 113(A9). doi:10.1029/2008ja013389
12. Moldwin MB, Phillips JL, Gosling JT, Scime EE, McComas DJ, Bame SJ, et al. Ulysses Observation of a Noncoronal Mass Ejection Flux Rope: Evidence of Interplanetary Magnetic Reconnection. *J Geophys Res* (1995) 100(A10):19903–10. doi:10.1029/95ja01123
13. Moldwin MB, Ford S, Lepping R, Slavin J, Szabo A. Small-scale Magnetic Flux Ropes in the Solar Wind. *Geophys Res Lett* (2000) 27(1):57–60. doi:10.1029/1999GL010724
14. Feng HQ, Wu DJ, Lin CC, Chao JK, Lee LC, Lyu LH. Interplanetary Small- and Intermediate-Sized Magnetic Flux Ropes during 1995-2005. *J Geophys Res* (2008) 113:a–n. doi:10.1029/2008JA013103

15. Feng HQ, Wu DJ. Observations of a Small Interplanetary Magnetic Flux Rope Associated with a Magnetic Reconnection Exhaust. *ApJ* (2009) 705(2):1385–7. doi:10.1088/0004-637x/705/2/1385
16. Feng HQ, Wang JM. Observations of Several Unusual Plasma Compositional Signatures within Small Interplanetary Magnetic Flux Ropes. *Astrophys J* (2010) 809:11. doi:10.1088/0004-637X/809/2/112
17. Feng HQ, Wu DJ, Wang JM, Chao JW. Magnetic Reconnection Exhausts at the Boundaries of Small Interplanetary Magnetic Flux Ropes. *A&A* (2011) 527: A67. doi:10.1051/0004-6361/201014473
18. Feng H, Wang J, Wu D. The Evidence for the Evolution of Interplanetary Small Flux Ropes: Boundary Layers. *Chin Sci Bull* (2012) 57:1415–20. doi:10.1007/s11434-011-4960-7
19. Feng HQ, Zhao GQ, Wang JM. Counterstreaming Electrons in Small Interplanetary Magnetic Flux Ropes. *J Geophys Res Space Phys* (2015) 120: 175–10. doi:10.1002/2015JA021643
20. Tian H, Yao S, Zong Q, He J, Qi Y. Signatures of Magnetic Reconnection at Boundaries of Interplanetary Small-Scale Magnetic Flux Ropes. *ApJ* (2010) 720(1):454–64. doi:10.1088/0004-637x/720/1/454
21. Janvier M, Démoulin P, Dasso S. *In Situ* properties of Small and Large Flux Ropes in the Solar Wind. *J Geophys Res Space Phys* (2014) 119(9):7088–107. doi:10.1002/2014ja020218
22. Janvier M, Démoulin P, Dasso S. Are There Different Populations of Flux Ropes in the Solar Wind? *Sol Phys* (2014) 289(7):2633–52. doi:10.1007/s11207-014-0486-x
23. Huang J, Liu YCM, Peng J, Li H, Klecker B, Farrugia CJ, et al. A Multispacecraft Study of a Small Flux Rope Entrained by Rolling Back Magnetic Field Lines. *J Geophys Res Space Phys* (2017) 122:6927–39. doi:10.1002/2017JA023906
24. Huang J, Liu YC-M, Peng J, Qi Z, Li H, Klecker B, et al. The Distributions of Iron Average Charge States in Small Flux Ropes in Interplanetary Space: Clues to Their Twisted Structures. *J Geophys Res Space Phys* (2018) 123:7167–80. doi:10.1029/2018ja025660
25. Zhao Y, Feng H, Liu Q, Zhao G. Coalescence of Magnetic Flux Ropes within Interplanetary Coronal Mass Ejections: Multi-Cases Studies. *Front Phys* (2019) 7:151. doi:10.3389/fphy.2019.00151
26. Xu M, Shen C, Hu Q, Wang Y, Chi Y. Whether Small Flux Ropes and Magnetic Clouds Have the Same Origin: A Statistical Study of Small Flux Ropes in Different Types of Solar Wind. *ApJ* (2020) 904:122. doi:10.3847/1538-4357/abbe21
27. Yu W, Farrugia CJ, Lugaz N, Galvin AB, J. Kilpua EK, Kucharek H, et al. A Statistical Analysis of Properties of Small Transients in the Solar Wind 2007-2009: STEREO and Wind Observations. *J Geophys Res Space Phys* (2014) 119: 689–708. doi:10.1002/2013JA019115
28. Kilpua EKJ, Jian LK, Li Y, Luhmann JG, Russell CT. Observations of ICMEs and ICME-like Solar Wind Structures from 2007 - 2010 Using Near-Earth and STEREO Observations. *Sol Phys* (2012) 281:391–409. doi:10.1007/s11207-012-9957-0
29. Rouillard AP, Savani NP, Davies JA, Lavraud B, Forsyth RJ, Morley SK, et al. A Multispacecraft Analysis of a Small-Scale Transient Entrained by Solar Wind Streams. *Sol Phys* (2009) 256:307–26. doi:10.1007/s11207-009-9329-6
30. Rouillard AP, Sheeley NR, Jr., Cooper TJ, Davies JA, Lavraud B, Kilpua EKJ, et al. The Solar Origin of Small Interplanetary Transients. *ApJ* (2011) 734:7. doi:10.1088/0004-637x/734/1/7
31. Mandrini CH, Pohjolainen S, Dasso S, Green LM, Démoulin P, van Driel-Gesztelyi L, et al. Interplanetary Flux Rope Ejected from an X-ray Bright point. *A&A* (2005) 434:725–40. doi:10.1051/0004-6361:20041079
32. Chi Y, Zhang J, Shen C, Hess P, Liu L, Mishra W, et al. Observational Study of an Earth-Affecting Problematic ICME from STEREO. *ApJ* (2018) 863:108. doi:10.3847/1538-4357/aacf44
33. Cartwright ML, Moldwin MB. Heliospheric Evolution of Solar Wind Small-Scale Magnetic Flux Ropes. *J Geophys Res* (2010) 115:A08102. doi:10.1029/2009ja014271
34. Wang JM, Feng HQ, Zhao GQ. Observations of a Small Interplanetary Magnetic Flux Rope Opening by Interchange Reconnection. *ApJ* (2018) 853:94. doi:10.3847/1538-4357/aaa131
35. Zheng J, Hu Q. Observational Evidence for Self-Generation of Small-Scale Magnetic Flux Ropes from Intermittent Solar Wind Turbulence. *ApJ* (2018) 852:L23. doi:10.3847/2041-8213/aaa3d7
36. Lee LC, Fu ZF. A Theory of Magnetic Flux Transfer at the Earth's Magnetopause. *Geophys Res Lett* (2013) 12:105–8. doi:10.1029/GL012i002p00105
37. Lepping RP, Acũna MH, Burlaga LF, Farrell WM, Slavin JA, Schatten KH, et al. The Wind Magnetic Field Investigation. *Space Sci Rev* (1995) 71:207–29. doi:10.1007/BF00751330
38. Ogilvie KW, Chornay DJ, Fritzenreiter RJ, Hunsaker F, Keller J, Lobell J, et al. SWE, a Comprehensive Plasma Instrument for the WIND Spacecraft. *Space Sci Rev* (1995) 71:55–77. doi:10.1007/BF00751326
39. Smith EJ. The Heliospheric Current Sheet. *J Geophys Res* (2001) 106: 819–15832. doi:10.1029/2000ja000120
40. Shodhan S, Crooker NU, Kahler SW, Fitzenreiter RJ, Larson DE, Lepping RP, et al. Counterstreaming Electrons in Magnetic Clouds. *J Geophys Res* (2000) 105:27261–8. doi:10.1029/2000JA000060
41. Hu Q, Sonnerup BUÖ. Reconstruction of Magnetic Flux Ropes in the Solar Wind. *Geophys Res Lett* (2001) 28:467–70. doi:10.1029/2000gl012232
42. Hu Q, Bu Ö S. Reconstruction of Magnetic Clouds in the Solar Wind: Orientations and Configurations. *J Geophys Res* (2002) 107(A7):1142. doi:10.1029/2001JA000293
43. Hu Q, Smith CW, Ness NF, Skoug RM. Double Flux-Rope Magnetic Cloud in the Solar Wind at 1 AU. *Geophys Res Lett* (2003) 30(7):1385. doi:10.1029/2002GL016653
44. Hu Q, Smith CW, Ness NF, Skoug RM. Multiple Flux Rope Magnetic Ejecta in the Solar Wind. *J Geophys Res* (2004) 109:A03102. doi:10.1029/2003JA010101
45. Sonnerup BUÖ, Cahill LJ. Magnetopause Structure and Attitude from Explorer 12 Observations. *J Geophys Res* (1967) 72:171. doi:10.1029/JZ072i001p00171
46. Sonnerup BUÖ, Guo M. Magnetopause Transects. *Geophys Res Lett* (1996) 23: 3679–82. doi:10.1029/96gl03573
47. Sonnerup BUÖ, Scheible M. *Minimum and Maximum Variance Analysis* (1998). Bern, Switzerland: ISSI Scientific Reports Series
48. Yan L, Luhmann J. Solar Cycle Control of the Magnetic Cloud Polarity and the Geoeffectiveness. *J Atmos Solar-Terrestrial Phys* (2004) 66(3-4):323–31. doi:10.1016/j.jastp.2003.12.001
49. Tan B. The Characteristics of valley Phase as Predictor of the Forthcoming Solar Cycle. *Adv Space Res* (2019) 63(1):617–25. doi:10.1016/j.asr.2018.08.004

Conflict of Interest: The authors declare that the research was conducted in the absence of any commercial or financial relationships that could be construed as a potential conflict of interest.

frontiers in Physics

ORIGINAL RESEARCH
published: 16 November 2021
doi: 10.3389/fphy.2021.750410

The Relationship Between Solar Wind Dynamic Pressure Pulses and Solar Wind Turbulence

Mengsi Ruan[1], Pingbing Zuo[1], Zilu Zhou[2], Zhenning Shen[1], Yi Wang[1], Xueshang Feng[1], Chaowei Jiang[1], Xiaojun Xu[2], Jiayun Wei[1], Yanyan Xiong[1] and Ludi Wang[1]*

[1]Institute of Space Science and Applied Technology, Harbin Institute of Technology, Shenzhen, China, [2]State Key Laboratory of Lunar and Planetary Sciences, Macau University of Science and Technology, Macao, China

Solar wind dynamic pressure pulses (DPPs) are small-scale plasma structures with abrupt and large-amplitude plasma dynamic pressure changes on timescales of seconds to several minutes. Overwhelming majority of DPP events (around 79.13%) reside in large-scale solar wind transients, i.e., coronal mass ejections, stream interaction regions, and complex ejecta. In this study, the intermittency, which is a typical feature of solar wind turbulence, is determined and compared during the time intervals in the undisturbed solar wind and in large-scale solar wind transients with clustered DPP events, respectively, as well as in the undisturbed solar wind without DPPs. The probability distribution functions (PDFs) of the fluctuations of proton density increments normalized to the standard deviation at different time lags in the three types of distinct regions are calculated. The PDFs in the undisturbed solar wind without DPPs are near-Gaussian distributions. However, the PDFs in the solar wind with clustered DPPs are obviously non-Gaussian distributions, and the intermittency is much stronger in the large-scale solar wind transients than that in the undisturbed solar wind. The major components of the DPPs are tangential discontinuities (TDs) and rotational discontinuities (RDs), which are suggested to be formed by compressive magnetohydrodynamic (MHD) turbulence. There are far more TD-type DPPs than RD-type DPPs both in the undisturbed solar wind and large-scale solar wind transients. The results imply that the formation of solar wind DPPs could be associated with solar wind turbulence, and much stronger intermittency may be responsible for the high occurrence rate of DPPs in the large-scale solar wind transients.

Keywords: solar wind dynamic pressure pulse, discontinuity, turbulence, intermittency, data analysis

OPEN ACCESS

Edited by:
Heng Qiang Feng,
Luoyang Normal University, China

Reviewed by:
Jia Huang,
University of Michigan, United States
Keiji Hayashi,
Stanford University, United States

****Correspondence:***
Pingbing Zuo
pbzuo@hit.edu.cn

Specialty section:
This article was submitted to Stellar and Solar Physics, a section of the journal Frontiers in Physics

Received: *30 July 2021*
Accepted: *05 October 2021*
Published: *16 November 2021*

Citation:
Ruan M, Zuo P, Zhou Z, Shen Z, Wang Y, Feng X, Jiang C, Xu X, Wei J, Xiong Y and Wang L (2021) The Relationship Between Solar Wind Dynamic Pressure Pulses and Solar Wind Turbulence. Front. Phys. 9:750410. doi: 10.3389/fphy.2021.750410

1 INTRODUCTION

Small-scale plasma structures with abrupt and large-amplitude plasma dynamic pressure changes (increase or decrease) on timescales of seconds to several minutes and small pressure variations in the preceding and succeeding regions, are frequently observed in the solar wind. They are usually named as solar wind dynamic pressure pulses (DPPs) [1–5]. DPPs are associated with many fundamental physical processes, such as plasma instability [1, 6], turbulence [7], magnetic reconnection [8], and interactions between different kinds of solar wind streams [9]. Meanwhile, DPPs are very geoeffective, which could affect the transport of energy and momentum from the solar wind to the magnetosphere-ionosphere coupling system [10], compress the Earth's magnetosphere and cause various types of disturbances in the magnetosphere and ionosphere [5, 11–14]. It is important to

investigate the origin of DPPs and their evolution in interplanetary space to understand the basic plasma physical process and the space weather effects.

In the past two decades, the properties of DPPs have been investigated in depth. The sudden dynamic pressure changes of DPPs, which are accompanied by variations in the magnetic field and proton temperature, result mainly from increase or decrease in density, rather than the bulk speed change [1–3]. For the majority of DPPs, the sum of the thermal pressure and magnetic pressure remains in equilibrium. Barkhatov et al. [15] indicated that the balance of the total pressure across the sharp pressure changes could affect the evolution of small-scale solar wind structures. Nearly constant total pressure across the small-scale structures can be regarded as the evidence of pressure balance [6, 16]. Hence, most DPPs can be considered as pressure balance structures (PBSs). According to the jump conditions, Dalin et al. (2002) [1] and Riazantseva et al. (2005a) [16] indicated that most DPPs can be classified into tangential discontinuities (TDs), or rotational discontinuities (RDs) with anisotropic thermal pressure. Zuo et al. (2015b) [3] performed a statistical survey on the properties of DPPs based on nearly 20 years of observations from the WIND spacecraft, and verified that the main components of DPPs may be shocks and directional discontinuities (DDs) and the occurrence rate of shocks is extremely smaller comparing with that of DDs. Specially, DPPs have the feature of grouping occurrence and may exist in specific solar wind environments. Zuo et al. (2015b) [4] and Xie et al. (2015) [2] both found that the overwhelming majority of DPP events in different solar phases reside in large-scale solar wind transients, i.e., coronal mass ejection-related flows, stream interaction regions (SIRs), as well as complex ejecta. Since interplanetary coronal mass ejections (ICMEs), SIRs and complex ejecta, which usually containing sustaining southward interplanetary magnetic field (IMF), are the main drivers of geomagnetic storms [17–20], Zuo et al. (2015b) [4] proposed that the feature of grouping occurrence may be regarded as an indicator of space weather events. Zuo et al. (2015c) [5] inferred that DPPs in different solar wind flows may have different origins. *In-situ* observations and numerical simulations of magnetohydrodynamic (MHD) turbulence show that magnetic discontinuities closely relate to the intermittent turbulence [21–27]. Zuo et al. (2015b) [4] also found some clues that DPPs may be the product of magnetic turbulence or repeated magnetic reconnections.

In this paper, we comparatively analyze the different features of intermittency and component of DPP events in the undisturbed solar wind and in the large-scale solar wind transients based on nearly 21 years of WIND observations (1995–2016). The origin of DPPs is also discussed. In **Section 2**, we briefly introduce the data set and DPP event selection approach. **Section 3** presents the results of statistical and comparative investigation of the dynamic pressure change and the relative dynamic pressure change in the undisturbed solar wind and solar wind transients. We then compare the intermittency during the time intervals in the undisturbed solar wind and in large-scale solar wind transients with clustered DPP events, respectively, as well as in the undisturbed solar wind without DPPs in **Section 4**. In the next section, the classification of DPPs is shown. A brief discussion and summary are given in the last section.

2 DATA AND EVENT SELECTION

In this investigation, we primarily use high time resolution solar wind plasma and magnetic field data from the Three-Dimensional Plasma and Energetic Particle Investigation (3DP) [28] and the Magnetic Field Investigation (MFI) [29] instruments onboard the WIND spacecraft, respectively. The solar wind plasma and magnetic field data during the period from 1995 to 2016, used to the DPP event identification, analysis on DPPs component and associated intermittency, are available with a cadence of 3-s in this work.

To identify DPPs in the solar wind, we apply an automated DPP-hunting computer procedure developed by Zuo et al. (2015a) [3]. The procedure is capable of: 1) correctly identifying the DPPs, 2) functionally determining their transition region where abrupt dynamic pressure changes occur, 3) and simultaneously selecting representative preceding and succeeding regions as the upstream and downstream, for which there are very small variations in solar wind dynamic pressure to represent the quiet plasma status. The selection criteria are guided as follows: 1) The sharp change of dynamic pressure exceeds a given threshold value dp_0 = 1 nPa in less than dt_0 = 5 min. 2) The transition region should be isolated in the sense that only small variations in dynamic pressure occur in the preceding and succeeding 3 min. The preceding and succeeding 3-min regions are selected to be representative of the upstream and downstream region. 3) In the upstream and downstream regions, the change in the amplitude of the dynamic pressure is less than 60% of that in the transition region, and the ratio of the square deviation of the dynamic pressure to its corresponding average value is less than 0.6. In order to ensure that the detected DPPs do not occur in the magnetosphere and its foreshock region, the events are discarded if the spacecraft was located in the region with $X_{WIND} < 60R_E$ and $\sqrt{Y_{WIND}^2 + Z_{WIND}^2} < 60R_E$ (X_{WIND}, Y_{WIND}, *and* Z_{WIND} are coordinates of WIND location in GSM. R_E is the radius of the Earth).

An example of DPP event in the solar wind on January 2, 2016 is presented in **Figure 1**. The region between two red vertical lines is defined as the transition region and the code-given adjacent upstream and downstream regions are marked by the red transverse lines. The top four panels present the magnetic field magnitude, the three magnetic components (in GSM coordinates), latitude angle and azimuthal angle of the magnetic field. As seen in **Figure 1**, the magnetic field magnitude drops from ~7.5 to ~1.0 nT, with abrupt directional changes (latitude angle change: $\Delta\theta > 50^{\circ}$), suggesting the existence of intermittent structures. The subsequent panels show the proton temperature, proton number density, solar wind bulk speed and solar wind dynamic pressure from the 3DP instruments. The values of the four plasma parameters all increase from upstream to downstream.

ICMEs and SIRs are two types of dominant solar wind transients [30–32]. A combined ICME list in 1995–2016 is obtained from publicly available catalogues compiled by Chi

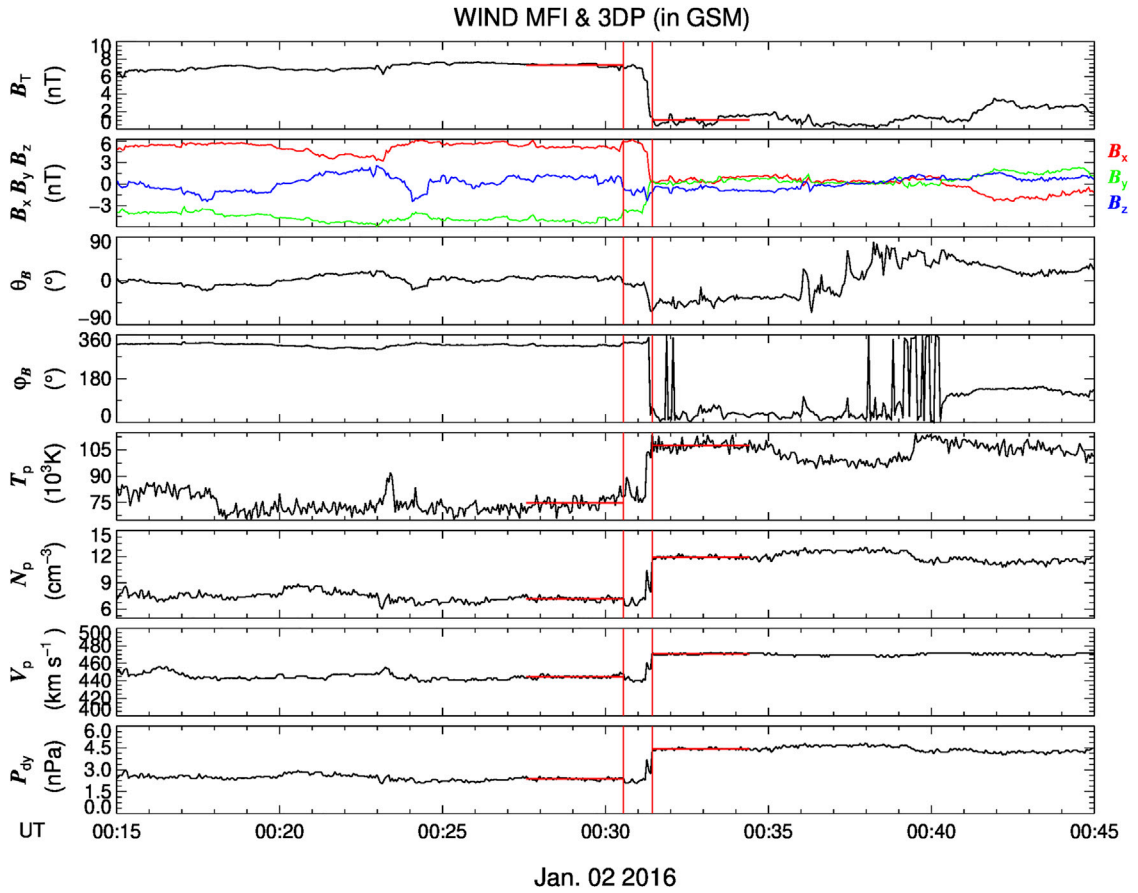

FIGURE 1 | One typical DPP event in the solar wind observed by WIND on January 2, 2016. The boundaries of the DPP transition region are marked by the red vertical lines, and the transverse lines before and after the DPP transition region denote DPP's upstream and downstream regions. The panels from top to bottom are: magnetic-field magnitude, the three components (x, y, z) of the magnetic field in Geocentric Solar Magnetospheric (GSM) coordinates, magnetic-field latitude angle, magnetic-field azimuthal angle, proton temperature, proton density, proton bulk speed, and solar wind dynamic pressure, respectively.

Yutian (USTC list)[1], Jian Lan (UCLA list)[2] and Richardson & Cane (R& C list)[3]. The lists of SIRs obtained from the websites[4, 5] are also referred. We classify the near-Earth solar wind into two types: the undistributed solar wind and the large-scale solar wind transients including ICMEs, CIRs and the complex ejecta formed due to their interaction. A DPP event is considered to be associated with the solar wind transients if its transition region occurs within the time interval of the solar wind transient passages.

3 STATISTIC OF DPP EVENTS

12,077 DPP events in the solar wind from 1995 to 2016 are identified with the automatic searching code. There are 2,521 (20.87%) and 9,556 (79.13%) DPP events residing in the undisturbed solar wind and solar wind transients, respectively. **Table 1** shows the annual number of DPPs in undisturbed solar wind and solar wind transients. **Figure 2** shows the distribution of DPPs that are associated with the undisturbed solar wind (indian red) and solar wind transients (sky blue) in each year during 1995–2016. It is found that except for 1996 (55.81%), the proportion of DPPs in undisturbed solar wind is much lower than that related to the solar wind transients, ranging from 3.46 to 28.99%, which is consistent with Zuo et al. (2015b) [4].

Figure 3 presents the comparison of the dynamic pressure change in the undisturbed solar wind (indian red) and solar wind transients (sky blue). The distribution of the absolute value of the dynamic pressure amplitude change from upstream to downstream, i.e., $dP_{dy} = |p_{down} - p_{up}|$, is displayed in **Figure 3A**. The value of $d_{P_{dy}}$ for the events in the undisturbed solar wind varies from 1.0 to 14.65 *nPa* with an average value of 1.63 *nPa*, and the value of dP_{dy} in solar wind transients varies from 1.0 to 41.94 *nPa* with an average value of 2.18 *nPa*, which is 33.74% larger than that in the undisturbed solar wind. It is found that the distributions of dP_{dy} about the cases both in the undisturbed solar wind and solar wind transients peak at

[1]http://space.ustc.edu.cn/dreams/wind_icmes/index.php.
[2]https://link.springer.com/content/pdf/10.1007/s11207-006-0133-2.pdf.
[3]http://www.srl.caltech.edu/ACE/ASC/DATA/level3/icmetable2.htm#.
[4]https://link.springer.com/content/pdf/10.1007/s11207-006-0132-3.pdf.
[5]http://link.springer.com/content/pdf/10.1007/s11207-016-0971-5.pdf.

TABLE 1 | List of Solar Wind Dynamic Pressure Pulses (DPPs) in the undisturbed solar wind and solar wind transients.

Type 1	Year	1995	1996	1997	1998	1999	2000	2001	2002	2003	2004	2005
	No.	204	288	162	220	40	173	168	83	140	94	149
	Year	2006	2007	2008	2009	2010	2011	2012	2013	2014	2015	2016
	No.	8	31	22	20	31	98	129	121	106	135	99
Type 2	Year	1995	1996	1997	1998	1999	2000	2001	2002	2003	2004	2005
	No	548	228	497	687	448	669	741	562	388	462	792
	Year	2006	2007	2008	2009	2010	2011	2012	2013	2014	2015	2016
	No.	223	194	258	49	198	412	370	405	319	701	405
Total	(1995–2016)		Type 1: 2,521				Type 2: 9,556					

Type 1: DPP events in the undisturbed solar wind.
Type 2: DPP events in the solar wind transients.

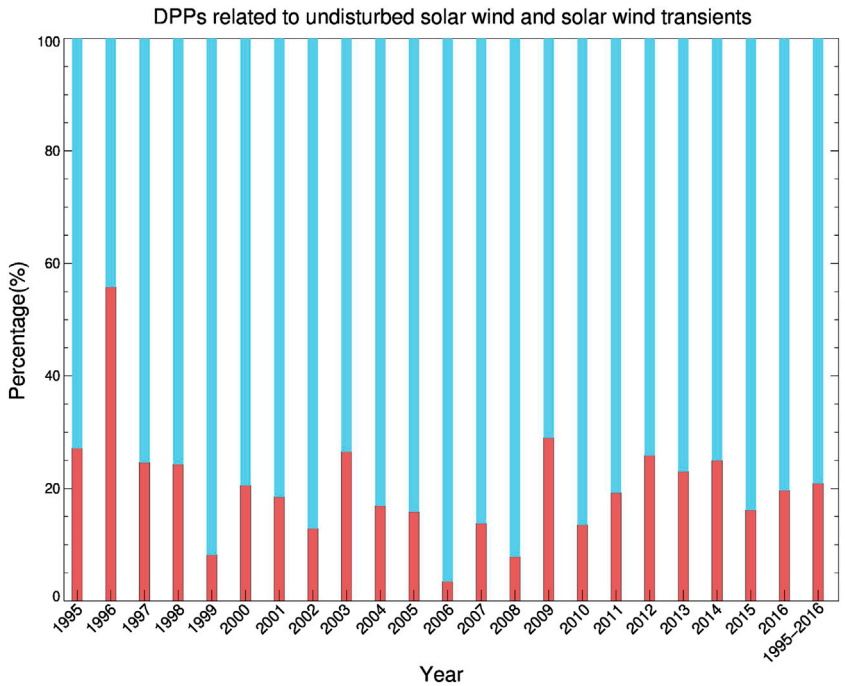

FIGURE 2 | Proportion of DPPs associated with the undisturbed solar wind (indian red) and solar wind transients (sky blue).

1.0–2.0 *nPa*, and there are about 82.43 and 67.12% of the cases, respectively, in this range. Zuo et al. (2015b) [4] defined that strong DPPs should have dynamic pressure changes over 3 nPa in 5 min. It is noteworthy that there are fewer strong DPPs in the undisturbed solar wind than that in solar wind transients. Only 6.45% of the DPP events are strong DPPs in the undisturbed solar wind, while in solar wind transients this proportion accounts for 15.70%

The strength of the DPP compared with the background condition it resides in is determined by the ratio of the absolute value of the dynamic pressure amplitude change to the average dynamic pressure value, i.e., $dp_{relative} = dP_{dy}/[(p_{up} + p_{down})/2]$ [2]. **Figure 3B** shows the distribution of the relative dynamic pressure change. Comparison between the two types of solar wind flows suggests little difference in the distributions. The most probable relative pressure changes are 0.2–0.4 in the undisturbed solar wind and solar wind transients. The value of $d_{relative}$ for all cases in the undisturbed solar wind varies from 0.20 to 1.97 with an average value of 0.47, and 3.00% of the events have values greater than 1.0. The value of $dp_{relative}$ for all cases in solar wind transients varies from 0.20 to 1.99 with an average of 0.44, and about 3.40% of the events have values greater than 1.0. However, the most probable relative pressure changes are 0.4–0.6 for strong DPPs (**Figure 3C**). About 24.54% of the strong DPPs in the undisturbed solar wind and 14.02% of the strong DPPs in solar wind transients have a value of relative change larger than 1.0.

4 TURBULENCE ASSOCIATED WITH DPP EVENTS

Turbulence in the solar wind describes the fluctuation of solar wind parameters over different spatial and temporal scales [33].

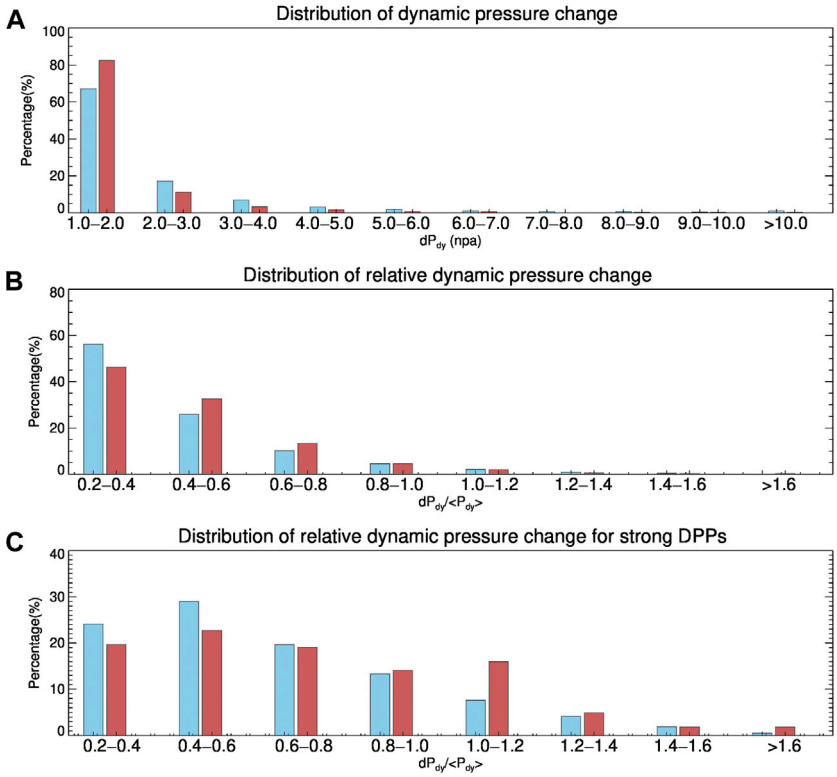

FIGURE 3 | The distributions of absolute dynamic pressure changes for all DPPs **(A)**, relative pressure changes for all DPPs **(B)** and relative pressure changes for strong DPPs **(C)** in the undisturbed solar wind (indian red) and solar wind transients (sky blue).

Intermittency, manifesting inhomogeneity in the energy transfer between scales [34–37], is a typical feature of turbulence [38]. If the probability distribution function (PDF) of the fluctuations for a given solar wind parameter is not Gaussian at different scales and increasingly departs from a normalized distribution when the time-scale gets smaller, it reveals the presence of intermittency [36].

DPPs mainly reside in the solar wind transients. Here we selected sixteen events containing ICME, CIR or complex ejecta with clustered DPP occurrence, and in front of the solar wind transient, clustered distributed DPPs are also existed. So it is convenient to compare the intermittency during the successive intervals of the undisturbed solar wind without DPPs, the undisturbed solar wind with DPPs, and the solar wind transient with DPPs. For simplicity, these regions are termed as the ndpp-USW region, the dpp-USW region, and the dpp-LSSWT region, respectively. The time information of these events is listed in **Table 2**. Considering the pressure changes of DPPs are dominated by density variations, we analyzed the intermittency of density fluctuation in this work. The proton density increments are defined by $\delta\rho(\tau) = \rho(t + \tau) - \rho(t)$, and the function $[\delta\rho(\tau) - \langle\delta\rho(\tau)\rangle]$ represents the fluctuations of proton density increments. Here, ρ and τ are the proton density, and the time lag between two samples, respectively. The angle bracket denotes ensemble averaging over time.

Figure 4 presents the magnetic field and plasma data observed by WIND during September 14–19, 2000. An ICME, which started at 16:09:00 UT on September 17, 2000 and ended at 06:25:00 UT on September 19, 2000, was observed to interact with a SIR during 18:30:00 UT on September 16 and 23:21:25 UT on September 17, 2000, and formed a complex ejecta. Four remarkably different regions labeled by the red vertical lines can be defined in sequence: the ndpp-USW region, the dpp-USW region, the dpp-LSSWT I region and the dpp-LSSWT II region. The dpp-LSSWT I and dpp-LSSWT II regions are both inside the complex ejecta. The time information of each region is given for the Event with NO. 6 in **Table 2**. The time scale of ndpp-USW region is same as that of the dpp-USW region and different from that of two dpp-LSSWT regions. The center position of the transition regions of the captured DPP events are marked by sky blue vertical lines. The number of DPP events captured in the dpp-USW, dpp-LSSWT I, dpp-LSSWT II regions is six, eleven and forty-eight, respectively (see also in **Table 2**).

Figure 5 shows the PDFs of solar wind proton density increments normalized to the standard deviation, i.e., $[\delta\rho(\tau) - \langle\delta\rho(\tau)\rangle]/\sigma_\rho$, for different time lags τ of the corresponding ndpp-USW region (**Figure 5A**), dpp-USW region (**Figure 5B**), dpp-LSSWT I region (**Figure 5C**) and dpp-LSSWT II (**Figure 5D**), respectively. σ_ρ is the standard deviation of $\delta\rho(\tau)$. The black curves in **Figure 5** denote the standard Gaussian distribution with $\langle\delta\rho(\tau)\rangle = 0$ and $\sigma\rho = 1$. The different degrees of red lines illustrate the actual distribution function among different time lags (τ = 12, 24, 48, 96, 192, and

TABLE 2 | The time information of selected 16 events. The start time, end time, time duration, and number of DPP events are listed separately. The time duration of ndpp-USW region is same as that of the dpp-USW region and listed in Column 6.

No.	ndpp-USW region		dpp-USW region				dpp-LSSWT region			
	Start [UT]	End [UT]	Start [UT]	End [UT]	Time duration [hr]	No. of DPPs	Start [UT]	End [UT]	Time duration [hr]	No. of DPPs
1	19950115/06:54:35	19950115/09:31:38	19950116/06:54:35	19950116/09:31:38	2.618	5	19950118/03:58:35	19950118/11:55:59	7.957	10
2	19960215/03:22:16	19960215/07:40:29	19960216/03:22:16	19960216/15:02:16	11.677	12	19960218/02:11:26	19960218/08:24:25	6.223	7
3	19960221/02:04:44	19960221/06:31:38	19960222/02:04:44	19960222/06:31:38	4.448	8	19960224/00:18:08	19960224/13:42:18	13.428	7
4	19980726/17:24:57	19980728/01:01:24	19980730/17:24:57	19980801/01:01:24	31.608	49	19980801/11:41:41	19980802/10:49:16	23.126	27
5	20000822/16:02:09	20000822/18:13:26	20000823/16:02:09	20000823/18:13:26	2.188	6	20000824/01:54:22	20000824/08:56:20	7.033	7
6	20000914/19:00:00	20000914/21:12:46	20000915/19:00:00	20000915/21:12:46	2.213	6	20000916/20:01:34	20000917/03:25:30	6.401	11
							20000917/13:54:08	20000918/18:30:55	28.738	48
7	20010406/00:23:30	20010406/05:17:15	20010407/00:23:30	20010407/05:17:15	4.896	5	20010408/11:16:07	20010409/00:53:49	13.619	16
8	20030225/00:01:41	20030225/08:54:08	20030226/08:01:41	20030226/16:54:08	8.874	10	20030226/17:54:47	20030227/00:37:29	6.88	6
9	20041106/14:26:27	20041106/16:57:31	20041107/14:26:27	20041107/16:57:31	2.518	5	20041107/19:32:48	20041108/06:46:32	12.863	23
							20041109/18:21:35	20041110/18:59:32	24.563	44
							20041111/16:44:43	20041112/17:40:38	24.863	29
10	20041229/04:28:46	20041229/16:36:04	20041230/04:28:46	20041230/16:36:04	12.122	12	20050101/16:07:12	20050102/07:05:06	14.965	14
11	20050512/12:36:53	20050512/15:12:06	20050513/12:36:53	20050513/15:12:06	2.587	9	20050515/02:30:13	20050515/22:28:07	19.965	41
			20050512/22:29:07	20050513/03:04:26	4.589	8				
12	20120615/05:29:32	20120615/08:54:14	20120616/15:29:32	20120616/18:54:14	3.412	6	20120616/19:57:21	20120617/11:26:12	15.481	26
13	20131106/09:15:16	20131106/11:20:16	20131107/09:15:16	20131107/11:20:16	2.083	6	20131109/01:52:34	20131109/08:08:05	6.259	7
14	20140911/04:45:09	20140911/08:53:35	20140911/22:45:09	20140912/02:53:35	4.141	5	20140912/15:35:44	20140913/07:03:39	15.553	19
15	20150909/22:29:16	20150910/02:39:05	20150910/17:29:37	20150910/21:39:05	4.158	5	20150910/22:53:44	20150911/08:53:41	9.999	9
16	20160505/00:32:58	20160505/05:08:15	20160506/17:32:58	20160506/22:08:15	4.588	7	20160508/00:27:12	20160508/07:42:28	7.254	18

384 s). It can be seen that the PDFs in the ndpp-USW region are near-Gaussian with all given time lags ranging from 12 to 384 s. But the PDFs are obviously non-Gaussian and the distributions become more self-similar at larger time lags in the dpp-USW, dpp-LSSWT I, dpp-LSSWT II regions. Deviation from a Gaussian distribution indicates that intermittency exists in the dpp-USW and two dpp-LSSWT regions.

In order to unravel the intermittent character of the density fluctuations, the method described in Bruno et al. (2003, 2014) [39, 40] is used to estimate the flatness factor F at different time lags. The flatness factor F, the fourth-order moment of distribution, is defined as: $F(\tau) = \langle \delta\rho(\tau)^4 \rangle / \langle \delta\rho(\tau)^2 \rangle^2$. The larger the flatness factor F is, the longer the tail of the distribution becomes. For a standard Gaussian distribution, the flatness factor F should equal to 3 [7]. The flatness factor F at the time lags ranging from 3 to 3,072 s in the ndpp-USW region, dpp-USW region and two dpp-LSSWT regions, are shown in **Figure 6**. The flatness factor F approximately equal to 3 in the ndpp-USW region, while the flatness factors in the dpp-USW and two dpp-LSSWT regions are all larger than 3, and the values start to increase at larger time lags and reach higher values at small time lags. It indicates that distributions become more intermittent for small time lags and more Gaussian for larger time lags. This is consistent with the qualitative assessment of distribution shapes discussed in **Figure 5**. Moreover, the flatness factors in two dpp-LSSWT regions are obviously larger than those in the dpp-USW region. Hence, density fluctuations in two dpp-LSSWT regions can be considered to be more intermittent than those in the dpp-USW region. If the flatness factor remains constant within a certain range of time lags, it indicates that solar wind turbulence is

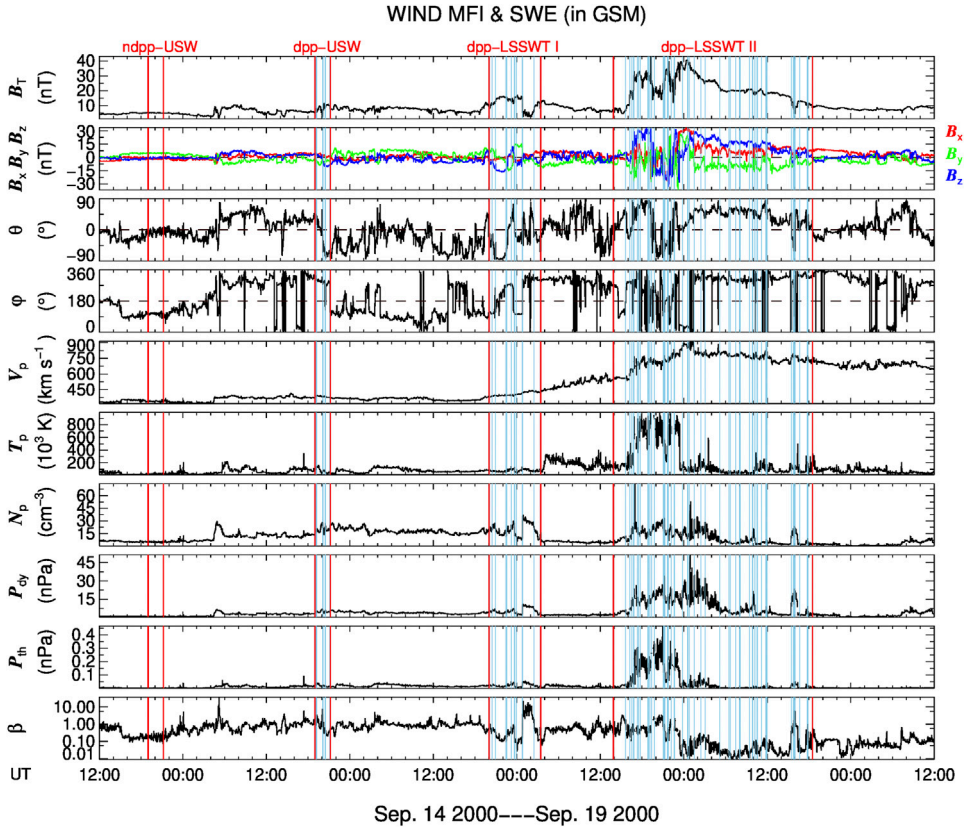

FIGURE 4 | Magnetic field and plasma parameters of solar wind observed by WIND from 12:00 UT on September 14, 2000 to 12:00 UT September 19, 2000. The panels from top to bottom are: magnetic-field magnitude, the three components (x, y, z) of the magnetic field in Geocentric Solar Magnetospheric (GSM) coordinates, magnetic-field latitude angle, magnetic-field azimuthal angle, proton bulk speed, proton temperature, proton density, solar wind dynamic pressure, proton thermal pressure, and plasma beta, respectively. The solar wind dynamic pressure, the thermal pressure and plasma beta are calculated as the functions, $P_{dy} = m_p N_p V_p^2$, $P_{th} = N_p K T_p$, and $\beta = P_{th}/(B^2/2\mu_0)$, respectively. The four discussed regions, ndpp-USW region, dpp-USW region, dpp-LSSWT I region and dpp-LSSWT II, are labeled by the red vertical lines, respectively. The center of the transition regions of the captured DPP events are marked by sky blue vertical lines separately.

not intermittent but self-similar [7]. Flatness factor in the ndpp-USW region is nearly 3.

Figure 7 presents the solar wind data observed by WIND during May 11–17, 2005. A typical ICME preceded by a driven strong shock is detected during May 15–17, 2005. Before the ICME, one ndpp-USW and two dpp-USW regions can be found, which are marked by red vertical lines in the figure. A dpp-LSSWT region is inside the ICME and the sheath region. The time information of each region is given for the Event with NO. 11 in **Table 2**. The PDFs of solar wind proton density increments normalized to the standard deviation for the four regions are shown in **Figure 8**. Similarly, as seen in **Figure 8A**, the PDFs are near-Gaussian distributions in the ndpp-USW region, while the PDFs progressively deviate from a Gaussian distribution in two dpp-USW regions and one dpp-LSSWT region shown in **Figures 8B–D**. We also calculate corresponding flatness factors F for these four regions. **Figure 9** displays the distributions of flatness factor F. It can be found that the flatness factors in the ndpp-USW region are about to 3 and keep self-similar substantially. The F curves for two dpp-USW regions approximately overlap. It indicates that the density fluctuations in the two dpp-USW regions exhibit the same level of intermittency. Besides, the flatness factors in the dpp-LSSWT region are dominantly higher than those in other three regions, which illustrates more intermittent in the dpp-LSSWT region.

In above analysis we have taken two events as examples to compare the intermittency features in the regions with and without DPP occurrence. Both the distributions of PDFs and flatness factor clearly reveal that intermittency does not exist in the ndpp-USW region, but exists in the dpp-USW and dpp-LSSWT regions. Furthermore, the intermittency in dpp-LSSWT regions is stronger than that in the dpp-USW regions. The remaining events, although not discussed here, have the similar distributions of PDFs and flatness factor according to our analysis. **Figure 10** illustrates the statistical distributions of the average values of flatness factor F of all dpp-LSSWT regions, dpp-USW regions and ndpp-USW regions for the selected sixteen events. It is found that the average of flatness factor in dpp-USW regions are evidently smaller than that in dpp-LSSWT regions at all discussed time lags.

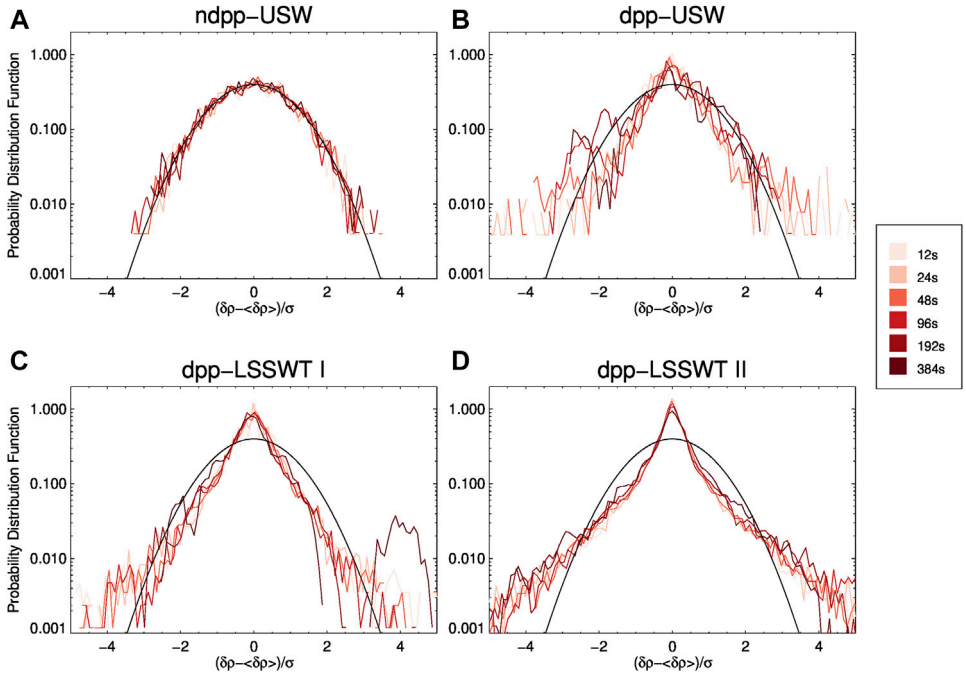

FIGURE 5 | Probability distribution functions of solar wind proton density increments normalized to the standard deviation for different time lags of ndpp-USW region **(A)**, dpp-USW region **(B)** and dpp-LSSWT I region **(C)** and dpp-LSSWT II region **(D)**. The time intervals of four distinct regions are presented in **Figure 4**. The black curve is the standard Gaussian distribution with unit variance. The different degrees of red lines illustrate the actual distribution function between different time lags ranging from 12 to 384 s.

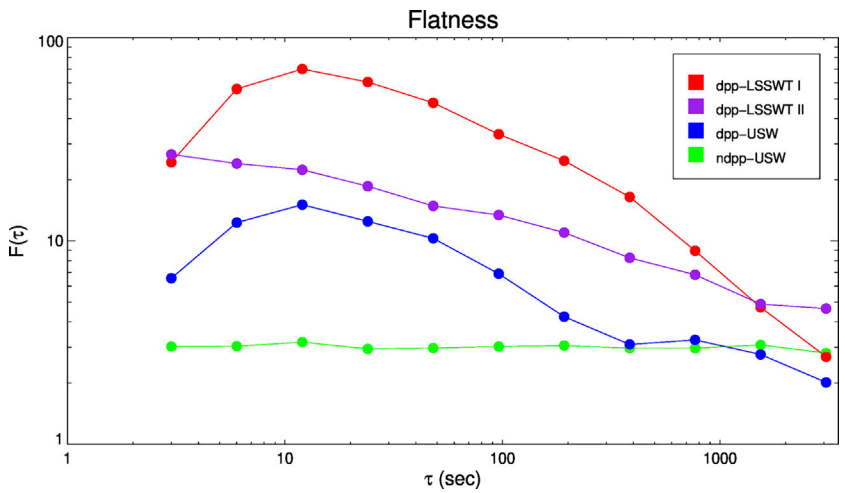

FIGURE 6 | Flatness factor F as a function of different time lags ranging from 3 to 3,072 s, relative to fluctuations of the plasma density observed in ndpp-USW region (green), dpp-USW region (blue), dpp-LSSWT I region (red), and dpp-LSSWT II region (pruple), respectively). The time intervals of four distinct regions are presented in **Figure 4**.

5 CLASSIFICATION OF DPP EVENTS

Recent studies about DPPs in the solar wind show that the main components of DPPs are directional discontinuities (DDs) or interplanetary (IP) shocks, but IP shocks are much rare in comparison with DDs so that they do not play a significant role in statistical investigation [4]. DDs are ubiquitous in interplanetary space and are considered to be a mixture of TDs and RDs [21, 41–45]. A TD, which does not propagate but is convected along with the solar wind, is a special kind of pressure-balance structure and usually separate two different plasma regions of solar wind [46]. A RD, which has a

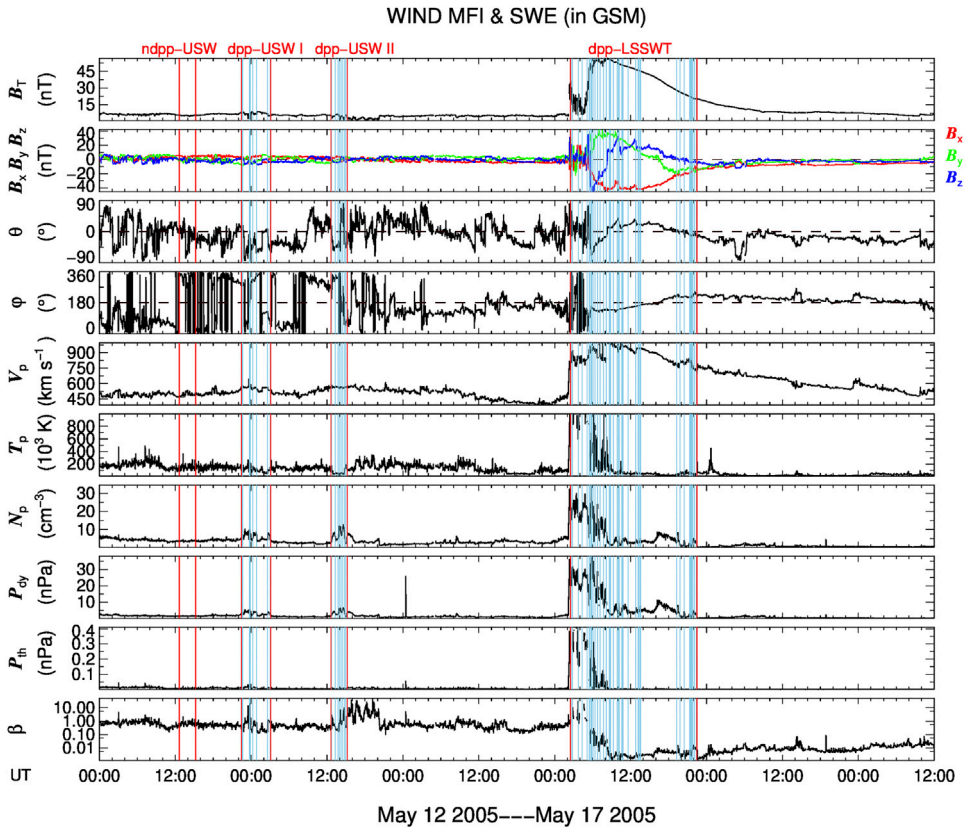

FIGURE 7 | Magnetic field and plasma parameters of solar wind observed by WIND from May 11, 2005 to May 17, 2005. The panels from top to bottom are: magnetic-field magnitude, the three components (x, y, z) of the magnetic field in Geocentric Solar Magnetospheric (GSM) coordinates, magnetic-field latitude angle, magnetic-field azimuthal angle, proton bulk speed, proton temperature, proton density, solar wind dynamic pressure, proton thermal pressure, and plasma beta, respectively. The four discussed regions, ndpp-USW region, dpp-USW I region, dpp-USW II region, and dpp-LSSWT region, are labeled by the red vertical lines, respectively. The center of the transition regions of the captured DPP events are marked by sky blue vertical lines separately.

magnetic field component normal to the discontinuity surface, is not a static structure and can be regarded as a large-amplitude Alfvén wave propagating along the magnetic field [45, 47, 48]. Due to plasma compression, TDs are less stable than RDs.

Previous studies proposed some criteria to categorize solar wind DDs into TDs and RDs [21, 41, 49–51]. In this study, we follow the criterion of Neugebauer et al. [41] in which only magnetic field data were used for classification. A DD is classified as: 1) TD: $|B_n|/B_{max} < 0.4$, $[B]/B_{max} \geq 0.2$; 2) RD: $|B_n|/B_{max} \geq 0.4$, $[B]/B_{max} < 0.2$; 3) Either discontinuity (ED): $|B_n|/B_{max} < 0.4$, $[B]/B_{max} < 0.2$; 4) Neither discontinuity (ND): $|B_n|/B_{max} \geq 0.4$, $[B]/B_{max} \geq 0.2$ [43]. Here $|B_n|$ is the normal field component, $[B]$ is the absolute change value of field magnitude across the transition, B_{max} is the maximum of the averaged magnetic field magnitude in the selected upstream region and that in the downstream region. EDs with a small field component normal to the discontinuity surface and small absolute magnitude change share the properties of TDs and RDs [41, 43, 52–54]. Thus it is difficult to judge whether an ED is a TD or a RD if only the magnetic field data is used.

To determine the surface normal vector of the DDs, the minimum variance analysis (MVA) [55] was employed. The minimum variance direction of the IMF vectors corresponds to the normal of the discontinuity plane. And the quality of the result has a positive correlation to the ratio of the intermediate (λ_2) to minimum (λ_3) eigenvalue, which gives information about the efficiency of the MVA technique. Here we adopt the consistency requirement to ensure the accurate MVA normal estimates $\lambda_2/\lambda_3 \geq 2$ [56].

Figure 11 illustrates the percentages of TD, RD, ED, ND for the DPPs in the undisturbed solar wind (**Figure 11A**) and in the solar wind transients (**Figure 11B**). In the undisturbed solar wind, 2,121 (84.13%) DPP events match the requirement, and the occurrence of TDs, RDs, EDs, and NDs accounts for 53.47, 9.48, 31.35, and 5.70%. In the solar wind transients, 8,018 (83.91%) DPP events are obtained, and the corresponding proportions of TD, RD, ED, and ND are 36.24, 17.88, 42.68, and 3.20%, respectively. By comparison, the ratio of TD type DPPs in the undisturbed solar wind is distinctly greater than that in the solar wind transients, while the ratio of RD-type DPPs in the solar wind transients is around twice of that in the undisturbed solar wind. Whether DPP events resides in the undisturbed solar wind or in the solar wind transients, TDs are obviously more than RDs.

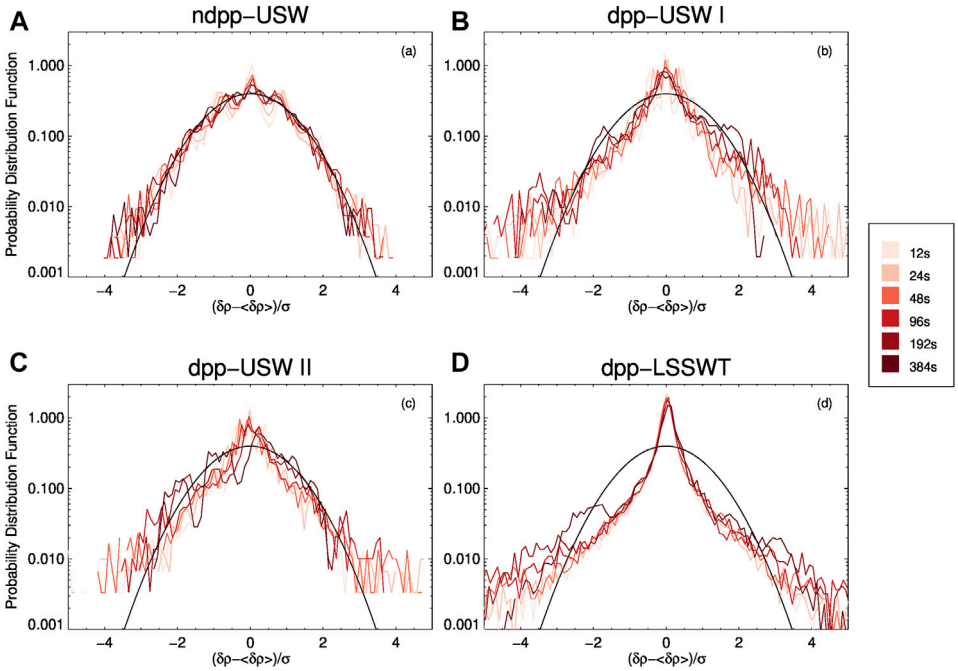

FIGURE 8 | Probability distribution functions of solar wind proton density increments normalized to the standard deviation for different time lags of ndpp-USW region **(A)**, dpp-USW I region **(B)**, dpp-USW II region **(C)**, dpp-LSSWT region **(D)**. The time intervals of four distinct regions are presented in **Figure 7**. The black curve is the standard Gaussian distribution with unit variance. The different degrees of red lines illustrate the actual distribution function between different time lags ranging from 12 to 384 s.

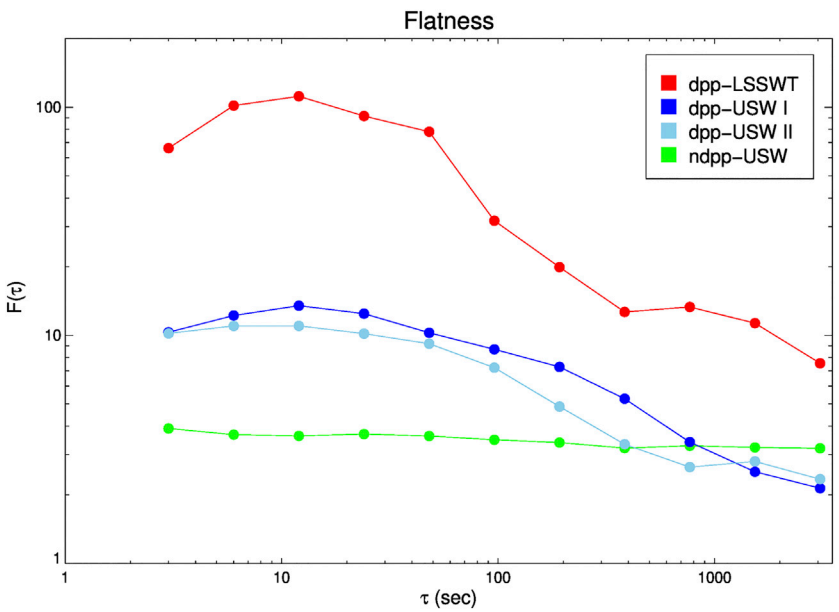

FIGURE 9 | Flatness factor F as a function of different time lags ranging from 3 to 3,072 s, relative to fluctuations of the plasma density observed in ndpp-USW region (green), dpp-USW I region (blue), dpp-USW II region (sky blue), dpp-LSSWT region (red), respectively. The time intervals of five regions are presented in **Figure 7**.

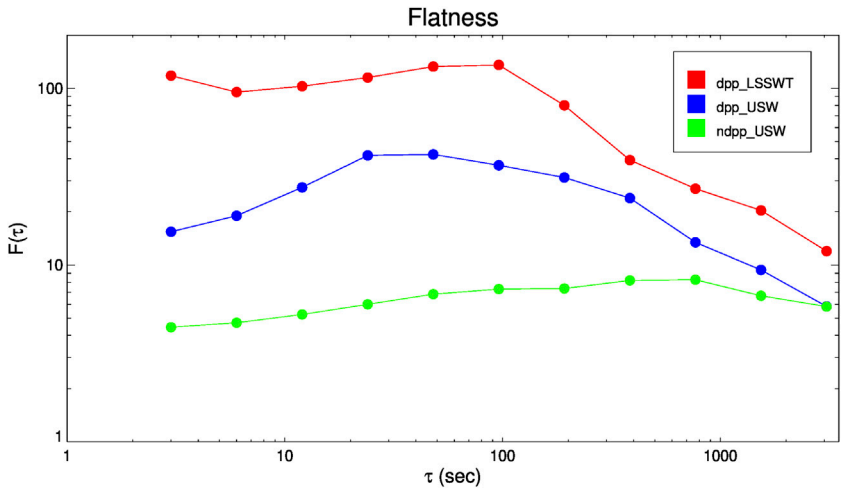

FIGURE 10 | The statistical distribution of the average values of flatness factor F of 16 selected events observed in ndpp-USW region (green), dpp-USW region (blue), dpp-LSSWT region (red), respectively.

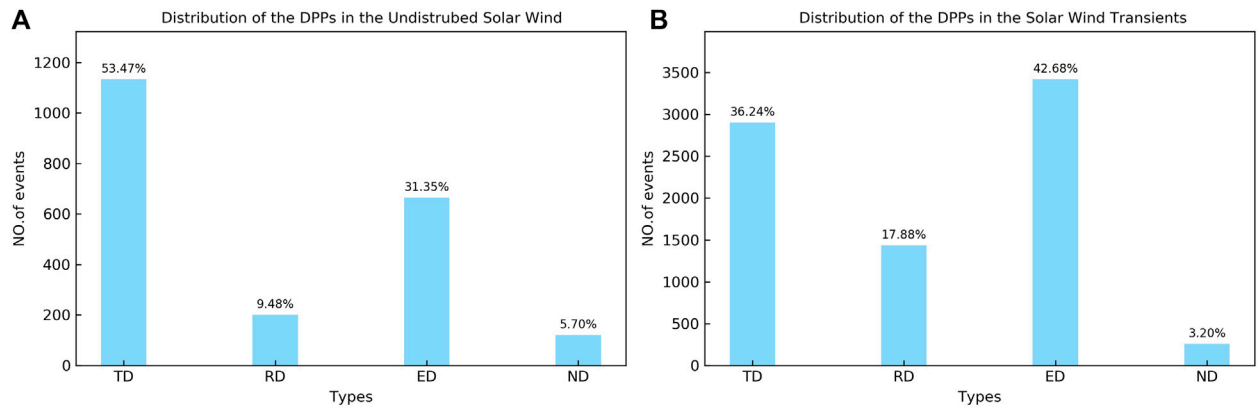

FIGURE 11 | Component of DPP events in two different types of solar wind flows: **(A)** in the undistributed solar wind; **(B)** in the solar wind transients. The fraction of each component of DPP events is marked above the bars.

6 SUMMARY AND DISCUSSION

DPPs are small-scale plasma structures which are ubiquitous in the solar wind. With the motivation to rapidly and automatically identify the numerous DPPs from the solar wind data for further research, we have developed an automated searching procedure. This code has been applied to hunt for DPPs from the observational data stream of WIND from 1995 to 2016. Totally 12,077 DPP events are identified. Based on these events, we perform a comparative analysis on the turbulence and component classification of DPPs in different types of solar wind. Note that, since we only consider the sharp front with sudden change of dynamic pressure on timescales of seconds to a few minutes, in our code, the crossing time of the transition region dt_0 is restricted to be less than 5 min, which can be easily operated. If we restrict the spatial length of the transition region, the number of samples of DPPs identified and used in the statistical investigation may be changed. But the statistical features of the intermittency of the region with and without clustered DPP occurrence should keep coincident since we don't consider the DPP itself but the study the turbulence of the environment that the DPPs resided in.

The main results of this investigation are as follows:

1) The absolute dynamic pressure changes of most DPP events, both in the undisturbed solar wind and solar wind transients, are 1.0–2.0 nPa. Statistically, the most probable values of the relative dynamic pressure change are 0.2–0.4 for all DPPs. In comparison, this parameter is larger for strong DPP events in two types of solar wind flows, being 0.4–0.6.
2) Intermittency is determined and compared during the time intervals in the undisturbed solar wind and large-scale solar

wind transients with clustered DPP events, as well as in the undisturbed solar wind without the occurrence of DPPs. It is found that the PDFs and the flatness factors in ndpp-USW region are almost self-similar at different time lags, while the PDFs and flatness factor in dpp-USW and dpp-LSSWT regions are not Gaussian. The intermittency in dpp-LSSWT region is obviously stronger than that in dpp-USW region.

3) Most DPP events are TDs and RDs, and there are far more TD-type DPPs than RD-type DPPs both in the undisturbed solar wind and solar wind transients. The occurrence of RD-type DPPs is higher in solar wind transients than that in the undisturbed solar wind, while the occurrence of TD-type DPPs in solar wind transients is smaller than that in the undisturbed solar wind.

In-situ observations and numerical simulations of MHD turbulence show that magnetic discontinuities may originate from MHD turbulence and closely relate to intermittent turbulence [21–27, 57]. By comparing the statistical analysis with simulations of MHD turbulence about the waiting-time and the PDFs of magnetic field increments, Greco et al. (2009a) [23] found that some discontinuities are reproduced by intermittent turbulence. Zhdankin et al. [57] studied the relationship between exponentially distributed angular discontinuities in the magnetic field and MHD turbulence. They proposed that strong discontinuities are associated with inertial-range MHD turbulence, while weak discontinuities emerge from dissipation-range turbulence. Meanwhile, they found that the structure functions of the magnetic field direction exhibit anomalous scaling exponents, which indicated the existence of intermittent structures. Yang et al. [26] conducted a simulation of decaying compressive MHD turbulence with a RD, and they found that the RD evolves from the steepening, which is caused by the non-uniformity of Alfvén speed in the MHD turbulence, of Alfvén waves. And then, they compared the TD's lifetime with the travel time of the solar wind from the Sun to 1 AU and inferred that TDs observed at 1 AU are more possibly to be generated by local turbulence [27].

This study shows that the PDFs in the solar wind with clustered DPPs are obviously non-Gaussian distributions and the intermittency is much stronger in the large-scale solar wind transients, while the PDFs in the undisturbed solar wind without DPPs are near-Gaussian distributions. It reveals that strong intermittency is more likely to occur in solar wind transients with clustered DPP events. On the other hand, the main components of the DPPs are two types of discontinuities: TDs and RDs, and the occurrence rate of DPPs is much higher in the solar wind transients than in the undisturbed solar wind. It is inferred that much stronger intermittency may be responsible for the high occurrence rate of DPPs in the large-scale solar wind transients.

DATA AVAILABILITY STATEMENT

The original contributions presented in the study are included in the article/Supplementary Material, further inquiries can be directed to the corresponding author.

AUTHOR CONTRIBUTIONS

MR carried out the analysis and wrote the draft of the manuscript. PZ was the leader of this study and led the data analysis. ZZ and ZS contributed to the revision and improvement of the manuscript. All the authors participated in discussions and agreed to the final text.

FUNDING

This work was partially supported by the NSFC grants 41731067, 42074205, the Guangdong Basic and Applied Basic Research Foundation (Grant No. 2019A1515011067) and Shenzhen Natural Science Fund (the Stable Support Plan Program GXWD20201230155427003-20200822192703001).

ACKNOWLEDGMENTS

We would like to thank the NASA CDAWEB for providing the public WIND 3DP, MFI, and SWE data. We also acknowledge Dr. Ian Richardson, Dr. Hilary Cane, Dr. Yutian Chi and Dr. Lan Jian for providing the lists of ICMEs and CIRs.

REFERENCES

1. Dalin PA, Zastenker GN, Paularena KI, and Richardson JD. *A Survey of Large, Rapid Solar Wind Dynamic Pressure Changes Observed by Interball-1 and IMP 8.*. Ann Geophys (2002) 20:293–299. doi:10.5194/angeo-20-293-2002
2. Xie Y, Zuo P, Feng X, and Zhang Y. Solar Wind Dynamic Pressure Pulses at 1 AU during the Deep Minimum between Solar Cycles 23 and 24. *Sol Phys* (2015) 290:1835–49. doi:10.1007/s11207-015-0700-5
3. Zuo P, Feng X, Xie Y, Wang Y, Li H, and Xu X. Automatic Detection Algorithm of Dynamic Pressure Pulses in the Solar Wind. *ApJ* (2015) 803: 94. doi:10.1088/0004-637X/803/2/94
4. Zuo P, Feng X, Xie Y, Wang Y, and Xu X. A Statistical Survey of Dynamic Pressure Pulses in the Solar Wind Based Onwindobservations. *ApJ* (2015) 808: 83. doi:10.1088/0004-637X/808/1/83
5. Zuo P, Feng X, Xie Y, Wang Y, and Xu X. Strong Solar Wind Dynamic Pressure Pulses: Interplanetary Sources and Their Impacts on Geosynchronous Magnetic fields. *ApJ* (2015) 812:152. doi:10.1088/0004-637X/812/2/152
6. Riazantseva MO, Zastenker GN, Richardson JD, and Eiges PE. Sharp Boundaries of Small- and Middle-Scale Solar Wind Structures. *J Geophys Res* (2005) 110:A12110. doi:10.1029/2005JA011307
7. Riazantseva MO, Khabarova OV, Zastenker GN, and Richardson JD. Sharp Boundaries of Solar Wind Plasma Structures and Their Relationship to Solar Wind Turbulence. *Adv Space Res* (2007) 40:1802–6. doi:10.1016/j.asr.2007.05.004

8. Khabarova OV, and Zastenker GN. Sharp Changes of Solar Wind Ion Flux and Density within and outside Current Sheets. *Sol Phys* (2011) 270:311–29. doi:10.1007/s11207-011-9719-4
9. Riazantseva MO, Dalin PA, Zastenker GN, and Richardson JD. Orientation of Sharp Fronts of the Solar Wind Plasma. *Cosmic Res* (2003) 41:382–91. doi:10.1023/a:1025061711391
10. Lyon JG. The Solar Wind-Magnetosphere-Ionosphere System. *Science* (2000) 288:1987–91. doi:10.1126/science.288.5473.1987
11. Borovsky JE. Contribution of Strong Discontinuities to the Power Spectrum of the Solar Wind. *Phys Rev Lett* (2010) 105:111102. doi:10.1103/physrevlett.105.111102
12. Hietala H, Phan TD, Angelopoulos V, Oieroset M, Archer MO, Karlsson T, et al. *In Situ* Observations of a Magnetosheath High-Speed Jet Triggering Magnetopause Reconnection. *Geophys Res Lett* (2018) 45:1732–40. doi:10.1002/2017gl076525
13. Plaschke F, Hietala H, Archer M, Blanco-Cano X, Kajdič P, Karlsson T, et al. Jets Downstream of Collisionless Shocks. *Space Sci Rev* (2018) 214:1–77. doi:10.1007/s11214-018-0516-3
14. Newman R, Vainchtein D, and Artemyev A. Solar Wind Transient Currents: Statistical Properties and Impact on Earth's Magnetosphere. *Sol Phys* (2020) 295:1–16. doi:10.1007/s11207-020-01695-z
15. Barkhatov NA, Korolev AV, Zastenker GN, Ryazantseva MO, and Dalin PA. MHD Simulations of the Dynamics of Sharp Disturbances of the Interplanetary Medium and Comparison with Spacecraft Observations. *Cosmic Res* (2003) 41:529–38. doi:10.1023/B:COSM.0000007951.49454.8a
16. Riazantseva MO, Khabarova OV, Zastenker GN, and Richardson JD. Sharp Boundaries of Solar Wind Plasma Structures and an Analysis of Their Pressure Balance. *Cosmic Res* (2005) 43:157–64. doi:10.1007/s10604-005-0030-8
17. Gonzalez WD, Joselyn JA, Kamide Y, Kroehl HW, Rostoker G, Tsurutani BT, et al. What is a Geomagnetic Storm. *J Geophys Res* (1994) 99:5771–92. doi:10.1029/93ja02867
18. Gonzalez WD, Tsurutani BT, and Clúa de Gonzalez AL. Interplanetary Origin of Geomagnetic Storms. *Space Sci Rev* (1999) 88:529–62. doi:10.1023/a:1005160129098
19. Zhang J, Richardson IG, Webb DF, Gopalswamy N, Huttunen E, Kasper JC, et al. Solar and Interplanetary Sources of Major Geomagnetic Storms (Dst≤ −100 nT) during 1996-2005. *J Geophys Res* (2007) 112:a–n. doi:10.1029/2007JA012321
20. Shen C, Chi Y, Wang Y, Xu M, and Wang S. Statistical Comparison of the ICME's Geoeffectiveness of Different Types and Different Solar Phases from 1995 to 2014. *J Geophys Res Space Phys* (2017) 122:5931–48. doi:10.1002/2016ja023768
21. Burlaga LF. Micro-scale Structures in the Interplanetary Medium. *Sol Phys* (1968) 4:67–92. doi:10.1007/BF00146999
22. Greco A, Chuychai P, Matthaeus WH, Servidio S, and Dmitruk P. Intermittent MHD Structures and Classical Discontinuities. *Geophys Res Lett* (2008) 35. doi:10.1029/2008GL035454
23. Greco A, Matthaeus WH, Servidio S, Chuychai P, and Dmitruk P. Statistical Analysis of Discontinuities in Solar WIND ACE Data and Comparison with Intermittent Mhd Turbulence. *ApJ* (2009) 691:L111–L114. doi:10.1088/0004-637x/691/2/l111
24. Greco A, Matthaeus WH, Servidio S, and Dmitruk P. Waiting-time Distributions of Magnetic Discontinuities: Clustering or Poisson Process? *Phys Rev E* (2009) 80:046401. doi:10.1103/PhysRevE.80.046401
25. Servidio S, Greco A, Matthaeus WH, Osman KT, and Dmitruk P. Statistical Association of Discontinuities and Reconnection in Magnetohydrodynamic Turbulence. *J Geophys Res* (2011) 116:a–n. doi:10.1029/2011JA016569
26. Yang L, Zhang L, He J, Tu C, Wang L, Marsch E, et al. The Formation of Rotational Discontinuities in Compressive Three-Dimensional MHD Turbulence. *ApJ* (2015) 809:155. doi:10.1088/0004-637X/809/2/155
27. Yang L, Zhang L, He J, Tu C, Li S, Wang X, et al. Formation and Properties of Tangential Discontinuities in Three-Dimensional Compressive MHD Turbulence. *ApJ* (2017) 851:121. doi:10.3847/1538-4357/aa9993
28. Lin RP, Anderson KA, Ashford S, Carlson C, Curtis D, Ergun R, et al. A Three-Dimensional Plasma and Energetic Particle Investigation for the Wind Spacecraft. *Space Sci Rev* (1995) 71:125–53. doi:10.1007/BF00751328
29. Lepping RP, Acũna MH, Burlaga LF, Farrell WM, Slavin JA, Schatten KH, et al. The Wind Magnetic Field Investigation. *Space Sci Rev* (1995) 71:207–29. doi:10.1007/BF00751330
30. Jian LK, Russell CT, and Luhmann JG. Comparing Solar Minimum 23/24 with Historical Solar Wind Records at 1 AU. *Sol Phys* (2011) 274:321–44. doi:10.1007/s11207-011-9737-2
31. Richardson IG, and Cane HV. Near-earth Solar Wind Flows and Related Geomagnetic Activity during More Than Four Solar Cycles (1963-2011). *J Space Weather Space Clim* (2012) 2:A02. doi:10.1051/swsc/2012003
32. Chi Y, Shen C, Luo B, Wang Y, and Xu M. Geoeffectiveness of Stream Interaction Regions from 1995 to 2016. *Space Weather* (2018) 16:1960–71. doi:10.1029/2018sw001894
33. Coleman PJJ. Turbulence, Viscosity, and Dissipation in the Solar-Wind Plasma. *ApJ* (1968) 153:371. doi:10.1086/149674
34. Horbury TS, Forman MA, and Oughton S. Spacecraft Observations of Solar Wind Turbulence: an Overview. *Plasma Phys Control Fusion* (2005) 47:B703–B717. doi:10.1088/0741-3335/47/12B/S52
35. Sorriso-Valvo L, Carbone V, and Bruno R. On the Origin of the Strong Intermittent Nature of Interplanetary Magnetic Field. *Space Sci Rev* (2005) 121:49–53. doi:10.1007/s11214-006-5559-1
36. Bruno R. Intermittency in Solar Wind Turbulence from Fluid to Kinetic Scales. *Earth Space Sci* (2019) 6:656–72. doi:10.1029/2018EA000535
37. Verscharen D, Klein KG, and Maruca BA. The Multi-Scale Nature of the Solar Wind. *Living Rev Sol Phys* (2019) 16:1–136. doi:10.1007/s41116-019-0021-0
38. Marsch E, and Tu C. Non-gaussian Probability Distributions of Solar Wind Fluctuations. *Ann Geophys* (1994) 12:1127–38. doi:10.1007/s00585-994-1127-8
39. Bruno R, Carbone V, Sorriso-Valvo L, and Bavassano B. Radial Evolution of Solar Wind Intermittency in the Inner Heliosphere. *J Geophys Res* (2003) 108:1130. doi:10.1029/2002JA009615
40. Bruno R, Telloni D, Primavera L, Pietropaolo E, D'Amicis R, Sorriso-Valvo L, et al. Radial Evolution of the Intermittency of Density Fluctuations in the Fast Solar Wind. *ApJ* (2014) 786:53. doi:10.1088/0004-637x/786/1/53
41. Neugebauer M, Clay DR, Goldstein BE, Tsurutani BT, and Zwickl RD. A Reexamination of Rotational and Tangential Discontinuities in the Solar Wind. *J Geophys Res* (1984) 89:5395–408. doi:10.1029/JA089iA07p05395
42. Horbury TS, Burgess D, Fränz M, and Owen CJ. Three Spacecraft Observations of Solar Wind Discontinuities. *Geophys Res Lett* (2001) 28:677–80. doi:10.1029/2000GL000121
43. Knetter T, Neubauer FM, Horbury T, and Balogh A. Four-point Discontinuity Observations Using Cluster Magnetic Field Data: A Statistical Survey. *J Geophys Res* (2004) 109:A06102. doi:10.1029/2003JA010099
44. Vasquez BJ, Abramenko VI, Haggerty DK, and Smith CW. Numerous Small Magnetic Field Discontinuities of Bartels Rotation 2286 and the Potential Role of Alfvénic Turbulence. *J Geophys Res Space Phys* (2007) 112:A11102. doi:10.1029/2007ja012504
45. Paschmann G, Haaland S, Sonnerup B, and Knetter T. Discontinuities and Alfvénic Fluctuations in the Solar Wind. *Ann Geophys* (2013) 31:871–87. doi:10.5194/angeo-31-871-2013
46. Tsurutani BT, and Ho CM. A Review of Discontinuities and Alfvén Waves in Interplanetary Space: Ulysses Results. *Rev Geophys* (1999) 37:517–41. doi:10.1029/1999RG900010
47. Hudson PD. Discontinuities in an Anisotropic Plasma and Their Identification in the Solar Wind. *Planet Space Sci* (1970) 18:1611–22. doi:10.1016/0032-0633(70)90036-x
48. Neugebauer M. Alignment of Velocity and Field Changes across Tangential Discontinuities in the Solar Wind. *J Geophys Res* (1985) 90:6627–30. doi:10.1029/JA090iA07p06627
49. Burlaga LF. Nature and Origin of Directional Discontinuities in the Solar Wind. *J Geophys Res* (1971) 76:4360–5. doi:10.1029/JA076i019p04360
50. Turner JM, and Siscoe GL. Orientations of Rotational and Tangential Discontinuities in the Solar Wind. *J Geophys Res* (1971) 76:1816–22. doi:10.1029/ja076i007p01816
51. Smith EJ. Identification of Interplanetary Tangential and Rotational Discontinuities. *J Geophys Res* (1973) 78:2054–63. doi:10.1029/JA078i013p02054

52. Neugebauer M. Comment on the Abundances of Rotational and Tangential Discontinuities in the Solar Wind. *J Geophys Res* (2006) 111:A04103. doi:10.1029/2005JA011497
53. Artemyev AV, Angelopoulos V, Halekas JS, Vinogradov AA, Vasko IY, and Zelenyi LM. Dynamics of Intense Currents in the Solar Wind. *Astrophysical J* (2018) 859:95. doi:10.3847/1538-4357/aabe89
54. Artemyev AV, Angelopoulos V, and Vasko IY. Kinetic Properties of Solar Wind Discontinuities at 1 AU Observed by ARTEMIS. *J Geophys Res Space Phys* (2019) 124:3858–70. doi:10.1029/2019JA026597
55. Sonnerup BU, and Scheible M. Minimum and Maximum Variance Analysis. *Anal Methods multi-spacecraft Data* (1998) 1:185–220.
56. Lepping RP, and Behannon KW. Magnetic Field Directional Discontinuities: 1. Minimum Variance Errors. *J Geophys Res* (1980) 85:4695–703. doi:10.1029/JA085iA09p04695
57. Zhdankin V, Boldyrev S, Perez JC, and Tobias SM. Energy Dissipation in Magnetohydrodynamic Turbulence: Coherent Structures or "Nanoflares"? *ApJ* (2014) 795:127. doi:10.1088/0004-637X/795/2/127

Conflict of Interest: The authors declare that the research was conducted in the absence of any commercial or financial relationships that could be construed as a potential conflict of interest.

frontiers in Physics

ORIGINAL RESEARCH
published: 26 November 2021
doi: 10.3389/fphy.2021.762488

Origin of Extremely Intense Southward Component of Magnetic Field (B_s) in ICMEs

Chenglong Shen[1,2]*, *Yutian Chi*[2], *Mengjiao Xu*[2] and *Yuming Wang*[1,2]

[1]CAS Center for Excellence in Comparative Planetology, University of Science and Technology of China, Hefei, China, [2]CAS Key Laboratory of Geospace Environment, Department of Geophysics and Planetary Sciences, University of Science and Technology of China, Hefei, China

The intensity of the southward component of the magnetic field (B_s) carried by Interplanetary Coronal Mass Ejections (ICMEs) is one of the most critical parameters in causing extreme space weather events, such as intense geomagnetic storms. In this work, we investigate three typical ICME events with extremely intense B_s in detail and present a statistical analysis of the origins of intense B_s in different types of ICMEs based on the ICME catalogue from 1995 to 2020. According to the *in-situ* characteristics, the ICME events with extremely high B_s are classified into three types: isolated ICMEs, multiple ICMEs, and shock-ICME interaction events with shocks inside ICMEs or shocks passing through ICMEs. By analyzing all ICME events with $B_s \geq 10$nT and $B_s \geq 20$nT, we find that 39.6% of $B_{s,mean} \geq 10nT$ events and 50% of $B_{s,mean} \geq 20nT$ events are associated with shock-ICME events. Approximately 35.7% of shock-ICME events have $B_{s,mean} \geq 10nT$, which is much higher than the other two types (isoloted ICMEs: 7.2% and multiple ICMEs: 12.1%). Those results confirm that the ICMEs interaction events are more likely to carry extreme intense B_s and cause intense geomagntic storms. Only based on the *in-situ* observations at Earth, some interaction ICME events, such as shock-ICME interaction events with shocks passing through the preceding ICME or ICME cannibalism, could be classified as isolated ICME events. This may lead to an overestimate of the probability of ICME carrying extremely intense B_s. To further investigate such events, direct and multi-point observations of the CME propagation in the inner heliosphere from the Solar Ring Mission could be crucial in the future.

Keywords: interplanetary coronal mass ejection, shock-ICME interaction, multiple ICMEs, intense Bs, interplanetary magnetic field

OPEN ACCESS

Edited by:
Qiang Hu,
University of Alabama in Huntsville, United States

Reviewed by:
Talwinder Singh,
University of Alabama in Huntsville, United States
Xochitl Blanco-Cano,
National Autonomous University of Mexico, Mexico

***Correspondence:**
Chenglong Shen
clshen@ustc.edu.cn

Specialty section:
This article was submitted to Stellar and Solar Physics, a section of the journal Frontiers in Physics

Received: *22 August 2021*
Accepted: *25 October 2021*
Published: *26 November 2021*

Citation:
Shen C, Chi Y, Xu M and Wang Y (2021) Origin of Extremely Intense Southward Component of Magnetic Field (B_s) in ICMEs. Front. Phys. 9:762488. doi: 10.3389/fphy.2021.762488

1 INTRODUCTION

Interplanetary Coronal Mass Ejections (ICMEs), the interplanetary counterparts of the Coronal Mass Ejections (CMEs), are considered to be the main source of geomagnetic storms, especially the intense geomagnetic storms [1–9]. By studing the intense geomagnetic storms from 1995 to 2014, Shen et al. [9] reported that 87% of intense geomagnetic storms with $Dst_{\min} \leq -100nT$ were caused by ICMEs. This result is consistent with the results obtained by Zhang et al. [3] and Kilpua et al. [10]. From another point of view, Shen et al. [9] found that 20% of ICMEs caused intense geomagnetic storms. This might be caused by the fact that ICMEs are the main sources of the southward component of the interplanetary magnetic field (B_s, the absolute value of the southward component

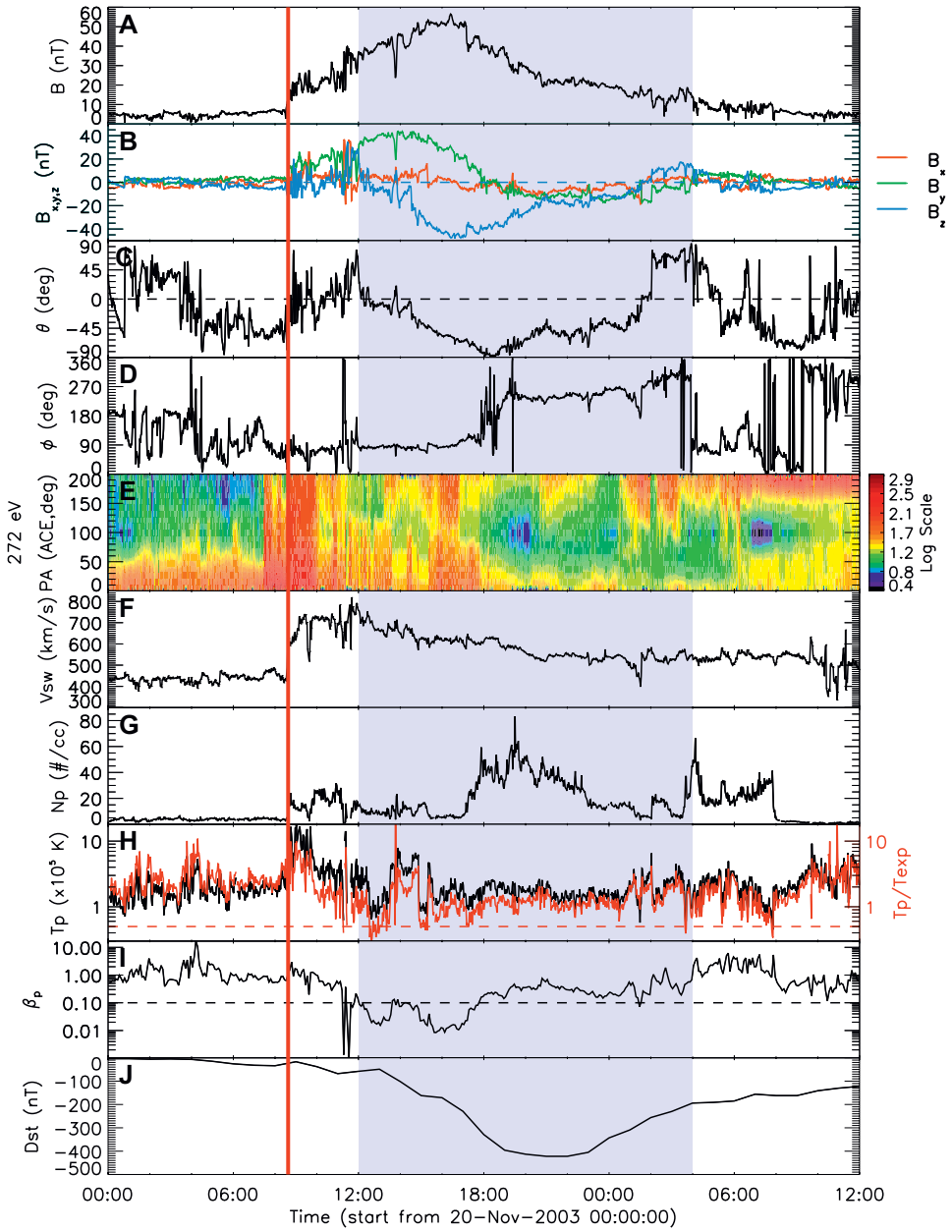

FIGURE 1 | Wind observations from 2003 November 20 00:00 to 2003 November 21 12:00. From top to bottom, the panels are: **(A)** the magnetic field strength (|*B*|), **(B)** the x,y, and z magnetic field components in GSE coordinates; **(C, D)** the elevation θ and azimuth ϕ of field direction in GSE; **(E)** the suprathermal electron pitch-angle distribution; **(F)** the solar wind speed; **(G)** the proton density N_p; **(H)** temperature (red, expected temperature); **(I)** proton β; **(J)** D_{st} index. The red vertical line indicates the arrival time of shock. The gray shadow regions indicate the intervals of the ICME.

of the magnetic field). When the southward magnetic field reaches the Earth, it will interact with the magnetosphere and then cause geomagnetic storms [11,12]. Thus, the intensities of B_s carried by ICMEs are important parameters in space weather studies and forecasting. Based on the ICMEs catalogue developed by the University of Science and Technology of China group [13], which is abbreviated as USTC ICME catalogue hereafter, the mean value of the B_s in the ICME ($B_{s,mean}$) varied from 0 to 35.39 nT with the mean value for all ICMEs of 4.40 nT.

According to the previous work, the intensities of geomagnetic storms caused by ICMEs are strongly associated with the intensities of B_s embedded with ICMEs ([9,14–16], and references therein). ICMEs with higher B_s are more likely to cause intense magnetic storms [17,18]. Thus, the origin of the intense B_s is an important question. Based on the literature, the interaction between multiple CMEs would enhance the magnetic field in the ICMEs [9,15,17–19]. In addition, as a special type of multiple ICMEs interaction, the interaction between previous

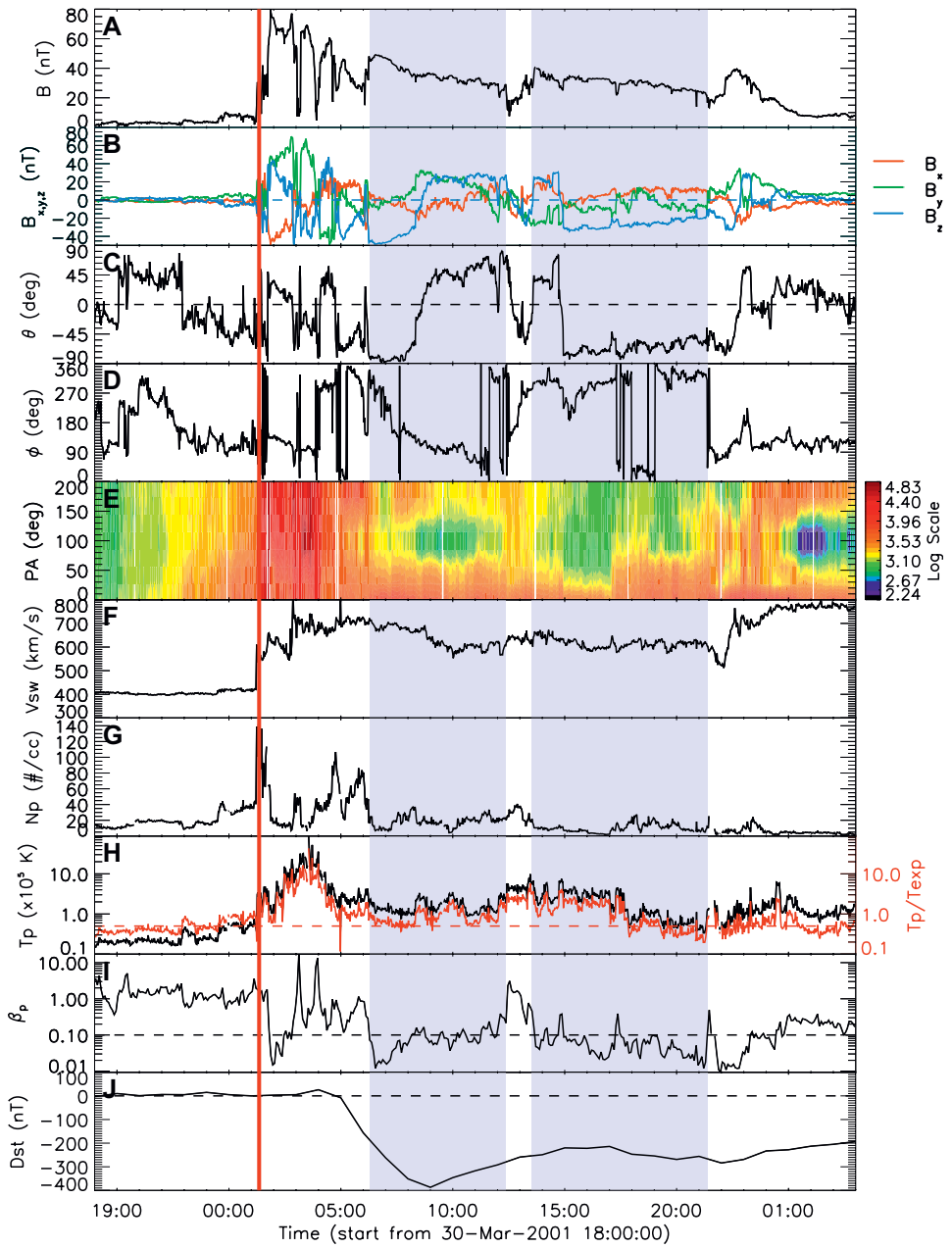

FIGURE 2 | Wind observations from 2001 March 30 18:00 to 2001 April 1 04:00 with the associated geomagnetic storm index (Dst). The panels are the same as in **Figure 1**.

ICMEs and following shocks could also enhance the B_s in the ICMEs significantly [9,20–24]. Shen et al. [18] found that in the shock-ICME interaction event of 6–11 September 2017, the shock compression enhanced B_s inside the ICME from 10 to 30 nT. In their following work, Xu et al. [21] analyzed 18 moderate to intense geomagnetic storms caused by shock-ICME interaction events, showing that the shock compression can enhance the intensities of B_s in ICME by a factor of 2. But, questions still remained. For example, is it possible for the isolated ICME to carry extremely strong B_s? If so, why? Are there any other possible explanations for the abnormally strong B_s in isolated ICMEs?

In this work, we discuss the possible origins of the extreme intense B_s in the ICMEs based on the typical events anaylsis. In **Section 2–5**, we will introduce some typical events with extremely high B_s in the ICMEs. In the last section, we will present some conclusions and discussions.

2 EXTREME B_S VALUE INSIDE ISOLATED ICME: 2003 NOVEMBER 20 EVENT

An ICME with extremely high B_s is the 2003 November 20 event. This event caused the strongest geomagnetic storms in the past 30 years with the peak value of Dst index of −422 nT [25–27]. As indicated in **Figure 1**, an obvious fast forward shock (red vertical line) was detected by Wind spacecraft at 08: 37 UT on November 20. Approximately 3.5 h later, an obvious ICME reached the Earth and lasted about 16 h, as shown by the gray shadow region in **Figure 1**. The ICME exhibits characteristics of magnetic clouds including a rise in magnetic field strength, a smooth rotation in magnetic field vector, and a drop in proton temperature and plasma beta. No additional ICME was detected by Wind spacecraft in 6 h preceding or after this ICME, indicating that this ICME was an isolated ICME event. It indicates that the isolated ICME events also have the potential to carry extremely intense B_s. The possible reasons are: 1) this ICME has a southward axial magnetic field with a high inclination (−73°) to the ecliptic plane [25], allowing a long duration and intense *Bs* to be embedded. 2) this ICME may have interacted with another narrow CME, which erupted an hour earlier than this CME from the same solar source region [27]. During propagation, the preceding narrow CME may be cannibalised by the subsequent large CME, or its propagating direction was deflected away from the Sun-Earth line during the interaction and thus not recorded by the WIND spacecraft.

3 EXTREME B_S DUE TO MULTIPLE ICME INTERACTION: 2001 MARCH 31 EVENT

Figure 2 shows an example of multiple ICME interaction event: the 2001 March 31 event. This event has been widely discussed by different authors [15,28]. As shown in **Figure 2**, an ICME (shown as the first gray shadow) was detected from 06:18 UT to 12:22 UT on March 31. During this period, the interplanetary observations show obvious ICME signatures with enhanced magnetic field strength, smoothly rotated magnetic field vector, low proton temperature, and low plasma beta. This ICME drove a shock ahead of it (red vertical line), featured by sudden and simultaneous enhancements of the magnetic field, solar wind speed, proton density, and temperature. B_s in this ICME was extremely strong with the mean value of 35.39 nT and maximum value of 48.44 nT. This is the ICME event with the strongest B_s recorded near the Earth from 1995 to 2020 based on the USTC ICME catalogue [13]. After the arrival of the extremely strong *Bs* carried by this ICME, there was an intense geomagnetic storm with $Dst_{\min}$ of -387 nT at 09:00 UT. About 1 h later, another ICME crossed the Earth from 13:30 UT to 21:22 UT on March 31. This ICME also carried intense B_s with the mean value of 25.36 nT and the maximum value of 35.38 nT. This is the sixth strongest ICME in B_s from 1995 to 2020. Between the two ICMEs, an interaction region exhibited with less regular magnetic field direction, lower magnetic field intensity, higher proton density, higher temperature, and higher plasma β compared with the values in ICMEs [15]. Those signatures are consistent with the magnetic reconnection between the two ICMEs, which may reduce the magnetic field strength and heat the plasma temperature [29]. The abnormally high plasma temperature in the first ICME and the first half of the second ICME suggested a strong interaction and compression between them. The velocity at the rear of the second ICME has obviously increased from 600–800 kms^{-1}. It might be caused by another ejecta, which was detected by the Wind spacecraft on April 1 at 05:26UT. The interval between the second ICME and the following ejecta exceeds 6 h. The following ejecta is not likely to interact with the second ICME adequately, according to the interaction criterion from Shen et al. [9]. Therefore, the interaction between CMEs was primarily responsible for the extraordinarily intense B_s in these two ICMEs.

4 EXTREME B_S DUE TO SHOCK-ICME INTERACTION

Another widely known mechanism that can cause extremely intense B_s is the interaction between shocks and ICMEs. This type of interaction event is identified when the shock driven by the subsequent ICME with a higher velocity propagates into the preceding ICME [20]. Based on the recent works, there are two types of shock-ICME interaction events, i.e., shock-ICME interaction event, and shock passing through preceding ICME event.

4.1 Typical Shock-ICME Interaction Event: 2001 November 5 Event

Figure 3 shows an example of the shock-ICME interaction event: 2001 November five event. This event has also been widely studied by many authors [20,30]. Wang et al. [20] first reported this event as a shock-ICME interaction event. It caused an intense geomagnetic storm with the peak value of the Dst index of −292 nT. An obvious ICME signature arrived at the Earth at 20:19UT on November 5, as shown in **Figure 3**. After 9 h, Wind spacecraft recorded the rare boundary of this ICME at 05:26 UT on November 6. During the passage of the ICME, an obvious shock was recorded at the time of 01:43 UT on November 6, which was caused by the subsequent ICME showing in **Figure 3** as the left gray shadow. The magnetic field intensity increased noticeably from 22 to 68 nT after the arrival of this shock. In particular, the magnitude of B_s increased from 5 to 52 nT. For this ICME, the B_s had a mean value of 23.07 nT and a maximum value of 74.47 nT. The following ICME also showed a strong B_s with a mean value of 25.41 nT. This shock-ICME event was the fifth strongest ICME in B_s from 1995 to 2020 based on the USTC ICME catelogue. The shock compression from the previous ICME generated this incredibly severe *Bs*. It's worth noting that this shock-ICME interaction increased not only the magnetic field's intensity but also the intensity of solar energy particles (SEP) within it [30]. Such enhancement is another important influence of shock-ICME interaction in the space weather effect of ICMEs.

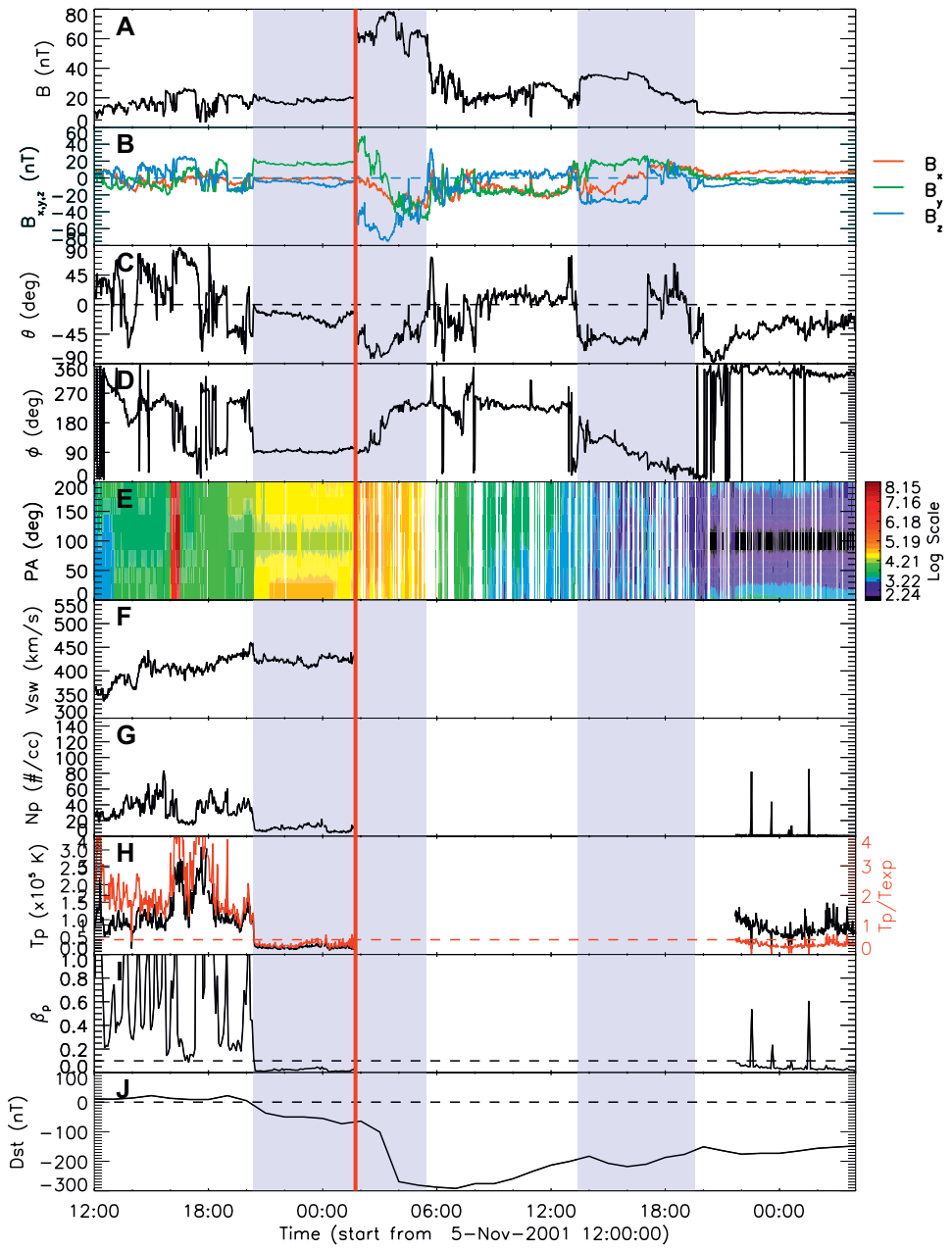

FIGURE 3 | Wind observations from 2001 November 5 12:00 to 2001 November 7 04:00. The panels are the same as in **Figure 1**.

4.2 Shock Passing Through Preceding ICME: The 2012 June 16 Event

On 2012 June 16, another ICME with extremely strong B_s was recorded near the Earth. This event caused a geomagnetic storm with the peak value of the *Dst* index of −71 nT. **Figure 4** shows the Wind observations of this ICME starting from 08:00 UT on 2012 June 16. From 22:07 UT on June 16, 2012, to 11:20 UT on June 17, 2012, a regular structure, shown as the first shaded region in the figure, passed through the Earth. During this period, the magnetic field intensity enhanced, the directions of the magnetic field rotated smoothly and the temperature and plasma β are relatively lower than those in the solar wind. These signatures indicated that this structure was an ICME. This ICME structure has also been reported by Srivastava et al. [31], Kilpua et al. [32], Scolini et al. [33] and Chi et al. [24]. About 3 h before the arrival of this ICME, two obvious shocks with the signatures of the obvious jumps of magnetic field intensity, solar wind velocity, proton density and proton temperature were recorded by Wind at 19:30 UT (red vertical line) and 20:53 UT (dashed red vertical line) on June 16. Based on the Wind observations, it is hard to identify which shock is related to the following ICME and what

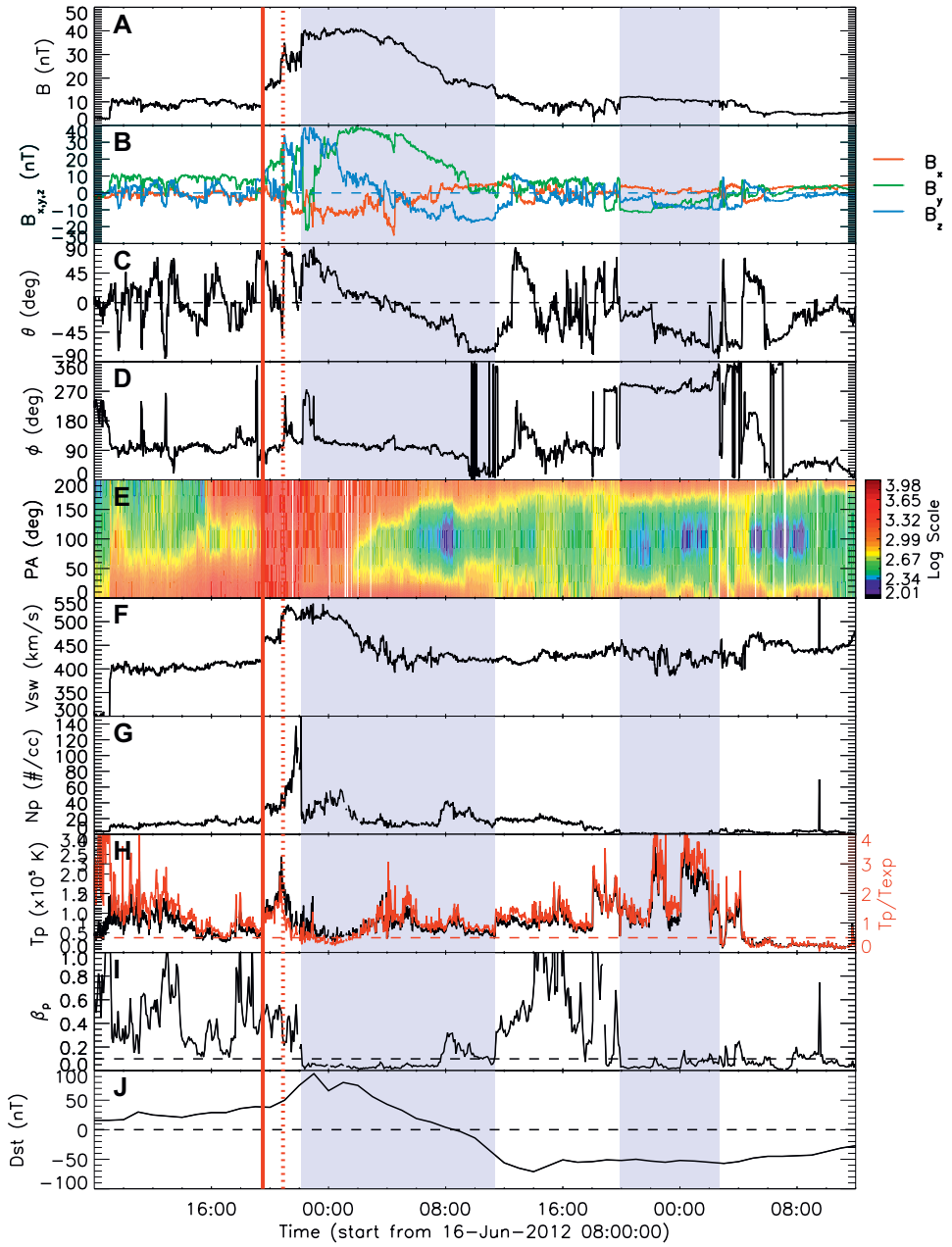

FIGURE 4 | Wind observations from 2012 June 16 to 2012 June 18. The panels are the same as in **Figure 1**.

the interplanetary sources of the two shocks are. At 20:02 UT on June 17, another ICME arrived at the Earth, lasting about 8 h (indicated as the left gray shadow). It should notice that the interval between these two ICMEs was 8.6 h, and there were no significant signatures of CME interaction. Thus, the interaction between these two ICMEs might be very weak.

The magnetic field intensity of the preceding ICME is extremely high. The maximum value and the mean value of the total magnetic field intensity are 41.14 and 30.31 nT, respectively. It is the top four strongest ICME in magnetic field strength, according to the ICME catalogue compiled by USTC ICME catalogue. It is caused by a weak interaction between two ICMEs, or by an 'isolated' ICME.

Fortunately, Venus is almost parallel to the Sun-Earth line, with a separation angle of only 5° at this time. Using the Venus Express observations [34], different authors studied the evolution of these structures during their propagation from the Sun to the Earth [24,32]. **Figure 5** shows the observations of this event near Venus. The intervals of data when Venus Express was close to or within the Venusian magnetosphere have been cut out based on the radial distance of the spacecraft to the centre of Venus (as shown in the last panel). An obvious shock-ICME structure with

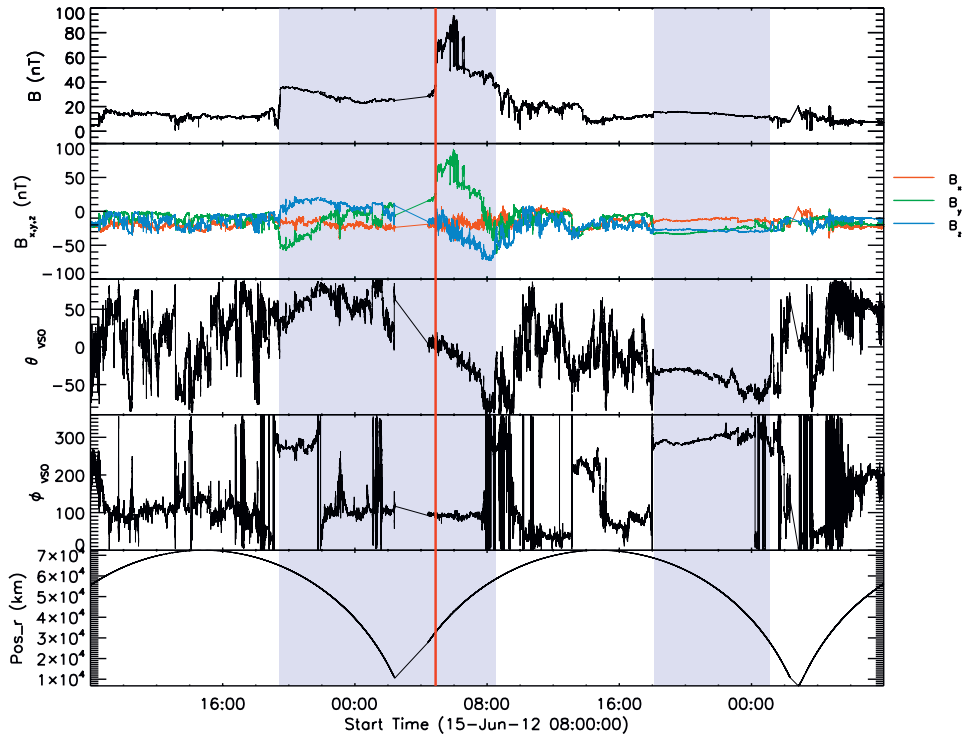

FIGURE 5 | Venus Express observations from 2012 June 16 to 2012 June 18. From top to bottom, the panels display magnetic field strength, x, y, and z components in VSO coordinates, elevation θ and azimuth ϕ of the magnetic field direction in VSO coordinates, and the radial distance of the spacecraft to the center of Venus. The arrival of the shock is indicated by the red vertical line. The intervals of the two ICMEs are shown by the gray shaded areas.

a sudden enhancement in magnetic field can be identified in **Figure 5**. Combined with the interplanetary observations near the Earth, we can suggest that the two ICMEs observed by Venus Express corresponded to the two ICMEs observed near the Earth. The shock inside the ICME recorded by Venus Express corresponded to the second shock before the first ICME near the Earth. This shock was driven by the second ICME, and it arrived at Venus at 04:53UT on June 16 and arrived at the Earth at the time of 20:53 UT. The time of the shock detected at Venus and Earth is comparable to the predicted arrival time of the second CME from EUHFORIA model [32] and Heliospheric Upwind eXtrapolation time model [24]. Combined with these observations, we can conclude that the shock driven by the second ICME has already passed through the first ICME. These analyses have also been done by Chi et al. [24]. This event show another origination of extremely intense B_s in side ICME: a shock driven by the following ICME passes through the preceding ICME.

5 STATISTICAL RESULT

To make a further analysis, we analyzed all the ICMEs events with $B_{s,mean} \geq 10nT$ during the period from 1995 to 2020 using the USTC ICME catalogue. Due to the lack of Venus Express observations for most events, we simply divided all the ICME events observed by Wind into three groups: isolated ICMEs (I-ICMEs), multiple ICMEs (M-ICMEs), and shock-ICME interaction events (S-ICMEs), using the same criteria from Shen et al. [9]. When the time interval between two ICMEs is less than 6 h, the two or three ICMEs are grouped together as an M-ICMEs event. It is characterised as an S-ICME when *in-situ* observations identify a shock generated by a subsequent ICME propagating into the preceding ICME or passing through the preceding ICME.

During this period, there are 48 ICME groups with $B_{s,mean} \geq 10nT$ and 8 ICMEs with $B_{s,mean} \geq 20nT$. **Table 1** shows the numbers of such events originated in different types of ICME

TABLE 1 | The numbers and percentages of ICME groups in different types with strong $B_{s,mean}$.

	I-ICMEs	M-ICMEs	S-ICMEs	Total
All events	333	33	56	422
$B_{s,mean} \geq 10$ nT	24 (7.2%)	4 (12.1%)	20 (35.7%)	48 (11.4%)
$B_{s,mean} \geq 20$ nT	3 (0.9%)	1 (3.0%)	4 (7.1%)	8 (1.9%)

events. It is found that 39.6% (20 in 48) of $B_{s,mean} \geq 10nT$ events and 50% (4 in 8) of $B_{s,mean} \geq 20nT$ events are associated with shock-ICME events. Meanwhile, we also present the percentage of different types of ICMEs with $B_{s,mean} \geq 10nT$ and $B_{s,mean} \geq 20nT$. It is found that the possibilities of S-ICMEs causing intense B_s are much higher than that of other groups. Meanwhile, I-ICMEs are much less likely to have intense B_s. These results suggest that the interaction between multiple CMEs, especially the interaction between shock and CME is the main cause of intense B_s in the interplanetary space. It is consistent with the prior results from Shen et al. [9,18] and Xu et al. [21], that the interaction between multiple CMEs has a greater chance of generating severe geomagnetic storms.

6 CONCLUSION AND DISCUSSION

In this work, we studied the origin of extremely intense B_s based on the typical events analysis and statistical analysis. In the analysis of the typical events, four events with extremely high B_s were studied in detail. Extremely intense B_s have been discovered to come from a variety of ICME types, including I-ICMEs, M-ICMEs, S-ICMEs with shocks inside ICMEs, and S-ICMEs with shocks passed through ICMEs. Furthermore, we studied all the ICME events with $B_{s,mean} \geq 10nT$ from 1995 to 2020, and found that the interaction events (i.e., M-ICMEs, and S-ICMEs) can result in extremely high B_s with a higher probability. The possible reason is the compression. For M-ICMEs, the compression between two ICMEs can enhance the magnetic field intensity. While, for S-ICMEs, the shock compression the magnetic field inside the previous ICME might be the main mechanism. When we compare the two interaction ICME types, we find that approximately 35.7% of S-ICMEs events had $B_{s,mean} \geq 10nT$, which is significantly higher than that of M-ICMEs (12.1%). It makes sense because the shock can intensify the pre-condition B_s by a factor of 3–6 [35]. The intensity of B_s embedded in the preceding ICME can be amplified when the shock driven by the subsequent ICME propagated into the preceding one. Because the intensity of B_s is a key parameter for intense geomagnetic storms, these findings confirm the previous results that ICME interaction events are more likely to cause intense geomagnetic storms [9,17].

It should be noted that, we reported a special type of ICMEs with extremely intense B_s: S-ICMEs with shocks passing through ICMEs. This type of S-ICME observed at 1AU appears to be an I-ICME. As a result, it is difficult to distinguish this type in the statistical analysis, only based on the interplanetary observations near the Earth. It is a plausible assumption that some I-ICMEs detected by Wind spacecraft may not be the real isolated ICME events. In addition, Lugaz et al. [17] reported another possibility that some multiple-ICMEs interaction events could also exhibit I-ICME signature [19,36]. These results suggest an overestimate of the possibility of I-ICMEs in carrying extremely intense B_s. The direct and multi-point observations of CME's propagation in interplanetary space from Solar Ring Mission [37] will be valuable in advancing our understanding of such phenomena.

DATA AVAILABILITY STATEMENT

Publicly available datasets were analyzed in this study. This data can be found here: https://cdaweb.gsfc.nasa.gov/index.html/.

AUTHOR CONTRIBUTIONS

CS design and made the main analysis of this work. YC and MX analyzed the typical events. YW take part in the discussion.

FUNDING

This work is supported by grants from the NSFC (41822405,41774181, 42004143, 41774178, 41904151), the Strategic Priority Program of CAS (XDB41000000), the Fundamental Research Funds for the Central Universities (WK2080000140, WK2080000122), project funded by China Postdoctoral Science Foundation (2019M652194), and Anhui Provincial Natural Science Foundation (1908085MD107).

ACKNOWLEDGMENTS

We acknowledge the Venus Express team and WIND team for providing the data.

REFERENCES

1. Gosling JT, McComas DJ, Phillips JL, Bame SJ. Geomagnetic Activity Associated With Earth Passage of Interplanetary Shock Disturbances and Coronal Mass Ejections. *J Geophys Res* (1991) 96:7831. doi:10.1029/91ja00316
2. Xue X, Wang C, Dou X. An Ice-Cream Cone Model for Coronal Mass Ejections. *J Geophys Res Space Phys* (2005) 110:A08103. doi:10.1029/2004ja010698
3. Zhang J, Richardson I, Webb D. Solar and Interplanetary Sources of Major Geomagnetic Storms (Dst ≤ −100 nT) During 1996–2005. *J Geophys Res Space Phys* (2007) 112:A10102. doi:10.1029/2007JA012321
4. Echer E, Gonzalez W, Tsurutani B. Interplanetary Conditions Leading to Superintense Geomagnetic Storms (Dst ≤ −250 nT) during Solar Cycle 23. *Geophys Res Lett* (2008) 35:L06S03. doi:10.1029/2007gl031755
5. Wu C-C, Lepping RP. Geomagnetic Activity Associated With Magnetic Clouds, Magnetic Cloud-Like Structures and Interplanetary Shocks for the Period 1995-2003. *Adv Space Res* (2008) 41:335–8. doi:10.1016/j.asr.2007.02.027
6. Richardson IG, Cane HV. Near-Earth Interplanetary Coronal Mass Ejections During Solar Cycle 23 (1996 - 2009): Catalog and Summary of Properties. *Sol Phys* (2010) 264:189–237. doi:10.1007/s11207-010-9568-6
7. Yermolaev YI, Nikolaeva N, Lodkina I, Yermolaev MY. Recovery Phase of Magnetic Storms Induced by Different Interplanetary Drivers. *J Geophys Res Space Phys* (2012) 117:A08207. doi:10.1029/2012ja017716
8. Wu C-C, Gopalswamy N, Lepping RP, Yashiro S. Terrestrial. *Atmos Oceanic Sci* (2013) 24:233. doi:10.3319/tao.2012.09.26.03(sec)
9. Shen C, Chi Y, Wang Y, Xu M, Wang S. Statistical Comparison of the ICME's Geoeffectiveness of Different Types and Different Solar Phases

from 1995 to 2014. *J Geophys Res Space Phys* (2017) 122:5931–48. doi:10.1002/2016ja023768
10. Kilpua E, Koskinen HE, Pulkkinen TI. Coronal Mass Ejections and Their Sheath Regions in Interplanetary Space. *Living Rev Solar Phys* (2017) 14:5. doi:10.1007/s41116-017-0009-6
11. Gonzalez WD, Joselyn JA, Kamide Y, Kroehl HW, Rostoker G, Tsurutani BT, et al. What Is a Geomagnetic Storm? *J Geophys Res* (1994) 99:5771. doi:10.1029/93ja02867
12. Gonzalez WD, Tsurutani BT, Clúa de Gonzalez AL. Interplanetary Origin of Geomagnetic Storms. *Space Sci Rev* (1999) 88:529–62. doi:10.1023/a:1005160129098
13. Chi Y, Shen C, Wang Y, Xu M, Ye P, Wang S. Statistical Study of the Interplanetary Coronal Mass Ejections From 1995 to 2015. *Sol Phys* (2016) 291:2419–39. doi:10.1007/s11207-016-0971-5
14. Wu C-C, Lepping R. Effect of Solar Wind Velocity on Magnetic Cloud-Associated Magnetic Storm Intensity. *J Geophys Res Space Phys* (2002) 107: SSH 3-1. doi:10.1029/2002JA009396
15. Wang YM, Ye PZ, Wang S. Multiple Magnetic Clouds: Several Examples During March–April 2001. *J Geophys Res Space Phys* (2003) 108:1370. doi:10.1029/2003JA009850
16. Wu C-C, Lepping RP. Relationships Among Geomagnetic Storms, Interplanetary Shocks, Magnetic Clouds, and Sunspot Number During 1995 - 2012. *Sol Phys* (2016) 291:265–84. doi:10.1007/s11207-015-0806-9
17. Lugaz N, Temmer M, Wang Y, Farrugia CJ. The Interaction of Successive Coronal Mass Ejections: A Review. *Sol Phys* (2017) 292:64. doi:10.1007/s11207-017-1091-6
18. Shen C, Xu M, Wang Y, Chi Y, Luo B. Why the Shock-ICME Complex Structure Is Important: Learning From the Early 2017 September CMEs. *Astrophysical J* (2018) 861:28. doi:10.3847/1538-4357/aac204
19. Chi Y, Zhang J, Shen C, Hess P, Liu L, Mishra W, et al. Observational Study of an Earth-Affecting Problematic ICME From STEREO. *Astrophysical J* (2018) 863:108. doi:10.3847/1538-4357/aacf44
20. Wang Y, Ye P, Wang S, Xue X. An Empirical Formula Relating the Geomagnetic Storm's Intensity to the Interplanetary Parameters: VB_z and Δt. *Geophys Res Lett* (2003) 30. doi:10.1029/2003GL017901
21. Xu M, Shen C, Wang Y, Luo B, Chi Y. Importance of Shock Compression in Enhancing ICME's Geoeffectiveness. *Astrophysical J* (2019) 884:L30. doi:10.3847/2041-8213/ab4717
22. Liu YD, Chen C, Zhao X. Characteristics and Importance of "ICME-In-Sheath" Phenomenon and Upper Limit for Geomagnetic Storm Activity. *Astrophysical J* (2020) 897:L11. doi:10.3847/2041-8213/ab9d25
23. Scolini C, Chané E, Temmer M, Kilpua EKJ, Dissauer K, Veronig AM, et al. CME-CME Interactions as Sources of CME Geoeffectiveness: The Formation of the Complex Ejecta and Intense Geomagnetic Storm in 2017 Early September. *Astrophysical J Suppl Ser* (2020) 247:21. doi:10.3847/1538-4365/ab6216
24. Chi Y, Scott C, Shen C, Owens M, Lang M, Xu M, et al. Using the "Ghost Front" to Predict the Arrival Time and Speed of CMEs at Venus and Earth. *Astrophysical J* (2020) 899:143. doi:10.3847/1538-4357/aba95a
25. Gopalswamy N, Yashiro S, Michalek G. Solar Source of the Largest Geomagnetic Storm of Cycle 23. *Geophys Res Lett* (2005) 32(12). doi:10.1029/2004gl021639
26. Yushkov K, Gnezdilov G, Markeev S. Solar and Heliospheric Disturbances that Resulted in the Strongest Magnetic Storm of November 20, 2003. *Geomagnetism and Aeronomy* (2005) 45:20.
27. Wang Y-M, Shen C-L, Ye P-Z, Wang S. Comparison of Space Weather Effects of Two Major Coronal Mass Ejections in Late 2003. *J Univ Sci Technology China* (2007) 37(8):859–867.
28. Farrugia C, Jordanova V, Thomsen M. A Two-Ejecta Event Associated With a Two-Step Geomagnetic Storm. *J Geophys Res Space Phys* (2006) 111:A11104. doi:10.1029/2006ja011893
29. Lugaz N, Manchester IV WB, Gombosi TI. Numerical Simulation of the Interaction of Two Coronal Mass Ejections From Sun to Earth. *Astrophysical J* (2005) 634:651–62. doi:10.1086/491782
30. Shen C, Wang Y, Ye P, Wang S. Enhancement of Solar Energetic Particles During a Shock - Magnetic Cloud Interacting Complex Structure. *Sol Phys* (2008) 252:409–18. doi:10.1007/s11207-008-9268-7
31. Srivastava N, Mishra W, Chakrabarty D. Interplanetary and Geomagnetic Consequences of Interacting CMEs of 13 - 14 June 2012. *Sol Phys* (2018) 293:5. doi:10.1007/s11207-017-1227-8
32. Kilpua EKJ, Good SW, Palmerio E, Asvestari E, Lumme E, Ala-Lahti M, et al. Multipoint Observations of the June 2012 Interacting Interplanetary Flux Ropes. *Front Astron Space Sci* (2019) 6:50. doi:10.3389/fspas.2019.00050
33. Scolini C, Rodriguez L, Mierla M, Pomoell J, Poedts S. Observation-Based Modelling of Magnetised Coronal Mass Ejections With EUHFORIA. *Astron Astrophysics* (2019) 626:A122. doi:10.1051/0004-6361/201935053
34. Zhang T, Baumjohann W, Delva M. Magnetic Field Investigation of the Venus Plasma Environment: Expected New Results From Venus Express. *Planet Space Sci* (2006) 54:1336. doi:10.1016/j.pss.2006.04.018
35. Yue C, Zong Q. Solar Wind Parameters and Geomagnetic Indices for Four Different Interplanetary Shock/ICME Structures. *J Geophys Res Space Phys* (2011) 116:A12201. doi:10.1029/2011ja017013
36. Dasso S, Mandrini CH, Schmieder B. Linking Two Consecutive Nonmerging Magnetic Clouds With Their Solar Sources. *J Geophys Res Space Phys* (2009) 114:A02109. doi:10.1029/2008ja013102
37. Wang Y, Ji H, Wang Y, Xia L, Shen C, Guo J, et al. Concept of the Solar Ring mission: An Overview. *Sci China Technol Sci* (2020) 63:1699–713. doi:10.1007/s11431-020-1603-2

Conflict of Interest: The authors declare that the research was conducted in the absence of any commercial or financial relationships that could be construed as a potential conflict of interest.

The handling editor declared a past co-authorship with one of the authors MX.

Advantages of publishing in Frontiers

OPEN ACCESS
Articles are free to read for greatest visibility and readership

FAST PUBLICATION
Around 90 days from submission to decision

HIGH QUALITY PEER-REVIEW
Rigorous, collaborative, and constructive peer-review

TRANSPARENT PEER-REVIEW
Editors and reviewers acknowledged by name on published articles

Frontiers
Avenue du Tribunal-Fédéral 34
1005 Lausanne | Switzerland

Visit us: www.frontiersin.org
Contact us: frontiersin.org/about/contact

REPRODUCIBILITY OF RESEARCH
Support open data and methods to enhance research reproducibility

DIGITAL PUBLISHING
Articles designed for optimal readership across devices

FOLLOW US
@frontiersin

IMPACT METRICS
Advanced article metrics track visibility across digital media

EXTENSIVE PROMOTION
Marketing and promotion of impactful research

LOOP RESEARCH NETWORK
Our network increases your article's readership